Diffractive gratings in high-precision interferometry for gravitational wave detection

by

Jonathan Mark Hallam

A thesis submitted to

The University of Birmingham

for the degree of

DOCTOR OF PHILOSOPHY

Astrophysics and Space Research Group

School of Physics and Astronomy

The University of Birmingham

December 2010

Abstract

Einstein's Theory of General Relativity describes gravity as the curvature of space-time and predicts gravitational waves. Laser interferometric gravitational wave detectors attempt to observe the strain gravitational waves exert on space-time, which is obscured by seismic, thermal and quantum among other noises.

Diffraction gratings have been proposed in all reflective configurations as core optical elements in future detectors. In this thesis phase changes are shown to occur due to lateral displacement of diffractive optics. These couple noise from interferometer alignment into the gravitational wave phase signal. For the end-mirror tilt of a 3 km Fabry-Perot arm cavity as used in gravitational wave detectors, this was found to set quite severe isolation requirements. This result was supported by a bench-top experiment, and by collaborative work on the Joint Interferometer Facility (JIF) diffractive cavity.

Using a steady-state technique to derive the coupling relations, a signal to noise ratio between lateral grating displacement and a notional gravitational wave signal was determined for each output port of the three-port coupled diffractive Fabry-Perot cavity. The forward-reflecting output port offers the highest SNR at low frequencies due to cancellation of the phase noise. The JIF cavity result confirmed this calculation.

Acknowledgements

Doctor Andreas Freise, who offered me this opportunity to be both student and colleague, ultimately my being here, and everything I've learnt, is down to him. Similarly, Doctors Stefan Hild and Simon Chelkowski, for a lively education in techniques theoretical and computational, and for imparting some few of the tricks to working in and operating a optics laboratory. Doctor Antonio Perreca, who made it just before I, and a steadfast comrade through every difficulty. So too Paul Fulda, who came a little later to the party but was surely the life of it, and whose clarity of thought brought an light into the dark places of my writing.

So to Doctors Keiko Kokeyama and Ludovico Carbone, who made useful contributions despite stepping in at the end of all things, and then made insightful comments on this very document. It would not be as good without them. Hasnain Panjwani and his supervisor Professor Clive Speake, for waiving their usual rates for the use of their EUCLID device. Deepali Lodhia, Stuart Aston, David Stops, John Bryant, Ron Cutler, Dave Hoyland, Anthony Page and Steve Brookes all, for sins too varied and useful to mention herein.

Finally, my parents, for getting me to the point of being able to do this incredible thing, and Jennifer. Hon, you were there every time things got more stressful than they should, always patient, eternally understanding. I couldn't have made it without you.

Thank you all

Yours,

Jonathan

Statement of Originality

This thesis presents research work undertaken primarily at the University of Birmingham between September 2006 and 2010.

Chapter One contains an introduction to the field of gravitational wave detection built on reviewing appropriately cited published works.

Chapter Two discusses the basics of interferometry in some greater mathematical depth. This chapter independently derives known results from appropriately cited starting points, drawn from various texts.

Chapter Three provides an introduction to diffraction gratings, reviewing prior work from cited papers and some basic theory from cited texts where required. It continues with a discussion of the origins of lateral grating displacement induced phase noise, and its coupling into gravitational wave signal. Much of this work was published by Freise et al *Phase and alignment noise in grating interferometers, New Journal of Physics*, 2007, from this group and in collaboration with the AEI Max Planck Institute for Gravitational Physics in Hannover. I was involved in some discussions prior to the publication of this paper, and later produced the expanded consideration presented in this chapter.

Chapter Four describes experimental work that I performed in the laboratory at the University of Birmingham, including predictions and the required data analysis. The diffraction grating was provided through the collaboration of this group with the AEI Max Planck Institute for Gravitational Physics in Hannover. Section 4.9 of this chapter details work carried out in collaboration with, and therefore only partially by this author, using the JIF at the University of Glasgow.

Chapter Five is almost entirely taken from the paper Hallam et al *Coupling of lateral grating*

displacement to the output ports of a diffractive Fabry-Perot cavity, Journal of Optics A: Pure and Applied Optics, 2009. I led both the work and the publication process in collaboration with the other authors.

Chapter Six is a concluding review of the work presented herein.

Appendix A contains schematics of various electronics used in the experiment. These schematics were obtained from various sources or designed by myself, and the appropriate attribution can be found in the header text.

Appendices B, C and D contain some details of work undertaking by myself in the University of Birmingham laboratories. Additionally, appendix D contains some details of the EUCLID device created by colleagues at the University of Birmingham, drawn from appropriately cited papers published or in press, and some personal correspondence and conversations.

Appendice E is entirely my own work calibrating the measured voltage axis of Figure E.3 to create the equivalent longitudinal motion per unit tilt axis of Figure 4.9.

Contents

List of Figures vii

List of Tables xiii

1 INTRODUCTION 1

1.1 Detection of gravitational waves 1

1.1.1 Gravitational waves 1

1.1.2 Expected gravitational observations... 3

1.2 Overview interferometric gravitational wave detectors and noise sources 5

1.2.1 Seismic and Newtonian noise 7

1.2.2 Quantum mechanical (shot and radiation pressure) noise 8

1.2.3 Thermal noises 11

1.3 Gratings and the motivations for their use 15

1.4 Elements to be addressed by this thesis 16

2 BASICS OF INTERFEROMETRY 19

2.1 Basic Optics 19

2.1.1 Description of a light field 19

2.1.2 Effect of transmission or reflection on power and field amplitude 20

2.1.3 Phase modulation of a light field 20

2.1.4 Michelson interferometer outputs 22

2.2 Signal Sources in a Michelson Interferometer 25
2.2.1 Gravitational Wave Phase Signal 26
2.2.2 Frequency Noise 27
2.3 Frequency domain modeling of Fabry-Perot cavities 27
2.3.1 Light fields in a cavity 27
2.3.2 Optical power in the cavity 30
2.3.3 Free-spectral range, full width at half maximum, and finesse 31
2.3.4 Impedance matched, undercoupled, overcoupled 32
2.3.5 Hermite-Gaussian beams 33
2.3.6 Cavity stability and resonator g-parameters 36
2.4 Feedback control schemes 39
2.4.1 Offset feedback control 40
2.4.2 Pound-Drever-Hall feedback control 41

3 ALIGNMENT SENSITIVITY 47

3.1 Alignment sensitivity of diffractive Fabry-Perot cavities 47
3.2 Functioning of a grating 50
3.2.1 Huygens-Fresnel principle 50
3.2.2 Fraunhofer diffraction from many slits 51
3.2.3 Littrow configuration 53
3.2.4 Quantities imposed by the Bragg equation 54
3.2.5 Differing reflection coefficients of a three-port grating 55
3.3 Phase changes caused by moving an optic 57
3.3.1 Displacement in the plane of the optic 57
3.3.2 Displacement perpendicular to the plane of the optic 59
3.3.3 Null vector 60
3.3.4 Rotation of the optic 61

3.4 Fabry-Perot cavities . . . 62
3.5 Case one: Two-mirror cavity . . . 64
3.5.1 Case one, effect one, response to end mirror displacement . . . 66
3.5.2 Case one, effect two, tilt induced phase change . . . 69
3.5.3 Case one, end mirror tilt isolation requirement . . . 71
3.6 Case two: Two-port coupled first order Littrow configuration grating cavity . . 73
3.6.1 Manufacturing techniques for high diffraction efficiency two-port grating 76
3.6.2 Case two, effect three, tilt induced phase change . . . 77
3.6.3 Case two, effect three, response to end mirror tilt . . . 80
3.6.4 Case two, effect one, response to a gravitational wave . . . 82
3.6.5 Case two, end mirror tilt isolation requirement . . . 82
3.7 Case three: Three-port coupled second order Littrow configuration grating cavity 84
3.7.1 Manufacturing techniques for low-loss, low-diffraction efficiency three-port gratings . . . 88
3.7.2 Case three, effect three, tilt induced phase change . . . 90
3.7.3 Case three, effect three, response to end mirror tilt . . . 92
3.7.4 Case three, effect one, response to gravitational wave . . . 94
3.7.5 Case three, end mirror tilt isolation requirement . . . 95
3.8 Summary . . . 97

4 EXPERIMENTAL DEMONSTRATION 101

4.1 Experimental demonstration of cavity response to end-mirror tilt . . . 101
4.2 Optical layout of experiment . . . 103
4.3 Expected result . . . 104
4.4 Experimental data analysis . . . 106
4.4.1 Schematic of the general case . . . 107
4.4.2 Open loop transfer function for effective cavity length . . . 110

4.4.3 End-mirror tilt induced signal . . . 113
4.5 Experimental Result . . . 117
4.6 Implementation of experimental cavities . . . 122
4.6.1 Cavity property selection . . . 123
4.6.2 Implementation of grating cavity . . . 124
4.6.3 End-mirror tilt actuator characterisation . . . 129
4.7 Measurement of residual longitudinal motion for a given angular tilt . . . 132
4.8 Calculation of expected signals with significant residual longitudinal motion . . . 135
4.8.1 Dominant noise source in the two-mirror case . . . 136
4.8.2 Calculating residual longitudinal motion for the two-mirror cavity . . . 137
4.8.3 Calculation of expected signal in grating case . . . 140
4.8.4 Comparison of grating and two-mirror cavity tilt response . . . 141
4.9 Suspended optic investigations at the University of Glasgow . . . 145
4.9.1 Configuration of the JIF cavity . . . 145
4.9.2 Translational driving of the JIF cavity . . . 147
4.9.3 Rotational driving of the JIF cavity . . . 150
4.10 Conclusions . . . 153

5 OUTPUT PORT PHASE-NOISE PERFORMANCE 155

5.1 Phase-noise performance of three-port coupled diffractive Fabry-Perot cavity output ports . . . 156
5.2 Frequency domain modeling of phase noise coupling in a grating cavity . . . 157
5.2.1 Coupling relations of a static grating . . . 158
5.2.2 Coupling relations of an oscillating grating . . . 159
5.2.3 Coupling relations of an oscillating grating as Fabry-Perot cavity input optic . . . 161
5.2.4 Carrier field solution . . . 163

5.2.5 Input sideband fields . . . 164
5.2.6 Sideband fields at outputs . . . 164
5.3 Signal coupling in a grating cavity . . . 165
5.4 Ratio of signal to noise at the outputs of a grating cavity . . . 166
5.4.1 Numerical result . . . 168
5.4.2 Suspension requirements . . . 170
5.5 Future work on interferometer configurations . . . 172
5.6 Summary and Outlook . . . 174

6 CONCLUSIONS 177

A ELECTRONIC CIRCUIT DIAGRAMS 181

A.1 Local Oscillator . . . 181
A.2 Photodetectors . . . 182
A.3 12 MHz Mixer . . . 182
A.4 Offset Box . . . 182
A.5 Buffer Box . . . 193
A.6 Servo . . . 193
A.7 High Voltage Amplifier . . . 193
A.8 Matrice Box . . . 205
A.9 Quadrant Photodetector . . . 206

B IMPLEMENTATION OF THE INITIAL BEAM 211

B.1 Laser beam characterisation . . . 211
B.1.1 Faraday isolator and other initial optics . . . 213
B.1.2 Beam-analysis and collimation . . . 214
B.1.3 Power splitting . . . 216
B.2 Cavity implementation . . . 216

C IMPLEMENTATION OF THE TWO-MIRROR CAVITY 219

C.1 Mode Matching 219

C.2 Offset Locking 221

C.2.1 End-mirror mount replacement 222

C.3 PDH Locking 224

D END MIRROR TILT ACTUATOR 229

D.1 Coupling matrix for tilt only motion 230

D.2 Longitudinal displacement effects 234

D.3 Minimisation of residual longitudinal motion 235

D.4 Functioning of EUCLID 238

E CALIBRATION OF FIGURE 4.9 243

E.1 Calibration of Figure 4.9 y-axis from measured voltages to longitudinal displacement per unit tilt 243

Bibliography 249

List of Figures

1.1 Gravitational Waves influencing a system of free test masses 2

1.2 Measured Virgo sensitivity curve 6

1.3 Calculated Virgo noise budget 7

1.4 Virgo quantum noise sensitivity limit 10

2.1 Simple Michelson Interferometer schematic 22

2.2 Two-mirror Fabry-Perot cavity schematic 28

2.3 Two-mirror Fabry-Perot cavity schematic, showing internal input only 29

2.4 Power gain in a Fabry-Perot cavity 30

2.5 Power transmitted, reflected from and circulating in Fabry-Perot cavity 33

2.6 Resonator g-parameter requirements of a cavity 38

2.7 Schematic diagram of idealised cavity-locking loop 39

2.8 Schematic diagram of practical offset locking loop 40

2.9 Schematic diagram of practical Pound-Drever-Hall feedback control loop . . . 41

2.10 Theoretical Pound-Drever-Hall error signal 44

3.1 Cartoon diagrams of diffractive Fabry-Perot cavities 48

3.2 Top sketch view of a diffractive optic 51

3.3 Sketch of Littrow configuration diffraction gratings 53

3.4 Sketch of three-port coupled diffraction grating 55

3.5 Phase change from Δx displacement of a grating 58
3.6 Phase change from Δz displacement of a grating 59
3.7 Vector for null phase change displacement of a grating 60
3.8 Schematic of two-mirror Fabry-Perot cavity with end mirror oscillation 64
3.9 Schematic diagram for misalignment of a two-mirror cavity 68
3.10 Two-port grating cavity configuration schematic 73
3.11 Schematic diagram for misalignment of a two port diffractive cavity 78
3.12 Three-port grating cavity configuration schematic 87
3.13 Schematic diagram for misalignment of a three port diffractive cavity 90

4.1 Physical diagram for intended experimental tilting of the end mirror 101
4.2 Experimental optical layout 103
4.3 Generic schematic diagram for transfer functions 108
4.4 Schematic diagram for open loop transfer function 111
4.5 Schematic diagram for practical end-mirror tilt transfer function 113
4.6 Physical diagram for transfer functions injected at error signal 116
4.7 Physical diagram for transfer functions injected to end-mirror tilt 116
4.8 Open loop transfer functions 118
4.9 End-mirror tilt to equivalent longitudinal displacement transfer function 119
4.10 Coherence of end-mirror tilt to equivalent longitudinal displacement 119
4.11 Grating Pound-Drever-Hall error signal in s-polarisation 124
4.12 Grating Pound-Drever-Hall error signal in p-polarisation 125
4.13 JAMMT model for cylindrical lenses 126
4.14 Grating cavity Pound-Drever-Hall error signal in p-polarisation and with cylindrical lenses. 127
4.15 Projection effect on beam shape interacting with a grating 127
4.16 EUCLID residual longitudinal motion measurements at 5 Hz and 50 Hz 132

4.17 EUCLID residual longitudinal motion measurements at 500 Hz 133
4.18 Lever arm measurement of angular change for actuator voltages 134
4.19 Two-mirror Fabry-Perot cavity with end-mirror displacement schematic 138
4.20 Schematic of the JIF cavity 146
4.21 JIF diffractive test-mass coil-magnet actuator mounting schematic 148
4.22 Lateral displacement response of JIF diffractive test mass to constant-amplitude input 148
4.23 JIF cavity phase response to various grating displacements 151

5.1 Light field amplitudes at a phase modulating grating schematic 158
5.2 Ports of a three-port coupled grating cavity schematic 161
5.3 Signal to noise ratio at output ports of a three-port grating gravity 169
5.4 Suspension requirement for the maximum tolerable lateral grating displacement 171
5.5 Sketch diagrams of various possible all-reflective interferometer configurations . 173

A.1 Local Oscillator Source Box 1/1. 183
A.2 Local Oscillator Source Box 1/1. 184
A.3 Local Oscillator Splitter Box 1/2. 185
A.4 Local Oscillator Splitter Box 2/2. 186
A.5 Universal (broadband) Photodetector used in transmission (for offset locking) 1/1.187
A.6 Broadband Photodetector used in back-reflection (for PDH locking) 1/2. . . . 188
A.7 Broadband Photodetector used in back-reflection (for PDH locking) 2/2. . . . 189
A.8 12 MHz Mixer 1/3. 190
A.9 12 MHz Mixer 2/3. 191
A.10 12 MHz Mixer 3/3. 192
A.11 Offset Box 1/2. 194
A.12 Offset Box 2/2. 195
A.13 Buffer Box 1/1. 196

A.14 Servo 1/4. 197
A.15 Servo 2/4. 198
A.16 Servo 3/4. 199
A.17 Servo 4/4. 200
A.18 High Voltage Amplifier 1/4. 201
A.19 High Voltage Amplifier 2/4. 202
A.20 High Voltage Amplifier 3/4. 203
A.21 High Voltage Amplifier 4/4. 204
A.22 Matrix Box 1/1. 205
A.23 Quadrant Photodetector 1/3. 207
A.24 Quadrant Photodetector 2/3. 208
A.25 Quadrant Photodetector 3/3. 209

B.1 The full optical layout used in the experiment, shown for the grating cavity configuration. 212
B.2 The initial optics of the laser, the collimation lenses and the power splitting and adjusting apparatus. 212
B.3 Uncollimated analysis of the laser beam 215
B.4 JAMMT collimating calculation 216
B.5 Additional optics used to implement two mirror Fabry-Perot cavity 217

C.1 Beam profile before mode matching improvement iterations 220
C.2 Beam profile after mode matching improvement iterations 220
C.3 Ramping of laser frequency in a Fabry-Perot cavity. 221
C.4 System used for offset locking of two-mirror Fabry-Perot cavity. 222
C.5 Transfer function of JPD2 223
C.6 Transfer function of servo JMH3. 223
C.7 FFT scan of cavity 224

C.8 System used for Pound-Drever-Hall locking of two-mirror Fabry-Perot cavity . 225
C.9 Transfer function of the reflected photodetector JPD3 226
C.10 Pound-Drever-Hall error signal with cavity ramping 227
C.11 Single Pound-Drever-Hall error peak 227
C.12 Spectrum of PDH locked cavity 228

D.1 Schematic diagram of the PI.311 three-axis piezo tilting device 230
D.2 Matrix box transfer function 230
D.3 Schematic of three axis piezo rotational position 231
D.4 Triangular geometry 232
D.5 Schematic of three axis piezo for combined longitudinal and tilt 235
D.6 Schematic diagram for misalignment of a cavity 236
D.7 Matrix box and actuator high voltage amplifier transfer functions 239

E.1 Open-loop transfer functions with longitudinal end-mirror and laser frequency actuation 244
E.2 Longitudinal end-mirror open-loop transfer function divided by laser frequency actuation open loop transfer function 244
E.3 End-mirror tilt voltage to feedback voltage transfer functions 245

List of Tables

4.1 Important values associated with the experimental optical systems 105

4.2 Key features of the cavities 117

4.3 Key transfer functions to be recorded 117

4.4 Table of results for residual longitudinal motion calibration 135

4.5 Subscript key 136

4.6 Key features of the JIF diffractive cavity 150

Chapter 1

INTRODUCTION

1.1 Detection of gravitational waves

1.1.1 Gravitational waves

According to Einstein's theory of general relativity compact concentrations of energy, for example matter, warp space-time. If the velocity of such an energy concentration changes then a space-time warpage results which propagates through the universe at the speed of light. Since gravity is a consequence of the curvature of space-time this propagating warpage is called a Gravitational Wave [1].

Gravitational waves are caused by acceleration of mass. The strength of a gravitational wave is measured as a strain h, the fractional change in length ΔL between free falling test masses ('space time events' [2]) separated by proper distance L due to a gravitational wave passing through the system [3], where L is aligned with one polarisation axis of the gravitational wave

[2],

$$h = 2\Delta L/L. \tag{1.1}$$

The strain measured by a gravitational wave detector is a function of the amplitude of the signal at the source (how strongly the source generates gravitational waves) and of the distance from the source r, with the signal strength falling off as $1/r$ [4]. Signals predicted to generate strains of $h = 10^{-22}$ at the earth are expected to occur only a few times a year [5]. This imposes the requirement for unprecedented position sensitivity. Mass can only have positive sign, hence gravitational waves are quadruples. The effect of a gravitational wave of h_+ or h_+ polarisation is shown in Figure 1.1.

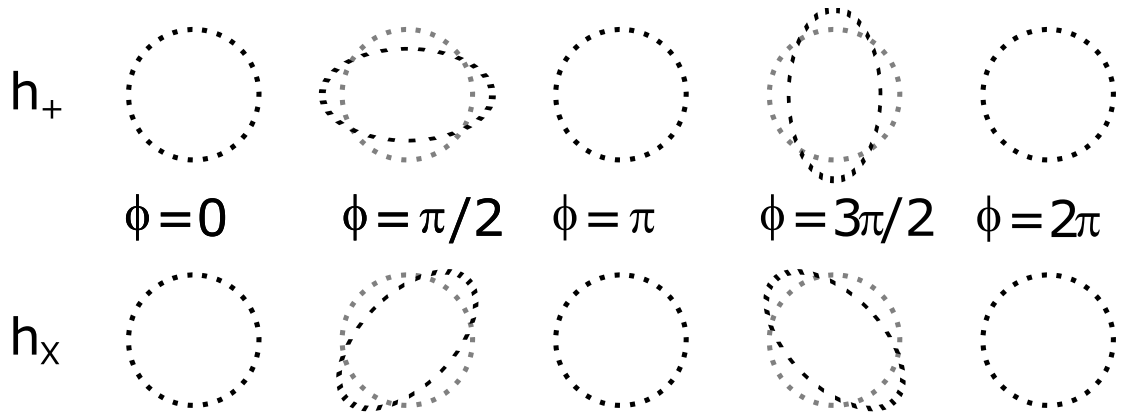

Figure 1.1: Gravitational Waves influencing a system of free test masses. The effect shown is for gravitational waves traveling perpendicular to the plane of the masses (i.e. into or out of the page). Both gravitational wave polarisations, h_+ and $h_\times$, are shown at particular phases along the wave (indicated by ϕ). These polarisations are base vectors which can be combined to form composite polarisations for a particular wave.

The phase-position in the wave is indicated, so initially (for the h_+ polarisation) the wave stretches the vertical axis and contracts the horizontal, then as the phase rotates through π with the passing of the wave, the vertical axis contracts and the horizontal stretches. A cross polarised wave, $\times$ or $h_\times$, rotates the axis of distortion by 45 degrees [5].

1.1.2 Expected gravitational observations...

...from future projects

Gravitational Waves are expected to be emitted from difference sources over a wide range of frequencies. In the range 10^{-18} to 10^{-15} Hz waves are expected to be imprinted on the cosmic background from primordial gravitational fluctuations in the early universe. This is the gravitational equivalent of the cosmic microwave background radiation, but because gravitational processes do not interact strongly they can theoretically be detected as remnants from the very early universe. An absolute lower limit on the origin time of the wave will exist where the wavelength of interest will not have been able to exist in a universe smaller than itself. In the frequency range 10^{-9} to 10^{-7} Hz sources are expected to be early universe processes and massive black hole binary systems (of combined mass of $\sim 2.6 \cdot 10^6$ solar masses) [6].

In the 10^{-4} to 1 Hz frequency band the proposed LISA (Laser Interferometer Space Antenna) detector is expected to observe mHz frequency binaries, which are known to exist from electromagnetic observations. Additional theoretically possible observations for LISA include the inspirals of compact objects (white dwarfs, neutron stars and black holes) into massive black holes [4].

...from current projects

Gravitational wave detectors have a particular designed sensitivity, which varies across the useful frequency band of the detector. Gravitational wave sources generate gravitational wave signals that reduce in strength by $1/r$ with distance r from the source. Therefore gravitational wave detectors are sensitive to events that strongly generate gravitational waves to a greater distance than to those events that only weakly generate gravitational waves. A particular design sensitivity can therefore be expressed as a detection horizon distance for a particular type of

event, which has a source strength determined from other data (electromagnetic observations and astrophysical theory). That detection horizon defines a volume of space surrounding the detector, and using other data to predict the number of those events within that horizon allows calculation of an expected event rate. It is worth noting at this point that design sensitivity is not the only critical property of gravitational wave detectors. Duty cycle (the fraction of time during which the detector is operational), and data quality (the presence or absence of 'glitches' in the data due to detector effects), are also important for making the first direct detection of a gravitational wave signal.

Ground based detectors such as LIGO (Laser Interferometer Gravitational-wave Observatory) [7] and Virgo [8] operate in the 40 Hz to 4 kHz frequency range. There has not yet been an identifiable gravitational wave detection from these devices; however, the last moments of black hole-black hole, black hole-neutron star and neutron star-neutron star are predicted to be detectable within a given distance of the detector depending on the sensitivity of the device. For mergers that involve a neutron star the tidal disruption of the neutron star by its companion should be observable with ground-based gravitational wave detectors. For the merging of two black holes it is the merge itself and the subsequent 'vibrational ringdown' of the combined black hole that is expected to generate the signal. These gravitational events can be compared with the gamma ray bursts expected from such mergers [4], providing a useful external check on the gravitational wave detection.

The detection range for an inspiral of two 1.4 solar mass neutron stars was twelve million parsecs for the LIGO S5 science run which occurred from 2005 to 2007 [7]. Data analysis for the LIGO S6 science run (July 2009 - October 2010) is in progress. Low mass rotating x-ray binaries, stellar core collapse, boiling of nascent neutron stars and accretion induced collapse of white dwarfs can all result in mass deformations at frequencies within the detection bands of ground based instruments, although the expected source strength is smaller than for inspirals [4]. Furthermore it is expected that new, optically unknown and theoretically unpredicted sources

of gravitational waves will be discovered with increases in detector sensitivity.

All gravitational waves passing through the plane of the interferometer will be observed superimposed on each other, so long as they are within the detectable frequency band [5]. Presently no signal has been observed above the noise of any detector, so the challenge of extracting small signals from the background is one for the future. It is worth noting that the expected event rates for detectable signal sources [4] and the detection range of the existing detectors science runs [7] are sufficiently low that not having made a direct detection of a gravitational wave signal is unsurprising.

1.2 Overview interferometric gravitational wave detectors and noise sources

In this section the primary noise sources that affect existing (first generation), substantially designed (second generation) and future (third-generation) ground-based gravitational wave detectors will be discussed. Existing ground based gravitational wave detectors are LIGO Hanford, LIGO Livingston, Virgo and GEO600. All of these use the geometry of the Michelson interferometer where light is split into two perpendicular beams then reflected and recombined destructively, with the arms out of phase such that the anti-symmetric port (shown $\mathrm{PD_B}$ in Figure 2.1 in the following chapter) receives no light (is at a 'dark fringe') [2]. When a gravitational wave of the correct polarisation passes through in the plane of the detector the quadrupole nature of the wave causes stretching of one beam-axis and contracting of the other (as shown in Figure 1.1), inducing a phase difference which breaks the destructive interference condition. This results in a detectable output of light at the anti-symmetric port, which can be monitored by a photodetector.

The sensitivity (signal to noise ratio) of a gravitational wave detector is a key measure of its

performance. The primary outstanding noise sources are shot and radiation pressure which are quantum mechanical in origin; seismic or Newtonian displacement of the end mirrors; or various thermal effects. Noise is particularly significant if it falls close to frequency bands of interest. For this reason interferometers such as LIGO and Virgo concentrate on optimising signal to noise ratio within a particular frequency 'bucket', in the case of LIGO 40 Hz to 4 kHz [7].

In sensitivity curves, such as the one shown in Figure 1.2 belonging to Virgo for October 20th 2009 from the VSR2 (Virgo Science Run 2) noise is of order $\sim 10^{-20}/\sqrt{\text{Hz}}$ at 10 Hz and falls to $\sim 10^{-22}$, $/\sqrt{\text{Hz}}$ by 100 Hz. A noise budget plot for Advanced Virgo is shown in Figure 1.3. This differs from the measured sensitivity curve in that the noise is broken down by source, with the theoretical contribution from each component shown. These noise sources will be discussed in more detail later in this chapter.

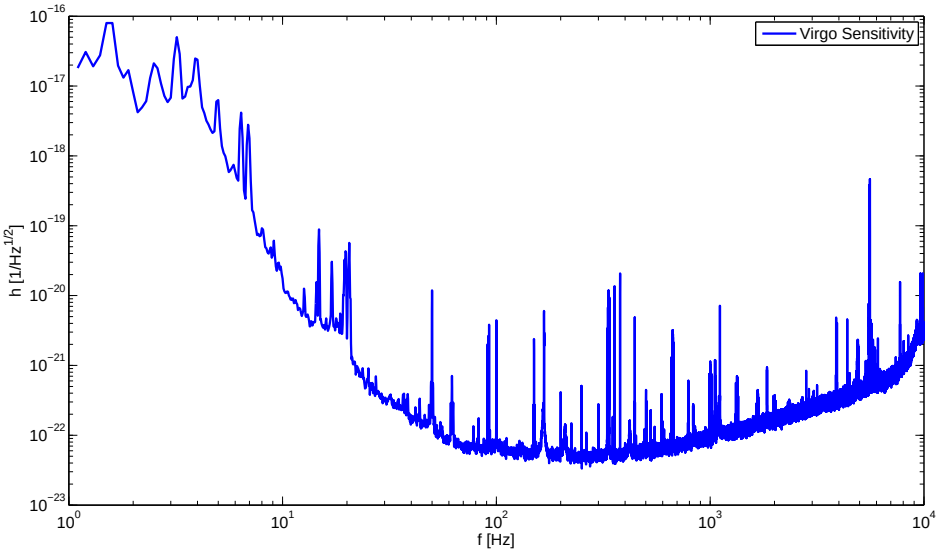

Figure 1.2: Measured Virgo sensitivity curve of October 20th 2009 from the VSR2 (Virgo Science Run 2), strain verses frequency, created from data provided online by the Virgo collaboration.

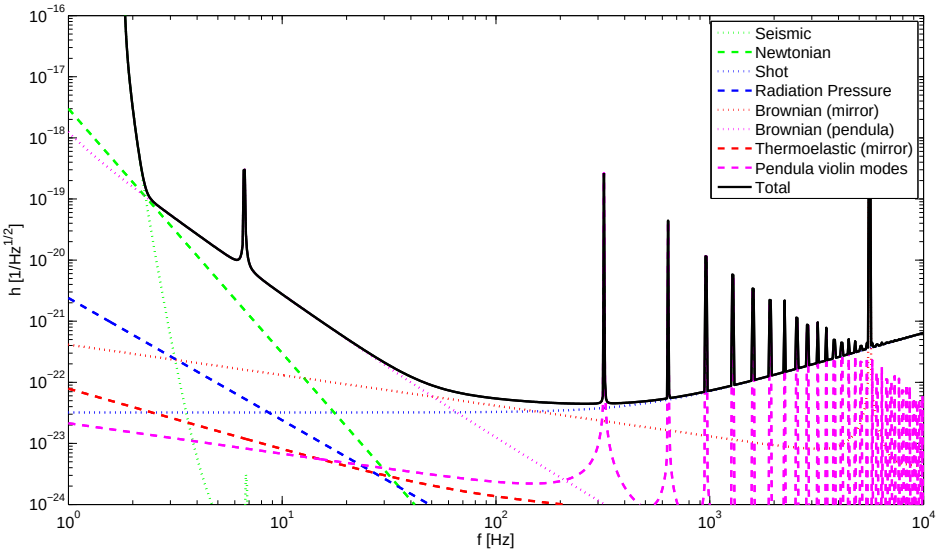

Figure 1.3: Virgo sensitivity curve [9] noise budget of 2004, strain verses frequency (data provided online by the Virgo collaboration). Total noise is shown along with the calculated contributions of various noise sources.

1.2.1 Seismic and Newtonian noise

Gravitational waves are detectable because they cause an effective length change in the arms of a Michelson interferometer. Seismic and Newtonian noise are physical length changes of those arms. To be certain that a particular signal from the interferometer is a gravitational wave rather than a noise induced displacement of the interferometer optics, the effect of the noise must be less than the gravitational wave signal.

Seismic noise is due to human activities and both geophysical and atmospheric phenomena. In the interferometer it is expressed as position and velocity uncertainty in the longitudinal, angular and lateral position of optical components. Seismic noise is typically reduced by suspending position critical optical components from pendula. A pendulum will suppress vibrations above its resonant frequency (except at multiples thereof). For a simple pendulum the resonant frequency is set by the length and material chosen for the pendulum. Virgo uses a chain of five connected pendulums to reduce the longitudinal and lateral components of seismic noise reaching the

suspended optic, and the top pendulum is suspended from a set of cantilever blades providing vertical isolation. The pendulums are position-controlled using a set of magnetic coil actuators, and stabilised using a feedback suppression loop [10]. Suitable siting can further reduce the seismic noise, particularly it is known that seismic noise is reduced underground [11] [12] and it is expected that third-generation gravitational wave detectors may be located in underground caverns [13].

Newtonian or gravity gradient noise is the gravitational effect of moving mass around the detector on the detector optics. It represents a firm lower limit on the reduction of seismic-like mass-motion noise for a given detector [14], although it may be possible to measure gravity gradient noise using a network of seismometers and use this information to compensate for its effects. Human sources of this noise can be limited by provision of 'exclusion zones' around the mirrors, suggested to be 10 m for people and 30 m for vehicles [15].

1.2.2 Quantum mechanical (shot and radiation pressure) noise

Shot noise

The best model for explaining the effects of quantum noise of light is to think in terms of vacuum fluctuations that enter the interferometer through the dark port (the interferometer arms are out of phase such that port B in Figure 2.1 is the dark port [2]). Fluctuations in the vacuum are coupled through the interferometer, interacting with the Fabry-Perot cavity test masses before being reflected back to the dark port and detected. This creates an uncertainty in the detected phase difference between the two interferometer arms, in which a gravitational wave signal would also appear. The shot noise contribution to the linear spectral density of the

gravitational wave strain amplitude detection limit is given by [16] [14],

$$h_{shot}(f) = \frac{1}{L}.\sqrt{\frac{\hbar\lambda c}{2\pi P_0}}. \tag{1.2}$$

It can be seen that the shot noise is a white noise: It has flat amplitude spectral density, depending only on interferometer length L and power P_0, with the shot noise sensitivity increasing by $\sqrt{P_0}$. This is shown for the Virgo interferometer [9] in Figure 1.4. Since gravitational wave signal increases proportional to P_0, the shot noise sensitivity limit decreases proportional to $\sqrt{P_0}$. Hence we can improve the signal to ratio verses shot noise by increasing the power.

Radiation pressure noise

Radiation pressure noise can be thought of as originating from amplitude vacuum fluctuations. It is similar to shot noise in that these fluctuations enter the interferometer through the dark port; however, these amplitude fluctuations lead to position uncertainty of the mirrors, and hence phase uncertainty between the arms (rather than directly to phase uncertainty as for shot noise). The radiation pressure contribution to the linear spectral density of the gravitational wave strain amplitude detection limit is given by, where m is the mass of the mirror test mass [17] [14],

$$h_{rp}(f) = \frac{1}{mLf^2}.\sqrt{\frac{\hbar P_0}{2\pi^3\lambda c}}. \tag{1.3}$$

Increasing the power (reducing shot noise contribution by $\sqrt{P}$) has the effect of increasing the radiation pressure noise contribution, also by $\sqrt{P}$, as shown in Figure 1.4. Radiation pressure noise falls off with a $1/f^2$ slope, and is inversely proportional to mirror mass, because more massive mirrors are better able to resist displacement by a given amplitude of vacuum fluctuation.

This combination of radiation pressure and shot noise defines the standard quantum limit, shown for Virgo [9] in Figure 1.4. The 'knee' of the combined shot and radiation pressure noises can be moved in the frequency-sensitivity phase space by adjusting the power, but cannot be positioned below the black line of the standard quantum limit, because the decreased shot noise sensitivity limit when increasing power is matched by increasing radiation pressure noise sensitivity limit, and vice versa. The position of this standard quantum limit is set by the features of the interferometer, for example the mirror mass contributes to setting the absolute level of radiation pressure noise.

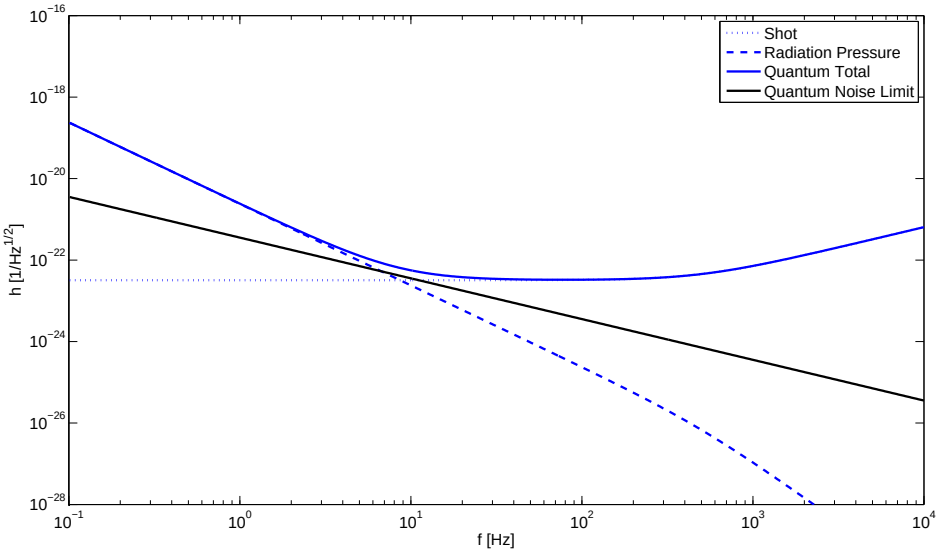

Figure 1.4: Virgo shot, radiation pressure, total quantum (shot plus radiation pressure) noise. The 'knee' of the total noise curve can be adjusted along the quantum noise limit (shown black) by adjusting the laser power. It cannot fall below the quantum noise limit due to the combination of radiation pressure and shot noise. Data from the Virgo sensitivity curve [9] noise budget of 2004, strain verses frequency.

The quadrature sum of shot and radiation pressure noise gives the optimal input power for a given frequency f positioning of the 'knee', where ω_0 is the angular frequency of the laser,

$$P_{SQL} = \frac{mL^2(2\pi f)^4}{4\omega_0}. \tag{1.4}$$

This semi-classical approach assumes that the shot and radiation pressure noise are uncorrelated [18]. In fact the radiation pressure noise is correlated with itself due to mechanical coupling in the interferometer.

It transpires that the required power to usefully position the 'knee' of the quantum noise curve is high, so high that no first-generation detector used it. They were dominated by shot noise in all quantum noise limited frequency regions as shown in Figure 1.3, even using power recycling mirrors to effectively increase the power [14].

1.2.3 Thermal noises

The term thermal noise refers to a combination of noise sources that obscure gravitational wave signals by displacing the surface of optics (either directly or by vibrating the suspending pendula), by delaying light within the interferometer, and by causing incorrect coupling of light within the interferometer that prevents its functioning as designed (for example, by causing a mis-mode matching between light input to a Fabry-Perot cavity and the cavity mirror properties, hence reducing the effective input light power - see Section 2.3 for an introduction to Fabry-Perot cavities). Brownian noise is associated with the absolute temperature of the detector optics. Thermoelastic, thermorefractive and thermal lensing are associated with differences in temperature within the optics of the detector. Such differences are primarily induced by partial absorption of the laser beam, which has a Gaussian cross-sectional profile. In general making the detector cooler will reduce all thermal noise sources, and increasing laser beam power will increase them.

Thermal noises are not the limiting factor in existing gravitational wave detectors, as shown in Figure 1.3; however, future detectors will both aim for increased sensitivity forcing thermal noises to be addressed, and they will reduce shot noise contributions by increasing laser power which will increase the thermal noise. Thermal noise can be broken down into different effects

and the different components of the interferometer that are affected by them.

Brownian noise

Brownian vibration energy $E = k_B T$ (Boltzmann constant multiplied by temperature in Kelvins) causes resonant modes of the mirrors, their coatings, and their supporting pendula to become excited. Resonances exciting the violin modes of the pendula (so called because the length of the pendulum oscillates like a plucked violin string) are particularly severe and itemised separately in Figure 1.3. For the supporting pendula Brownian noise causes the mirror mass to physically move as the pendulum vibrates. For the substrate and the coating it is the mirror surface that is displaced (one side of the substrate is coated with a high-reflective dielectric coating to create a mirror surface. The other is coated with an anti-reflective dielectric coating). The specific frequency of the effect varies depending on the exact setup of the interferometer. The stochastic force on the mirror can be represented by a power spectrum:

$$F^2(f) = 4k_B T \Re[z(f)], \tag{1.5}$$

where $z(f)$ is the mechanical impedance of the material. A material with low mechanical dispersion (high Q-factor) confines the vibration coupling to a narrow band around the resonant frequencies [19] [20]. These frequencies are then unusable for gravitational wave detection, so materials where these resonances fall outside the desired measurement band are preferred to manufacture pendula and optical substrates from. Where this is not possible, only a narrow segment of the usable frequency range will be lost with a sufficiently high Q-factor material. Virgo uses mirrors of a silica substrate, with $Q = 10^6$ having their first resonance mode at 3 kHz [14].

Thermoelastic and thermorefractive noise

Thermoelastic noise originates from thermodynamic fluctuations within the material. These induce strain within the substrate as the heating regions expand and cooling regions contract, which excites the resonant modes of the material. This thermoelastic noise leads to surface position uncertainties as in the case of Brownian noise. For the substrate fused silica has a small thermal expansion coefficient and therefore is less sensitive to thermoelastic noise compared to some alternatives. Sapphire, which has been proposed for gravitational wave interferometers due to its superior Brownian noise performance, has a relatively high thermal expansion coefficient. Thermoelastic noise may be the dominant thermal noise source in the case of Sapphire. The multilayer dielectric mirror coatings required for high reflection coefficients are more restricted in material choice, and this is expected to be a significant noise source for future detectors [21]. The anti-reflection coatings applied to the back face of mirrors, lenses and other optics have significantly fewer layers, and therefore proportionally less noise than high-reflection coatings.

Temperature variations across the material also affect refractive index, of both the substrate and the coating. Regions with a higher refractive index slow the portions of the light field which pass through them, causing phase shifts. This thermorefractive noise is dependent on the $\Delta n/\Delta T$ coefficient of the material chosen. It appears only when the field is transmitted through an optical coating or an optic optic, most notably the Michelson interferometer beam splitter and (if Fabry-Perot arm cavities are used) the cavity input mirrors. Transmission into optical coatings occurs even for all-reflective optics. Due to its relatively small contribution in current interferometers, thermorefractive noise is not separately itemised in Figure 1.3.

Thermal lensing

In our discussion of thermal noise we have so far considered it as induced by the natural temperature of the optics. However, all optical components have some absorption coefficient

from light fields, and the energy that they absorb is then dissipated typically as heat. When a TEM_{00} mode Gaussian laser beam light field is transmitted through an optic the Gaussian beam intensity profile and constant absorption coefficient means the heat created is not uniformly distributed. The beam width must be small compared to the optical component to prevent the loss of light field, so the initial thermal gradient can be quite extreme. This excess heat is mainly radiated from the surface of the mirror in the infrared. The exact distribution of thermal energy within the mirror depends on what equilibrium state (gradient) is established for this energy flow from heat input by laser beam absorption to the surface where infrared radiation is emitted. As discussed earlier in this section the energy flow (gradient) induces thermoelastic and thermorefractive noise; however, because the thermal gradient has a profile so to does the thermal expansion and change in refractive index. This gives rise to a lens within transmissive optics, and the expansion has similar surface deforming effects on non-transmissive optics. In the case of a Gaussian beam as in LIGO and the planned Advanced LIGO the thermal gradient is greater in the center of the beam effectively creating a convex lens. LIGO has a laser power of 6 W which couples to 10kW in the Fabry-Perot cavity of the detector arms. Advanced LIGO will have a laser power of approximately 100 W which will couple to 1 MW in the Fabry-Perot cavity [7]. Rather than appearing as a direct noise source in the manner of those shown in Figure 1.3 thermal lensing serves to mis-match the laser beam to the designed interferometer and Fabry-Perot cavity properties as discussed in Section 2.3.6, a significant problem [7]. Two oft-suggested solutions to these problems are compensatory heating to remove the thermal gradient across the substrate [22] or using materials with extremely low power absorption and a high thermal conductivity to reduce thermal gradients across the component.

1.3 Gratings and the motivations for their use

Historically reduction of thermal effects has been the primary motivation for proposing the use of diffraction gratings for Gravitational Wave interferometers. Gratings can be used to form all-reflective configurations by replacing transmissive cavity input mirrors and beam-splitters [23]. All reflective configurations eliminate thermorefractive noise, limit to the surface the absorption causing thermal lensing, and potentially allow opaque substrates (depending on the depth of evanescent field penetration into the substrate). Silicon in particular has superior Brownian noise performance, and thermoelastic performance better than that of sapphire (although worse than that of fused silica) but is opaque at the 1064 nm wavelength [21].

The two-port-coupled first-order-Littrow configuration diffraction grating cavity discussed in more depth in Section 3.6 requires a high diffraction efficiency. Therefore it has a rather different (and thinner) coating, and hence different coating thermal noise compared to the usual high-reflection efficiency coatings. This case has not been extensively studied because of the difficulty in producing high-diffraction efficiency gratings. Three-port-coupled second-order-Littrow configuration diffraction grating cavities require only traditional high-reflection coatings, but at a slightly lower thickness than when they are applied to a mirror [24]. It was thought that both grating cavities would have reduced coating thermoelastic and thermorefractive noise because their coatings are thinner; however, it has been found that the surface features of a grating cause a reduction in the Q-factor of the material used [25] which offsets any improvement made. Work is undergoing to improve the coating techniques used for diffraction gratings, and it is possible that in the future substantially advantageous coatings (or techniques for creating reflective gratings that do not require coatings) will be discovered.

In the interim, work on diffraction gratings has revealed that the new configurations made possible by diffraction gratings may have advantages that alone justify the use of diffraction gratings in gravitational wave interferometry. It has been mentioned herein that gratings allow all-

reflective interferometer configurations that are similar to the typical, transmissive Michelson interferometer with Fabry-Perot arm cavities. Besides the Michelson; there are the Mach-Zender, which is the interferometer typically proposed for displacement-noise-free or frequency-noise-free interferometry (i.e. insensitive to displacements or changes in frequency by combinations of beams) [26]; whilst variations of the Sagnac interferometer configuration are suggested for all-reflective interferometry [27]. It is worth noting that there are many other possible configurations and most are only partially understood. The use of diffraction gratings allows a greater region of this parameter space to be explored, and the interferometers in this space may have advantageous properties. A full appreciation of the phase relations of the three-port-coupled second-order-Littrow configured grating cavity, including the lateral translation phase-effects, is given in Chapter 5 and this is an important step toward being able to consider that cavity for use in such interferometer configurations.

1.4 Elements to be addressed by this thesis

The alignment noises of diffractively coupled cavities is the broad theme of this thesis. Lateral displacement of a laser beam across the surface of a diffractive optic generates a phase shift in all diffraction orders other than zero. We show the origin of this effect, and we consider its implications for increased phase noise in the Fabry-Perot arm cavities of Michelson interferometer gravitational wave detectors. Particularly, the isolation requirements for end-mirror tilt (which projects the cavity eigenmode across the surface of the diffractive input optic) are derived and compared to the two-mirror Fabry-Perot cavity case for some Virgo-esque advanced interferometer. Experimental work has been performed to verify this effect and calculation, both on optics tables in the University of Birmingham laboratory, and undertaken using the Joint Interferometer Facility prototype at (and in collaboration with) the University of Glasgow. The possibility of using the symmetry of the three-port coupled grating cavity to cancel this phase noise has been

considered, and we have found that noise reduction occurs in the forward-reflected output port. The implications of this for future diffractive interferometer configurations have been briefly considered. Although this lateral displacement is a significant noise source for gravitational wave interferometers using diffractive optics, we are positive that this problem can be alleviated by isolation systems and appropriate configuration choices. The gains made combating certain thermal noises, and the more speculative benefits made available by diffractive optical system configurations, are likely to outweigh the increased additional alignment issues this noise source induces.

In this chapter the subject of gravitational waves, and the most important noise sources in gravitation wave detectors, have been introduced. In Chapter 2 the relevant elements of interferometric theory are introduced and some consequences are discussed. In Chapter 3 the functioning of a grating and some related optical theory is introduced. This is then used to show that a phase shift occurs with lateral displacement between the beam and the diffraction grating. This phase shift is due to path length difference as the beam scans across the grating striations and will generate phase noise in the gravitational wave signal channel if the beam or the grating is laterally displaced with a noise spectrum. Due to the lever-arm formed by the arm cavity length, end-mirror tilt displaces the cavity eigenmode across the surface striations of the grating. We determine the isolation requirement for end-mirror tilt in a Virgo-esque advanced interferometer, such that a gravitational wave of strain $h = 10^{-23}/\sqrt{\mathrm{Hz}}$ will make a larger contribution to the output signal than this noise source. These isolation requirements are computed for a traditional two-mirror cavity for comparison purposes, and compared to a two-port-coupled first-order-Littrow configuration diffractive Fabry-Perot cavity and a three-port-coupled second-order-Littrow configuration diffractive Fabry-Perot cavity. These are the two most commonly proposed all-reflective cases using diffraction gratings. The two-mirror cavity was found to be the most insensitive to tilt; followed by the three-port-coupled case some five orders of magnitude more sensitive; with the two-port-coupled case having by far the worst

performance, a further two orders of magnitude more sensitive than the three-port-coupled case.

In Chapter 4 the ratio of the response to the three-port-coupled diffractive cavity and the two-mirror cavity to end-mirror tilt is experimentally determined. This ratio is demonstrated to be consistent with the theory up to the limits of capability of the measurement, which was set by the residual longitudinal motion of the tilt actuator rather than purely by tilt induced effects. Work prepared for and partially carried out during my various visits to the Joint Interferometer Facility 10 m prototype located at the University of Glasgow supports these results. Since both the grating and the end-mirror test-masses are triple-suspended from cantilever arms, and both optics and suspensions are located in a vacuum system, the Glasgow prototype offers far superior seismic and acoustic noise isolation than can be achieved on an optical bench.

In Chapter 5 we determine that there is some cancellation of this lateral grating displacement phase-noise source if the forward-reflected output port is selected as the readout port of a three-port coupled grating cavity [28], recovering a factor of 20 in the signal to noise ratio if the gravitational wave and lateral grating displacement obscuring it are at 10 Hz. The various coil-magnetic actuators and the freedom of movement allowed by the suspended system of the JIF allows a range of motions to be imparted to the diffractive optic, making the prototype highly suitable for investigating the theory outlined this chapter, and the data gathered supports the predicted result. This calculation and its confirmation is an important step toward being able to calculate the three-port-coupled diffractive cavity's performance as an element in variously configured interferometers. This chapter ends with a discussion of interferometer configurations that might be constructed using diffraction gratings, and some sketches of possible designs are shown. Chapter 6 reprises the key points of the work undertaken in this thesis and its results.

Chapter 2

BASICS OF INTERFEROMETRY

2.1 Basic Optics

2.1.1 Description of a light field

Before we discuss optical systems it is necessary to have a mathematical description of an electromagnetic wave (light field). We can describe an incident light field by the electric component of its electromagnetic field,

$$E = E_0 e^{-i(kz-\omega t+\Phi)}, \tag{2.1}$$

where E_0 is the amplitude of the beam, $kz - \omega t + \Phi$ is the phase of the beam with k being the wavevector, z the distance traveled in the direction of propagation from some fixed starting point; ω the angular frequency of the electromagnetic wave, t the time elapsed since some fixed starting time; and Φ the phase at the fixed starting points $t = 0$ and $z = 0$. Note that in most circumstances t and z are chosen such that $\Phi = 0$.

2.1.2 Effect of transmission or reflection on power and field amplitude

To calculate the transmission and reflection of a beam splitter, for both sides of the beam splitter we consider the transmission of power T and the transmission of light fields given by $\sqrt{T} = \tau$. Similarly R is the reflection of power, and the reflection of a light field is $\sqrt{R} = \rho$. Assuming a lossless ($T + R = 1$), 50:50 ($T = R$) beam splitter it is simple to determine the value of reflection and transmission of light fields to be,

$$\rho = \tau = 1/\sqrt{2}. \tag{2.2}$$

A consequence of energy conservation is that some phase will be introduced by transmission through or reflection from the beam splitter. These phase relations are important in performing frequency-domain Fabry-Perot cavity calculations in Chapters 3 and 5.

2.1.3 Phase modulation of a light field

Any phase change applied with a sinusoidal function to a light field $E_0 = a_0 e^{-i\omega t}$ will phase modulate the light field, resulting in the new field,

$$E_1 = a_0 e^{i\omega t} e^{im\cos(\omega_m t)}, \tag{2.3}$$

where m is the modulation index (or depth) of the phase modulation, equal to the amplitude of the phase change, and ω_m is the angular frequency with with the modulation is applied. The complex field amplitude resulting can be expanded using the Bessel function $J_n(m)$ [29], [30], to obtain,

$$E_1 = a_0 e^{i\omega t} \sum_{n=-\infty}^{\infty} i^n J_n(m) e^{in\omega_m t}. \tag{2.4}$$

In the limit of small m from the phase modulator, the field $n = 0$ retains both the frequency and amplitude of the input field ($J_0(m) = 1$). It is known as the carrier and propagates unchanged. The fields that result from $n > 0$ are known as the upper sidebands, and each one forms a matched pair (of order n) with the equivalent $n < 0$ lower sideband, frequency shifted from the carrier by $n\omega_m$. If we consider a Fabry-Perot cavity (which will be discussed further in Section 2.3) set to a length resonant for the carrier, both sidebands in a pair will have been detuned from this frequency by the same offset given by $\pm n\omega_m$. Equation 2.4 describes a carrier surrounded by an infinite number of sidebands; however, since Bessel functions decrease for large n, if $m \ll 1$ then they can be approximated by [31],

$$J_k(m) = \frac{1}{n!}\left(\frac{m}{2}\right)^n, \tag{2.5}$$

in which case it is sufficient to take only the first-order sidebands into account, allowing us to write,

$$E_1 = a_0 e^{i\omega t} \times \left(J_0(m) + iJ_1(m)e^{i\omega_m t} - iJ_{-1}(m)e^{-i\omega_m t} \right), \tag{2.6}$$

substituting in the relation $J_{-n}(m) = (-1)^n J_n(m)$ obtains with Equation 2.5,

$$E_1 = a_0 e^{i\omega t} \times \left(1 + i\frac{m}{2}\left(e^{i\omega_m t} + e^{-i\omega_m t}\right) \right), \tag{2.7}$$

which is the first-order approximation in modulation index m. Effectively therefore for $m \ll 1$ only the first-order sidebands, which are the terms linear in m, are considered.

An interesting consequence of this is that if field a_1 is then modulated again with a modulation

index $m \ll 1$, and a frequency ω_n obtaining,

$$\begin{aligned} E_2 &= E_1 e^{i\omega t} e^{-im\cos(\omega_m t)} \\ E_2 &= a_0 e^{i\omega t} \times \left(1 + i\frac{m}{2}\left(e^{i\omega_m t} + e^{-i\omega_m t}\right)\right) \times \left(1 + i\frac{m}{2}\left(e^{i\omega_n t} + e^{-i\omega_n t}\right)\right) \\ E_2 &= a_0 e^{i\omega t} \times \left(1 + i\frac{m}{2}e^{\pm i\omega_m t} + i\frac{m}{2}e^{\pm i\omega_n t} - \frac{m^2}{4}e^{\pm i\omega_m t} \cdot e^{\pm i\omega_n t}\right), \end{aligned} \tag{2.8}$$

then only the carrier field from the first modulation will create sidebands linear in m. I.e. first-order sidebands of first-order sidebands (the last term of the equation) are linear in m^2, the same as the (neglected) second-order sidebands of the carrier. This small modulation index $m \ll 1$ approximation therefore also implies that only the carrier field generates sidebands, and hence the sidebands from a given modulation propagate unchanged through any subsequent modulation.

2.1.4 Michelson interferometer outputs

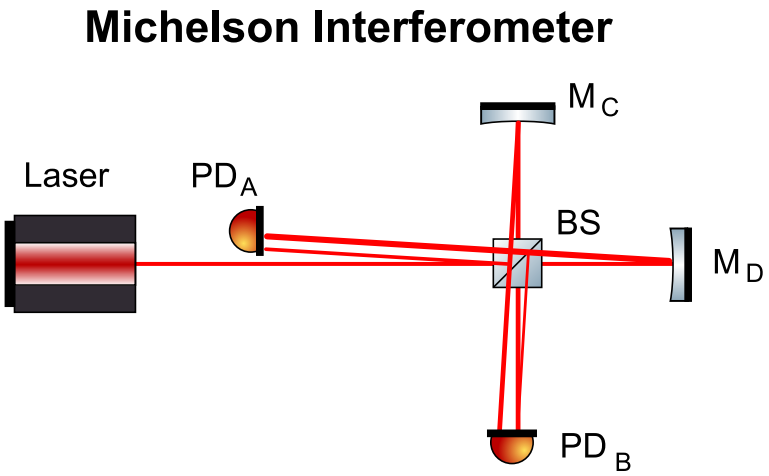

Figure 2.1: Schematic of a simple Michelson Interferometer, with a slight angular offset of the beam paths reflected from the end mirrors shown.

Since both LIGO and Virgo gravitational wave interferometers use a Michelson configuration, it is worthwhile here to introduce the field at the outputs of such an interferometer. We will

derive the effect of a small relative length change between the interferometer arms (at DC). The outputs shown A and B in Figure 2.1 are the only outputs of the Michelson Interferometer so long as no transmissive loss is experienced when the beams are turned at points C and D. Each of the two outputs will be a combination of two different beam paths through the interferometer. At output A there will be a beam component that has been twice reflected from the beam splitter, and a beam component that has been twice transmitted through the beam splitter, hence this port is known as the anti-symmetric port. For reasons that shall shortly be apparent, it is usually preferred to use the symmetric port as the output of the interferometer, and it is this port that will be solved explicitly.

From Snell's Law [32] it can be determined that a one-hundred-eighty degree phase change occurs in a light field on reflection from a denser medium than that which the light field is propagating in. Determining which is the denser medium can be non-trivial (e.g. the reflective surface of a beam splitter cube exists inside the cube, which is of a uniform refractive index). For this appreciation, we are free to choose the first reflection from the beam splitter as that which acquires the phase change, and as we shall shortly see this is functionally identical to the alternative. The field at the symmetric output is the linear sum of the beam component B_{rt} that has been reflected from the beam splitter (acquiring a one-hundred-eighty degree phase flip), traveled down the reflected arm of the Michelson (length l_r), reflected from the end mirror, made the return trip to and been transmitted through the beam splitter to the symmetric port,

$$B_{rt} = -Ee^{i\omega t+\psi}\frac{1}{2}e^{-2ikl_r}, \tag{2.9}$$

and B_{tr}, that as been transmitted through the beam splitter, twice traveled the transmitted arm

(length l_t) and then reflected from the beam splitter to the symmetric port.

$$B_{tr} = Ee^{i\omega t}\frac{1}{2}e^{-2ikl_t}, \tag{2.10}$$

hence the field at output B is given by,

$$B = -B_{rt} + B_{tr} = Ee^{i\omega t}\frac{1}{2}(-e^{-2ikl_r} + e^{-2ikl_t}), \tag{2.11}$$

we extract the common factor,

$$e^{i\Phi} = e^{-i\omega t}e^{-i(kl_r+kl_t)}, \tag{2.12}$$

and allow $l_t - l_r = \Delta l$ hence obtaining,

$$B = Ee^{i\Phi}\frac{1}{2}(-e^{-ik\Delta l} + e^{+ik\Delta l}). \tag{2.13}$$

the field at the symmetric output port of the Michelson interferometer, influenced by a relative length change between the arms (at DC). In order to measure this output field a photodetector will be used. The current produced by a photodiode is proportional to the power of the beam $P_{(X)}$, rather than the field amplitude $E_{(X)}$ in which this equation is formed. The relevant relationship is,

$$P_X \propto |E_X|^2 = E_X.E_X^*. \tag{2.14}$$

Applying this to Equation 2.13 obtain,

$$P_B = B.B^* = \frac{1}{4}E^2\left(2 - e^{-2ki\Delta l} - e^{2ki\Delta l}\right), \tag{2.15}$$

which would be of the same form even had we chosen the opposite side of the beam splitter

to acquire the phase flip in forming Equations 2.9 and 2.10. Using $e^{i\phi} + e^{-i\phi} = 2\cos(\phi)$ and $\cos 2\phi = 1 - 2\sin^2\phi$,

$$P_B = E^2 \sin^2(k\Delta l), \tag{2.16}$$

The power in the input beam can also be determined by this method and found to be $P_0 = E^2$ hence,

$$\frac{P_B}{P_0} = \sin^2(k\Delta l), \tag{2.17}$$

In the case of equal arm length $\Delta l = 0$ then the symmetric port (output B) is dark, and therefore any difference between the arm lengths of the interferometer will be detectable as a signal.

An alternative statement of the general rule (applying a one-hundred-eighty degree phase flip on reflection from a denser medium) to optical systems is that any transmitted field should be multiplied by $\sqrt{-1} = i$, equivalent to a ninety degree ($\pi/2$) phase shift on transmission [33]. This statement is useful (and used throughout the following work) since we deal with mirror substrates with multilayer dielectric coatings, and it can be far from obvious which boundary is from a lower to a higher refractive index.

2.2 Signal Sources in a Michelson Interferometer

In this section we will provide an overview of signal sources at the output of a Michelson interferometer by considering three example inputs at DC; a hypothetical gravitational wave; length displacement between the arms, and frequency noise injected at the laser.

2.2.1 Gravitational Wave Phase Signal

Assume the simplest case of a gravitational wave passing perpendicularly through the plane of the detector, with the polarisation of the wave aligned with the arms of the detector. The strength of the gravitational wave is defined by the strain h, where ΔL is the length change it imposes on a single arm of the detector. One arm of the Michelson will experience a phase change $-\varphi$ equivalent to a contraction of the arm length and the light in the other arm will experience a phase change φ equivalent to a expansion of the arm length. Thus we can modify Equation 2.9 with the addition of the $-\varphi$ phase component and Equation 2.10 with the addition of the φ phase component.

$$B_{rt} = -Ee^{i\omega t}\frac{1}{2}e^{i(2kl_r+\varphi)}, \tag{2.18}$$

and,

$$B_{tr} = Ee^{i\omega t}\frac{1}{2}e^{i(2kl_t-\varphi)}, \tag{2.19}$$

after the common factor given by Equation 2.12 has been extracted, the output power at the symmetric port to the input power is given by,

$$\frac{P_B}{P_0} = \sin^2(k\Delta l + \varphi), \tag{2.20}$$

This result transparently shows that any length or displacement noise is indistinguishable from a gravitational wave signal (using the symmetric port).

2.2.2 Frequency Noise

Frequency noise can be understood from the point of having obtained a signal linear in $k\Delta L$, which appears non-linearly in the output of the symmetric port (as derived in Equation 2.20. One method of linearising this signal is to use a modulation-demodulation scheme such as the Pound Drever Hall technique discussed in Section 2.4.2, which is used in gravitational wave interferometers [34]. Since k is given by $k = 2\pi f/c$ the wave propagation vector also contains a component of the frequency and hence the frequency noise. Thus the frequency noise is proportional to the term, $(l_t - l_r)\Delta f$which can be minimised by setting the two arm lengths as close to equal as possible, and by using a laser that is as stable in frequency as possible.

2.3 Frequency domain modeling of Fabry-Perot cavities

A two-mirror cavity, the most common example of a Fabry-Perot cavity, is a simple but very powerful optical element which can be included in gravitational wave interferometers to enhance the gravitational wave signal-to-noise ratio. In this section, a frequency-domain technique will be used to analyse a simple Fabry-Perot cavity, leading us to various conclusions about its use. Although this work has been extensively presented elsewhere it was necessary to repeat it, both to gain the experience required to perform the calculations of Chapters 4 and 5, and to be able to design and understand the operation of the experiment presented in Chapter 4.

2.3.1 Light fields in a cavity

We will consider plane waves of constant frequency in the linear two-mirror Fabry Perot cavity shown in Figure 2.2, which is defined by its length L, and the amplitude transmittance (τ_1, τ_2) and reflectance of its two mirrors (ρ_1, ρ_2). The input light field is given by $b_0(\omega)$, dependent on

the angular frequency ω of the light, and the fields at the outputs of and at different locations within the cavity are given by $a(\omega)$ in its various subscript and dashed forms. A superposition

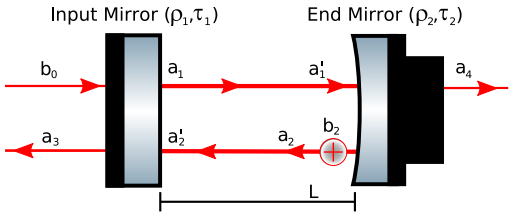

Figure 2.2: Two-mirror Fabry-Perot cavity schematic.

of fields is all that is required to calculate the total field at each location, as for:

$$a_1(\omega) = a_2'(\omega)\rho_1 + b_0(\omega)i\tau_1, \tag{2.21}$$

where the complex number maintains consistency with the ninety-degree $(\pi/2)$ phase shift generated by transmission through a mirror [33]. Using this technique a system of linear equations can be written for the cavity, where $k = \omega/c$, ω being the angular frequency of the light field, thus obtaining:

$$\begin{aligned} a_1'(\omega) &= a_1(\omega)e^{-ikL} \\ a_2(\omega) &= a_1'(\omega)\rho_2 \\ a_2'(\omega) &= a_2(\omega)e^{-ikL} \\ a_3(\omega) &= b_0(\omega)\rho_1 + a_2'(\omega)i\tau_1 \\ a_4(\omega) &= a_1'(\omega)i\tau_2. \end{aligned} \tag{2.22}$$

Solving this set of equations obtains:

$$\frac{a_1(\omega)}{b_0(\omega)} = \frac{i\tau_1}{1-\rho_1\rho_2 e^{-2ikL}} \tag{2.23}$$

which is the transfer function from the input field $b_0(\omega)$ to the interior field $a_1(\omega)$. We will later find $D(\omega) = 1/(1-\rho_1\rho_2 e^{-2ikL})$ useful.

Light field appearing inside the cavity

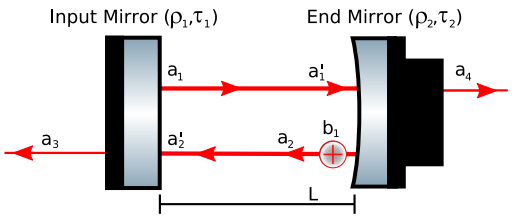

Figure 2.3: Two-mirror Fabry-Perot cavity schematic, showing internal input only.

It is possible to effectively generate the input inside the cavity shown as b_1 in Figure 2.3. If the externally input light field shown b_0 in Figure 2.2 is modulated by a gravitational wave or mirror displacement, the resulting field can be considered as the linear sum of the original 'carrier' field (angular frequency ω) plus many so called 'sidebands' at frequency ($\omega \pm n\omega_m$, with n an integer and ω_m the modulation frequency). The amplitude of these sidebands is proportional to the depth of the modulation and the amplitude of the carrier being modulated [29]. This frequency domain technique will be used and discussed more fully in later chapters. For now we will consider the coupling relations of the first upper sideband appearing $b_1(\omega+\omega_m)$. Using the relations of Equations 2.22 we obtain,

$$\begin{aligned} a_2(\omega+\omega_m) &= b_1(\omega+\omega_m) + a_2(\omega+\omega_m)\rho_1\rho_2 e^{-2i(k+k_m)L} \\ a_2(\omega+\omega_m) &= \frac{b_1(\omega+\omega_m)}{1-\rho_1\rho_2 e^{-2i(k+k_m)L}} \\ a_2(\omega+\omega_m) &= b_1(\omega+\omega_m)D(\omega+\omega_m), \end{aligned} \tag{2.24}$$

where $k+k_m$ is the wavevector associated with this new sideband frequency (recall that $k = \omega/c$).

2.3.2 Optical power in the cavity

It is also useful to calculate the power circulating in the cavity. Assuming an input power of unity, $b_0 b_0^* = 1$, where $T_1 = \tau_1^2$, $R_1 = \rho_1^2$, $T_2 = \tau_2^2$, $R_2 = \rho_2^2$, we obtain the power at the location of the field a_1 given by Equation 2.23 (in the absence of any modulation introducing an input b_1),

$$P_c = a_1 a_1^* = \frac{T_1}{1 + R_1 R_2 - 2\rho_1 \rho_2 \cos(2kL)} \tag{2.25}$$

thus we can plot Equation 2.25 in Figure 2.4, the gain of the Fabry-Perot cavity in power versus

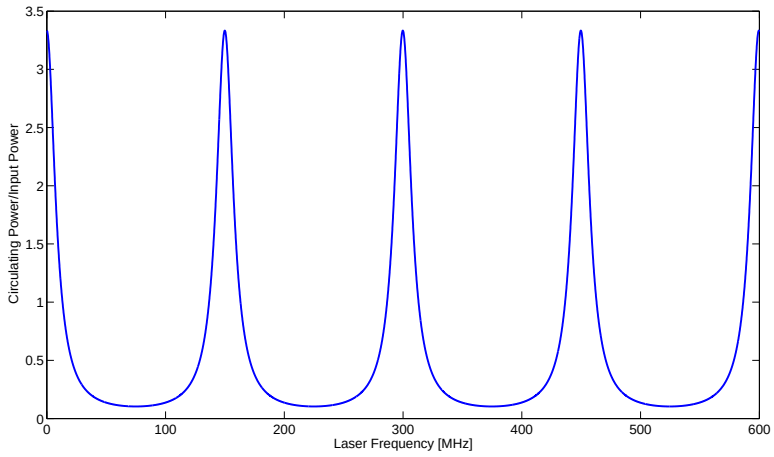

Figure 2.4: Power circulating in a linear, two-mirror Fabry-Perot cavity ($L = 1$ m, $R_1 = R_2 = 0.7$, $T_1 = 0.3$) as a function of the laser light frequency detuning from the resonant frequency of the cavity. Alternatively and equivalently, the same plot would be obtained by plotting as a function of the displacement from the resonant cavity length.

frequency detuning from the cavity resonance. An alternative, similar plot could be created with cavity length on the x-axis. This is a useful illustration that an adjustment of the laser-frequency is equivalent to a displacement of either mirror, as both frequency-dependent wavevector k and cavity length term L appear in the cosine. The power reaches a maximum when $kL = N\pi$ with N an integer, which is the resonant case, and a minimum for $kL = (N + 1/2)\pi$, which is the

anti-resonant case.

2.3.3 Free-spectral range, full width at half maximum, and finesse

Certain properties of the cavity can be determined from Figure 2.4. The free-spectral range (FSR) is the distance from one resonant peak to the next. To obtain it, we can use $k = 2\pi/\lambda$ and $c = f\lambda$ to write:

$$2k\mathrm{L} = 4\pi\mathrm{fL}/\mathrm{c} = 2\pi\mathrm{f}/\mathrm{FSR}, \tag{2.26}$$

where $\mathrm{FSR} = \mathrm{c}/2\mathrm{L}$. A similar and equally useful property is the full width at half maximum (FWHM) of the cavity, which is the width of a resonant peak at half its maximum power. To determine the FWHM we must calculate the frequency at which the circulating power becomes half the maximum, obtaining [35],

$$\mathrm{FWHM} = \frac{\mathrm{c}}{2\mathrm{L}}\frac{2}{\pi}\arcsin\left(\frac{1-\rho_1\rho_2}{2\sqrt{\rho_1\rho_2}}\right), \tag{2.27}$$

noting the presence of the FSR in this equation, we can re-write to obtain the finesse ($\mathcal{F}$), defined as,

$$\mathcal{F} = \frac{\mathrm{FSR}}{\mathrm{FWHM}} = \frac{\pi}{2\arcsin\left(\frac{1-\rho_1\rho_2}{2\sqrt{\rho_1\rho_2}}\right)}, \tag{2.28}$$

which in the case of high finesse (occurring when ρ_1 and ρ_2 are close to unity) is often approximated to:

$$\mathcal{F} \approx \frac{\pi\sqrt{\rho_1\rho_2}}{1-\rho_1\rho_2} \approx \frac{\pi}{1-\rho_1\rho_2} \tag{2.29}$$

because the argument of the arcsin function is suitably small. It is worth noting that this is proportional to our previously mentioned $D = 1/(1 - \rho_1\rho_2 e^{-2ikL})$ so long as the cavity is resonant, i.e. that $e^{-2ikL} = 1$. Therefore $\mathcal{F}$ is also an indicator of the cavity gain on resonance.

2.3.4 Impedance matched, undercoupled, overcoupled

Optimising power circulating in the Fabry-Perot arm cavities is important for an interferometric gravitational wave detector, since the gravitational wave signal is imprinted upon the phase of the light circulating in the cavity. As we have seen in Section 1.2.2 the signal-to-noise ratio improves with increased power. We will calculate the power that is transmitted, reflected and circulated by the cavity with a differing selection of input and end mirror reflectivities in order to inform the choice of mirror reflectivities. The circulating field was calculated in Equation 2.23, and the power of that field was calculated in Equation 2.25. From Equations 2.22 and 2.22 the same calculation can be made for both reflected and transmitted power. In this theoretical case we assume that there are no losses in either mirror such that $R + T = 1$, where R and T are the power reflectance and transmission respectively. An input power of one Watt to a resonant cavity that has reached the steady state is used. In order to create an educational plot in Figure 2.5 we set $T_1 + T_2 = 0.6$, with the x-axis varying with T_1. This clearly shows the different regions, but even in tabletop experiments far higher mirror reflectivities are used. The optimal coupling of signal to the reflected port of the Fabry-Perot cavity, as given by a_3 in Equation 2.22, is when the prompt reflection from the input mirror and the signal leaving the Fabry-Perot cavity are of equal amplitude. This occurs when the cavity mirrors obey the relation $T_1 = T_2$, called impedance-matched [36]. The under-coupled regime refers to $T_1 < T_2$, which is particularly undesirable due to the decrease in gravitational wave signal-enhancing circulating power, and therefore to avoid it most Fabry-Perot cavities are operated slightly in the over-coupled regime where $T_2 < T_1$.

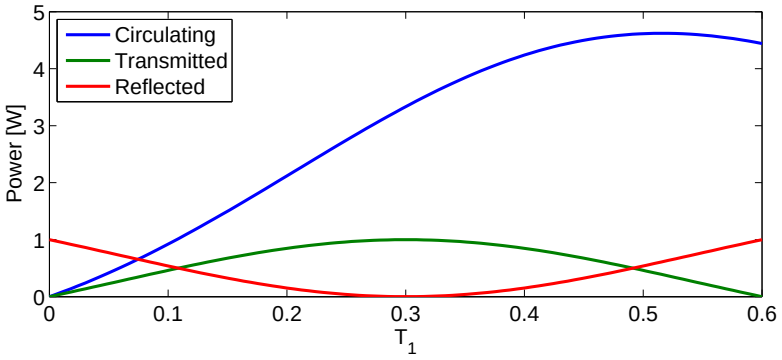

Figure 2.5: Power transmitted, reflected from and circulating in a resonant, steady state Fabry-Perot cavity composed of lossless mirrors with one Watt input power. Mirror transmissions are set such that $T_1 + T_2 = 0.6$, which is far higher transmission than any useful cavity in order to show the impedance matched, overcoupled and undercoupled regions clearly.

2.3.5 Hermite-Gaussian beams

Previously we have considered a light field as a single, non-dispersive beam propagating through space. However, even using a highly collimated beam source such as a laser as the beam propagates one must consider the dispersion of the propagating wavefronts. This is of particular importance with respect to a beam which we wish to resonate between the two mirrors in a Fabry-Perot cavity, as for that cavity to function the wavefronts of the beam must be mode-matched to the reflective surfaces of the mirrors. Siegman provides a thorough discussion of beam-dispersion and modes in 'Lasers', chapter 16 [37], a shortened version of which has been reproduced here for the convenience of the reader.

Consider a Gaussian beam emitted from a laser source, and assume that the beam is constant, exists for all time and - at first - in free space. At some position along the beam there will be a location with planar wavefronts $R_0 = \infty$ and characterised by a particular spot size w_0. We call this the beam-waist, because we will shortly find that it has the smallest diameter of any point along the beam, and assign it for convenience the location $z = 0$, where z is a linear dimension perpetually parallel to the beam (even if the beam is turned by a mirror).

The field of this Gaussian beam at any other location along the z-axis will be given by [37]:

$$\tilde{u}(x,y,z) = \left(\frac{2}{\pi}\right)^{1/2} \frac{\tilde{q}_0}{w_0 \tilde{q}(z)} e^{-ikz - ik\frac{x^2+y^2}{2\tilde{q}(z)}} \tag{2.30}$$

$$\tilde{u}(x,y,z) = \left(\frac{2}{\pi}\right)^{1/2} \frac{e^{-ikz+i\psi(z)}}{w(z)} e^{-\frac{x^2+y^2}{w^2(z)}} e^{-ik\frac{x^2+y^2}{2R(z)}} \tag{2.31}$$

where both formulations are useful, the first given by Equation 2.30 more for beam propagation since the complex radius of curvature $\tilde{q}(z)$ leaves the propagation term $\exp(-ikz)$ isolated, and obeys the propagation law [37],

$$\tilde{q}(z) = \tilde{q}_0 + z = z + iz_r, \tag{2.32}$$

where z_r is the Rayleigh range, given by [37],

$$\tilde{q}_0 = i\frac{\pi w_0^2}{\lambda} = iz_r, \tag{2.33}$$

The second formulation for the Gaussian beam field given in Equation 2.31 is more useful for calculations relating to the spot size $w(z)$, the radius of curvature $R(z)$ and the phase $\psi(z)$. These are related to $\tilde{q}(z)$ by [37],

$$\frac{1}{\tilde{q}(z)} \equiv \frac{1}{R(z)} - i\frac{\lambda}{\pi w^2(z)}, \tag{2.34}$$

thus we can obtain the important parameters of the Gaussian beam from the spot size w_0 at the beam waist and the ratio of the current position z to the Rayleigh range z_r [37].

$$w(z) = w_0\sqrt{1+(z/z_r)^2}, \tag{2.35}$$

$$R(z) = z + z_r^2/z, \tag{2.36}$$

$$\psi(z) = \arctan(z/z_r). \tag{2.37}$$

Therefore, so long as the beam waist and wavelength are known, the entire Gaussian beam profile is characterised. It is important to know that introducing a spherical lens or spherically curved mirror will create a different Gaussian beam, which then has its own properties. Such lenses are used to match a Gaussian beam to the mirror curvatures of a particular cavity. This is of particular importance with respect to the Gaussian beam which will resonate between the two mirrors in a Fabry-Perot cavity, the circumstance of which is discussed further in Section 2.3.6.

Higher order Hermite-Gaussian beams

There exists a complete set of higher-order solutions to the paraxial wave equation. The Hermite-Gaussian set, $u_{n,m}(x,y,z)$, can be separated into two orthogonal functions, one in the x and one in the y direction, $u_{n,m}(x,y,z) = u_n(x,z)u_m(y,z)$, where n and m are the mode order in the x and y directions respectively. It is worth noting that Equations 2.30 and 2.31 are written for the lowest order Hermite-Gaussian mode. We can write, where H_m is a Hermite polynomial of order m [37],

$$u_m(y,z) = \left(\frac{2}{\pi}\right)^{1/4} \left(\frac{e^{i(2m+1)\psi(z)}}{2^m m! w(z)}\right)^{1/2} \times H_m\left(\frac{\sqrt{2}y}{w(z)}\right) e^{-ikz - i\frac{ky^2}{2R(z)} - \frac{y^2}{w^2(z)}}, \tag{2.38}$$

it is important to note that (because of the rapid variation across the beam), the higher order modes (Hermite polynomials) have a net phase shift compared to the lowest order mode, which causes the higher-order modes to resonate in a cavity at a slightly different frequency to the zero-zero mode. This becomes relevant in Section C.1, where we see a 'forest of modes' as the laser frequency is ramped against a fixed Fabry-Perot cavity.

2.3.6 Cavity stability and resonator g-parameters

So far, we have discussed fields in cavities and our diagrams have implied that the laser light within the cavity follows a narrowly collimated ray-like path. This is in fact not so, as we have seen in section 2.3.5. Similar to how one must consider the dispersion of the propagating wavefronts when a beam is propagating, when a beam is present in a cavity one must consider the interaction of these wavefronts with the cavity mirror surfaces. In order to match our calculation based on a point laser beam interacting with a point on the mirror surface, the radius of curvature of the Gaussian beam must match the mirror curvature at each mirror - i.e. every point on the wavefront must touch the mirror surface at the same moment. Since the spatial mode parameters that satisfy this requirement are unique, this mode is known as the cavity eigenmode. Where z_r the Rayleigh range of the beam, $R(z)$ its radius of curvature; z_1 is the position of the input optic, R_1 its radius of curvature; and similarly z_2 and R_2 for the cavity end mirror. We can thus write the relations,

$$R(z_1) = z_1 + z_r^2/z_1 = -R_1, \tag{2.39}$$

$$R(z_2) = z_2 + z_r^2/z_2 = +R_2, \tag{2.40}$$

$$L = z_2 - z_1, \tag{2.41}$$

the two resonator g-parameters are defined for the input and end mirror respectively as:

$$g_1 \equiv 1 - \frac{L}{R_1}, \tag{2.42}$$

$$g_2 \equiv 1 - \frac{L}{R_2}, \tag{2.43}$$

from these equations we can derive the Rayleigh range for that particular cavity, and hence the size of the beam waist is found to be:

$$w_0^2 = \frac{L\lambda}{\pi}\sqrt{\frac{g_1 g_2(1-g_1 g_2)}{(g_1+g_2-2g_1 g_2)^2}}. \tag{2.44}$$

By looking at the numerator within the square-root, we can see that the beam waist will be real and positive only if,

$$0 \leq g_1 g_2 \leq 1, \tag{2.45}$$

this product is known as the resonator stability parameter [37]. This parameter is shown plotted in Figure 2.6. Anywhere in the region between the axis and the $0 \leq g_1 g_2 \leq 1$ lines represents a stable resonator.

It is non-trivial to match the input Gaussian laser beam waist to the cavity eigenmode, defined by the waist size calculated above and its position given by Equation 2.35 (spherical lenses must be used to modify the Gaussian beam input to the cavity). Fortunately even imperfect matching of the input beam will couple that portion of the input beam power which is appropriately matched into the eigenmode. An iterative process of adjustment to the input beam can then more closely match to the cavity eigenmode. More details on the experimental implementation of this matching process, which is not quite so straightforward as presented here, are included in Section B.1.2 for the initial collimation of the beam and Section C.1 for the mode-matching into the cavity.

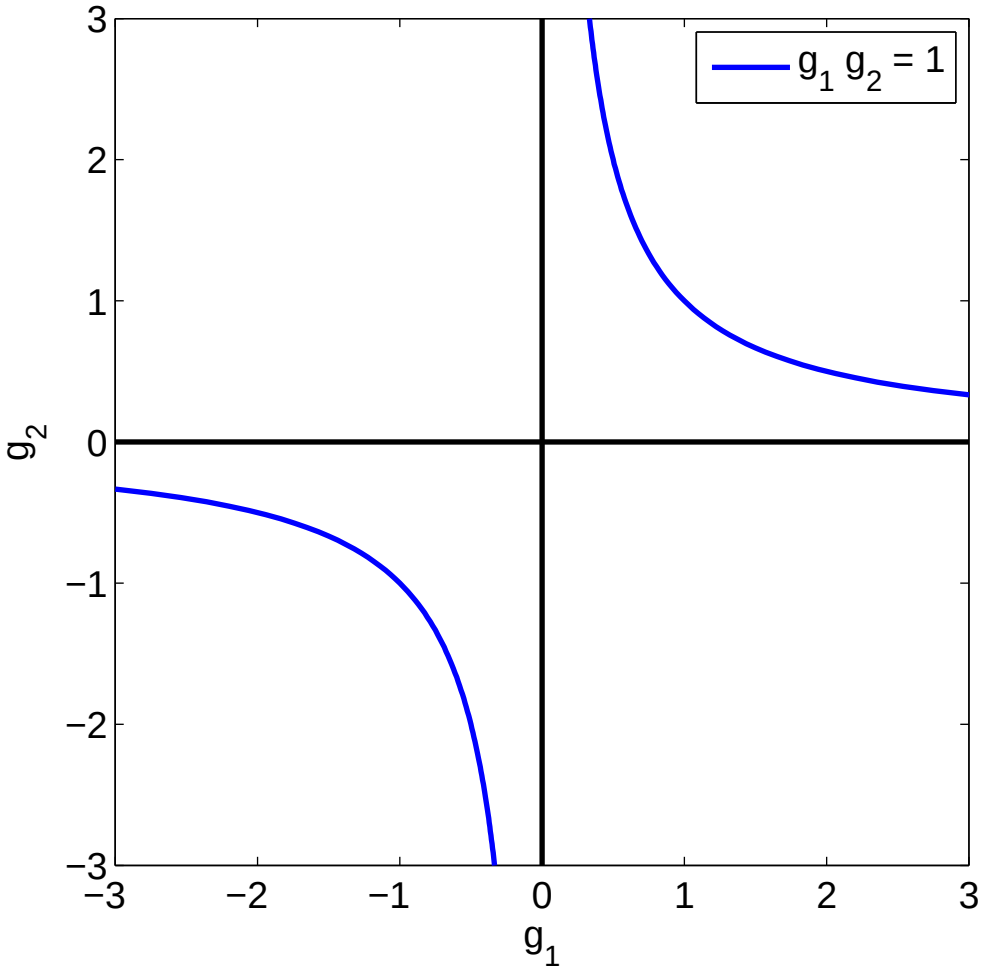

Figure 2.6: Resonator $0 \leq g_1 g_2 \leq 1$ parameters requirement. Anywhere in the region between the axis and the blue lines represents a stable resonator

2.4 Feedback control schemes

Fabry-Perot cavities have a particular resonance where the length of the cavity is a multiple of the wavelength of the light ($\exp -ikL = 1$), as shown in Figure 2.4. In order to be maintained at this point against various disruptive influences (the noises discussed in Chapter 1) Fabry-Perot cavities require a feedback loop of locking electronics. The point at which the feedback loop holds the cavity (which does not have to be the resonant point) is known as the operating (or locking) point, and when the loop is operational the cavity is known as 'locked'. A fuller discussion of feedback loops can be found in Section 4.4 and in Friedland's Control System Design [38].

Disruptions in vacuum isolated gravitational wave interferometers are typically either seismic in origin despite the best isolation systems can do, or due to longer-term effects such as temperature drift. In a small laboratory experiment 'seismic' disruptions are usually anthropomorphic in origin, although on a vibration isolated optical table the primary disruptions are acoustic in origin (movement of the air). Laser frequency changes would be an issue, but these are typically independently stabilised with an additional, separate feedback loop typically featuring its own Fabry-Perot cavity. A schematic of such a locking-loop is shown in Figure 2.7, with some unknown disruption to the cavity shown occurring.

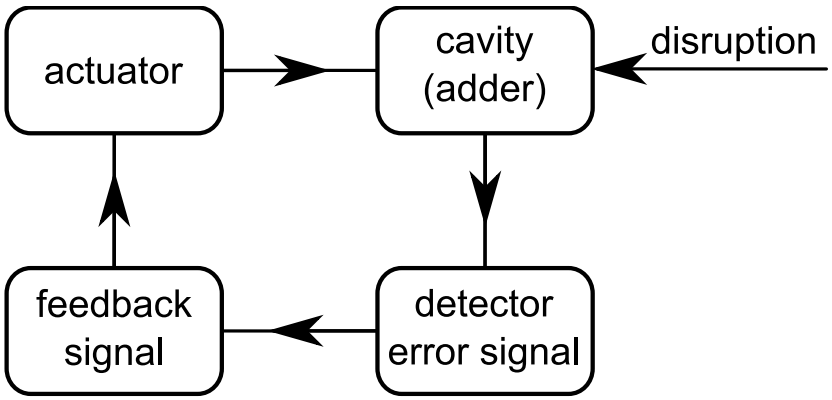

Figure 2.7: Schematic diagram of an idealised cavity-locking loop with some chance disruption of the cavity shown.

In order for the cavity to remain locked, the error signal must have a consistent slope and be centered on zero. That is, when the cavity drifts in one direction a positive feedback must be applied to the actuator, and when it drifts in the other direction a negative feedback must be applied. When the cavity is on resonance (at the resonant point), no feedback should be applied. In its simplest sense the detector will be a photodiode at either the reflected (a_3) or transmitted (a_4) output port of the cavity shown in Figure 2.2. It will detect the power present in the light field, which will be proportional to that shown in Figure 2.4. This curve is unsuitable for use as a feedback signal because it does not cross zero at any point and therefore the response would always have the same sign. Also the regions of this curve with a linear slope (gradient) which might make a suitable operating point (if offset to zero) are not at the resonant point. Therefore additional detection and locking electronics are required after the photodiode to create an appropriate feedback signal. We will address the two most common such sets of electronics: Those used in the comparatively simple 'offset locking' technique and those used in the more complex modulation-demodulation Pound-Drever-Hall technique.

2.4.1 Offset feedback control

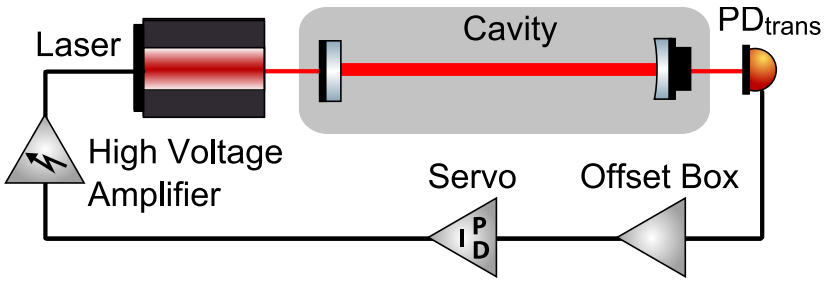

Figure 2.8: Schematic diagram of practical offset locking loop

It is worthwhile to briefly discuss the offset locking technique for locking a cavity, first because the principles involved will help in generating an understanding of the more complicated Pound-Drever-Hall locking scheme, and second because the offset locking scheme was used to perform some initial tests for the tabletop experimental cavity described in Chapter 4. We will use that

cavity as an example to aid understanding of locking systems generally. In Figure 2.8 we see a viable offset locking loop: The photodiode ($\mathrm{PD_{trans}}$) produces an error signal proportional to that shown in Figure 2.4. The offset box then applies a variable offset to this signal, allowing the zero volt crossing point to be positioned as desired. In this case it is positioned somewhere on either one of the side-slopes of the resonance peak. This fulfils the criteria of the locking loop, that the error signal should have opposite sign in each direction from the operating point and be zero at the operating point. However, it is important to realise that if offset locking is used the operating point is shifted away from the resonant point. A more complex modulation-demodulation scheme, such as the Pound-Drever-Hall scheme [39] must be used to obtain a suitable error signal slope at the top of the resonance peak.

2.4.2 Pound-Drever-Hall feedback control

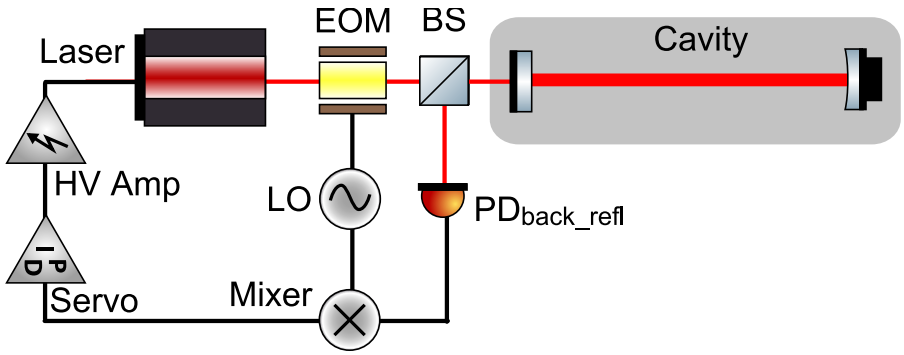

Figure 2.9: Schematic diagram of a practical Pound-Drever-Hall feedback control loop. It is instructive to compare this figure to Figure 2.8 for an offset feedback control loop. Note the addition of the electro-optic modulator (EOM), the beam splitter (BS) required by the switch to detecting the reflected port of the cavity, and the mixer which demodulates the inputs from the reflected port of the cavity (via the photodetector) with the same local oscillator (LO) signal source that drives the EOM. Typical EOM modulation frequencies are in the radio frequency (MHz) range. For example, in the experiment detailed in Chapter 4 a 12 MHz modulation was utilised.

Pound-Drever-Hall (PDH) locking [39], [40], [41] as shown in Figure 2.9, modulates the the frequency (or phase) of the laser. Consider a frequency-modulated laser beam in a Fabry-Perot cavity. If that cavity is above resonance, the power in the reflected beam will increase while

the frequency increases. Below resonance, it is decreasing the frequency that increases the reflected power. Which side of the resonant peak the cavity is presently on can be determined by modulating the system (dithering the frequency back and forth) at much higher frequency than the expected disruption shifting the cavity away from the operating point, and determining whether the reflected power varies in phase or out of phase with the modulation.

A typical implementation of this requires an electro-optic modulator to perform the modulation of the light beam at radio frequencies (for example 12 MHz); a mixer to perform the demodulation of the photodiode signal proportional to the light field, and a beam splitter as for reasons that will shortly become apparent the demodulation should be carried out using the beam reflected from the cavity.

Modulation of the incident beam

The phase modulation of the incoming beam by the electro-optic modulator converts the initial field given by $E_0 e^{-i\omega_0 t}$ to one of the form, with m the modulation depth and ω_m the modulation frequency,

$$\begin{aligned} b_0(\omega_0) + b_0(\omega_0+\omega_m) + b_0(\omega_0-\omega_m) &= E_0 e^{-i(\omega_0 t + m\sin\omega_m t)}, \\ b_0(\omega_0) + b_0(\omega_0+\omega_m) + b_0(\omega_0-\omega_m) &= E_0\left[J_0(m)e^{-i\omega_0 t} + J_1(m)e^{-i(\omega_0+\omega_m)t} + J_{-1}(m)e^{-i(\omega_0-\omega_m)t}\right]. \\ &\quad . \end{aligned} \tag{2.46}$$

The function $J_n(m)$ is a Bessel function. For a small modulation index m, the first term of the Bessel function (J_0) will be close to unity [31] and therefore leaves the input light field effectively unchanged . The J_1 and J_{-1} terms are the first-order pair of higher-order sideband terms, of which only the first pair are given. It is necessary for all sidebands to be considered for the conservation of power, as only the summation of all the Bessel function terms to $n = \infty$ is equal

to the $(\exp(-i(\omega t + m\sin\omega_m t))$ exponential; however, in the limit of the approximation $m << 1$ it is reasonable to use only the first two sidebands, because the higher-order Bessel function terms become exceedingly small. The modulation analysis technique using Bessel functions is discussed somewhat more fully in Chapter 5.

Demodulation of the reflected beam

We have the equation for the reflected beam from Equation 2.22, and we can substitute in our previously written $D(\omega) = 1/(1-\rho_1\rho_2 e^{-2ikL})$ given that wavevector $k = \omega/c$. We thus obtain:

$$a_3(\omega) = F(\omega) = b_0(\omega)\rho_1 - b_0 D(\omega)\tau_1^2\rho_2 e^{-2ikL}, \tag{2.47}$$

to which our Bessel function from Equation 2.46 can be applied as the input field $b_0(\omega)$, obtaining:

$$\begin{aligned} a_3 \quad & (\omega_0) + a_3(\omega_0+\omega_m) + a_3(\omega_0-\omega_m) = \\ E_0 \quad & \left[F(\omega_0)J_0(m)e^{-i\omega_0 t} + F(\omega_0+\omega_m)J_1(m)e^{-i(\omega_0+\omega_m)t} + F(\omega_0-\omega_m)J_{-1}(m)e^{-i(\omega_0-\omega_m)t}\right], \end{aligned} \tag{2.48}$$

however, it is power rather than field which is measured by the detecting photodiode. Therefore we really wish to obtain, where P_c is the power in the carrier light field and P_s the power in the first order sidebands,

$$\begin{aligned} a_3 \cdot a_3^* &= P_c F(\omega)\cdot F(\omega)^* + P_s\left[F(\omega+\omega_m)\cdot F(\omega+\omega_m)^* + F(\omega-\omega_m)\cdot F(\omega-\omega_m)^*\right] \\ &+ 2\sqrt{P_c P_s}\left[\Re[F(\omega)F^*(\omega+\omega_m) - F^*(\omega)F(\omega-\omega_m)]\cos(\omega_m t)\right. \\ &+ \left.\Im[F(\omega)F^*(\omega+\omega_m) - F^*(\omega)F(\omega-\omega_m)]\sin\omega_m t\right] \\ &+ \text{terms at frequency } 2\omega_\mathrm{m}. \end{aligned} \tag{2.49}$$

from which we must obtain a signal proportional to $a_3(\omega_0)$ which is an appropriate error signal around the operating point. The mixer achieves this by extracting the terms proportional to $\sin\omega_m t$ (or $\cos\omega_m t$). It is here that we see the importance of observing the reflected beam, because it is this 'beat' between the carrier and the sidebands that exist at a frequency detectable by the photodiode. The mixer extracts the term of this equation that is proportional to $\sin(\omega_m t)$ [40], and thus we obtain for the error signal [40]:

$$\varepsilon = 2\sqrt{P_c P_s}\Im[F(\omega)F^*(\omega+\omega_m) - F^*(\omega)F(\omega-\omega_m)]. \tag{2.50}$$

which can be plotted as shown in Figure 2.9. In principle, this could allow any one of three operating points, one for the carrier and one for each of the sidebands. If the system is configured for a positive gradient feedback signal then the lock will occur to one of the sidebands rather than the carrier. Practically, the sign of the gradient of the error signal is controlled by the inverter switch on the servo.

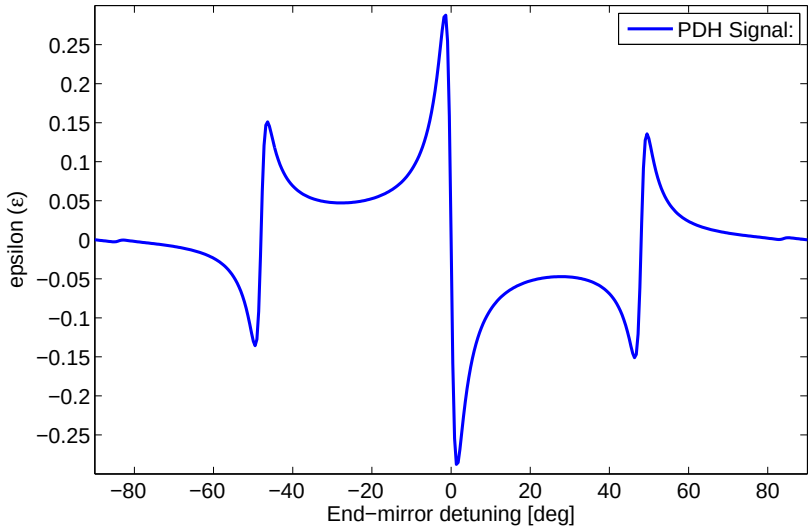

Figure 2.10: Theoretical Pound-Drever-Hall error signal as calculated in Equation 2.50, ε. The x-axis shown end mirror detuning measured in degrees. This is a change in position of the end mirror, where 360^o is equivalent to a mirror displacement of one wavelength.

It can be seen that Figure 2.10 is a good feedback signal with good linear properties, though it should be noted that, unlike the offset locking approach, the PDH system does require the cavity to be close to the operating point in order to lock to the operating point. This is why the offset controls of the high-voltage amplifier are so important, allowing the cavity to be manually scanned to the operating point. At the operating point interference between the prompt reflection from the input mirror and the reflection from the cavity can be seen on both the reflected photodiode signal and an appropriately placed CCD camera, so finding the operating point is not difficult in practice.

/

Chapter 3

ALIGNMENT SENSITIVITY

3.1 Alignment sensitivity of diffractive Fabry-Perot cavities

All-reflective optical configurations for interferometric gravitational wave detectors are made possible through the use of reflective diffraction gratings. Such configurations eliminate thermal lensing and substantially reduce Brownian thermal noise in the substrate. Interferometric gravitational wave detectors require high finesse Fabry-Perot cavities, and hence the coupling coefficient retaining light in the cavity should approach unity at least in the case of the end mirror. Presently this is achieved by multilayer dielectric overcoating, and hence coating noise is currently not significantly suppressed by using an all-reflective scheme. The coating noise from the input optic will depend on whether a diffraction order is used to retain light in the cavity, as in the two-port grating cavity configuration; or the reflection order (zeroth diffraction order) is used, as in the three-port grating cavity configuration. Coating thermal noise has recently been found to dominate substrate thermal noise in standard transmissive Fabry-Perot cavities

[42].

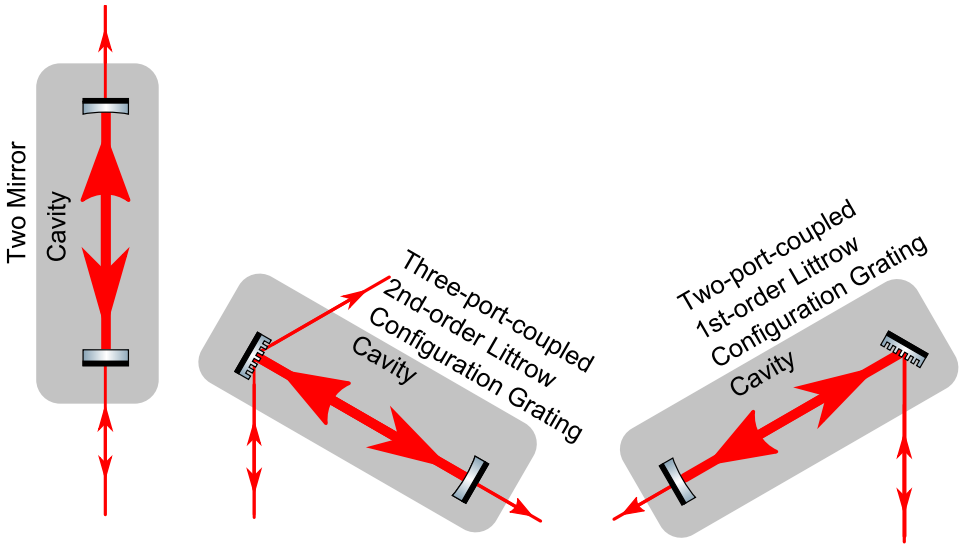

Figure 3.1: Cartoon diagrams of Fabry-Perot cavities from left to right: case one, two mirror; case three, three-port coupled second-order Littrow configuration grating; and case two, two-port coupled first-order Littrow configuration grating. Red lines and arrows show laser fields and directions. The cavities have been aligned such that the input field is from the bottom of the page.

In this chapter the functioning and optical properties of diffraction gratings are presented. Using these properties, a phase shift will be shown to occur with lateral displacement between the beam and the diffraction grating (Section 3.3.1). Further we will investigate the effect of the noise this phase shift induces on gravitational wave detectors. Three phase effects will be considered:

1. Effect one: End mirror longitudinal displacement. The direct lengthening or shortening of the cavity (and hence its eigenmode). It occurs in all three types of cavity. In this chapter it is used to determine the phase signal of a hypothetical gravitational wave.

2. Effect two: End mirror tilt induced length change of the cavity eigenmode. Tilting of the cavity end mirror misaligns the cavity, causing a displacement of the eigenmode to a portion of the cavity with a slightly changed length. This length change is shown schematically in Figure 3.9. It is the only end mirror misalignment phase noise for a

two-mirror cavity. It also occurs in the grating cavities, but there it is dominated by effect three.

3. Effect three: End mirror tilt laterally displaces the cavity eigenmode across the input optic. Where the input optic is a grating, this displacement induces a phase change proportional to the diffraction order the light is coupled in (the cause of the phase change is discussed in Section 3.3.1). Effect three will differ between two-port and three-port grating cavities since they couple light in different diffraction orders.

The two tilt-induced phase effects (two and three) are used to derive the isolation requirement required against end mirror tilt for a Virgo-esque interferometer [43] to detect a hypothetical gravitational wave (effect one). This isolation requirement will be computed for three different possible arm cavities, shown in cartoon form in Figure 3.1:

1. Case one: Transmissive two-mirror cavity, shown left in Figure 3.1. Discussed for comparison purposes to the grating cavities in Sections 3.6 and 3.7.

2. Case two: All-reflective two-port coupled first-order Littrow configuration grating cavity, shown right in Figure 3.1 and discussed in Section 3.6.

3. Case three: All-reflective three-port coupled second-order Littrow configuration grating cavity, shown center in Figure 3.1 and discussed in Section 3.7.

It will be found that the end mirror tilt isolation requirements are significantly increased by using a grating cavity, and that of the grating cavities the two-port coupled cavity has a far more stringent isolation requirement than the three-port cavity.

3.2 Functioning of a grating

It is useful to introduce the theoretical and mathematical approaches that explain the existence of diffraction gratings in the wave-picture of light. The Huygens-Fresnel principle provides an overview of diffraction grating functionality, and was put onto a sounder mathematical basis the integral theorem of Helmholtz and Kirchhoff [44] [45] [46], which is presented for a more modern reader in Born and Wolf 'Principles of Optics', chapter 8 [47], relevant equations from which have been re-presented here in a narrative presenting the required understanding. In our case the integral theorem allows the approximate but simpler form of Kirchhoff's diffraction theory to be used. This theory has two applicable parameters spaces, that of Fresnel diffraction and that of Fraunhofer diffraction. For diffraction gratings, Fraunhofer diffraction applies, resulting in the Bragg diffraction equation, [32],

$$d(\sin\theta_i - \sin\theta_\mu) = \mu\lambda, \tag{3.1}$$

which is used variously throughout this thesis. The basic principle behind it will be discussed immediately, followed by its derivation, followed by a discussion of some restrictions on the validity of that derivation.

3.2.1 Huygens-Fresnel principle

The functioning of a grating can be conceptualised using the Huygens-Fresnel principle. The Huygens construction states that every point of a wave-front can be considered as the source of spherical wavelets, and the wave-front at some later time will be the envelope of these wavelets [48]. Fresnel used this construction to explain diffraction, by postulating that these secondary wavelets mutually interfere. A sketch of this is shown as Figure 3.2 for a transmissive and reflective diffraction grating. The yellow dots mark example sources of secondary wavelets,

with the wavelets themselves being shown in red, are are the arrows indicating the maxima of the resulting wave-front.

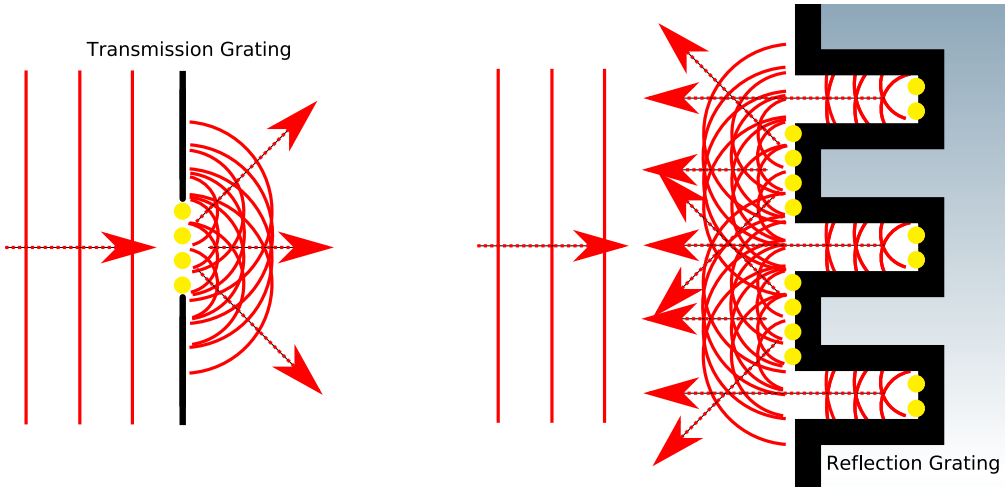

Figure 3.2: Top sketch view of a transmissive diffractive optic (right) and a reflective diffractive optic (left), when an infinite plane wavefront interacts with them. The yellow dots mark the arbitrary locations designated as example sources of secondary wavelets, with the wavelets themselves being shown in red, as are the arrows indicating the maxima of the resulting wave-front.

3.2.2 Fraunhofer diffraction from many slits

The light distribution after Fraunhofer diffraction has occurred can be given as the solution to the Kirchhoff integral for a single aperture A, summed over n apertures in the diffraction grating [47],

$$U(p,q) = C\sum_{n} e^{-ik[p\xi_n + q\eta_n]} \int\int_{A} e^{-ik(p\xi'_n + q\eta'_n)} d\xi' d\eta' \tag{3.2}$$

where ξ and η define a plane, and p and q the position on that plane. In the absence of the diffraction grating the electromagnetic field disturbance in that plane would be given by $V_0(\xi,\eta,\omega) = A\cdot\exp[ik(l_o\xi + m_0\eta)]\cdot\exp[-i\omega t]$. Putting this into the context of Equation 3.2 we have $\xi_n = nd$ with d the grating periodicity and n a positive integer, $p = \sin\theta - \sin\theta_0$, and

both $\eta_n = 0$ and $q = 0$. This then obtains [47],

$$U(p) = U^{(0)}(p)\sum_{n=0}^{N-1} e^{-ikndp} = U^{(0)}(p)\frac{1-e^{-iNkdp}}{1-e^{-ikdp}} \tag{3.3}$$

$$U^{(0)}(p) = C\int_A \frac{V(\xi,\eta)}{V_0(\xi,\eta)} e^{-ikp\xi} d\xi \tag{3.4}$$

hence we can calculate for the intensity of that field after the diffraction grating, with $\left|U^{(0)}(p)\right|^2 = I^{(0)}(p)$,

$$I(p) = |U(p)|^2 = \left|U^{(0)}(p)\right|^2 \frac{1-e^{-iNkdp}}{1-e^{-ikdp}} \cdot \frac{1-e^{iNkdp}}{1-e^{ikdp}} = I^{(0)}(p)\frac{\sin(Nkdp/2)}{\sin(kdp/2)}, \tag{3.5}$$

According to Equation 3.3, consistent with the Huygens-Fresnel principle, the light distribution is the same as for a set of coherent secondary sources numbering N characterised by amplitude function $\left|U^{(0)}(p)\right|^2$, with phases differing by integer multiples of kdp. This formula can be considered to be made up of the term due to a single period of the grating $I^{(0)}$, and a periodic function representing the interference effects of light from different periods. This second function has maxima (of height N^2) when the denominator $\sin^2(kdp/2) = 0, \pi, 2\pi...$, which occurs when, (recalling that wavevector $k = 2\pi/\lambda$),

$$p \equiv \sin\theta - \sin\theta_0 = \mu\lambda/d, \tag{3.6}$$

with μ a positive or negative integer, which we choose to call the diffraction order. Thus we have derived the Bragg diffraction Equation 3.1. The use of the Fraunhofer diffraction model (and, quite similarly, the Huygens secondary sources approach) is valid so long as certain conditions of the Kirchhoff diffraction theorem are met. First that the wavelength of the light must be less than the slit separation of the diffraction grating; and second that the slit separation must be much less than the distance from the grating at which the pattern of diffracted light is viewed. If these conditions are not met then Fresnel diffraction occurs instead. Kirchoff showed that this

principle can be regarded as an approximate form of an integral theorem expressing the solution of the homogeneous wave equation [46], by integrating over the field entering and leaving a volume of a surface. A full discussion of this in a form more penetrable for the modern reader can be found in Born and Wolf, 'Principles of Optics' 7th edition, section 8.3 [47].

In our case $\lambda = 1064\,\text{nm}$, slit (since reflective gratings are used, it takes the form of a groove) has period $d = 1500\,\text{nm}$ and the distance at which we operate from the diffractive optic is no less than 20 cm. This is far into the region where Fraunhofer diffraction is suitable, and hence Equation 3.1 applies to grating cavities of the type that may be used with gravitational wave detectors, and to experiments simulating some of their aspects such as ours.

3.2.3 Littrow configuration

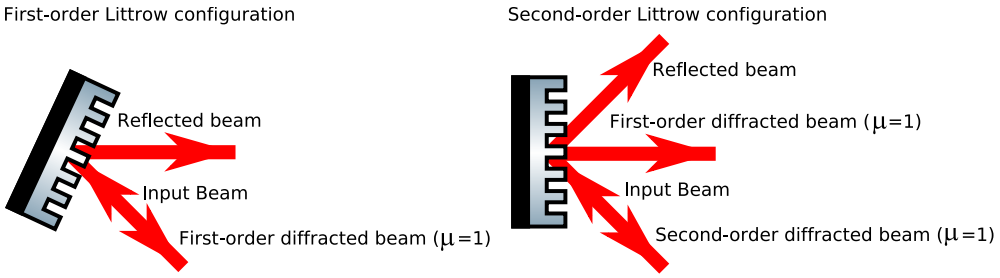

Figure 3.3: Sketch of first-order Littrow configuration diffraction grating (left); and second-order Littrow configuration diffraction grating (right).

Littrow configuration is the particular alignment of a reflective diffraction grating such that one of the diffracted beams is returned along the path of the incident beam [49]. The order of the Littrow configuration is given by which diffracted beam this is. In first-order Littrow configuration the first-order diffracted beam is aligned with the input beam. In second-order Littrow configuration the second-order diffracted beam is aligned with the input beam. Both of these configurations are shown in Figure 3.3. It is not conventional to refer to the alignment of the directly reflected beam (zeroth-order diffracted beam) with the input beam as zeroth-order Littrow configuration.

3.2.4 Quantities imposed by the Bragg equation

The forgoing derivation of the Bragg equation allows us to determine some of the requirements of the grating as applied to gravitational wave interferometers. Using gratings offers specific advantages when considered in the context of all-reflective interferometers, so long as we are aware of these restrictions. By appropriate selection of grating properties and laser input angle to set the number of ports (and their efficiencies) gratings can be used either as Fabry-Perot cavity input optics or as beam splitters. Herein we will consider the cavity input optic case. Using a high-diffraction efficiency grating with an intense first diffraction order ($\mu = |1|$) to retain light in the cavity, a two-port coupled grating can be used as a Fabry-Perot cavity input optic (in first-order Littrow configuration) . Alternatively, using a low-loss low-diffraction efficiency grating with an intense reflection order (zeroth diffraction order, $\mu = 0$ to retain light in the cavity, a three-port coupled grating can also be used as a Fabry-Perot cavity input optic (in second-order Littrow configuration).

The Bragg equation can explain the familiar interference patterns of light which, when diffracted at different orders (μ values) interferes constructively or destructively. This feature is undesirable in an interferometer where typically two, three, or four output beams are required depending on whether the input optic for a two-port coupled cavity, a three-port coupled cavity, or a beam splitter is desired. The intensity of the beam from other undesirable diffraction orders can be reduced almost to zero by altering features of the grating such as depth, spacing and the reflectivity of the material [50]. The exception is the zeroth order, which in reflective gratings represents specular reflection and is always present.

In the two-port coupled grating case, the light is retained in the cavity by first-order diffraction. Therefore the output port returning light to the cavity must be co-incident with the input port from the cavity. This is called Littrow configuration, and specifically first-order Littrow configuration because the co-incidence is between input and output separated by first-order

diffraction. From the Bragg Equation 3.1, it requires specific alignment conditions by imposing that $\theta_i = -\theta_\mu$, thus resulting in,

$$\sin\theta_i = \frac{\mu\lambda}{2d}. \tag{3.7}$$

Similarly, second order Littrow configuration is used in the three-port coupled grating case. This aligns the input beam with its second-order diffraction, and more relevantly with the first-order diffraction of the light resonating in the cavity. This reduces scattered light within the interferometer and maintains similarity to the two-mirror case, for example in the functioning of Pound-Drever-Hall demodulation schemes and power recycling.

In order to reduce the signal losses through power loss to undesirable diffraction orders it is necessary to select the grating period such that the grating equation only allows those diffraction orders that will be used, imposing,

$$\lambda < d < 2\lambda. \tag{3.8}$$

since it is necessary only for the zeroth (η_0), first (η_1) and (in the three-port case) second (η_2) diffraction orders to exist [51].

3.2.5 Differing reflection coefficients of a three-port grating

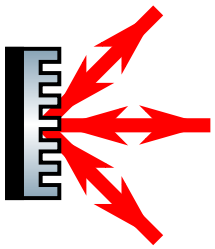

Figure 3.4: Sketch of three-port coupled diffraction grating, with inputs and outputs present at all ports.

A three-port grating such as that sketched in Figure 3.4 has the scattering matrix [33]:

$$S_{3p} = \begin{bmatrix} \eta_2 e^{-i\phi_2} & \eta_1 e^{-i\phi_1} & \eta_0 \\ \eta_1 e^{-i\phi_1} & \rho_0 & \eta_1 e^{-i\phi_1} \\ \eta_0 & \eta_1 e^{-i\phi_1} & \eta_2 e^{-i\phi_2} \end{bmatrix}, \tag{3.9}$$

from which conservation of power allows us to derive the following relations for the amplitude coupling coefficients [33]:

$$\begin{aligned} \rho_0^2 + 2\eta_1^2 &= 1, \\ \eta_0^2 + \eta_1^2 + \eta_2^2 &= 1, \end{aligned} \tag{3.10}$$

leading to the derivation of the phase shifts associated with coupling through the grating, where the convention that there is no phase shift on reflection has been adopted as the starting point [33]:

$$\begin{aligned} \phi_0 &= 0, \\ \phi_1 &= -\frac{1}{2}\arccos\left(\frac{\eta_1^2 - 2\eta_0^2}{2\rho_0\eta_0}\right), \\ \phi_2 &= \arccos\left(\frac{-\eta_1^2}{2\eta_2\eta_0}\right), \end{aligned} \tag{3.11}$$

these phase differences are functions of the diffraction efficiencies given in Equation 3.10, unlike in the mirror or two-port coupled grating cases where they are independent of the amplitude coupling coefficients. From these equations the upper and lower possible limits of the zeroth (reflection) diffraction order and second diffraction order have been derived [33]:

$$\eta_{0,\frac{\max}{\min}} = \eta_{2,\frac{\max}{\min}} = \frac{1 \pm \rho_0}{2}, \tag{3.12}$$

in the context of a three-port coupled Fabry-Perot cavity, the η_2 term is essentially a loss term,

setting a theoretical minimum on the efficiency of even the best diffraction grating, as will be seen in Chapter 5.

3.3 Phase changes caused by moving an optic

Displacing a diffractive optic beneath an incident laser beam induces a phase change of that beam. This effect has been calculated by Freise et al 2007 [52], and their geometrical approach has been used in this section to reproduce their calculation for the extent of the phase change. Some readers may prefer to conceptualise the lateral displacement induced phase change (Section 3.3.1) as the superposition of Huygen's secondary wavelets, with the Huygen's secondary wavelet sources being displaced when the grating is shifted by a fraction of the grating period (slit separation plus slit width). The phase-change effect of lateral grating displacement is therefore periodic with lateral displacement, the periodicity being the same as the grating period. It shall shortly be seen that this intuitive result also emerges from the geometrical approach.

3.3.1 Displacement in the plane of the optic

In isolation, moving a laser beam on an optic or moving an optic beneath a laser beam are functionally identical. Similarly, if we consider a uniform, plane optic (flat mirror, with radius of curvature $R_c = \infty$) then any displacement in that plane (Δy or Δx or any vector combination thereof) will create no path length difference for the light, and therefore no phase change of the light. We will show that this is entirely due to a symmetrical effect of the optical geometry, because the input and output angle are equivalent in reflection, by considering a more general case. When this general case is applied to the diffraction grating we find that, because the output angle is dependent on the diffraction order μ there is a phase change resulting from Δx displacement of the grating, where x is defined as the direction across its striations. Defining

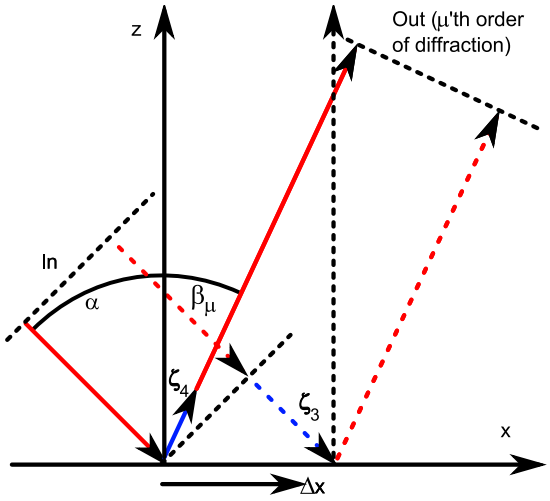

Figure 3.5: Phase change from Δx displacement of a grating or other asymmetric optic. Both α and β_μ are positive as pictured, (i.e. α is measured anti-clockwise and β_μ is measured clockwise).

the x axis this way means that the y axis is entirely uniform, and translation of or across it does not create a phase change.

Consider the case shown in Figure 3.5 where an input light field from some source is incident on an optic at angle α to the normal, interacts with the optic and is outlet from it at angle β_μ to the normal, where in the diffraction grating case μ refers to the diffraction order. Translating incident beam or optic by Δx, and measuring from a common plane at both input and output we observe path length difference between the beams of ζ_3 and ζ_4, given by,

$$\zeta_3 - \zeta_4 = -\Delta x(\sin\alpha - \sin\beta_\mu), \tag{3.13}$$

where the negative sign appears because the length ζ_3 is additional length experienced by the new (dashed) path, whereas ζ_4 is part of the old (solid) path length which is not experienced by the new (dashed) path. If we go to the grating case by using the Bragg Equation 3.1, this can be re-written as the path length difference,

$$\Delta\zeta_{\Delta x} = -\Delta x\frac{\mu\lambda}{d}. \tag{3.14}$$

Understanding that if the grating were translated by one striation period d there would be effectively no change, we expect that this effect should be periodic with d, and indeed we can see that the factor $1/d$ appears in the equation. This can be more easily understood by converting path length difference to phase change $\Delta\phi = 2\pi\Delta\zeta_{\Delta x}/\lambda$, since phase change is measured in units of angle and is itself periodic, thus obtaining,

$$\Delta\phi_{\Delta x}\frac{\lambda}{2\pi} = \Delta x\frac{\mu\lambda}{d}. \tag{3.15}$$

Path length difference or phase change are proportional to the diffraction order μ, which is zero in the case of reflection. This is consistent with our understanding that translating a mirror causes no path length difference and therefore creates no phase change, due to the cancellation of ζ_3 with ζ_4 since $\alpha = \beta_\mu$. A diffraction grating; however, will experience a path length difference induced phase change when displaced across the grating striations.

3.3.2 Displacement perpendicular to the plane of the optic

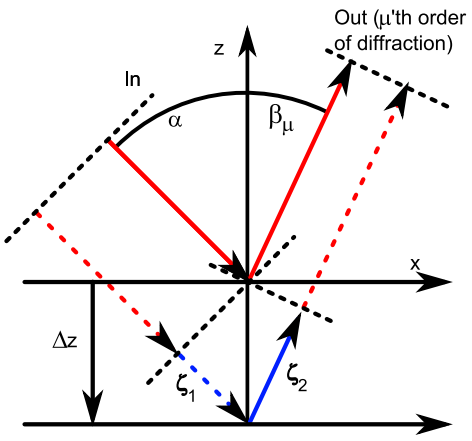

Figure 3.6: Phase change from Δz displacement of a grating or other asymmetric optic.

We turn to the general case of motion perpendicular to the plane (Δz direction), and such a motion generates path length difference and therefore phase change in all cases. Note that in this section Δz is not, as is conventional in Fabry-Perot cavity calculations, a distance metric

that follows the laser beam whatever its orientation. Such situation is shown for a diffraction grating in Figure 3.6. From this geometry, we can write an equivalent for Equation 3.13, obtaining:

$$\Delta\zeta_{\Delta z} = \zeta_1 + \zeta_2 = \Delta z(\cos\alpha + \cos\beta_\mu), \tag{3.16}$$

where ζ_1 and ζ_2 are the path length differences experienced by the incoming and outgoing beams. Once again converting to phase change we obtain,

$$\Delta\phi_{\Delta z} = -\Delta z\frac{2\pi}{\lambda}(\cos\alpha + \cos\beta_\mu), \tag{3.17}$$

where this time we have taken the $2\pi/\lambda$ to the RHS of the equation. This clearly shows the periodicity with wavelength λ, because if the path length distance is adjusted by a full wavelength their will be no change to the phase, which is essentially a measure of position along the wave-structure.

3.3.3 Null vector

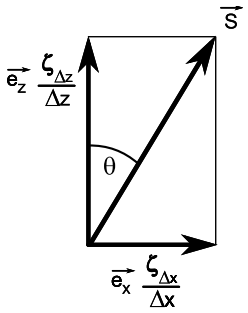

Figure 3.7: Vector for null phase change null of a grating or other asymmetric displaced optic in combined longitudinal ($\vec{e_z}$) and lateral ($\vec{e_x}$) motion.

As we have calculated phase change generating path-length difference in both the previous sections, we can understand that for some vector combination of Δz and Δx motion no phase change, or phase change by an integer multiple of 2π will occur. For the mirror this is in the

plane of the optic, pure Δx. For the grating case, this null eigenvector is perpendicular to some vector $\vec{S}$ between the $\vec{e_x}$ and $\vec{e_z}$ unit vector axis as shown in Figure 3.7. We can write the ratio of the between the slopes of the optical path length change per unit displacement by dividing Equation 3.15 by Equation 3.17, obtaining:

$$\frac{\Delta\phi_{\Delta x}/\Delta x}{\Delta\phi_{\Delta z}/\Delta z} = \frac{\mu\lambda}{d(\cos\alpha+\cos\beta_\mu)} = \frac{(\sin\alpha+\sin\beta_\mu)}{(\cos\alpha+\cos\beta_\mu)} = \tan\left(\frac{\alpha+\beta_\mu}{2}\right), \tag{3.18}$$

where $\theta = (\alpha+\beta_\mu)/2$, defining the bisection between incoming and outgoing beams. Although this is in principle quite interesting, this null eigenvector is unique and different for every diffraction order μ, so only a single diffraction order can be fully insensitive to noise. An all-reflective Fabry-Perot cavity must input and output the light into the cavity in one order and retain it in the cavity in another, so the best case that can be achieved is that the light is retained in the cavity by an null-noise order, which allows the noise acquired on input and output to be suppressed versus the signal by the finesse of the cavity. This is already achieved by the three-port coupled grating cavity. Additionally, much work on gravitational wave detectors has focused on neutralising motion in the Δz direction for the two-mirror Fabry-Perot cavities, where z is also along the beam axis, and this work can be utilised more directly for three-port coupled grating cavities.

3.3.4 Rotation of the optic

While there are changes in alignment caused by rotation of an optic, our previous method of considering the optic in isolation (as in Figures 3.5 and 3.6) is not useful for describing them. Rotation and alignment issues must be discussed in the context of an interferometric system, which shall be undertaken in the following sections considering Fabry-Perot cavities.

3.4 Fabry-Perot cavities

In the following three sections we focus on the use of diffraction gratings to form all-reflective Fabry-Perot cavities, as a potential optical element for inclusion in third generation gravitational wave detectors. The results of this work (Equations 3.39, 3.53 and 3.73) were initially presented in Freise et al 2007 [52], without the derivations of the induced phase noise coupling to the output performed herein. Three possible cavity configuration cases will be considered:

1. Case one: Two-mirror case: Transmissive two-mirror cavity, shown left in Figure 3.1. Discussed for comparison purposes to the grating cavities in Sections 3.6 and 3.7.

2. Case two: Two-port case: All-reflective two-port coupled first-order Littrow configuration grating cavity, shown right in Figure 3.1 and discussed in Section 3.6.

3. Case three: Three-port case: All-reflective three-port coupled second-order Littrow configuration grating cavity, shown center in Figure 3.1 and discussed in Section 3.7.

The three phase modulation effects necessary to calculate the effect of end mirror tilt on a gravitational wave detector will be considered for each of these cases. These effects are:

1. Effect one: End mirror longitudinal displacement. The direct lengthening or shortening of the cavity (and hence its eigenmode). It occurs in all three cases (case one, two-mirror, Section 3.5.1; case two, two-port, Section 3.6.5; case three, three-port, Section 3.7.4). In this chapter it is used to determine the phase signal of a gravitational wave with strain $h = 2\Delta L/L$. In chapter 4 a direct length change due to imperfect orthogonality of the end mirror tilt actuator introduces phase noise, and the same mathematics are used to predict its effects.

2. Effect two: End mirror tilt induced length change of the cavity eigenmode. Tilting of the cavity end mirror misaligns the cavity, causing a displacement of the eigenmode which

typically results in the length of the cavity eigenmode changing. The length change is discussed fully in the following Section 3.5.2, and shown in Figure 3.9. It is the only end mirror misalignment phase noise in case one (the two-mirror case). Although it occurs in the grating cavity cases, it is dominated by effect three.

3. Effect three: End mirror tilt laterally displaces the cavity eigenmode across the input optic. In cases two (two-port, Section 3.6.3) and three (three-port, Sections 3.7.3 and 3.7.3) this induces a phase change due to the lateral grating displacement effect discussed in Section 3.3.1. Effect three will differ between case two and case three because the first diffraction order ($\mu = 1$) is used to retain light in the cavity in case two; and to couple light into and out of the cavity in case three.

The isolation requirement for end mirror tilt (such that a hypothetical gravitational wave could be detected) will be calculated for the Virgo detector later in this chapter (case one, Section 3.5.3; case two, Section 3.6.5; case three, Section 3.7.5). This calculation will be performed by requiring that the hypothetical gravitational wave signal of effect one be greater than the considered end mirror tilt effect. In case one (the two-mirror case) the only end mirror tilt effect is effect two. The isolation requirement due to effect two is independent of the cavity considered, since both effect one and two appear at the same location within the cavity and therefore always have the same frequency-dependent coupling to whichever output is chosen. In cases two and three (the grating cavities) effects two and three both apply when the end mirror is tilted, and we will consider only the isolation requirement of the dominant effect three. In both cases effect three will be found to set a stringent isolation requirement for end mirror tilt.

The notable difference between the grating cases is that in case two (the two-port cavity) both the effect one (gravitational wave) phase signal and the effect three (tilt induced lateral displacement) phase noise appear inside the cavity and are enhanced by the cavity resonance

effect. Conversely in the case three (the three-port cavity) the effect three (tilt induced lateral displacement) phase noise appears as the light is diffracted out of the cavity. Therefore only the effect one (gravitational wave) phase signal is enhanced by the cavity resonance effect. Thus the signal to noise ratio, and hence the isolation requirement, is improved in case three (the three-port cavity) over case two (the two-port cavity), and the factor of improvement is approximately the finesse [52]. Thus the three-port cavity case is favoured over the two-port cavity case for grating cavity implementation.

In Chapter 4 we will experimentally verify this calculation for end mirror tilt in the two-mirror and three-port cases (since this is the favoured grating case). In Chapter 5 we will use the symmetry of the three-port case to show that the phase noise is unevenly distributed between the three output ports, and therefore a careful selection of the readout port can be used to reduce the severity of the isolation requirement calculated in this chapter [28].

3.5 Case one: Two-mirror cavity

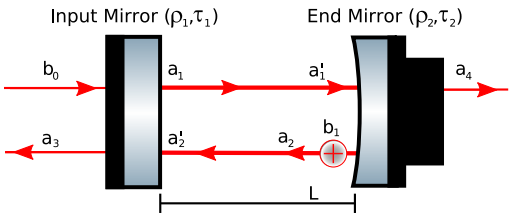

Figure 3.8: Case one, two-mirror cavity configuration, shown schematically, with end mirror oscillation. In reality the laser-beams overlap. This is the same figure as presented in Section 2.3.1, and the same theory applies for the externally input carrier field b_0, except with the introduction of an additional input b_1 at the oscillated mirror. This will be used for the phase modulation sideband input consistent with Section 2.1.3.

In this section case one (the two mirror cavity) is addressed for comparison purposes to case two (the two-port grating cavity) discussed in Section 3.6 and case three (the three-port grating cavity) discussed in Section 3.7. Phase modulation effect two (due to eigenmode length change

induced by end mirror tilt) will be calculated, and compared to phase modulation effect one (longitudinal end mirror displacement equivalent to a gravitational wave with strain $h = 2\Delta L/L$). An isolation requirement, such that phase modulation effect one is detectable above effect two, will be computed for a Virgo-esque gravitational wave interferometer [43].

To perform the above calculation we first solve the steady state field equations for case one (the two mirror cavity, as shown in Figure 3.8). The approach outlined in Section 2.3 will be followed, with the addition of an internal input b_1 to be used for phase modulation sidebands consistent with the method of Section 2.1.3. Both phase modulation effect one and effect two induce sidebands to appear at this location.

The cavity input mirror has the coupling matrix:

$$\begin{pmatrix} a_1 \\ a_3 \end{pmatrix} = \begin{bmatrix} \tau_0 e^{-i\phi_1} & \rho_0 \\ \rho_0 & \tau_0 e^{-i\phi_1} \end{bmatrix} \begin{pmatrix} b_0 \\ a_2' \end{pmatrix}. \tag{3.19}$$

where ρ_0 is the amplitude reflection coefficient of the input mirror, τ_0 is the amplitude transmission coefficient of the input mirror and $e^{-i\phi_0} = i$ is the phase-change experienced by the light-field on transmission. Using the coupling relations for the two-mirror cavity (with both inputs at a single presently undefined frequency) obtains,

$$a_1 = b_0 i\tau_1 + a_2'\rho_1 \tag{3.20}$$

$$a_1' = a_1 e^{-ikL} \tag{3.21}$$

$$a_2 = a_1'\rho_2 + b_1 \tag{3.22}$$

$$a_2' = a_2 e^{-ikL} \tag{3.23}$$

$$a_3 = b_0\rho_1 + a_2' i\tau_1, \tag{3.24}$$

This general set of equations will be solved for the carrier input frequency and the sideband

input frequency independently in the following Section 3.5.1 for effect one.

3.5.1 Case one, effect one, response to end mirror displacement

Two-mirror cavity response to end mirror displacement

In order to determine an isolation requirement for end mirror tilt in case one (the two-mirror cavity) it is necessary to compare effects one and two. In this section, we calculate the signal-sidebands at the output due to effect one. The end mirror displacement of effect one can be considered as being due to a hypothetical gravitational wave signal of strain $h = 2\Delta L/L$ where ΔL is the cavity length change. Solving first for the carrier field of angular frequency ω we obtain,

$$\begin{aligned}
a_1(\omega) &= b_0(\omega) i\tau_1 + a_2'(\omega)\rho_2 \\
a_2(\omega) &= a_1'(\omega)\rho_2 \\
a_2(\omega) &= \rho_2 e^{-ikL} \frac{b_0(\omega) i\tau_1}{1-\rho_1\rho_2 e^{-2ikL}} \\
a_2(\omega) &= \rho_2 e^{-ikL} b_0(\omega) i\tau_1 D(\omega) \\
a_3(\omega) &= b_0(\omega)\rho_1 + \rho_2 e^{-2ikL} \frac{b_0(\omega) i^2\tau_1^2}{1-\rho_1\rho_2 e^{-2ikL}} \\
a_3(\omega) &= b_0(\omega)\rho_1 + \rho_2 e^{-2ikL} b_0(\omega) i^2\tau_1^2 D(\omega), \qquad (3.25)
\end{aligned}$$

where $D(\omega) = 1/(1-\rho_1\rho_2 e^{-2ikL})$, $\omega = 2\pi f$ with f the frequency, and wavevector $k = \omega/c$ with c the speed of light.

If some length change ΔL is made to the cavity by adjusting the end mirror position the round-trip path length difference experienced by the light is given by $2\Delta L$, where $\Delta\phi$ is the

phase-change and $\lambda = 1064\,\text{nm}$ is the wavelength, thus obtaining,

$$\Delta\phi = 2\pi \cdot (2\Delta L/\lambda), \tag{3.26}$$

Assuming that the end mirror, as in Figure 3.8 is oscillated with amplitude ΔL and angular frequency ω_m, this will produce a phase modulation with modulation index $\Delta\phi$, and the angular frequency ω_m. We have already calculated the carrier field $a_2(\omega)$ (Equation 3.25) which generates the sideband $b_2(\omega+\omega_m)$, obtaining for the upper sideband (consistent with Equation 2.7),

$$\begin{aligned} b_1(\omega+\omega_m) &= i\frac{m}{2}a_2(\omega)e^{i\omega_m t}, \\ b_1(\omega+\omega_m) &= i\frac{m}{2}\rho_2 e^{-ikL}b_0(\omega)i\tau_1 D(\omega)e^{i\omega_m t}, \end{aligned} \tag{3.27}$$

where ω_m is the modulation angular frequency, m is the phase modulation index (depth, given by the maximum phase change, Equation 3.26), and following the $m \ll 1$ approximation that only the carrier light field generates sidebands, a_2 is for the carrier field only (given by Equation 3.22). Note that the LHS of this equation contains the function $\exp(i(\omega+\omega_m)t)$. This is matched on the RHS by the explicit $\exp(i\omega_m t)$, and the $\exp(i\omega t)$ contained within $a_2(\omega)$ (or $b_0(\omega)$). Solving the set of Equations 3.24 for the $b_1(\omega+\omega_m)$ (upper sideband) input alone obtains,

$$\begin{aligned} a_1(\omega+\omega_m) &= a_2'(\omega+\omega_m)\rho_1 \\ a_2(\omega+\omega_m) &= a_1'(\omega+\omega_m)\rho_2 + b_1(\omega+\omega_m) \\ a_2(\omega+\omega_m) &= \frac{b_1(\omega+\omega_m)}{1-\rho_1\rho_2 e^{-2i(k+k_m)L}} \\ a_2(\omega+\omega_m) &= b_1(\omega+\omega_m)D(\omega+\omega_m) \\ a_3(\omega+\omega_m) &= i\tau_1 e^{-i(k+k_m)L}b_1(\omega+\omega_m)D(\omega+\omega_m) \\ a_3(\omega+\omega_m) &= i^3\tau_1^2 b_0(\omega)\frac{m}{2}\rho_2 e^{-i(k+k_m)L}e^{-ikL}D(\omega)D(\omega+\omega_m)e^{i\omega_m t}, \end{aligned} \tag{3.28}$$

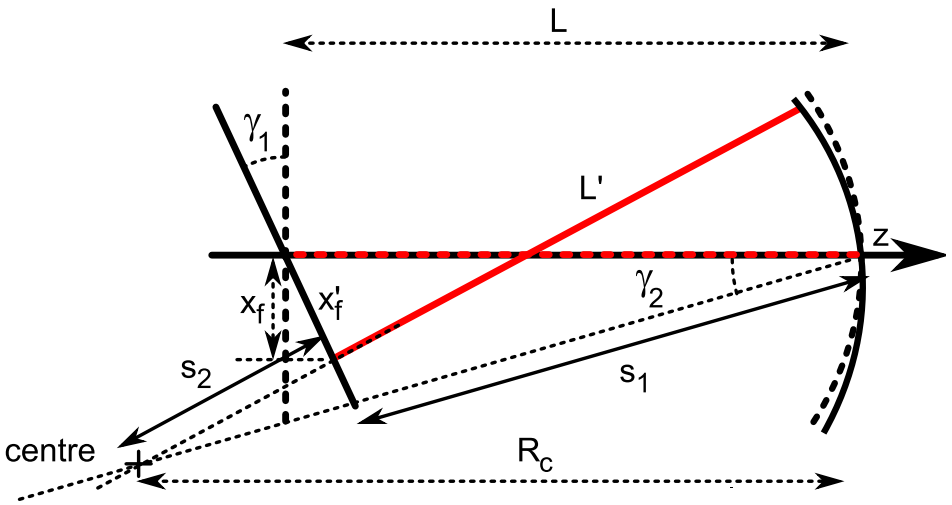

Figure 3.9: Schematic diagram for misalignment of case one (two-mirror cavity). A similar figure is used in Freise et al 2007 [52]

The equivalent to Equation 3.28 for the lower sideband with angular frequency $(\omega - \omega_m)$ can be obtained by the same method.

It is worth noting that any phase modulation occurring at the same location within the cavity will have the same frequency response as this, and can be expressed with some constant of proportionality as an end mirror equivalent displacement. I.e. Effect two has the same frequency response as calculated herein for effect one. It is therefore sufficient to know Equation 3.28, the phase change (modulation index) and modulation frequency to fully describe the output from a phase modulation occurring at input port b_1. Therefore effect one and effect two can be directly compared by their modulation indices, as will shortly be used to calculate the end mirror tilt isolation requirements for case one (the two-mirror cavity).

3.5.2 Case one, effect two, tilt induced phase change

Phase change in a two-mirror cavity due to end mirror tilt

In order to determine an isolation requirement for end mirror tilt in case one (the two-mirror cavity) it is necessary to compare effects one and two. Having calculated the phase signal sidebands at the cavity output due to effect one in the previous section, in this section we could calculate the phase noise sidebands at the output due to effect two (the only end mirror tilt effect occurring in case one, the two mirror cavity). However, since both effect one and two appear at the same location inside the cavity, they share the same frequency response obtained by coupling out of the cavity.

Therefore it is sufficient to compare their modulation indices by determining the effective cavity length change due to each effect. The cavity length change of effect one, due to the gravitational wave, is given by its strain $h = 2\Delta L/L$. The cavity length change of effect two (eigenmode displacement caused by end mirror tilt) can be determined from the geometry of the end mirror tilt as shown in Figure 3.9 [52]. From this geometry we can obtain $L' = R_c - s_2$, where L' is the new cavity length, and also [52]:

$$s_1 = L\frac{\cos\gamma_1}{\cos(\gamma_2-\gamma_1)}, \tag{3.29}$$

and also [52],

$$s_2 = (R_c - s_1)\cos(\gamma_2-\gamma_1) = R_c\cos(\gamma_1-\gamma_2) - L\cos\gamma_1. \tag{3.30}$$

Obtaining the new cavity length [52]:

$$L' \;=\; R_c - R_c\cos(\gamma_2-\gamma_1) + L\cos\gamma_1. \tag{3.31}$$

So for small angles [52]:

$$L' \approx L - R_c\gamma_2\gamma_1 + \frac{R_c}{2}\gamma_2^2 + \frac{R_c - L}{2}\gamma_1^2. \tag{3.32}$$

This yields a quadratic dependency on each misalignment angle. It is the change in cavity length $\Delta L = L - L'$ which institutes the phase-change. We can break the misalignment of the input mirror and end mirror into two parts. A DC component of misalignment caused by imperfect cavity setup, and a term dependent on frequency f at which we apply the signal to the end mirror. This can be written as $\gamma_2 = \gamma_{2,dc} + \gamma_2(f)$ for the end mirror, the only place where the signal frequency f is applied [52].

$$\begin{aligned} L' &\approx L - R_c(\gamma_{2,dc} + \gamma_2(f))(\gamma_{1,dc} + \gamma_1(f)) \\ &+ \frac{R_c}{2}(\gamma_{2,dc} + \gamma_2(f))^2 + \frac{R_c - L}{2}(\gamma_{1,dc} + \gamma_1(f))^2. \end{aligned} \tag{3.33}$$

Thus, the phase noise at a given frequency f is given by the mix-terms between the DC components and the $\gamma_2(f)$ component at frequency f. Physically, we can see that the DC misalignments generate a fixed noise level, and that the $\gamma_2(f)^2$ terms will be very small, as the initial $\gamma_2(f)$ itself will be small in so well isolated a device as an interferometric gravitational wave detector. Using the mix terms alone we obtain for the length change [52],

$$\Delta L(f) = R_c\gamma_{1,dc} \cdot \gamma_2(f) - R_c\gamma_{2,dc} \cdot \gamma_2(f_n), \tag{3.34}$$

and hence [52],

$$\Delta L(f) = R_c\gamma_2(f)(\gamma_{1,dc} - \gamma_{2,dc}). \tag{3.35}$$

The actual response of the cavity to end mirror tilt is that given by Equation 3.28, where the above determines the modulation index by substitution into Equation 3.26 for ΔL. Note

that no signal from angular actuation of the end mirror will exist unless there is some initial misalignment of either the end or input mirror. Only components of DC misalignment in the same plane as the f_n misalignment will generate this phase noise. Path length difference is $\Delta\zeta = 2\Delta L$, and converting to phase change using $\Delta\phi = 2\Delta L \cdot 2\pi/\lambda$ obtains:

$$\Delta\phi(f) = \frac{4\pi}{\lambda} R_c \cdot \gamma_2(f)(\gamma_{1,dc} - \gamma_{2,dc}), \tag{3.36}$$

We see that absent other factors and roll-offs we would obtain phase-noise as a number independent of frequency and proportional to $(\gamma_{1,dc} - \gamma_{2,dc})$ for any given $\gamma_2(f)$. This phase change is the modulation index (depth) creating the phase noise sidebands due to effect two (eigenmode length change induced by end mirror tilt) in case one (the two-mirror cavity). Since these sidebands have the same frequency response as those from effect one (gravitational wave equivalent end mirror longitudinal displacement) Equation 3.36 can be directly compared with the modulation index given by the gravitational wave strain $h = 2\Delta L/L$, the calculation of which will be performed in the following section and used to determine isolation requirements for a Virgo-esque interferometer.

3.5.3 Case one, end mirror tilt isolation requirement

For case one, the two-mirror cavity, we will calculate the end mirror tilt isolation requirement for some Virgo-esque cavity properties [43]. This will make the prior calculations of end mirror tilt to path length difference to phase signal more easily comparable between the three cases, and provide the relevant interferometric gravitational wave detector context. This will be based on a hypothetical gravitational wave signal appearing via effect one, and requiring that it be detectable over the dominant end mirror tilt noise source, effect two in case one (the two mirror cavity) and effect three in cases two and three (the two grating cavities). A gravitational wave signal can be expressed by its strength, defined as strain h, where L is the cavity length, and

ΔL the change in cavity length.

$$h = \frac{2\Delta L}{L}, \tag{3.37}$$

and the factor of two appears since for a h_+ polarised gravitational wave passing perpendicularly through a Michelson interferometer with Fabry-Perot arm cavities, this ΔL will be experienced with opposite sign by both cavities, the signals from which are then subtracted to obtain $2\Delta L$ at the detection port.

We demand that the end mirror tilt isolation requirement be such that the noise signal from end mirror tilt (effect two) is less than the gravitational wave signal. Since the gravitational wave strain h is expressed as a cavity length change and the gravitational wave signal generates sidebands at the end mirror, the derivation of Equation 3.28 for longitudinal end mirror displacement (effect one) also applies to the gravitational wave signal. Therefore it is sufficient to compare the magnitude of the cavity length change given by Equation 3.37 (for effect one) and substituting in from Equation 3.35 (for effect two),

$$\gamma_2(f) = \frac{hL}{2R_c(\gamma_{1,dc} - \gamma_{2,dc})}. \tag{3.38}$$

It is now possible to set the isolation requirement for $\gamma_2(f)$, allowing a gravitational wave induced strain of $h = 10^{-23}/\sqrt{\text{Hz}}$ (effect one) to be detected with at least equal strength as this noise source (effect two), in the absence of any other noise sources. This obtains the isolation requirements of [52]:

$$\gamma_2(f) < 2.14 \times 10^{-16} \frac{\text{rad}}{\sqrt{\text{Hz}}} \left(\frac{h}{10^{-23}/\sqrt{\text{Hz}}}\right) \left(\frac{L}{3\,\text{km}}\right) \left(\frac{3.5\,\text{km}}{R_c}\right) \left(\frac{20\,\text{nrad}}{\gamma_{1,dc} - \gamma_{2,dc}}\right) \tag{3.39}$$

where we have chosen the DC misalignment of the mirrors to be in the opposite direction, as this represents the worst-case misalignment scenario, and we expect the interferometer to explore

the full range of DC misalignment possibilities over time due to very low frequency effects such as temperature drift. This result provides a reference which we can compare to the two grating cavity cases we will study in Sections 3.6 and 3.7. It is implicit in the statement that effect one and effect two originate at the same location, and therefore share a frequency response, that this isolation requirement will remain the same for effect one verses effect two irrespective of the cavity (whether case one, two or three is considered). Therefore the following appreciations in Sections 3.6 and 3.7 need only to consider effects one and three. It will be found in both cases a more stringent isolation requirement is set, and therefore that end mirror tilt induced phase noise is dominated by effect three with a much smaller effect two (so long as a grating cavity is consider, else effect three does not exist at all).

3.6 Case two: Two-port coupled first order Littrow configuration grating cavity

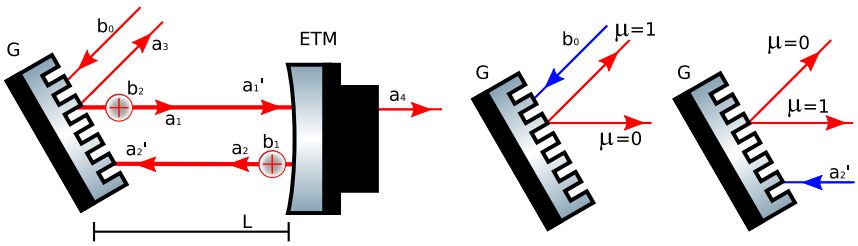

Figure 3.10: Case two, two-port grating cavity configuration, shown schematically. In reality the laser-beams overlap. G is the diffractive input optic, and ETM the end mirror. The diagram on the left shows the electromagnetic fields entering, within and leaving the cavity. Additional input ports b_1 (which will be used for the sidebands from a potential gravitation wave signal or cavity length change, effect one or two), and b_2 (which will be used for the sidebands from end mirror tilt induced effect of lateral displacement of the a_2' field across the grating, effect three) are also shown. The diagrams on the right show the diffraction order μ of the grating output ports (shown red). As these are different for each field incident on the grating (shown blue), two diagrams are required, one for the external input (center) and one for the cavity field (far right).

In this section case two (the two-port cavity) is addressed. Phase change effect three (grating lateral displacement effect due to end mirror tilt) will be calculated, and compared to phase modulation effect one (longitudinal end mirror displacement equivalent to a gravitational wave with strain $h = 2\Delta L/L$). An isolation requirement, such that phase modulation effect one is detectable above effect three, will be computed for a Virgo-esque gravitational wave interferometer [43].

In this cavity configuration the first diffraction order ($\mu = 1$) is used to retain light in the cavity. The first diffraction order must therefore diffract the light from the cavity back along the same path (from a_2' to a_1 in Figure 3.10). Meeting this requirement is termed first-order Littrow configuration. The first diffraction order must also have a coupling coefficient approaching unity (high diffraction efficiency) for the cavity to have a high finesse. The reflection order (zeroth diffraction order, $\mu = 0$) is used to couple light into and out of the cavity (from b_0 to a_1, and from a_2' to a_3, in Figure 3.10). Since the grating is in first order Littrow configuration the externally input light field from the laser will also be diffracted back along its input path (from b_0 to a_3 in Figure 3.10). Thus interference occurs between this light and the light reflected out of the cavity, which can be used for Pound-Drever-Hall feedback control or other similar modulation-demodulation techniques. Additional transmission through the cavity end mirror also outcouples light, as with all cavities. This outcoupling is reduced by achieving very high end mirror reflectivities of a few parts per million loss and transmission term combined.

To perform the above calculation we first solve the steady state field equations for case one (the two-mirror cavity, as shown in Figure 3.10). Internal input port b_1 will be used for phase modulation sidebands of effect one, and similarly b_2 will be used for the sidebands of effect three. This is analogous to the methods of Sections 3.5 and 3.7. Effect two will not be separately considered, as it has the same isolation requirement as given in Section 3.5.3 (see that section for details).

The diffraction grating has the coupling matrix:

$$\begin{pmatrix} a_1 \\ a_3 \end{pmatrix} = \begin{bmatrix} \eta_0 e^{-i\phi_0} & \eta_1 \\ \eta_1 & \eta_0 e^{-i\phi_0} \end{bmatrix} \begin{pmatrix} b_0 \\ a_2' \end{pmatrix}, \tag{3.40}$$

which is comparable to that of the cavity input mirror given in Equation 3.19, where η_0 is the amplitude coupling coefficient for the zeroth diffraction order (reflection, $\mu = 0$), η_1 is the amplitude coupling coefficient for the first diffractive order ($\mu = 1$), and $e^{-i\phi_0}$ is the term for the phase change experienced by the light field on reflection (zeroth-order) diffraction, which obeys the relation $e^{-i\phi_0} = i$ if there is no phase change on first-order diffraction. This can be intuitively understood, as the matrix has the same form as for a transmissive input mirror, therefore the same phase relations must comprise a valid solution. Using the coupling relations for case two (the two-port grating case, with all inputs at a single presently undefined frequency) obtains,

$$\begin{aligned} a_1 &= b_0 i\eta_0 + \eta_1 a_2' + b_2 \\ a_1' &= a_1 e^{-ikL} \\ a_2 &= a_1' \rho_2 + b_1 \\ a_2' &= a_2 e^{-ikL} \\ a_3 &= b_0 \eta_1 + a_2' i\eta_0, \end{aligned} \tag{3.41}$$

We will solve this set of equations for the carrier input frequency and the sideband input frequency independently in Section 3.6.3.

3.6.1 Manufacturing techniques for high diffraction efficiency two-port grating

In case two, the two-port coupled grating cavity, the first-diffraction order is used to retain light in the cavity and directly diffract light back along the input beam path. Reflection couples light into and out of the cavity. Other diffraction orders are essentially loss terms and can be eliminated by an appropriate selection of grating properties, specifically the period (d), width, depth and overall designed shape of the grating striation. Width is distinct from period, as a grating may have a wide peak and a narrow trough, whilst maintaining the same peak-to-peak distance as another, quite different grating with a narrow peak and a wide trough.

Depending on the microscopic design of the diffraction grating, it may require coating with a dielectric stack of specified properties. It has been shown [42] that in the case of mirrors coated with highly reflective dielectric stacks, the thermoelastic and thermorefractive noise in the coating dominates the thermoelastic and thermorefractive noise of the optical substrate. This is because the substrate is highly uniform and is selected for its high Q-factor and, in the case of a mirror, its transparency at the appropriate wavelength. All reflective optics such as diffraction gratings allow non-transmissive substrates with higher Q-factors. Thermal lensing is eliminated in the substrate and the freedom of the mounting permits a greater range of thermal compensation options for the coating. The coating thickness required for the grating can also be reduced compared to that of a mirror, resulting in a lower absorption and therefore lower thermal noise effects, although the structure a grating coating may require can reduce the Q-factor of the substrate substantially [25].

Retaining light in the cavity using the first diffraction order requires a high diffraction efficiency if the cavity finesse is to be high, because the first-diffracted beam is analogous to the reflected beam from the input mirror in case one (the two-mirror cavity). Therefore the finesse of the cavity is limited by the diffraction efficiency of the grating. In 1998 Sun and Byer proved the

principle by simulating Michaelson and Sagnac interferometers and a Fabry-Perot cavity using gratings. They achieved diffraction efficiencies of 0.482 and 0.476 for the interferometers and 0.91 for the Fabry-Perot cavity [49]. Although these values give only a modest cavity finesse of 53 for the Fabry-Perot cavity [50] which depended heavily on the choice of end mirror reflectance it was speculated by them and other authors [53] that coating multiple layers of thin dielectric film onto a metallic grating would increase the diffraction efficiency.

A further problem with the metallic gratings used was that they tended to fail under the high laser powers required but dielectric gratings were known to have a higher damage threshold [54] which were expected to be able to fulfill the requirements for Advanced LIGO and Virgo. More recently research into high-power chirped pulse amplification has developed a technique where the periodic grating structure is etched directly into a dielectric stack using lithography. However later experiments have shown that even using this new technique diffraction efficiencies of 0.95 [55] are common even among high-end gratings and the highest known to have been produced is 0.99. Thus cavity finesses that can be generated by gratings suitable for the case two (the two-port cavity) configuration are simply too low for gravitational wave detection. Work is ongoing to improve diffraction efficiencies, and in the expectation of success we shall consider the effects of grating-induced phase changes in generating phase noise in a two-port grating cavity installed in a gravitational wave detector.

3.6.2 Case two, effect three, tilt induced phase change

Phase change in a two-port grating cavity due to end mirror tilt

In this section we calculate the phase change due to effect three, the lateral displacement of the cavity eigenmode (light field inside the cavity) across the grating striations. This requires determining the lateral displacement Δx due to end mirror tilt, for which we consider the cavity

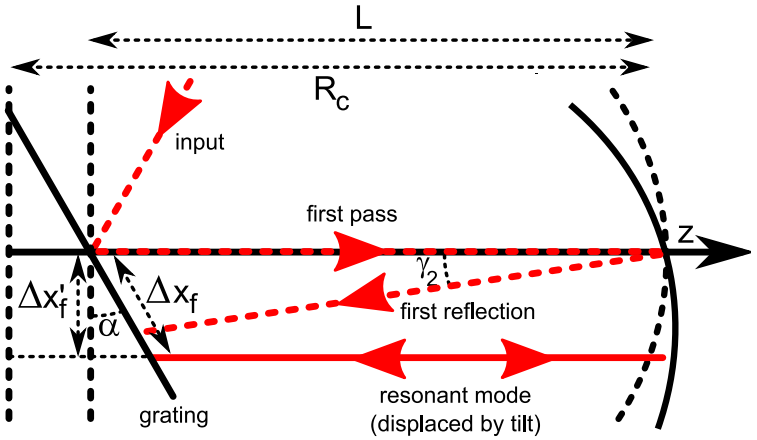

Figure 3.11: Schematic diagram for misalignment of case two, end-mirror tilt of a two port diffractive cavity. The displacement of the eigenmode of the cavity (the resonant mode) from the center of the cavity is determined (once the stable position has been reached after sufficient cavity round trips) by the radius of curvature of the end mirror R_c and the angle at which the end mirror is tilted γ_2. The displacement of the cavity eigenmode across the striations of the grating is then determined by the angle of the grating to the cavity α.

geometry shown in Figure 3.11 (as we have done in case one for the two-mirror cavity). The same assumptions are made, that the input optic has an infinite radius of curvature (rather, it is flat macroscopically whilst still having grating striations) and that the end mirror is a section of a spherical surface. Note that case two (the two-port grating cavity) will experience the effect three phase noise calculated here in addition to the effect two phase noise calculated in Section 3.5 (for the two mirror cavity), because effect two is purely a result of the shared cavity geometry. However, we will see that effect three dominates overwhelmingly, and hence effect two can be neglected. From the geometries shown in Section 3.5.2 the displacement of the optical axis when the end mirror is misaligned by $\gamma_2(f)$ can be approximated to [52]:

$$\Delta x'(f) \approx R_c \gamma_2(f), \tag{3.42}$$

so by transforming into the grating co-ordinate system we obtain [52]:

$$\Delta x(f) = \frac{\Delta x'_{\gamma_2}(f)}{\cos(\alpha)} = \frac{R_c}{\cos(\alpha)} \gamma_2(f), \tag{3.43}$$

which as shown in Section 3.3.1 generates a path length change given by [52]:

$$\Delta\zeta(f) = \frac{\Delta x(f)\mu\lambda}{d}, \tag{3.44}$$

where this path length difference is experienced due to a shift in the position of the cavity light field a_2' in Figure 3.10 and does not effect the external input field b_0. Therefore it only applies to the diffraction orders from the light field a_2' shown in the right hand side diagram. The coupling to the external output occurs in the reflection order ($\mu = 0$), and therefore we only have to consider the field returning to the cavity in the first diffraction order ($\mu = 1$). Thus we obtain by substituting $\mu = 1$ and transforming to the grating co-ordinate system using Equation 3.43 [52],

$$\Delta\zeta(f) = \frac{R_c}{\cos(\alpha)}\frac{\lambda}{d}\gamma_2(f). \tag{3.45}$$

This $\Delta\zeta(f)$ includes both the incoming (ζ_3, in Figure 3.5) and outgoing (ζ_4) trips to the grating as the light field circulates in the cavity. It is a path length difference equivalent to a $2\Delta L$ end mirror displacement, save for its position in the cavity.

From Equation 3.45 the end mirror tilt isolation requirement can be computed for our Virgo-esque gravitational wave interferometer; however, for completeness we also calculate the phase change induced by this path length difference using the relation $\Delta\zeta = \Delta\phi\lambda/2\pi$, given by,

$$\Delta\phi(f) = \frac{2\pi}{d}\frac{R_c}{\cos(\alpha)}\gamma_2(f). \tag{3.46}$$

Effect three (lateral displacement of the cavity eigenmode across the surface of the grating) in the case two (the two-port grating) cavity configuration will therefore generate a phase change given by Equation 3.46. This can then be used to calculate the extent of the sidebands induced by the effect three phase modulation at the output of the cavity. Note that it was possible

in case one to compare effect one (a hypothetical gravitational wave) and effect two (due to end mirror tilt) directly using the phase modulation, because they shared an input port and hence frequency response. In case two (the two-port grating cavity) this is not possible, since effect one introduces sidebands at input port b_1 in Figure 3.10, whereas effect three introduces sidebands at the input port b_2. Therefore we must use Equation 3.46 to calculate the sidebands induced by effect three at the output of the two-port grating cavity.

3.6.3 Case two, effect three, response to end mirror tilt

Two-port grating cavity response to end mirror tilt

Having determined the phase modulation index of effect three in case two (the two-port coupled grating cavity, given by Equation 3.46) it is now possible to calculate the sidebands induced by this phase modulation at the output of the cavity. This is necessary to compare to the sidebands induced by a hypothetical gravitational wave (effect one) in case two, and hence to determine end mirror isolation requirements. Solving the coupling relations given in Equations 3.41 for the carrier field of angular frequency (ω) alone obtains (where there is no carrier field input at either b_1 or b_2),

$$\begin{aligned}
a_1(\omega) &= b_0(\omega) i\eta_0 + \eta_1 a_2'(\omega) \\
a_1(\omega) &= \frac{b_0(\omega) i\eta_0}{1-\eta_1\rho_2 e^{-2ikL}} \\
a_1(\omega) &= b_0(\omega) i\eta_0 D(\omega) \\
a_3(\omega) &= b_0(\omega)\eta_1 + \rho_2 e^{-2ikL}\frac{b_0(\omega) i^2\eta_0^2}{1-\eta_1\rho_2 e^{-2ikL}} \\
a_3(\omega) &= b_0(\omega)\eta_1 + \rho_2 e^{-2ikL} b_0(\omega) i^2\eta_0^2 D(\omega), \qquad (3.47)
\end{aligned}$$

where $D(\omega) = 1/(1-\eta_1\rho_2 e^{-2ikL})$. An end mirror tilt oscillation will generate phase sidebands at internal input port b_2 (consistent with Equation 2.7) as shown in Figure 3.10, and by substituting

in Equation 3.47 to determine that the upper sideband is given by,

$$\begin{aligned} b_2(\omega+\omega_m) &= i\frac{m}{2}a_1(\omega)e^{i\omega_m t+\Phi} \\ b_2(\omega+\omega_m) &= i\frac{m}{2}b_0(\omega)i\eta_0 D(\omega)e^{i(\omega_m t+\Phi)}, \end{aligned} \tag{3.48}$$

where ω_m is the modulation frequency, m is the phase modulation index (depth, given by the maximum phase change), and following the $m \ll 1$ approximation that only the carrier light field generates sidebands, $a_1(\omega)$ is for the carrier field only (given by Equation 3.47). Φ is some fixed phase defining the starting position of the phase modulation. Solving the set of Equations 3.41 for the upper sideband angular frequency $(\omega+\omega_m)$ alone obtains (where such sidebands only appear at b_2),

$$\begin{aligned} a_1(\omega+\omega_m) &= \frac{b_2(\omega+\omega_m)}{1-\eta_1\rho_2 e^{-2i(k+k_m)L}} \\ a_1(\omega+\omega_m) &= b_2(\omega+\omega_m)D(\omega+\omega_m) \\ a_3(\omega+\omega_m) &= i\eta_0\rho_2 e^{-2i(k+k_m)L}b_2(\omega+\omega_m)D(\omega+\omega_m) \\ a_3(\omega+\omega_m) &= i^3\eta_0^2 b_0(\omega)\frac{m}{2}\rho_2 e^{-2i(k+k_m)L}D(\omega)D(\omega+\omega_m)e^{-i(\omega_m t+\Phi)}, \end{aligned} \tag{3.49}$$

this upper sideband result for effect three can then be compared to the upper sideband result for effect one (for a hypothetical gravitational wave appearing at input b_1) to obtain the isolation requirement. Effect one, for the gravitational wave, will be calculated in the following section and the comparison will be made in Section 3.6.5.

3.6.4 Case two, effect one, response to a gravitational wave

Two-port grating cavity response to a hypothetical gravitational wave

For effect one (a hypothetical gravitational wave) no input is present at b_2 and the gravitational wave sidebands appear at b_1. The derivation for this case is the almost identical to that used for Equation 3.28 in case one (the two-mirror cavity), effect one, where the gravitational wave strain $h = 2\Delta L/L$. The only difference is that instead of using the mirror coupling matrix in Equation 3.19 the coupling matrix for the two-port grating given in Equation 3.40 is used. This obtains for the effect one sideband at the output, where the subscript h has been introduced to distinguish the sideband due to effect one (gravitational wave strain) from that of Equation 3.49 for effect three (dominant end mirror tilt effect).

$$a_{3,\mathrm{h}}(\omega+\omega_m) = i^3\eta_0^2 b_0 \frac{m}{2}\rho_2 e^{-i(k+k_m)L}e^{-ikL}D(\omega)D(\omega+\omega_m)e^{i(\omega_m t+\Phi)}. \tag{3.50}$$

This equation can now be compared to Equation 3.49 for the effect three sideband, to obtain the isolation requirement for the case two (two-port grating) cavity. The comparison will be performed in the following section.

3.6.5 Case two, end mirror tilt isolation requirement

To derive the end mirror isolation requirement for case two (the two-port grating cavity) we require that effect three (for end mirror tilt) be smaller than effect one (for the gravitational wave). The upper sidebands induced by these effects are given at the output of the cavity by Equation 3.49 for effect three and Equation 3.50 for effect one. The subscript γ_2 has been introduced to Equation 3.49 to distinguish the effect three sidebands (due to end mirror tilt) from the entirely separate effect one sidebands (due to hypothetical gravitational wave),

obtaining,

$$\begin{aligned} a_{3,\mathrm{h}}(\omega+\omega_m) &> a_{3,\gamma_2}(\omega+\omega_m) \\ m_h e^{-ikL} e^{-i\Phi} &> m_{\gamma_2} e^{-i(k+k_m)L} \\ m_h &> m_{\gamma_2} \end{aligned} \tag{3.51}$$

where we have chosen phase offset Φ to represent the worst case of confusion between the gravitational wave signal and the noise, when they are in phase. This can then be used to derive the isolation requirement for a given gravitational wave signal (creating effect one) which we assume to have a sensitivity of strain $h = 10^{-23}/\sqrt{Hz}$. We use the same Virgo-esque interferometer parameters [43] as we did for case one (the two-mirror cavity), and no other noise sources. Remembering that the phase modulation index is equal to the amplitude of the phase change ($m = \Delta\phi$), which for effect one (the gravitational wave) is given by Equation 3.26 and $h = 2\Delta L/L$, and for effect three (the end mirror tilt) Equation 3.46. These substitutions into Equation 3.51 result in,

$$\frac{hL\cos(\alpha)}{R_c}\frac{d}{\lambda} > \gamma_2(f), \tag{3.52}$$

which can now be used to set the isolation requirement for $\gamma_2(f)$, allowing a gravitational wave induced strain of $h = 10^{-23}/\sqrt{\mathrm{Hz}}$ to be detected with at least equal strength as this noise source, in the absence of any other noise sources. This obtains the isolation requirements of [52]:

$$\gamma_2(f) < 7.42\times10^{-24}\frac{\mathrm{rad}}{\sqrt{Hz}}\left(\frac{h}{10^{-23}/\sqrt{Hz}}\right)\left(\frac{L}{3\,\mathrm{km}}\right)\left(\frac{\cos(\alpha)}{\cos(30^{\mathrm{o}})}\right)\left(\frac{3.5\,\mathrm{km}}{R_c}\right)\left(\frac{d}{\lambda}\right). \tag{3.53}$$

Where d is the grating striation period, and λ the wavelength of the light. From our prior discussion of grating design in Section 3.2.4 we can recall the relationship between them given in Equation 3.8, $\lambda < d < 2\lambda$. For these purposes we will assume the best-case scenario that

can be achieved of $d = \lambda$, both for simplicity and because it aligns with our assumption at the beginning of this section that we expect improvement in grating technology to both allow for higher diffraction efficiencies and allow the limits of Equation 3.8 to be approached. Even in this case, we can see that case two (the two-port cavity) has a much larger coupling of alignment noise into gravitational wave signal than case one (the two-mirror case) solved in 3.5, and hence much more stringent end mirror alignment requirements. As with case one, in case two the cavity resonance does not suppress the noise, because both effects one and three (gravitational wave signal and end mirror tilt induced noise) appear inside the cavity (since the $\mu = 1$ term retains light inside the cavity). We will shortly see that this is different for case three, the three-port coupled grating cavity.

3.7 Case three: Three-port coupled second order Littrow configuration grating cavity

In this section case three (the three-port cavity) is addressed. Phase change effect three (grating lateral displacement effect due to end mirror tilt) will be calculated, and compared to phase modulation effect one (longitudinal end mirror displacement equivalent to a gravitational wave with strain $h = 2\Delta L/L$). An isolation requirement, such that phase change effect one is detectable above phase change effect three, will be computed for a Virgo-esque gravitational wave interferometer [43].

To perform the above calculation we first solve the steady state field equations for case three (the three-port grating cavity, as shown in Figure 3.12). Internal input port b_1 will be used for phase modulation sidebands of effect one, and similarly b_2 will be used for the sidebands of effect three. This is analogous to the method of Sections 3.5 and 3.6. Once again effect two will not be separately considered, as it has the same isolation requirement as given in Section

3.5.3 (see that section for details).

In case three (the three-port cavity) the reflection order (zeroth diffraction order, $\mu = 0$) is used to retain light in the cavity, and therefore must have a coupling coefficient approaching unity (low-loss, low diffraction efficiency). The first diffraction order ($\mu = 1$) is used to couple light into and out of the cavity. Light so coupled out of the cavity (to a_4 in Figure 3.12) is called back-reflected light, and interferes with the light directly diffracted in the second order ($\mu = 2$) from the grating, hence 'second order Littrow configuration'. Light is also forward-reflected out of the cavity in the direction in the minus-first diffraction order $\mu = -1$ (to a_3), which interferes with the input light directly-reflected from the grating. Assignment of the negative sign is arbitrary with the setup of the system, i.e. a negative sign can be added to all diffraction orders without consequence. Diagrammatically, this choice determines whether one counts positively in the clockwise or counterclockwise direction from the reflection order $\mu = 0$. The third output port of the cavity is the same as for all cavities - transmission through the end mirror. Thus, the diffraction grating has the more complex coupling matrix, where 'a' and 'b' are electromagnetic fields associated with the location shown in Figure 3.12 and previously stated as a general coupling matrix in Equation 3.9:

$$\begin{pmatrix} a_4 \\ a_1 \\ a_3 \end{pmatrix} = \begin{bmatrix} \eta_2 e^{-i\phi_2} & \eta_1 e^{-i\phi_1} & \eta_0 \\ \eta_1 e^{-i\phi_1} & \rho_0 & \eta_{-1} e^{-i\phi_1} \\ \eta_0 & \eta_{-1} e^{-i\phi_1} & \eta_{-2} e^{-i\phi_2} \end{bmatrix} \begin{pmatrix} b_0 \\ a_2' \\ 0 \end{pmatrix}. \tag{3.54}$$

where η_{n} is the amplitude coupling coefficient and ϕ_{n} the phase change in the n'th diffraction order ($\mu = \mathrm{n}$), η_0 being for the reflection order and ρ_0 for the special case of reflection normal to the grating surface. Note that by definition $\eta_{-1} = \eta_1$, and similarly $\eta_{-2} = \eta_2$. The use of minus-signs in the indices of the equation above is to improve the clarity of which 'side' of the matrix represents the negative diffraction orders. This special case exists because the presence of the additional port complicates the system as shown in Figure 3.12, and specifically because

when the input light field is at the normal to the grating both first ($\mu = 1$) and negative-first ($\mu = -1$) diffraction orders exist. Hence to maintain energy conservation a lower coupling coefficient is required, governed by the Equation 3.10 [33]. This analysis also shows us that the phase relations of the three-port grating are not independent of the amplitude coupling coefficients, as they are for a two-port optic such as a mirror or two-port grating. It transpires this places fundamental limits on the diffraction efficiency of a grating to be used in reflective configuration [33]. The details of the three-port grating coupling relations are discussed further in Section 3.2.5. When writing the coupling relations for the three-port coupled grating cavity, it is helpful to use the following simplified notation, where $G_{\mathrm{n}} = \eta_{\mathrm{n}} \exp(-i\phi_{\mathrm{n}})$, obtaining for the coupling matrix,

$$\begin{pmatrix} a_4 \\ a_1 \\ a_3 \end{pmatrix} = \begin{bmatrix} G_2 & G_1 & G_0 \\ G_1 & \rho_0 & G_1 \\ G_0 & G_1 & G_2 \end{bmatrix} \begin{pmatrix} b_0 \\ a_2' \\ 0 \end{pmatrix}. \tag{3.55}$$

Using this coupling matrix for the grating we can write the coupling relations for case three (as shown in Figure 3.12), obtaining, with all inputs at a single, presently undefined frequency,

$$\begin{aligned} a_1 &= b_0 G_1 + a_2' \rho_0 \\ a_1' &= a_1 e^{-ikL} \\ a_2 &= a_1' \rho_2 + b_1 \\ a_2' &= a_2 e^{-ikL} \\ a_4 &= b_0 G_2 + a_2' G_1 + b_2, \end{aligned} \tag{3.56}$$

This three-port grating is considered advantageous because it retains light in the cavity through reflection. Thus it is the maximum reflectivity of the grating at normal incidence that determines the cavity finesse. Multilayered gratings can routinely achieve reflectivities of greater than 0.9998 [51] by overcoating with the same multilayer dielectric coatings that are used for mirrors.

We will shortly see by comparing Section 3.7.5 to Section 3.6.5 that this also creates some insensitivity to effect three phase noise compared to the case two (two-port grating) cavity. This improvement applies since in case three (the three-port grating cavity) the effect three (lateral grating displacement due to end mirror tilt) phase noise only occurs outside the cavity and is therefore not enhanced by the cavity effect - whilst the hypothetical gravitational wave is, leading to an improved signal to noise ratio. In Chapter 5 it will be shown that the symmetry of case three (the three-port cavity) also improves insensitivity to phase noise introduced by input beam pointing or lateral displacement of the grating itself, provided that the forward-reflected output port (a_3 in Figure 3.12) is used for detection.

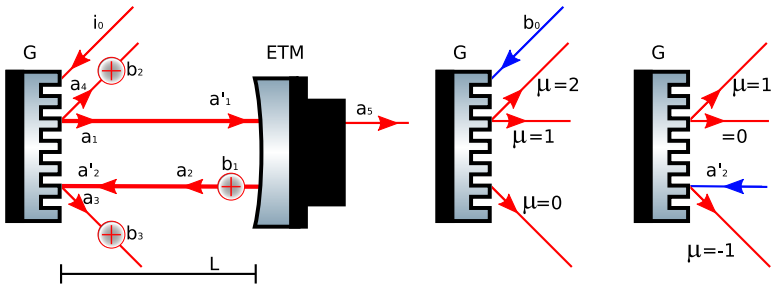

Figure 3.12: Case three (three-port grating) cavity configuration, shown schematically. In reality the laser-beams overlap. The diagram on the left shows the electromagnetic fields entering, within and leaving the cavity. The sidebands (b_2 and b_3) induced by lateral displacement of the a_2' field across the grating due to effect three (end mirror tilt induced displacement of the eigenmode across the grating striations) are shown, as are those (b_1) induced by effect one (a hypothetical gravitational wave signal). The diagrams on the right show the diffraction orders of the grating output ports (shown red). As these are different for the two fields incident on the grating (shown blue) two diagrams are required, one for the external input (center) and one for the cavity field (far right). It has been assumed that there is no field incident on the third port.

3.7.1 Manufacturing techniques for low-loss, low-diffraction efficiency three-port gratings

In case three, the three-port grating case, reflection from the grating (zeroth order diffraction) is used to retain light in the cavity. The first diffraction order is used to couple light into and out of the cavity back along the beam path. Second-order diffraction of the input light directly diffracts light back along the input beam path, since second-order Littrow configuration is used. This (a_4 in Figure 3.12) is known as the back-reflected port. Direct reflection from the grating generates the forward-reflected port (a_3), and minus-first order diffraction couples light out of the cavity into this port. All terms higher than second-order diffraction are loss terms and can be eliminated by selecting appropriate grating properties as discussed in Section 3.6.1. The second-order diffraction term of input field b_0 can itself be considered as a loss term which cannot be eliminated by these means, since it is co-incident with the required first-order diffraction term of the cavity field a_2' (see Figure 3.12, center and right hand side images). Power recycling could be used to retrieve some of the power lost to this port (as with light directly reflected from the input mirror of a two-mirror cavity), and the efficiency of second-order diffraction can in any case be minimised by grating design [56].

Although the analogy with case one (the two-mirror cavity) is not precise, from the point of view of cavity finesse a high reflection coefficient is required in case three (the three-port cavity). A high reflection coefficient imposes both low diffraction coefficients and low loss. Two methods of producing high reflection efficiency gratings have been considered. Both involve combining a highly reflective (HR) dielectric stack with electron-beam lithography and reactive ion beam etching [56]. Since both include a HR stack, neither case provides improvement verses coating thermal noises (see Section 1.2.3 for an introduction to thermal noise sources). If the HR stack is applied first, then only the top layer is etched with the diffraction grating. Most light is transmitted by this grating, with only low-efficiency diffraction occurring. The HR stack

beneath the grating then reflects the transmitted light resulting in high reflection efficiency. The diffractive efficiency of the grating depends in a complex way upon the relationship between the depth of the etching and the thickness of the etched layer. The mathematics involved to select regions of the parameter space with favourable properties is presented in Clausnitzer et al [56]. Therein it was found that with an overall layer thickness of 550 nm, a groove depth of between 150 and 350 nm offers diffraction efficiencies as low as 2.5 percent, and the possibility of a correspondingly high reflection coefficient.

The second technique for creating a grating with a high reflection coefficient is to etch the substrate followed by overcoating with the HR stack. In this case the features of the grating are partially 'filled in' by the overcoated layers, resulting in a smoother surface. This reduces errors introduced by the etching process including roughness, periodical fill factor variations and sharp edges. It is expected that this will reduce photon scattering, and therefore lost light power [56], and therefore led to favouring this type of overcoated grating. Later research has shown that mechanical Q-factor (important for reducing Brownian thermal noise, see Section 1.2.3) is significantly reduced with poor surface quality of each layer the light interacts with. The inherent roughness of gratings reduces surface quality (due to phonon scattering, which should not be confused with the photon scattering previously discussed [25]). The overcoated grating has surface roughness at every layer, compared to the grating-on-top approach where only the top layer is rough. Hence the overcoated approach has a significantly reduced Q-factor (and hence increased sensitivity to thermal noise). The grating-on-top of the previous paragraph was found to have a Q-factor (and hence thermal noise performance) little worse than that of a undisturbed HR stack [25]. From the point of view of grating translation phase noise, the two techniques are equivalent, and for practical reasons we used a grating of this second, overcoated type in the experiment detailed in Chapter 4. Since the tabletop experiment was insufficiently sensitive to detect thermal noise this did not present a practical problem.

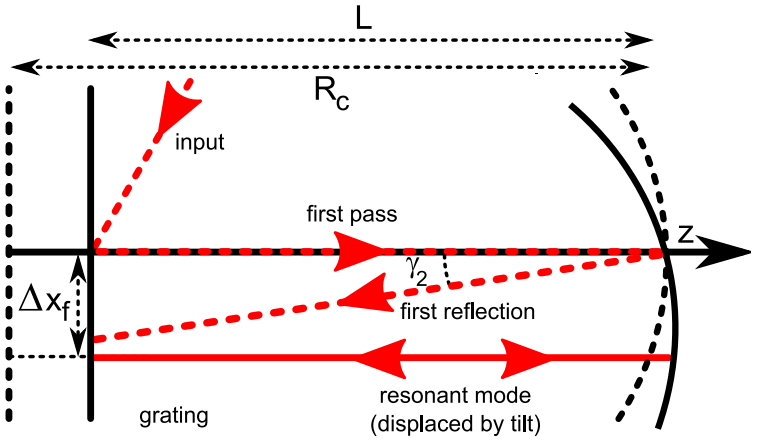

Figure 3.13: Schematic diagram for misalignment of three, end-mirror tilt of a three port diffractive cavity. This is similar to Figure 3.11, in that the radius of curvature R_c and the end mirror tilt angle γ_2 determine the displacement of the resonant mode. It differs in that the grating is aligned with the cavity, hence angle α is zero.

3.7.2 Case three, effect three, tilt induced phase change

This section calculates the phase change in a three-port coupled grating cavity due to end mirror tilt, which laterally displaces the eigenmode across the grating striations. It is important to note that effect two, due to misalignment of the end mirror and discussed in Section 3.5.2 for case one (the two-mirror cavity), will also appear in the case three (the three-port grating) cavity. This section deals with the additional noise due to the grating striation, and the lateral translation of the beam across it (effect three). The depth of the phase modulation (the maximum phase change caused by effect three) will be determined. In order to do this, we must first compute the displacement of the cavity eigenmode from the position of neither mirror being misaligned (using the geometry shown in Figure 3.13, a simplified version of Figure 3.11 applying to case three, the three-port grating cavity). We find that the center of the sphere radius R_c is at position [52],

$$x_c = -R_c \sin(\gamma_2), \tag{3.57}$$

and therefore the x-position where the eigenmode of the cavity impinges on the diffractive input optic is given by [52],

$$x_f = x_c + s_2 \sin(\gamma_1) = (\sin\gamma_1)(R_c\cos(\gamma_2-\gamma_1) - L\cos\gamma_1) - R_c\sin\gamma_2, \tag{3.58}$$

so in the grating co-ordinate system x' we obtain the position of the eigenmode of [52],

$$x'_f = \frac{x_f}{\cos\gamma_1} = R_c\sin(\gamma_1-\gamma_2) - L\sin\gamma_1. \tag{3.59}$$

The small angle approximation [52],

$$x'_f \approx= -R_c\gamma_2 + (R_c - L)\gamma_1, \tag{3.60}$$

will be useful. Note that the response is linear to angular misalignment. I.e. we only need to consider the change in the position of the cavity eigenmode due to the varying angular component $\gamma_2(f_n)$ applied to the end mirror to determine the phase noise, and not - provided they are anyway suitably small - the starting misalignment positions of the two mirrors. This is useful for our experiment, but actually unfortunate as grating-translation phase-noise will not be much reduced by improving DC optical alignment. Thus we obtain,

$$\Delta x'_{\gamma_2}(f) = R_c\gamma_2(f), \tag{3.61}$$

where $\Delta x'_{\gamma 2}(f_n)$ is the length x'_f, varying due to angular dithering of the end mirror of amplitude γ_2 at frequency f_n, and the minus sign can be neglected since it is irrelevant which direction along the x axis is moved by a clockwise or counterclockwise rotation of the end-mirror. The displacement is transformed to the co-ordinate system x of the grating as,

$$\Delta x_{\gamma_2} = \frac{\Delta x'_{\gamma_2}}{\cos(\alpha)}, \tag{3.62}$$

although α is the angle between the cavity-beam and the input beam which for this configuration is zero. For comparison purposes to Equation 3.36 and 3.46 we can convert this displacement to a phase change using $\Delta\phi = -2\pi\Delta x\mu/d$, from Equation 3.15 obtains,

$$\Delta\phi_{\gamma_2}(f) = \frac{2\pi R_c \mu}{d\cos\alpha}\gamma_2(f). \tag{3.63}$$

Alternatively, by substitution from Equation 3.14 we can obtain for the path length difference,

$$\Delta\zeta_{\gamma_2} = \frac{R_c\gamma_2(f)\mu\lambda}{d\cos(\alpha)}. \tag{3.64}$$

Having obtained the phase modulation in case three (three-port grating cavity) due to effect three, it is now possible to calculate the sidebands which will appear at the output of the cavity due to effect three. These sidebands will be calculated in the following section, and will themselves be compared to the effect one sidebands (hypothetical gravitational wave, calculated in Section 3.7.4) to obtain the end mirror tilt isolation requirement (in Section 3.7.5).

3.7.3 Case three, effect three, response to end mirror tilt

Three-port grating cavity response to end mirror tilt

It is now necessary to solve the coupling relations for the case three (the three-port grating) cavity, and obtain the sideband field at the output due to effect three. The path length difference and phase change of effect three only occur in diffraction orders other than zero, so they only occur as the cavity field couples through the grating and out of the cavity. This is effectively equivalent to applying this noise to some optic external to the cavity. As we are only displacing the cavity field a_2' we only need to consider the outputs in the right hand side diagram of Figure 3.12.

We choose to look at the back-reflected (a_4) output port, which experiences the first diffraction order ($\mu = 1$), for consistency with the case one (two-mirror) and two (two-port grating) cavities. Therefore we neglect the forward-reflected a_3 port, which in this appreciation experiences an equal phase change, depending only on the absolute value of the diffraction order $|\mu|$. Note that this only applies when it is the a_2' field that is displaced across the grating surface (in this case by end mirror tilt). We will examine the alternative case of lateral translation of the physical grating in Chapter 5, where some cancellation of the phase change due to symmetry is found to occur in the forward-reflected port. In this section we consider effect three (lateral displacement of the a_2' field across the surface of the grating) the phase modulation which creates sidebands as shown in Figure 3.12, where b_2 (and b_3, which we will neglect in this appreciation) serve as the inputs for those sidebands. We solve for the carrier angular frequency (ω), which has no input at b_1 or b_2, to obtain,

$$\begin{aligned} a_1(\omega) &= b_0(\omega)G_1 + a_1(\omega)\rho_0\rho_2 e^{-2ikL} \\ a_1(\omega) &= b_0(\omega)G_1 D(\omega) \\ a_2(\omega) &= b_0(\omega)G_1\rho_2 e^{-ikL} D(\omega) \\ a_2'(\omega) &= b_0(\omega)G_1\rho_2 e^{-2ikL} D(\omega), \end{aligned} \tag{3.65}$$

where $D(\omega) = 1/(1-\rho_0\rho_2\exp(-2ikL))$, and the upper set of lateral grating displacement phase modulation sidebands, with angular frequency $(\omega+\omega_m)$ are given by,

$$\begin{aligned} b_2(\omega+\omega_m) &= i\frac{m}{2}G_1 a_2'(\omega)e^{i\omega_m t} \\ b_2(\omega+\omega_m) &= i\frac{m}{2}b_0(\omega)G_1^2\rho_2 e^{-2ikL}D(\omega)e^{i\omega_m t}, \end{aligned} \tag{3.66}$$

and thus at the back-reflected output we obtain,

$$a_4(\omega+\omega_m) = b_2(\omega+\omega_m) = i\frac{m}{2}b_0(\omega)G_1^2\rho_2 e^{-2ikL}D(\omega)e^{-i\omega_m t}. \tag{3.67}$$

It has not been necessary to solve the cavity relations for the $(\omega+\omega_m)$ frequency, because the sidebands appears only at the output, and are therefore not influenced by the frequency response of the cavity. A similar appreciation can be performed for the lower sideband at the $(\omega-\omega_m)$ frequency. The upper sidebands at the output, induced by effect three, will be compared to the upper sidebands at the output due to a hypothetical gravitational wave signal calculated in the next section. That comparison will be used to determine isolation requirements for the end mirror tilt in Section 3.7.5 such that that hypothetical signal would be detectable.

3.7.4 Case three, effect one, response to gravitational wave

Three-port grating cavity response to a hypothetical gravitational wave

The derivation for effect one (hypothetical gravitational wave signal) appearing at input b_1 in Figure 3.12 is the same as that for case one (the two-mirror cavity) with the result given by Equation 3.28. The only change is the replacement of the mirror coupling matrix given by Equation 3.19 by the three-port grating coupling matrix given by Equation 5.1; however, due to the greater complexity of this coupling matrix we will solve the introduced sidebands for effect one in case three explicitly. The carrier frequency solution remains unchanged from Equations 3.65 for effect three, since we know from Section 2.1.3 that the carrier is unaffected by sideband generation. Using the Equations 3.56 for the case three, allowing no input at b_2 or b_3, and allowing the effect one (gravitational wave) sidebands to appear at b_1, we obtain the internal gravitational wave upper sideband input field,

$$\begin{aligned} b_1(\omega+\omega_m) &= i\frac{m}{2}\frac{b_0(\omega)G_1e^{-ikL}\rho_2}{(1-\rho_0\rho_2e^{-2ikL})}e^{i\omega_m t} \\ b_1(\omega+\omega_m) &= i\frac{m}{2}b_0(\omega)G_1e^{-ikL}\rho_2 D(\omega)e^{i(\omega_m t+\Phi)}, \end{aligned} \tag{3.68}$$

where Φ is once again the offset of the effect one (gravitational wave) phase modulation to the effect three (end mirror tilt induced lateral grating displacement) phase modulation. We then solve the set of Equations 3.56 for the sideband input b_1 at angular frequency $(\omega+\omega_m)$ obtaining,

$$\begin{aligned}
a_2(\omega+\omega_m) &= \frac{b_1(\omega+\omega_m)}{1-\rho_0\rho_2 e^{-2i(k+k_m)L}} \\
a_4(\omega+\omega_m) &= \frac{b_1(\omega+\omega_m)G_1 e^{-i(k+k_m)L}}{1-\rho_0\rho_2 e^{-2i(k+k_m)L}} \\
a_4(\omega+\omega_m) &= b_1(\omega+\omega_m)G_1 e^{-i(k+k_m)L} D(\omega+\omega_m) \\
a_4(\omega+\omega_m) &= i\frac{m}{2} b_0(\omega) G_1^2 e^{-i(k+k_m)L} e^{-ikL} \rho_2 D(\omega) D(\omega+\omega_m) e^{i(\omega_m t+\Phi)}, \qquad (3.69)
\end{aligned}$$

which can then be used together with Equations 3.65 to determine in the following section the end mirror isolation requirement in case three, for the three-port coupled diffractive cavity.

3.7.5 Case three, end mirror tilt isolation requirement

In this section we compare the isolation requirement in case three (three-port grating cavity) with those in cases one (Equation 3.39, two-mirror cavity) and two (Equation 3.53, two-port grating cavity). The same assumptions are made, that the input optic has an infinite radius of curvature and that the end mirror is a section of a spherical surface. Once again and as with case two, case three will experience effect two in addition to effect three, which will slightly increase the isolation requirement for end mirror tilt. Effect three; however, clearly dominates. Virgo-esque properties have again been used [43]. We require that effect one given by Equation 3.69 (the hypothetical gravitational wave signal sideband at the output) be larger than the noise introduced by effect three given by Equation 3.67 (the end mirror tilt via displacing the cavity eigenmode atop the diffraction grating). Thus we obtain the comparison, where h and γ_2 appear as subscripts on effect one (gravitational wave) and effect three (end mirror

misalignment) respectively,

$$\begin{aligned} a_{4,\gamma_2}(\omega+\omega_m) &< a_{4,\mathrm{h}}(\omega+\omega_m) \\ i\frac{m_{\gamma_2}}{2}b_0(\omega)G_1^2\rho_2 e^{-2ikL}D(\omega)e^{-i\omega_m t} &< i\frac{m_{\mathrm{h}}}{2}b_0(\omega)G_1^2\rho_2 e^{-i(k+k_m)L}e^{-ikL}D(\omega)D(\omega+\omega_m)e^{i(\omega_m t+\Phi)} \\ m_{\gamma_2}e^{-ikL} &< m_{\mathrm{h}}e^{-i(k+k_m)L}D(\omega+\omega_m)e^{i\Phi}, \end{aligned} \tag{3.70}$$

where the modulation index for the gravitational wave signal is given by Equation 3.26, and for the lateral grating displacement effect in the three-port coupled case by Equation 3.63, and we set $e^{i\Phi}$ such that the gravitational wave and lateral grating displacement are at the point of greatest confusion, when they are in-phase, thus obtaining,

$$\begin{aligned} \frac{2\pi R_c\mu}{d\cos(\alpha)}\gamma_2(f) &< 2\pi\cdot(hL/\lambda)D(\omega+\omega_m) \\ \gamma_2(f) &< \frac{hL\cos(\alpha)}{R_c}\frac{d}{\lambda}D(\omega+\omega_m), \end{aligned} \tag{3.71}$$

which if we impose that $e^{-ikL}=1$, the cavity resonance condition for the carrier, becomes,

$$\begin{aligned} \frac{2\pi R_c\mu}{d\cos(\alpha)}\gamma_2(f) &< 2\pi\cdot(hL/\lambda)D(\omega+\omega_m) \\ \gamma_2(f) &< \frac{hL\cos(\alpha)}{R_c}\frac{d}{\lambda}D(\omega_m), \end{aligned} \tag{3.72}$$

It is now possible to set the isolation requirement for $\gamma_2(f)$, and requiring a a gravitational wave induced strain of $h=10^{-23}/\sqrt{\mathrm{Hz}}$ to be detectable with signal strength equal to the noise, in the absence of any noise sources other than the end mirror tilt induced lateral grating displacement effect. The most interesting gravitational wave sources will be those within the bandwidth of the detector, because it is signals within the bandwidth of the detector that are enhanced by the cavity effect (D factor), hence the detector design will ensure this feature. Physically, it is this enhancement of the signal against the noise that causes the D factor to appear in Equation 3.72. The D factor is a frequency-dependent complex number, but at DC it is related to the

cavity Finesse $\mathcal{F}$ by $\mathcal{F} = \pi D$, for sufficiently high mirror reflectivities as will be used in an interferometric gravitational wave detector (see Section 2.3.3). Hence, and because it is more a more familiar term within the gravitational wave field, we will use the Finesse rather than the D factor to write the isolation requirement of [52],

$$\gamma_2 < 1.71 \times 10^{-21} \frac{\text{rad}}{\sqrt{Hz}} \left(\frac{h}{10^{-23}/\sqrt{Hz}} \right) \left(\frac{L}{3\,km} \right) \left(\frac{\mathcal{F}}{200} \right) \left(\frac{\cos(\alpha)}{\cos(0^o)} \right) \left(\frac{3.5\,km}{R_c} \right) \left(\frac{d}{\lambda} \right), \quad (3.73)$$

where the angle of the grating with respect to the cavity is zero because of the change in configuration. Case three (the three port cavity) is distinct from case one (two-mirror cavity) and case two (two port grating cavity), where both signal and noise occur inside the cavity and are therefore both enhanced.

3.8 Summary

It has been demonstrated that there is a path length difference on lateral displacement of a diffraction grating relative to a light field for the non-zero diffraction orders, which causes a phase change of the field. Due to the combination of path length differences on lateral and longitudinal displacement of the diffraction grating, a null vector of displacement with respect to path length difference (and therefore phase change) made up of a combination of lateral and longitudinal movement was derived. However, as the lateral grating displacement effect is proportional to the diffraction order and to use a grating as a Fabry-Perot cavity input coupler requires at least two ports with different diffraction orders, the null vector approach cannot be used to eliminate the phase noise introduced by the lateral grating displacement effect.

The lateral grating displacement effect causes phase noise to appear in a gravitational wave

interferometer when the diffraction grating is used as an input coupler to a Fabry-Perot cavity. The noise coupling is from the lateral motion of the grating itself and from end mirror tilt causing displacement of the cavity eigenmode atop the grating. Isolation requirements for end mirror tilt of a Virgo-esque interferometer of $2 \times 10^{-16}\,\mathrm{rad}/\sqrt{\mathrm{Hz}}$ given by Equation 3.39 for case one (the two-mirror cavity); $7 \times 10^{-24}\,\mathrm{rad}/\sqrt{\mathrm{Hz}}$ given by Equation 3.53 for case two (the two-port grating cavity); and $1 \times 10^{-21}\,\mathrm{rad}/\sqrt{\mathrm{Hz}}$ given by Equation 3.73 for case three (the three-port coupled grating cavity) have been computed. These tell us that the using a grating cavity significantly increases sensitivity to end mirror tilt. This is an important new noise source, and a major problem for grating cavities. Although we deal with equivalently difficult isolation requirements for cavity length this does not have the unfortunate coupling to end mirror tilt calculated in this chapter. Further, because case one (the two-mirror cavity) is relatively insensitive to end mirror tilt preceding work on gravitational wave interferometers has not focused on alignment control to the same extent as length control. The conclusion to draw is that there should be a strong motivation to use the grating cavity to justify the noise coupling to end mirror tilt. Where such reasons exist, case three (the three-port coupled diffractive cavity) is to be preferred for its much reduced coupling of end mirror tilt to phase noise compare to case two (the two-port case).

It should also be recalled that input beam pointing has the potential to generate a phase noise due to the grating effect, by also displacing the beam across the grating. This will not occur in case two (the two-port case) because the incoupling occurs in the reflection (zeroth, $\mu = 0$) diffraction order and therefore no phase change occurs consistent with our calculation in Section 3.3.1. In case three (the three-port grating cavity) the extent of this phase noise will depend on the details of the input optics, but as these will not include the 3 km lever arm of the cavity it is expected the additional noise will be small. Additionally, lateral displacement of the grating itself will generate phase noise, again expected to be small due to isolation systems and the absence of the 3 km lever-arm. In Chapter 5 we will see that the symmetry of case three (the

three-port grating cavity) reduces by cancellation at the forward-reflected (a_3 in Figure 3.12) output port the phase-noise due to grating translation and input beam tilt.

Chapter 4

EXPERIMENTAL DEMONSTRATION

4.1 Experimental demonstration of cavity response to end-mirror tilt

We want to prove by experiment that the theoretical calculation carried out in the previous chapter is correct, ideally demonstrating that the isolation requirement for end-mirror tilt calculated in Equation 3.73. This calculation was made for the Virgo gravitational wave detecting

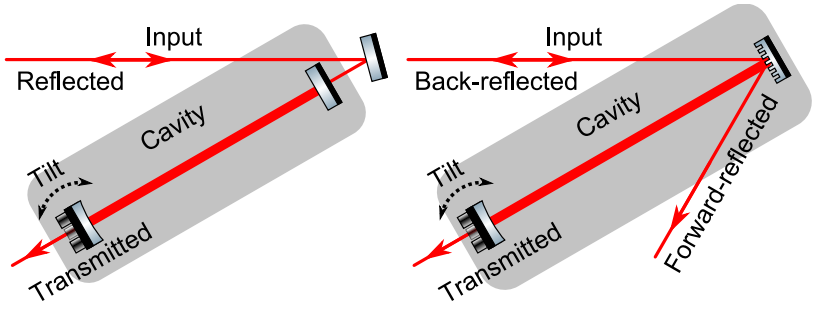

Figure 4.1: Physical diagram for intended experimental tilting of the end mirror. Left; for two-mirror cavity where the signal will be demodulated at the reflected port. Right; for the three-port coupled grating cavity where the signal will be demodulated at the back-reflected port.

interferometer. If the isolation requirement given in Equation 3.73 is met, then the end-mirror tilt contribution will be the same magnitude as our hypothetical gravitational wave signal. Since Virgo is a low-noise device designed to detect gravitational wave signals above the other noise sources shown in Figure 1.3, the end-mirror tilt should also be visible on a spectrum from the dark-port photodetector output of the interferometer. This should match an independently recorded spectrum of the end-mirror tilt.

It is not possible to perform tests of this type using an interferometric gravitational wave detector. Instead a coherent tilt is injected at an enhanced strength sufficient to dominate the noises of a smaller optical system. The tilt induced signal voltage at the output is then detected and divided by the input signal to obtain a transfer function. A prediction for a tabletop experiment based on the work of Chapter 3 is made in Section 4.3. In Section 4.5 the results are presented and found to be inconsistent with this prediction. This was found to be due to the end-mirror actuator, which was creating significant residual longitudinal motion as well as tilt, and these results are presented (along with the details of the experimental setup for context) in Section 4.6. A new prediction, comparing this measured residual longitudinal motion (equivalent to effect one in Chapter 3) to eigenmode displacement across the grating (effect three) is made in Section 4.8, and found to be substantially in agreement with the measured results. Further similar measurements have been carried out in collaboration with the University of Glasgow at the Joint Interferometer Facility (JIF). This facility provides interferometers with a substantially better phase sensitivity due to vacuum tube isolation from acoustic noise and multiple-pendulum suspension system isolation from seismic noise. The details of this work are presented in Section 4.9, and it supports the existence of the lateral grating displacement effect discussed in Chapter 3, as well as the further cavity configurations work outlined in Chapter 5.

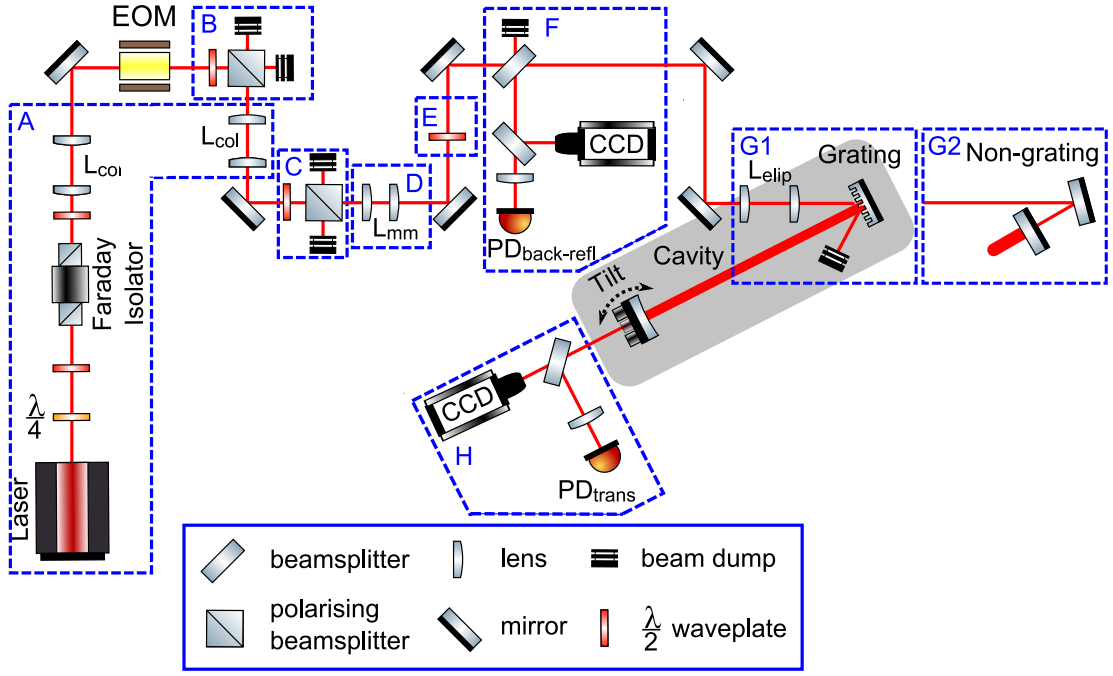

Figure 4.2: Physical diagram of experimental optics as laid out on the optical table.

4.2 Optical layout of experiment

The experimental layout on the optical table is as shown in Figure 4.2. The laser, the Faraday Isolator required to prevent light returning from the experiment entering and destabilising the frequency of the laser, the $\lambda/4$ (quarter) and $\lambda/2$ (half) waveplates needed for implementation of the Faraday Isolator, and the collimating lenses required to create a uniform beam are shown in the blue-dashed box A (see Sections B.1.1 and B.1.2). The electro-optical modulator (EOM) applying the 12 MHz phase modulation to the beam required for the Pound-Drever-Hall modulation-demodulation feedback control scheme is shown (see Section 2.4.2). A half waveplate and polarising beam splitter combination are used to adjust the power split between this and other experiments on the same optical table, shown in Box B (see Section B.1.3). A second such arrangement is shown in Box D, required to adjust the power into this experiment alone. A pair of lenses that match the Hermite-Gaussian mode of the beam into the Fabry-Perot cavity are shown in Box D (see Sections C.1 and 2.3.5). A half waveplate used to set the

polarisation of the beam (on which grating performance is dependent) is shown in Box E (see Section 4.6.2). The photodiode in back-reflection used for the Pound-Drever-Hall scheme is shown in Box F, along with a bare-detector CCD used to image the beam (see Section C.3 for its use). The elliptical lenses required to adjust for the projection-distortion effect of the beam onto the surface of the grating, along with the grating itself, are shown in Box G1 (see Section 4.6.2). The optics in Box G2, a steering mirror and the cavity input mirror are used instead of those in Box G1 when the two-mirror cavity case is being studied (see Section B.2). The grey shadowed area indicates the cavity, which is implemented with a tilt capable end mirror. The optics for detection and imaging of the beam transmitted through the cavity are shown in Box H (see Section C.2 for its use).

4.3 Expected result

The expected response to end-mirror tilt is given by the isolation requirement equations determined (for the Virgo interferometer) in the previous chapter. We rearrange Equation 3.38 (equivalently the form given in Equation 3.39 could be used) for the two-mirror cavity to find h, the equivalent longitudinal strain $\Delta L/L$ for a particular injected end-mirror tilt $\gamma_2(f)$, and hence a more experimentally useful number $\Delta L/\gamma_2$, the equivalent longitudinal displacement [meters] per unit of input end-mirror tilt [Radians].

$$h = \frac{\Delta L}{L} = \frac{2\gamma_2(f)R_c(\gamma_{1,dc} - \gamma_{1,dc})}{L} \tag{4.1}$$

$$\frac{\Delta L}{\gamma_2(f)} = \frac{2R_c(\gamma_{1,dc} - \gamma_{1,dc})}{L} \tag{4.2}$$

A similar rearrangement can be performed using Equation 3.73 for the three-port coupled grating cavity. The properties of our tabletop experimental cavity required to solve these Equations numerically are shown in Table 4.1). Since some work was also carried out at the

Joint Interferometer Facility prototype at and in collaboration with the University of Glasgow, the numbers for the JIF cavity are also presented.

Quantity	Unit	Tabletop Grating Cavity	Tabletop Two-mirror Cavity	JIF Grating Cavity	Notional JIF Two-mirror Cavity
Finesse	-	300	300	1150	1150
Length	m	0.25	0.3	10	10
d	nm	1500	-	1500	-
R_c	m	1	1	15	15
λ	nm	1064	1064	1064	1064

Table 4.1: Important values associated with the optical systems (tabletop and JIF) required for predicting the end-mirror tilt induced phase signal in different cases. α is the angle between the cavity-beam and the input beam in the three-port grating case.

Thus we obtain for the tabletop experiment grating cavity and two-mirror cavity respectively,

$$\frac{\Delta L}{\gamma_2(f)} = 2.4\cdot 10^{-3}\frac{\mathrm{m}}{\mathrm{rad}}\left(\frac{300}{\mathcal{F}}\right)\left(\frac{\cos(0^\mathrm{o})}{\cos(\alpha)}\right)\left(\frac{R_c}{1\mathrm{m}}\right)\left(\frac{\lambda}{1064\mathrm{nm}}\right)\left(\frac{1500\mathrm{nm}}{d}\right), \tag{4.3}$$

$$\frac{\Delta L}{\gamma_2(f)} = 4\cdot 10^{-8}\frac{\mathrm{m}}{\mathrm{rad}}\left(\frac{R_c}{1\mathrm{m}}\right)\left(\frac{20\,\mathrm{nrad}}{\gamma_{1,dc}}\right). \tag{4.4}$$

As we will see in the following section it is not possible to obtain these numbers directly in the case of the tabletop experiment since there are other obscuring transfer functions included in the measurement. Therefore we take a measurement that obtains the ratio of Equation 4.3 to Equation 4.4, giving an expected response to tilt a factor of approximately 10^5 greater for the grating cavity compared to the two-mirror cavity. This high expected ratio allows for some error in the values for $\gamma_{1,dc}, \gamma_{2,dc}$ misalignment substituted into Equation 4.4, where the 10 nrad values for input and end-mirror misalignment are taken from the Virgo interferometer, and are probably overly optimistic for our case. 10 μrad misalignment is perhaps more reasonable, and would result in an expected response factor of 10^2 between two-mirror and grating cases.

There will be small changes between the two-mirror and grating cavities due to the different optics used in each. Since the ratio predicted to exist between the effect in each case is so large (either 10^5 or 10^2) any small change introduced by the change in optics is unlikely to dominate.

However, should there be a common noise source in both cavities it might exceed effect two (the noise from the length change due to displacement of the eigenmode) but not effect three (eigenmode displacement across the grating striations). The ratio between the common noise source and effect three would then be observed instead. If this common noise source were larger than both effect two and effect three it would obscure both and we would observe only that noise source.

The expected values for the JIF grating cavity, and a notional two-mirror cavity that could be used to replace it, are respectively,

$$\frac{\Delta L}{\gamma_2(f)} = 9.3\cdot 10^{-3}\frac{\mathrm{m}}{\mathrm{rad}}\left(\frac{1150}{\mathcal{F}}\right)\left(\frac{\cos(0^{\mathrm{o}})}{\cos(\alpha)}\right)\left(\frac{R_c}{15\mathrm{m}}\right)\left(\frac{\lambda}{1064\,\mathrm{nm}}\right)\left(\frac{1500\,\mathrm{nm}}{d}\right), \quad (4.5)$$

$$\frac{\Delta L}{\gamma_2(f)} = 6\cdot 10^{-7}\frac{\mathrm{m}}{\mathrm{rad}}\left(\frac{R_c}{15\mathrm{m}}\right)\left(\frac{20\,\mathrm{nrad}}{\gamma_{1,dc}-\gamma_{2,dc}}\right). \quad (4.6)$$

It is also difficult to take these exact measurements using the JIF, since the grating cavity has already been installed and replacing it with a similarly configured two-mirror cavity would involved significant additional work. Therefore an alternative approach was taken to verify the existence of the end-mirror tilt effect using the JIF, and this work is presented in Section 4.9.

4.4 Experimental data analysis

The result of the final experiment will be two transfer functions from a voltage driving the end-mirror tilt actuator to the feedback-signal voltage locking the cavity, one for the two-mirror cavity (case one, see Chapter 3 for an introduction to the different cavity cases) and one for the three-port grating cavity (case three). The feedback-signal voltage is proportional to the tilt-induced phase-signal after modification by the servo. The data analysis approach for these transfer functions is fully addressed later in this section, including the unity gain point matching technique used to compensate for the differences between the two-mirror and grating cavities

(requiring an additional two open-loop transfer functions). These calculations apply both to the tabletop experiment, and the work carried out using the JIF cavity. A comprehensive set of measurements were taken for the tabletop experiment, allowing various consistency and error checks to be performed on these transfer functions, and these are addressed in Section 4.5.

4.4.1 Schematic of the general case

Both two-mirror and grating Fabry-Perot cavities used in this experiment can be represented by the schematic shown in Figure 4.3. H is the transfer function of the servo modifying the error signal voltage to feedback signal voltage [volts to volts] using integrators, adjustable gain (for adjustment of error signal slope gradient) and an optional inverter. The actuator and driving electronics are shown as G_1, which converts the feedback signal voltage to an effective cavity length change [volts to meters]. Practically, this signal is sent to the laser, adjusting the wavelength of the light to maintain the cavity at the operating point The optics of the cavity are shown as G_2, transforming any cavity length change to a phase change of the light field leaving the cavity [meters to radians of phase]. The Pound-Drever-Hall detection system is shown as G_3. This compares the phase of the carrier reflected by the cavity with the Pound-Drever-Hall sidebands which serve as static local oscillator fields. This is because the sidebands are 12 MHz offset from the carrier, sufficient that they do not resonate in the cavity (and therefore do not experience the associated phase changes). The carrier light field does resonate in the cavity (and therefore does experience the associated phase changes). The phase-difference between carrier and static local oscillator is output as an error signal voltage [radians of phase to volts]. This closes the feedback loop to the input of servo H in volts, which are modified into the feedback signal, and fed into the actuator to lock the cavity.

In Figure 4.3 end-mirror tilt is used as a source of disturbance from the cavity operating point. This tilt contributes an effective cavity length change by displacing the cavity eigenmode from

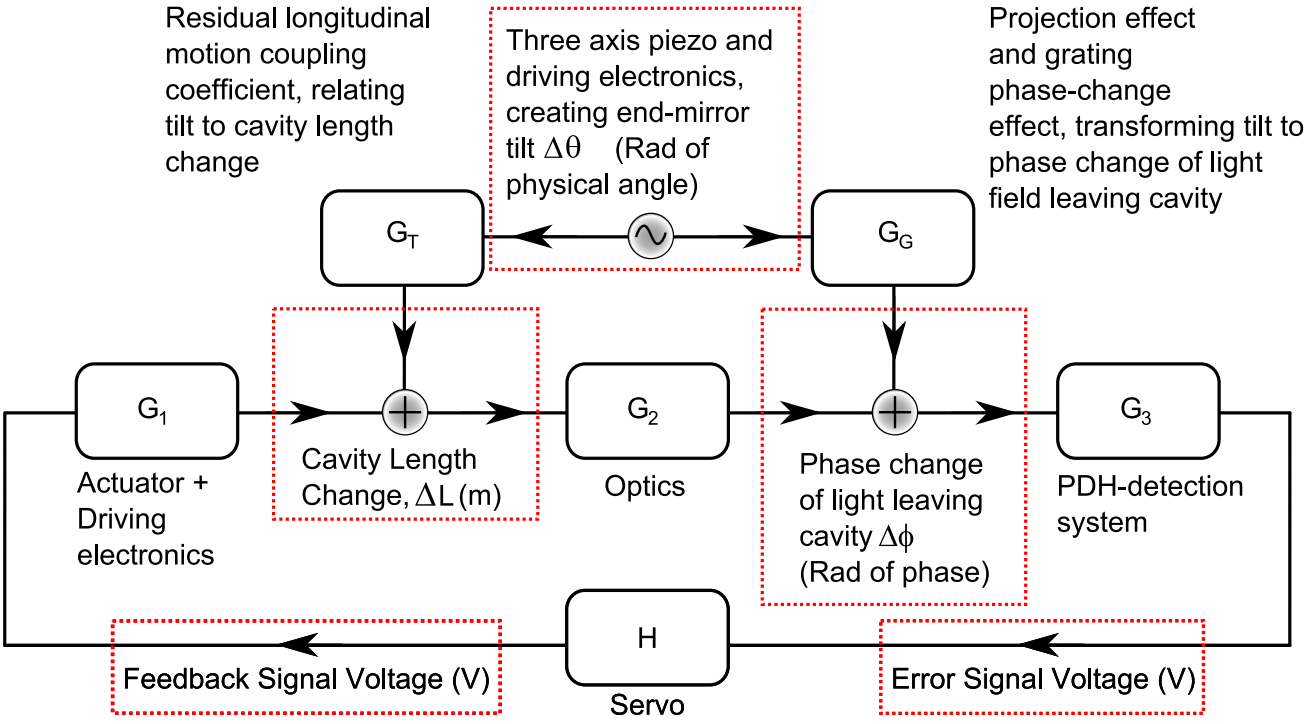

Figure 4.3: Schematic diagram of the general case of either a grating or two-mirror Fabry-Perot cavity with an end-mirror that may be tilted. H, G_1, G_2 and G_3 are transfer functions of the cavity locking feedback system. Where they appear together $G = G_1G_2G_3$ for simplicity. H is the transfer function of the servo alone (from error signal voltage [Volts] to feedback signal voltage [Volts]). The actuator and its driving electronics G_1 convert this feedback signal voltage [Volts] to an effective cavity length change [meters]. The optics of the cavity itself G_2 convert from effective cavity length change [meters] to the induced phase change of the light leaving the cavity [Radians of phase]. The Pound-Drever-Hall detection system G_3 converts from phase change [Radians of phase] to an output voltage [Volts]. G_T is the transfer function from an input end-mirror tilt [Radians of physical angle] to effective cavity length change [meters] due to lateral displacement induced length change of the cavity eigenmode (effect two, Chapter 3) and any residual longitudinal motion of the end-mirror (effect one) caused by residual longitudinal motion of the tilting device (see Section 4.6.3). G_G is the transfer function from end-mirror tilt [Radians of physical angle] to phase change at the output of the cavity [Radians of phase] caused directly by lateral displacement of the eigenmode across the grating striations (effect three, detailed in Section 3.3.1).

the perfectly aligned optical axis to a slightly shorter or longer offset location (effect two, given by Equation 3.35). Effect one, longitudinal motion of the end-mirror, will be minimised by optimising the driving matrix of the end-mirror three-axis actuator for tilt only. For the two-mirror cavity these are the only tilt induced effects, converted from input tilt to an effective cavity length change by transfer function G_T ([Radians of physical angle] to [meters]). For the grating cavity we must also consider the displacement of the cavity eigenmode across the striations of the grating (effect three), which directly generates a phase-change at the output of the cavity. Through considering the eigenmode displacement effect (and hence the grating phase-change effect described in Section 3.7) G_G converts from end-mirror tilt to phase-change of the light leaving the cavity [Radians of physical angle to Radians of phase].

Since the scheme shown in Figure 4.3 applies to both grating and two-mirror cavities it is important to consider how these cases differ. Most obviously G_G exists in the grating case but does not in the two-mirror case (it takes a null value). G_T is a specific property of the end-mirror tilting device in a given driving configuration, which is unchanged between the two cavities. G_3 comprises the Pound-Drever-Hall detection system which is unchanged. As a fixed property of the high-voltage amplifier and the actuator of the laser frequency G_1 is also unchanged. G_2 represents the optics of the cavity, and despite the best design efforts to match the grating properties to the input-mirror properties, maintain a constant cavity length, and the same DC optical alignment, there will be some differences between the two-mirror and grating cavities. The optical gain is also a property of the cavity, and hence G_2 is proportional to the input power. In principle H can also be fixed so long as the servo settings are not adjusted, but in practice it is useful to use the servo gain H to compensate for the changes in G_2. Practically, this is undertaken by maintaining the location at which $HG_1G_2G_3 = HG = 1$ at a single frequency, known as the unity gain point. In order to check that this practical compensation has been correctly performed , an open-loop transfer function recording $HG_1G_2G_3 = HG$ will be taken for both cavities. Various alternative methods of measuring HG will be used, serving as a check,

including an independent measurement of H. Multiplying H by the tilt-to-error-signal transfer function (T_{TE}) should obtain the tilt-to-feedback-signal transfer function (T_{TF}), so independent measurement of H also serves to check those measurements against each other.

Therefore at least four transfer functions are required: End-mirror tilt to feedback signal for both grating and two-mirror cavities; and open-loop transfer functions HG for both grating and two-mirror cavities. The equations of the transfer functions for the specific cavities, and the data analysis required to obtain G_G and G_T in a suitable form are presented in the following sections.

4.4.2 Open loop transfer function for effective cavity length

It is necessary to know the open loop transfer function of the system for each of the two-mirror and grating cavities. Various external disturbances, primarily acoustic motion of the air in the laboratory, prevent direct measurement of a true open loop transfer function. Thus an electronic feedback loop is used to maintain the cavity on resonance, with a combination of output signals being used to retrieve the effective open loop transfer function. Accessing particular output signals allows the requisite combination of signals to be made prior to the signal analyser recording the transfer function, so no post-processing is required to extract the effective open loop transfer function. The physical arrangement for taking these transfer function is shown in Figure 4.6 and a schematic is shown in Figure 4.4. In this case we do not have an input from the end-mirror tilt, and instead introduce an adder to the cavity locking error signal path. We can write the following two equations for x_A, x_B and x_S,

$$x_B = x_A + x_S \tag{4.7}$$

$$x_A = x_B HG \tag{4.8}$$

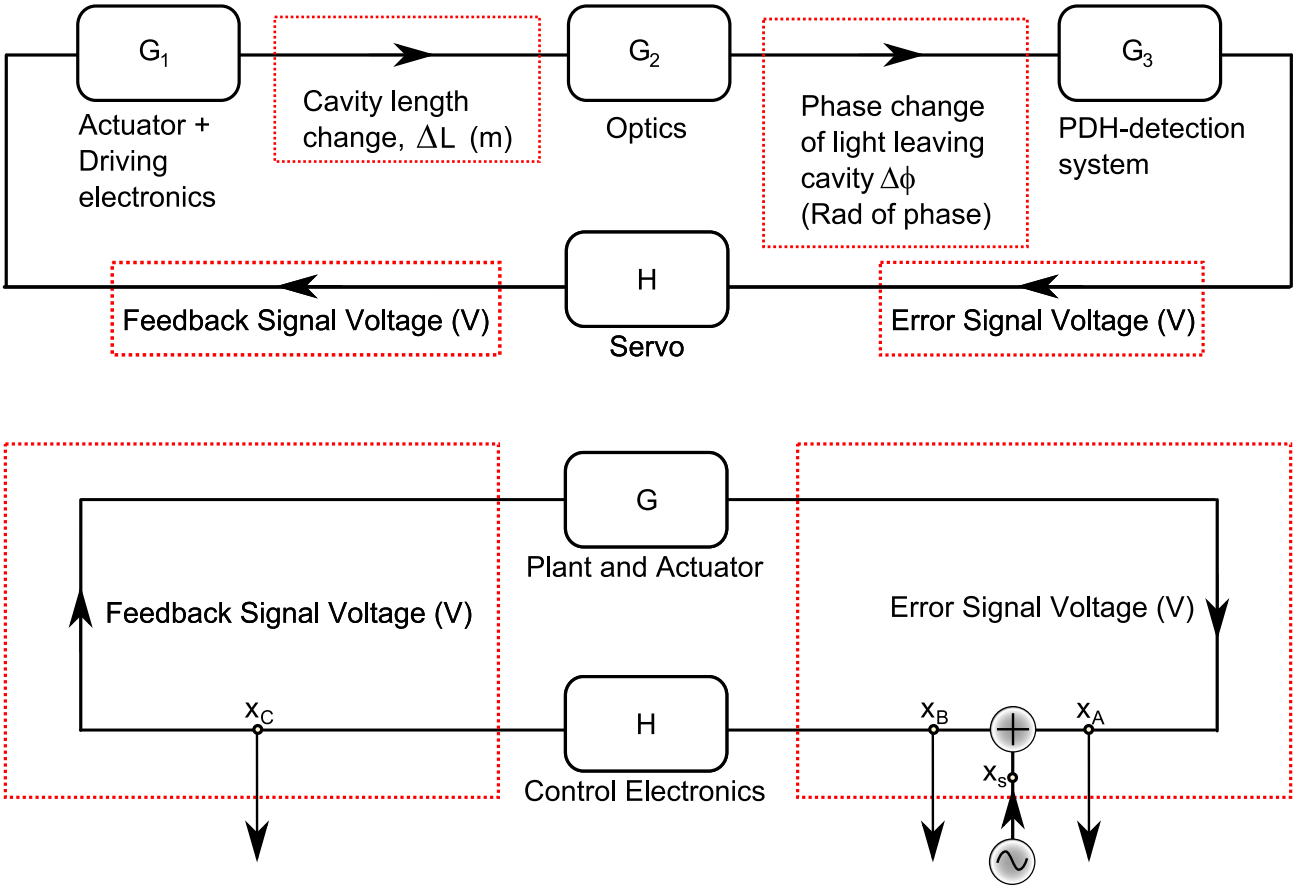

Figure 4.4: Schematic diagram for open loop transfer function, where H, G_1, G_2 and G_3 are the transfer functions described in Figure 4.3, and in the simplified lower figure $G = G_1 G_2 G_3$. Input x_s from the signal analyser is shown, as are outputs x_A, x_B and x_C.

from which we can derive by substitution,

$$x_B = HGx_B + x_S \tag{4.9}$$

$$x_B/x_S = 1/(1-HG) \tag{4.10}$$

$$x_A = x_A HG + x_S HG \tag{4.11}$$

$$x_A/x_S = HG/(1-HG) \tag{4.12}$$

$$x_A/x_B = HG \tag{4.13}$$

where Equation 4.13 can either be measured directly or calculated from Equation 4.12 and 4.10. Both methods will be performed as a check. Introducing x_C allows us to write two additional equations,

$$x_C = x_B H \tag{4.14}$$

$$x_C/x_B = H \tag{4.15}$$

$$x_A = x_C G \tag{4.16}$$

$$x_A/x_C = G \tag{4.17}$$

where the derivation of the directly measurable Equations 4.15 and 4.17 is trivial. The directly obtained H and G can then be confirmed by multiplying them to check they match Equation 4.13. Two separate versions of these five transfer functions (Equations 4.10, 4.12, 4.13, 4.15 and 4.17) exist, one set each for the two-mirror cavity (subscript M) and one for the grating cavity (subscript G). Although the Pound-Drever-Hall detection system G_3 and the actuator G_1 were the same for both cavity transfer functions, G_2 is slightly changed by switching the input optic.The primary adjustment to achieve cavity lock and to match the unity gain point of the grating cavity (case three) to the two-mirror cavity (case one) was by adjusting the electronic gain of the servo control electronics H. Only the gain was changed, the choice of integrators remained fixed and the inverter was not tripped.

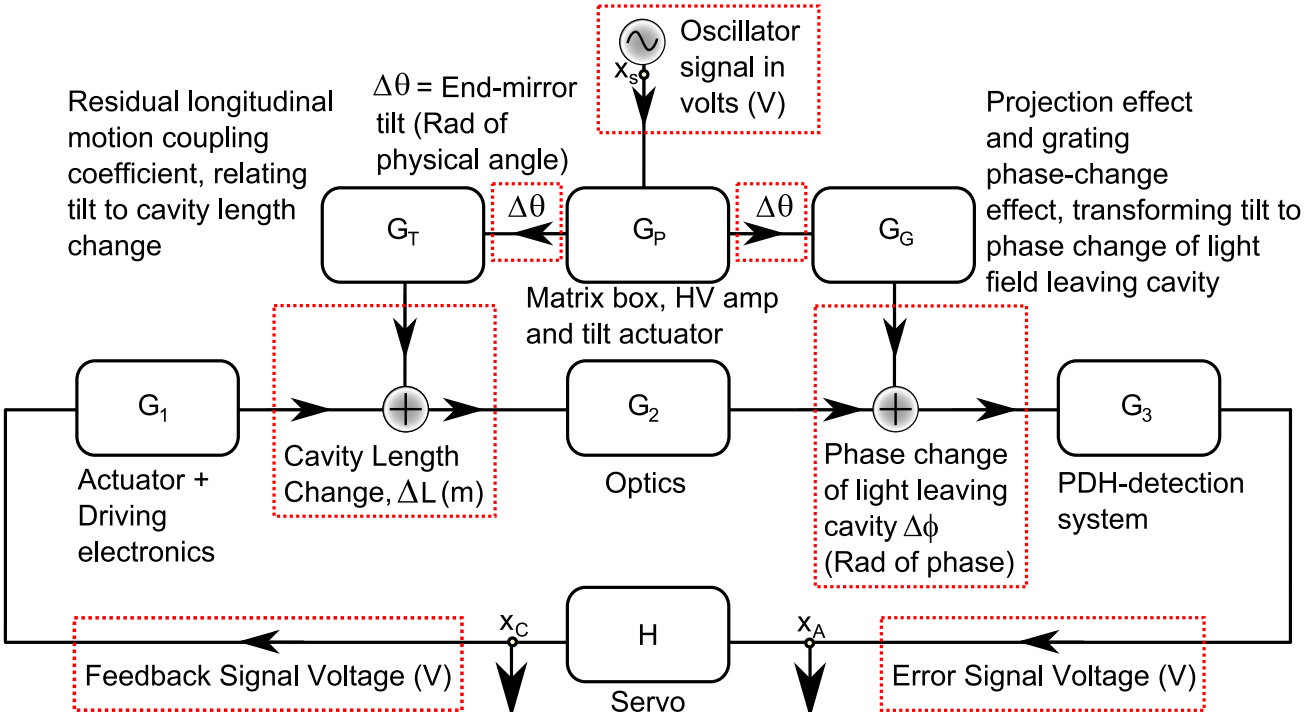

Figure 4.5: Schematic diagram for either a grating or two-mirror Fabry-Perot cavity with a end-mirror that may be tilted. H, G_1, G_2, G_3, G_T and G_G take their meanings from Figure 4.3. G_P is the transfer function of the end-mirror tilt actuator which converts an input [Volts] to a tilt [Radians of physical angle]. This is required so that a transfer function measurable with a signal analyser exists (between voltage input and cavity locking feedback signal voltage). In this case, $x_A = x_B$, hence the latter does not appear.

The transfer functions derived in Equations 4.10, 4.12, 4.13, 4.15 and 4.17 comprise in each of the two-mirror cavity (case one) and the three-port grating cavity (case three) a complete set which can be comprehensively error-checked against each other. We derive in the following two sections the tilt-to-error-signal and tilt-to-feedback-signal transfer functions, and will see how Equation 4.15 can be used to error-check them against each other.

4.4.3 End-mirror tilt induced signal

It is now necessary to calculate the transfer functions that will be taken from end-mirror tilt to cavity locking feedback signal. These transfer functions will be taken with a signal analyser and

therefore must be taken between two points with a voltage unit of measurement. The feedback signal voltage is naturally in [Volts]. In Figure 4.3 the disturbance is shown applied as a tilt in units of [Radians of physical angle]. This tilt is generated by an actuator and associated electronics which take an input in [Volts] and output [Radians of physical angle], connected by a transfer function (G_P, as shown in Figure 4.5) which must be included in our appreciation. Thus from Figure 4.5 we can obtain the equations,

$$\begin{aligned} x_A &= x_A H G_1 G_2 G_3 + x_S G_3 G_G G_P + x_S G_3 G_2 G_T G_P \\ T_{TE} &= \frac{x_A}{x_S} = \frac{G_3 G_G G_P + G_3 G_2 G_T G_P}{1 - HG}, \qquad (4.18) \\ x_C &= x_A H \qquad (4.19) \\ T_{TF} &= \frac{x_C}{x_S} = H T_{TE} \qquad (4.20) \end{aligned}$$

where we have chosen to define T_{TE} as the transfer function from tilt to error signal, and T_{TF} as the transfer function from tilt to feedback signal. The open loop transfer function $HG = HG_1G_2G_3$ from Equation 4.13 has been substituted into Equation 4.18 for clarity.

The open loop transfer function of the two-mirror cavity will be matched to that of the grating cavity by adjusting the gain of the servo H to compensate for changes in the cavity transfer function G_2 due to the different optics (as shown in Figure 4.8). Hence it is reasonable to directly compare the feedback signals of these two cavities. The feedback signals must be equal and opposite to the distortion applied to the cavity for the cavity to remain locked at the operating point, and therefore they exactly measure the distortion applied. They may be written for the two-mirror cavity and grating cavity respectively as,

$$\begin{aligned} T_{TMF} &= \frac{H_M G_3 G_{2M} G_T G_P}{1 - H_M G_M} \qquad (4.21) \\ T_{TGF} &= \frac{H_G G_3 G_G G_P + H_G G_3 G_{2G} G_T G_P}{1 - H_G G_G} \qquad (4.22) \end{aligned}$$

where G_G does not exist for the two-mirror cavity (subscript M). As discussed previously the servo transfer function H is used to compensate for differences in the optical transfer function G_2 (which appears and causes changes in $G = G_1 G_2 G_3$), and so both are made unique by the use of the cavity-specific subscripts M (for the two-mirror cavity) and G (for the grating cavity). The feedback signal calculated in Equation 4.20 is plotted for both two-mirror cavity and grating cavity in Figure 4.9. It is shown with an axis adjusted to equivalent longitudinal motion per unit tilt of the end-mirror [m/rad] in Figure 4.9. Taking the ratio of the expected feedback signal for the two cavities (Equation 4.22 divided by Equation 4.21) obtains,

$$\frac{T_{TGF}}{T_{TMF}} = \frac{H_G G_G + H_G G_{2G} G_T}{H_M G_{2M} G_T} = \frac{H_G}{H_M} \frac{G_G}{G_{2M} G_T} + 1 \tag{4.23}$$

where the $G_G/(G_{2M}G_T)$ in the first term represents the comparison between effect three for the grating cavity (for lateral displacement of the eigenmode across the grating G_G, which does not experience the cavity) and effects one and two for the two-mirror cavity (G_T, which is coupled out via the cavity transfer function G_{2M}). Mathematically this is equivalent to the division of Equation 4.4 by Equation 4.3 in Section 4.3 which obtained the expected result 10^5 (with DC misalignment 10 nrad). The H_G/H_M modifies this to account for the differences between the cavities, and must be multiplied out using our independent measurement of H for both cavities. The the plus one represents effects one and two (the residual longitudinal motion, and eigenmode length change directly induced by end mirror tilt), which occur equally in both cavities. As the unity gain points of the cavities have been matched at 50 kHz (they have the same response) the numerator and denominator of this term are still equal at the output, hence the term reduces to unity.

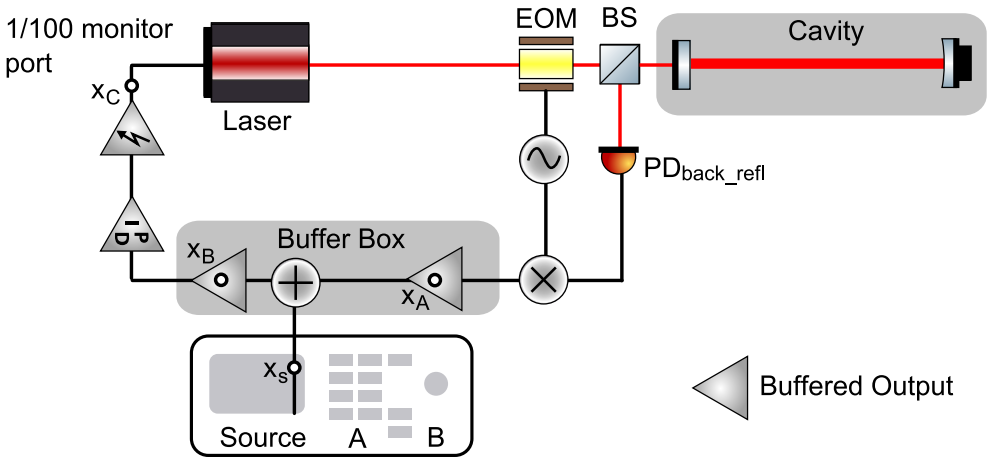

Figure 4.6: Physical diagram for transfer functions with disturbing signal x_S injected into the error signal. Note that this digram, although it shows the two-mirror case, is identical for the grating case save for the angle of the input optic. The connection of ports A and B of the signal analyser (measuring A/B) depends on the transfer function being taken. It is the physical manifestation of the schematic shown in Figure 4.4

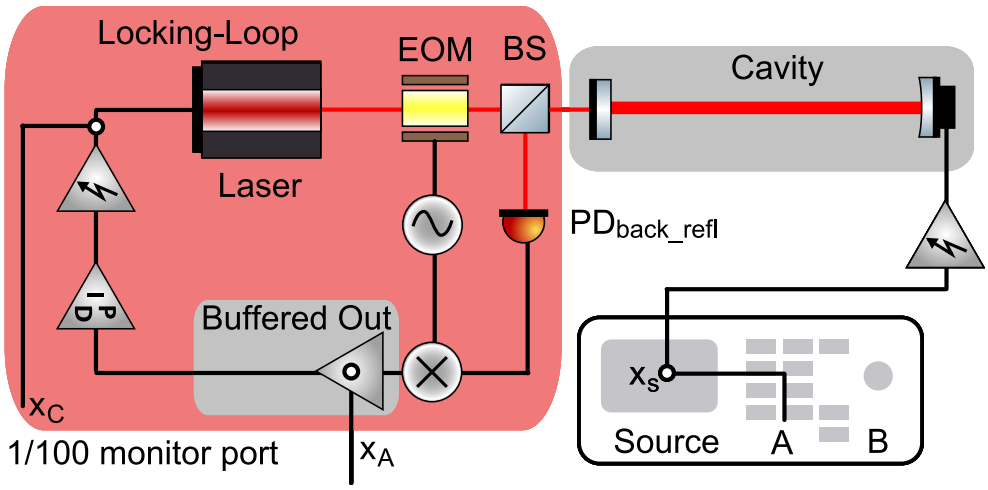

Figure 4.7: Physical diagram for transfer functions injected to end-mirror tilt. Note that this digram, although it shows the two-mirror case, is identical for the grating case save for the angle of the input optic. Port B of the signal analyser (measuring A/B) may be connected to either x_A or x_C depending on the measurement. It is the physical manifestation of the schematic shown in Figure 4.5

4.5 Experimental Result

For ease and quick reference, we herein include Table 4.2 detailing the key features of both two-mirror and grating cavities, and the physical-schematic diagram of Figure 4.6 for the method of taking the open loop transfer function shown as a block-diagram in Figure 4.4, and its equivalent 4.5 for the end-mirror tilt transfer function shown as a block-diagram in Figure 4.5. Whilst both schematics show the two-mirror cavity case, they are fundamentally identical for the grating cavity excepting the adjustments to the input optics.

Quantity	Unit	Two-Mirror	Grating
Finesse	-	300	300
D (ω)	-	95	95
Length	m	0.25	0.3
Unit Gain Point	kHz	50	50
Integrators by roll-off	kHz	0.144, 6	0.144, 6
Grating Period	nm	-	1500

Table 4.2: Key features of two-mirror and grating cavities

Number	Injection	Measurement	Obtains	Equation
1	Error sig	x_A/x_S	$HG/(1-HG)$	4.10
2	Error sig	x_B/x_S	$1/(1-HG)$	4.12
3	Error sig	x_A/x_B	HG	4.13
4	Error sig	x_C/x_B	H	4.15
5	Error sig	x_A/x_C	G	4.17
6	Tilt	x_A/x_S	$(G_3G_GG_P+G_3G_2G_TG_P)/(1-HG)$	4.18
7	Tilt	x_C/x_S	$(HG_3G_GG_P+HG_3G_2G_TG_P)/(1-HG)$	4.20

Table 4.3: Key transfer functions to be recorded for both two-mirror and grating cavities. The equations refer to those where the transfer functions were first mentioned in Section 4.4, and the definition of the various transfer function components can be found in Figure 4.3.

For an overview, in Table 4.3 is a list of the transfer functions that will be taken. The equations refer to those where the transfer functions were first mentioned in Section 4.4, and the definition of the various transfer function components can be found in Figure 4.3. The significant elements

of the physical set up are shown schematically in Figure 4.6 for the error signal injection point and Figure 4.7 for the tilt injection point.

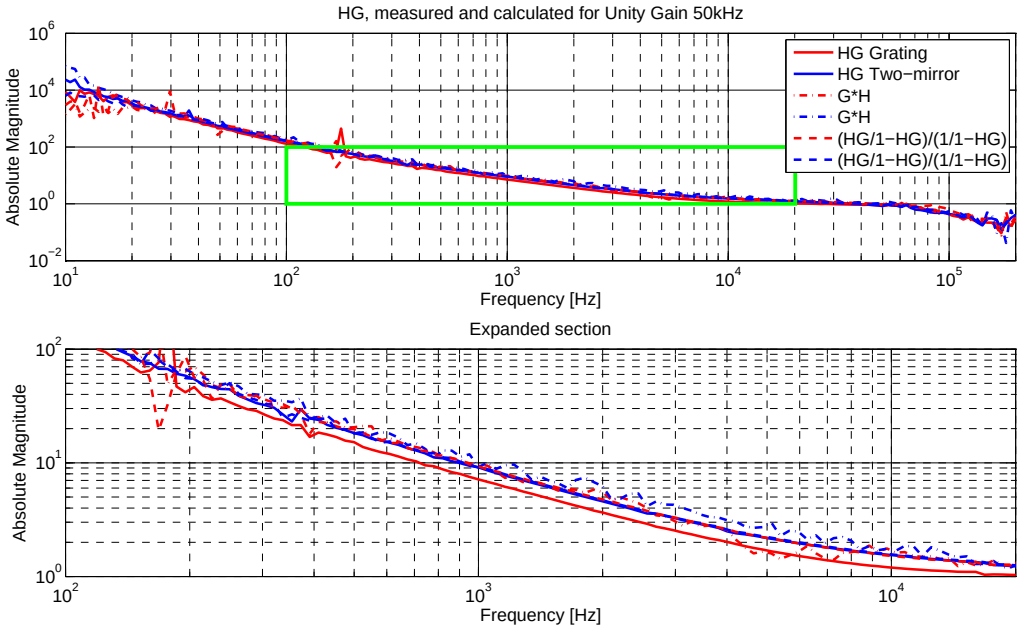

Figure 4.8: Open loop transfer functions, calculated from measurements and measured directly (see table 4.3 for quick reference), for both two-mirror and grating cavities.

The two cavities were both (in turn) set up and locked, and the gain of the servo (transfer function H) was adjusted such that the unity gain point (where $HG = 1$) was set to 50 kHz. This did not require adjustment of the optical gain by changing the input power to the cavity (transfer function G_2, hence affecting G). The transfer functions which can be calculated to obtain HG are plotted in Figure 4.8.

The transfer functions which can be calculated to obtain the tilt to feedback signal transfer function $((HG_3G_GG_P + HG_3G_2G_TG_P)/(1-HG))$are plotted in Figure 4.9. Thus the measurements of $(HG/(1-HG))$ and $(1/(1-HG))$ primarily serve as a check on the direct measurement of HG, and both of these serve as a check on the independent measurements of H and G. The tilt to feedback signal transfer function T_{TF} can be directly measured and calculated from the tilt to error signal transfer function T_{TE} and H.

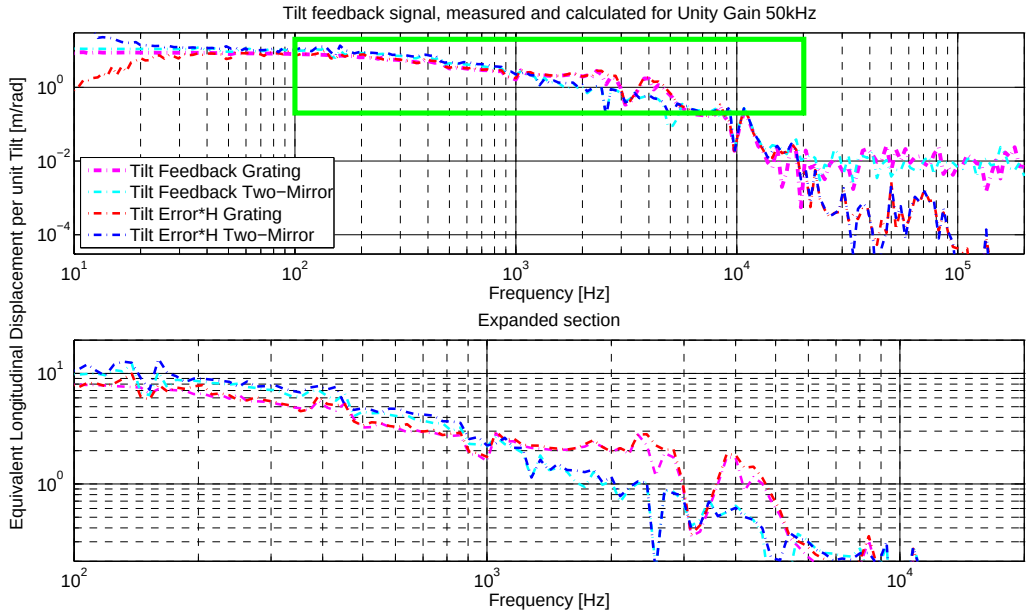

Figure 4.9: Tilt to equivalent longitudinal displacement transfer function for both grating and two-mirror cavities, with y-axis recalibrated from Figure E.3 using the method outlined Appendix E. Figure E.3 shows tilt driving voltage to feedback signal voltage transfer functions, calculated from measurements and measured directly.

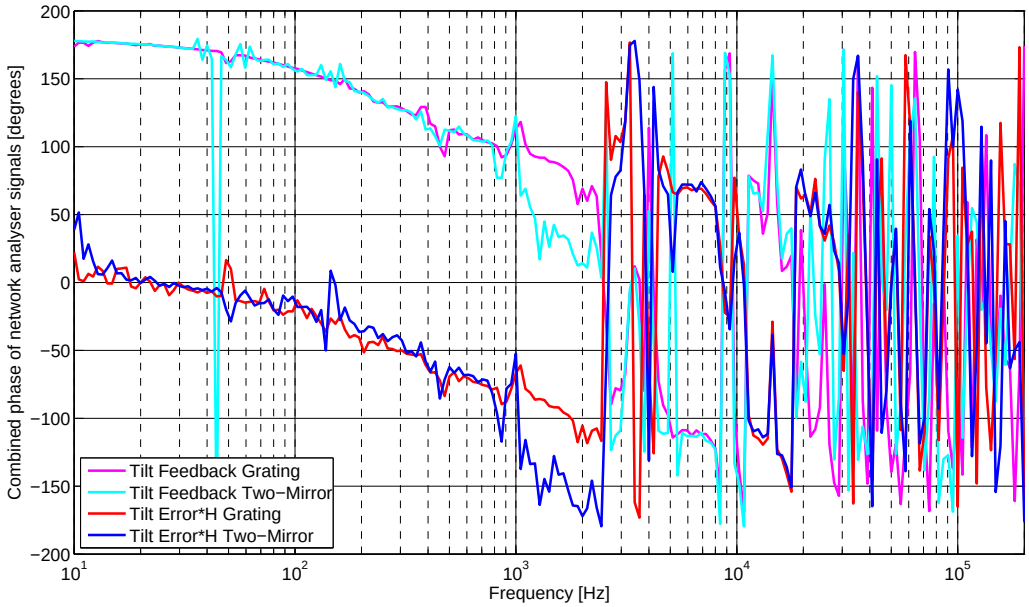

Figure 4.10: Coherence for the phase offset existing between the input signal and the output signal in Figure 4.9, for the tilt to equivalent longitudinal displacement transfer function for both grating and two-mirror cavities.

An attempt was made to perform these transfer functions at unity gain point 1 kHz; however, it was not possible to reduce the servo gain for the two-mirror cavity (transfer function H_M) sufficiently far to obtain that unity gain point, due to the higher optical gain (transfer function G_{2M}, affecting G_M). This occurs despite designing the cavity properties to be similar, since the grating cavity outputs to both first and minus-first diffraction orders, and the power in the minus-first order directed to the forward-reflected port is lost. Some work on utilising this output port is shown in the following chapter. From Figure 4.8 the open loop gain was well matched between the grating cavity and the two-mirror cavity, and has good agreement with its alternative measurements, except in the case of the direct measurement three of HG for the grating cavity.

Figure 4.9 shows the transfer functions from tilt-actuator driving voltage to feedback-signal voltage locking the cavity, both measured directly and calculated from a combination of other transfer functions. The y-axis has been calibrated to equivalent longitudinal motion (applied by feedback control system) per unit of injected tilt signal. The short measurement campaign and the mathematics required for this calibration is discussed in Appendix E, and the raw dimensionless transfer functions are shown in Figure E.3.

It can clearly be seen from Figure 4.9 that we do not see the expected ratio of 10^5 between the grating cavity tilt induced noise and the two-mirror cavity tilt induced noise. Examining the coherence between the input and output signals shown in Figure 4.10 it can be seen that up to approximately 20 kHz there is reasonable coherence, indicating that the output is a response to the input signal and not some other noise appearing elsewhere in the system. Above approximately 1 kHz, however, there are resonances in the piezo which cause various phase shifts, most notably the one-hundred-and-eighty degree phase flip at approximately 3.5 kHz which is associated with a dip in the magnitude of the response in Figure 4.9. Above around 20 kHz there is effectively no coherence, and the system detects only its own noises, which are believed to principally be a wildly varying set of internal piezo resonances. There is a one-hundred-eighty

degree phase separation between the error-signal derived phase and the feedback signal derived phase, which is due to the direction of slope of the Pound-Drever-Hall error signal being the opposite to that required to direct the cavity back to the operating point.

Since the result of Figure 4.9 is coherent it is a real effect, and therefore there is some mistake in the method of the experiment or in the theory previously presented. It was suspected that this result was due to enhanced noise in the two mirror cavity, due to either effect one (residual longitudinal motion of the end-mirror) or effect two (eigenmode length change due to eigenmode lateral displacement). The eigenmode length change depends on the values for DC misalignment of the input and end-mirrors given in Equation 4.4. These are necessarily an estimate; however, it is unlikely for them to be wrong by a factor of 10^5 (millirads rather than tens of nanorads DC misalignment). Such an extreme misalignment would be obvious in the transmitted photodiode signal, for example. Tens of microrads is probably a more reasonable expectation, in which case we would expect the ratio between the grating and two-mirror cases to be 10^2. Therefore it was suspected that this result was due to excessive residual longitudinal motion of the tilt-actuator (a three-axis piezo). This could be caused by either insufficient optimisation of the three-axis piezo driving matrix, or a design limitation of the device itself. Obtaining an additional angle insensitive longitudinal displacement detecting device called EUCLID allowed characterisation of the residual longitudinal motion of the tilt configured end-mirror actuator. This residual longitudinal motion (effect one) was found to dominate the eigenmode length change due to displacement (effect two). The overall experimental method will be presented in the following section (with some details in the appendices), along with the EUCLID characterisation of the end-mirror tilt actuator. A new prediction will be generated, requiring some additional analytical calculation, and compared to the results presented in Figure 4.9.

4.6 Implementation of experimental cavities

A variety of steps were performed in order to implement the experimental cavities required. Preliminary steps included characterisation of the beam emitted directly by the laser, the installation of a Faraday Isolator and associated wave plates as initial optics, beam profile analysis and collimation of the beam from these initial optics and implementing systems for controlling the laser beam power independent of other experiments using the same beam source. These steps are detailed in Appendix B, implementation of the initial beam.

Initial work was then undertaken to design both cavities, in Section 4.6.1 involving selection of cavity properties including resonator g-parameters and defining the extent to which the cavity would be over coupled. The two-mirror cavity was then installed, in work detailed in Appendix C, implementation of the two-mirror cavity. The laser beam was mode-matched into the cavity, and the cavity was locked by adjusting the laser wavelength (frequency). Locking was first accomplished using an offset-lock, and later using the Pound-Drever-Hall modulation-demodulation technique. Some improvements were made to the system using data gathered at this stage, for example the end-mirror mount was exchanged for a more stable design based on the spectrum of the cavity locking error signal leading to some reduction in the noise of the system. The steps undertaken to implement the grating cavity were based largely on the work of Bunkowski et al [57], [56], [50], and private discussions of mine with those authors, who had once locked a three-port coupled diffractive cavity of the type successfully operated in our laboratory. Since our diffractive cavity is one of only a handful in existence, the unique steps relating to its implementation are detailed here (rather than in Appendix C as for the two-mirror cavity, which is a well known optical technology [58]).

4.6.1 Cavity property selection

In order to install either cavity, it was first necessary to make an appropriate selection of cavity mirrors and cavity length, which is discussed in this section. We want the input optic to be interchangeably either a grating or a mirror, and gratings must be etched onto flat surfaces. Therefore, it was necessary to design a flat-curved cavity. From Equation 2.42 we know that $g_1 \equiv 1-(L/R_1)$ which, since for a flat optic the radius of curvature is infinite, means that $g_1 = 1$ and therefore the stability parameter given by Equation 2.45 for the end-turning mirror becomes:

$$R_2 \geq L, \tag{4.24}$$

imposing that the end-turning mirror have a radius of curvature longer than the length of the cavity. Additionally, as can be seen from Equation 3.63 the phase change inducing the tilt-effect we aim to measure is proportional to the radius of curvature, while other noise sources and particularly residual longitudinal motion are not. Due to this a relatively high radius of curvature (compared to the cavity length) of $R_c = -1$ m was chosen for the end-turning mirror. As discussed in Section 2.3.4 it is ideal to be impedance matched, but therefore desirable to be in the slightly over coupled regime to be sure of avoiding the under coupled regime. It is not possible to use the mirror power transmission T, because the grating does not have a traditional measure of transmission. The essential component of calculating which regime the cavity is in is how much power is retained in the cavity, so we shall instead utilise power reflection coefficient R, for the grating the reflection at the normal to the grating surface. The three-port low-diffraction efficiency grating had reflection coefficient $\rho_0^2 = R = 0.997$ for maximum finesse, and therefore an end-mirror reflectance of $R_2 = 0.999$ was chosen.

4.6.2 Implementation of grating cavity

A variety of steps were used to convert the two-mirror cavity, the implementation of which is detailed in Appendix C, to a three-port coupled grating cavity. The diffraction grating used was a low-diffraction efficiency grating formed using the overcoating method outlined in Section 3.7.1 and having the properties detailed in Table 4.2. This grating was made available through the collaboration of this group, the AEI Max Planck Institute for Gravitational Physics in Hannover, and the University of Jena. In order to obtain a functional Fabry-Perot cavity using a diffractive input optic certain additional optics are required. These optics and the reasons for their use are detailed in this section.

Light field polarisation

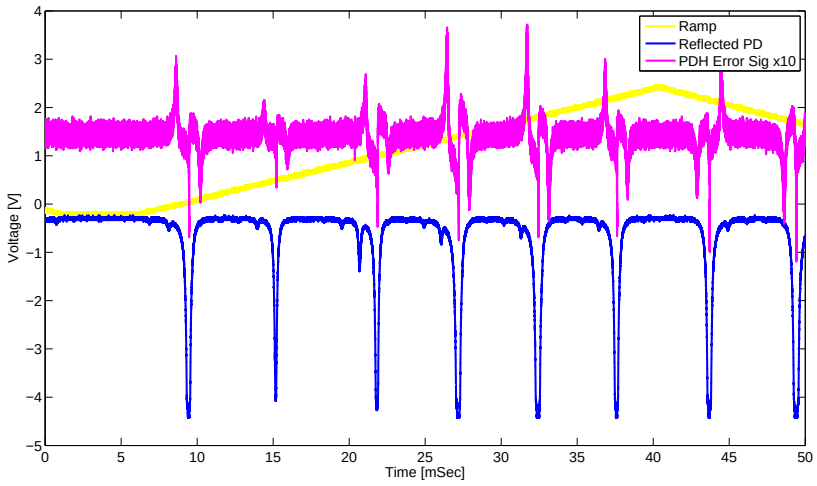

Figure 4.11: Pound-Drever-Hall error signal (multiplied by ten) of a grating cavity, with s-polarised input light.

Diffraction grating performance depends on the polarisation of the incident light [51]. Any optical beam is a physical expression of a propagating electromagnetic-field, which can itself be described by a combination of sinusoidal waves. The polarisation of this field depends on its source, and wave-plates modify the polarisation of a beam. Consider a plane, defined by the

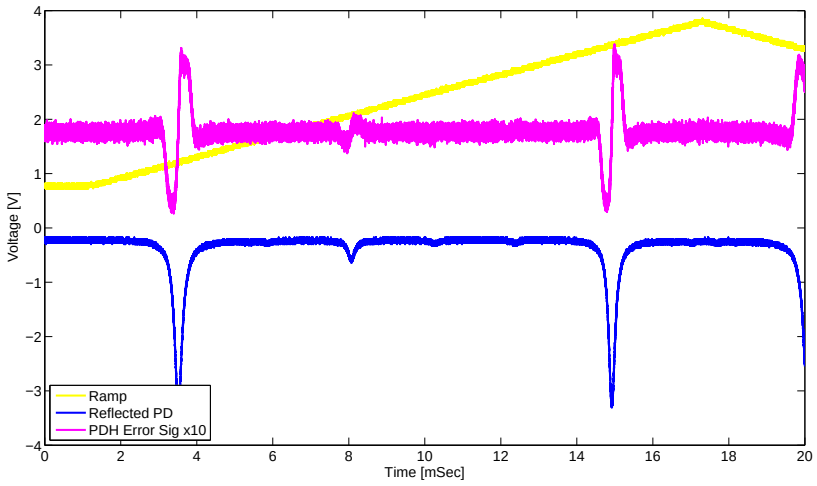

Figure 4.12: Pound-Drever-Hall error signal (multiplied by ten) of a grating cavity, with p-polarised input light (and without cylindrical lenses).

direction of propagation of the beam and a vector normal to the surface of some reflective optic (which in our case will be parallel to the surface of our optical table). We define p-polarisation (alternatively, transverse-magnetic) to be a beam whose electric field oscillates within this plane. Rotating this plane by ninety degrees about the beam axis gives the plane in which s-polarised (alternatively, transverse electric) oscillates. Light fields can be composed of a combination of p- and s-polarised light [37]. For a diffractively coupled cavity to exist in the plane of the table, the striations of the grating must fall perpendicular to the surface of the optical table. The reflectance of the grating and the performance of a diffractively coupled cavity depends on the polarisation of the incident light, as we see in Figure 4.12 showing the error-signal for p-polarised light and Figure 4.11 for s-polarised light [59]. For the designed performance of the grating it is necessary to use p-polarised light, as can be seen by comparing the quality of the error signal slopes at the locking point. Therefore an additional $\lambda/2$ wave plate was installed to adjust polarisation after the polarising beam-splitter. As shown in the full optical layout in Figure B.1 for practical reasons of space this wave plate appears after the mode-matching lenses and the coarse alignment-control, but it would function properly in any location between that beam-splitter and the grating.

Cylindrical lenses

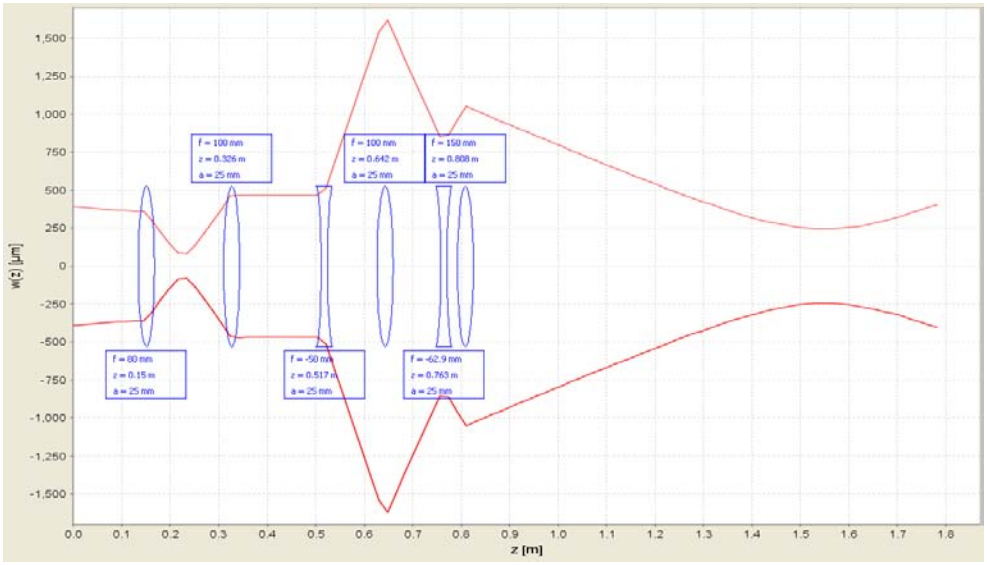

Figure 4.13: JAMMT model for required cylindrical lens positions to compensate for projection effect ellipticity. The last two lenses shown are cylindrical, and therefore effect only the x-direction beam cross section. The y-direction cross section remains unchanged and as shown in Figure B.3

Associated with the phase-change effects detailed in Section 3.3.1, caused by interacting with an optic in an anti-symmetrical way, is a projection effect on the beam that distorts its shape in the transverse direction. In the case of a grating, this is in the plane across the striations because the striations create the anti-symmetrical effect. The projection effect is shown in isolation in Figure 4.15 (a) where a uniformly circular Gaussian input beam (shown in transverse electromagnetic zero-zero mode for convenience) becomes elliptical. This means that a circular beam coupled into a three-port coupled Fabry-Perot cavity will be elliptical for its first trip to the end-mirror. For that elliptically distorted mode to resonate, an appropriately matched elliptical end-mirror would have to be installed so the elliptical wavefronts of the beam would meet an appropriately elliptical surface (see the discussion deriving resonator g-parameters in Section 2.3.6). Such an elliptical end-mirror would also be sensitive to rotation about an axis normal to its surface, which perfectly symmetrical mirrors are not. In any case no such elliptical mirror with equivalent quality to a spherical mirror presently exists.

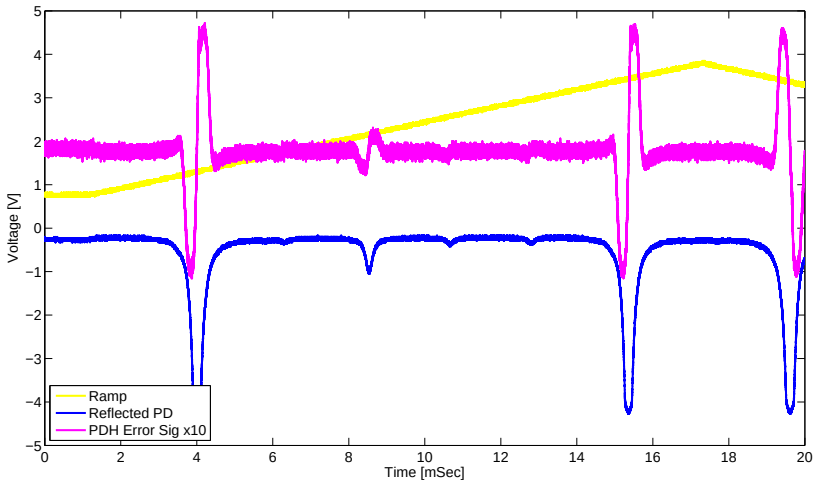

Figure 4.14: Grating Fabry-Perot cavity ramping, well aligned, in p-polarisation and with cylindrical lenses compensating for the projection effect.

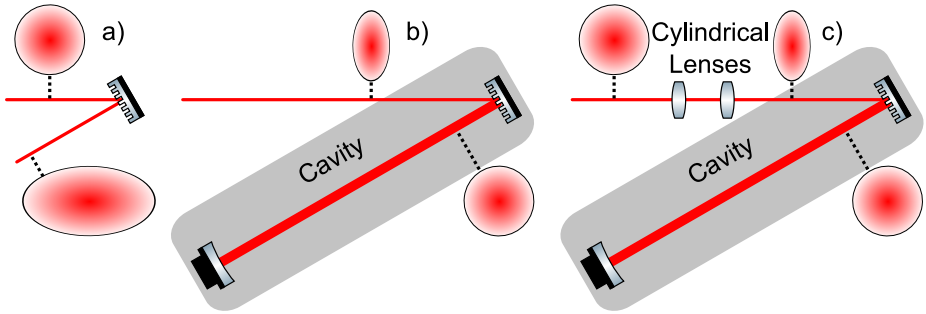

Figure 4.15: Projection effect on beam shape interacting with a grating (a) in isolation; (b) in a three-port coupled grating Fabry-Perot cavity; and (c) with appropriate compensation from cylindrical lenses. Cross sections of the beam (taken to be transverse electro-magnetic zero-zero mode for convenience) are shown at relevant locations.

The result of coupling such an elliptical beam into a cavity with a spherical end-mirror is a mode-mismatch between the elliptical beam which incouples and the circular beam which the cavity is designed to resonate for. The circular mode will always exist in the cavity, because the cavity will preferentially select it out from the input elliptical mode. Effectively this reduces the input power to the portion of the power of the elliptical beam that is in the circular mode. Such a mode-match therefore appears to reduce the cavity gain and prevents the cavity reaching its designed specification. The projection effect then applies in reverse, transforming the circular cross-section beam in the cavity to an elliptical beam in the return path as shown in Figure 4.15 (b). How serious the mode-mismatch is depends on the degree of ellipticity, which in turn depends on how far (in physical angle) the diffraction order doing the coupling (first, in a three-port coupled grating cavity) is from the reflection (zeroth-order). The mode-matching for the experimental three-port coupled grating Fabry-Perot cavity with the input light field in this elliptical combination of modes, reasonably well aligned, with an input angle of $\pi/4$ between the zeroth and first order is shown in Figure 4.12.

The fix for this projection-effect induced mode-mismatch (as detailed in Figure 4.15 (c)) is to introduce a deliberate and compensating ellipticity to the beam with cylindrical lenses before interaction with the grating (as shown in the JAMMT simulation of Figure 4.13 for the experimental cavity). This elliptical beam is then, after the projection effect, mode-matched to the circular end-mirror of the cavity. This also restores the circularity of the beam in the return path. The transmitted beam is naturally circular, but the forward reflected beam, were it to be used as we propose in Chapter 5 would require an additional identical pair of cylindrical lenses in the identical position relative to the grating to restore it to the circular form. The improvement in mode-matching caused by these lenses can be seen by comparing Figure 4.12, ramping of the laser frequency of a Fabry-Perot cavity with the cylindrical lenses to Figure 4.12, the same cavity before these lenses were installed. The effect is seen in the increase in signal (increased negative voltage) to the reflected photodiode at the resonance peaks of the cavity,

which increase from just over three volts to a little more than four with this improvement in mode matching.

4.6.3 End-mirror tilt actuator characterisation

Our experimental result will be a pair of transfer-functions, comparing the phase signal generated by coherent injection of end-mirror tilt into the two-mirror cavity to that from injection into the grating cavity. In order to take these transfer functions, it is necessary to have a method of generating a consistent end-mirror tilt. To generate this end-mirror tilt, the end-mirror was mounted on three-axis piezo actuator, (which was itself mounted in a Thorlabs micro positioning mirror-holder for cavity alignment purposes). The actuator design features three piezoelectric stacks arranged in a triangular formation. By differentially driving these three piezos it is possible to make any combination of motion on three axis: z (longitudinal), θ_y (vertical tilt or pitch) and θ_x (lateral tilt or yaw). It is the last of these which provides tilt that displaces the cavity eigenmode across the grating striations. The actuator is driven by a single input to a matrix box which adjustably attenuates the channels with respect to each other and inverts one channel with respect to the other two. One piezo must 'push' whilst the other two 'pull' to create tilt, and the amplitude of that motion depends on the distance of that piezo from the desired tilt axis. The mathematics behind the coupling matrix used and some implications for its implementation in are discussed in Appendix D.

Most coupling matrices will generate a combination of tilt motion (about some axis including both pitch and yaw) and longitudinal motion. A discussion of such combinations can be found in Section D.2 of Appendix D. The longitudinal motion is essentially due to mis-centering of the cavity eigenmode on the mirror. It is not the same as that unavoidable component due to tilt calculated in Section 3.5.2, where beam centering was assumed. This residual longitudinal motion is an experimental error to be minimised, as the experiment is designed for θ_x tilt-only

motion of the end-mirror, projecting the beam across the surface of either a diffraction grating for the three-port coupled grating cavity or a mirror for the two-mirror cavity. The geometry and minimisation of this longitudinal displacement will be discussed in the next section, and in more detail in Appendix D.

The rotational axis θ_x' about which an arbitrary tilt occurs is separate from the lateral tilt (yaw, θ_x) rotational axis, and this separation can be measured with a lever arm and CCD camera. This allows us to optimise the driving matrix for tilt over longitudinal motion on any rotational axis θ_x', then rotate the three-axis piezo actuator about its own central cylindrical axis in the Thorlabs mirror mount. Thus θ_x' can be made coincident with θ_x (the rotational axis for yaw, or lateral tilt), where the beam spot detected at the end of the lever arm sweeps parallel to the surface of the optical table.

Minimising the longitudinal motion will be achieved by adjusting the driving matrix to minimise a particular readout signal. This was achieved for the final result by using the EUCLID device as an additional readout sensitive to longitudinal mirror motion and insensitive to angle. A CCD camera was used to image both scattered light from the laser beam on the mirror surface, and to directly detect that light in transmission of the end-mirror to ensure that the EUCLID sensing beam interacted with the same spot on the end-mirror as the cavity eigenmode.

There is a minimum of both angular and longitudinal motion for the $(0,0,0)$ coupling matrix, when the matrix box attenuates the input voltage signal to zero. Similarly, under certain circumstances it is possible to shift from a nearly tilt-only driving matrix to a tilt-plus-longitudinal driving matrix and still see a reduction in signal (longitudinal via EUCLID or cavity locking error signal). This can occur if adjusting the matrix reduces the mirror motion such that it closely approaches the $(0,0,0)$ minimum, rather than the local minimum of tilt-only motion. Practically this can occur when the proportion of residual longitudinal motion increases, but the absolute value measured by EUCLID is lower because the overall attenuation of the matrix box has

increased). In order to avoid this $(0,0,0)$ minimum, a constant V_{RMS} sum of the inputs to the piezoelectric stacks was maintained. Such an approach will be successful at identifying a matrix for pure tilt motion, so long as the coefficient κ linking applied voltage to extension of the piezo is similar for all three piezos, which we expect to be the case in a consistently produced device (small deviations from equality are to be expected, and will be handled by the optimisation procedure).

In the process of selecting the best possible pure tilt case the following procedure was used. Initially a 117 V amplitude 10 Hz sawtooth-wave signal was applied to each of the three-axis-piezo's three piezoelectric actuators. The sum of the root-mean-square (RMS) of the three actuator signals was 203.2 V. This generated pure longitudinal motion, which was checked using a 2 m long lever arm and a CCD camera. The control-matrix of the three actuators was tweaked to minimize longitudinal motion in the following manner: Inverting two of three channels, simultaneously adjusting their attenuation with respect to the third, then adjusting their attenuation with respect to each other. The input power was then in- or decreased such that the 203.2 V RMS-sum was maintained, to allow equivalent comparison between cases with different attenuations on the different channels. Each of the three possible 'pairs' of actuators (one-two; one-three; two-three) were combined and adjusted in this way to discover the best-performing pair (although the piezo is well-built and uniform, idiosyncrasies in the mounting of the mirror can have an affect). As this pair had to scan the beam across the grating striations in the x direction, the lever arm and CCD camera were again used to determine the angle of scanning and the three-axis piezo actuator (and attached end-mirror) were rotated in the Thorlabs mount so tilt occurring was lateral (yaw, θ_x).

4.7 Measurement of residual longitudinal motion for a given angular tilt

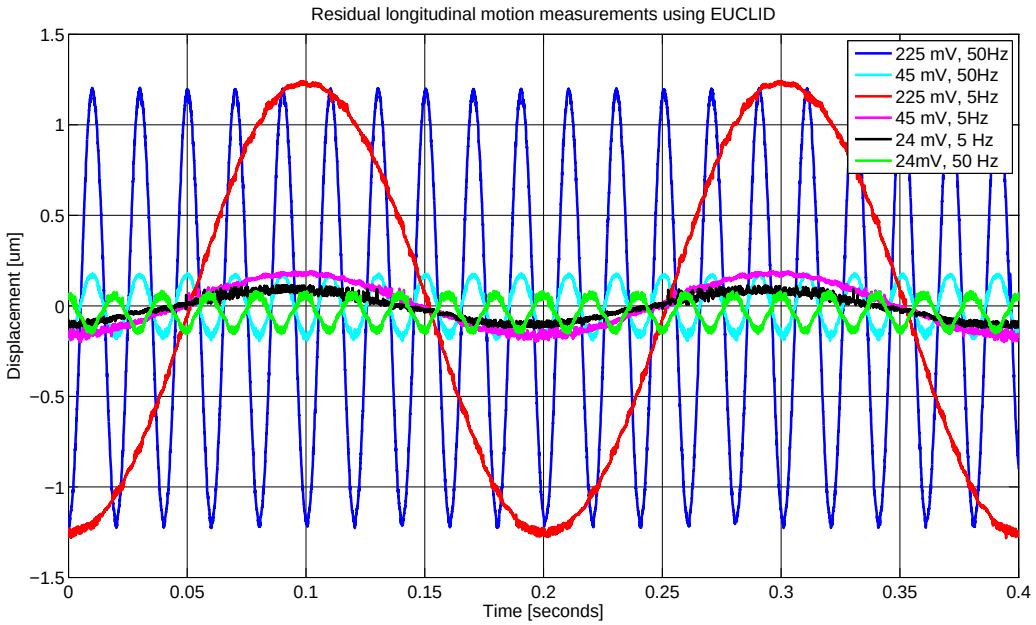

Figure 4.16: EUCLID residual longitudinal motion measurements at 5 Hz and 50 Hz, 225 mV, 45 mV and 24 mV peak-to-peak input signal. Note that the peak-to-peak displacement is smaller for both input voltages with the higher frequency.

In order to measure the residual longitudinal motion, EUCLID measurements were taken, with a sinusoidal signal of known voltage and frequency input to the matrix box used for driving the piezo. These results are shown in Figures 4.16 and 4.17 with the legends showing the input frequency and voltage. To calibrate this measurement of residual longitudinal motion to the tilt being generated by the actuator, a lever arm and beam-analysing CCD camera were used. All these results are summarised for the peak-to-peak voltages and measured longitudinal and angular displacements in Table 4.4. The angular tilt calibration was performed using a 30 cm long lever arm pointing to the WinCamD beam analysing device. This gives beam position measurements accurate to a few micrometers across the device CCD. Due to the WinCamD maximum sampling rate of 1 Hz this experiment was performed using DC input voltages to the

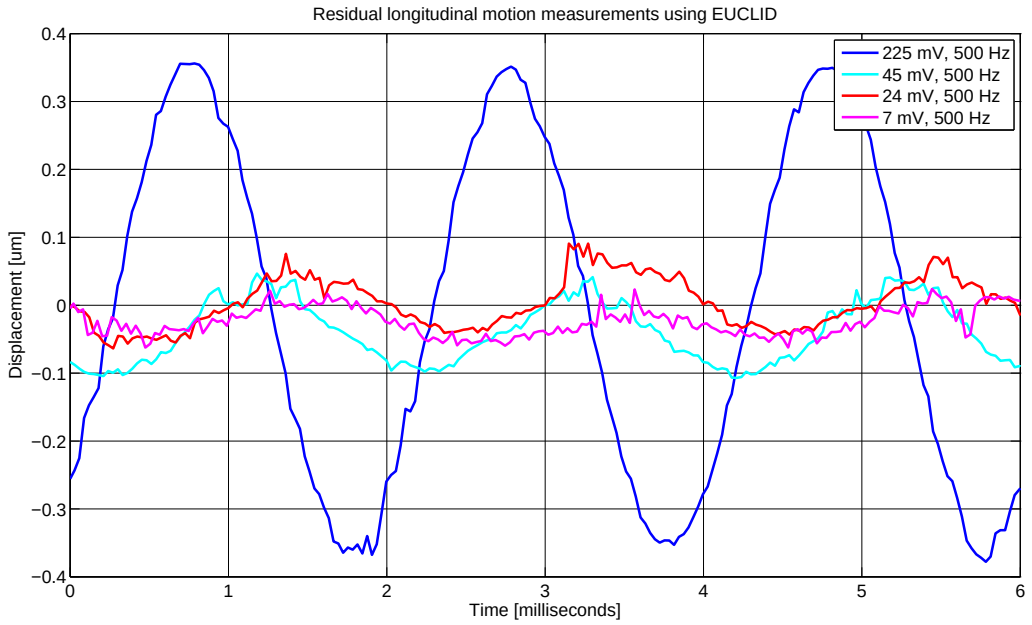

Figure 4.17: EUCLID residual longitudinal motion measurements at 500 Hz, 225 mV, 45 mV, 24 mV and 7 mV peak-to-peak input signal. Note that the peak-to-peak displacement is significantly smaller for all input voltages compared to Figure 4.16 at this higher frequency.

tilt-creating matrix box. These results are shown in Figure 4.18, and were used to calibrate the 'angular displacement' column of Table 4.4. It was recalled that, so long as the tilt occurs across the plane of the beam, the angular beam displacement is twice the angular change applied to the actuator. It can be seen from the residual angular displacement of the beam recorded in the vertical direction, and shown in Figure 4.18 to be approximately 1/100th of the horizontal displacement, is sufficiently small that the θ_x angular displacement can be considered to be in the plane of the beam. This determines the residual longitudinal motion ΔL associated with a particular angular displacement γ to be (also shown in the $[\gamma_2/\Delta L]$ column of Table 4.4,

$$\frac{\gamma_2}{\Delta L} = \frac{1.15\,\text{mrad}}{2.5\,\mu\text{m}} = 460\left[\frac{\text{rad}}{\text{m}}\right], \tag{4.25}$$

this value is for the 225 mV input signal, which is the lower value. Other values can be seen in the $[\gamma_2/\Delta L]$ column of Table 4.4. These values allow us to determine the ratio of phase signal

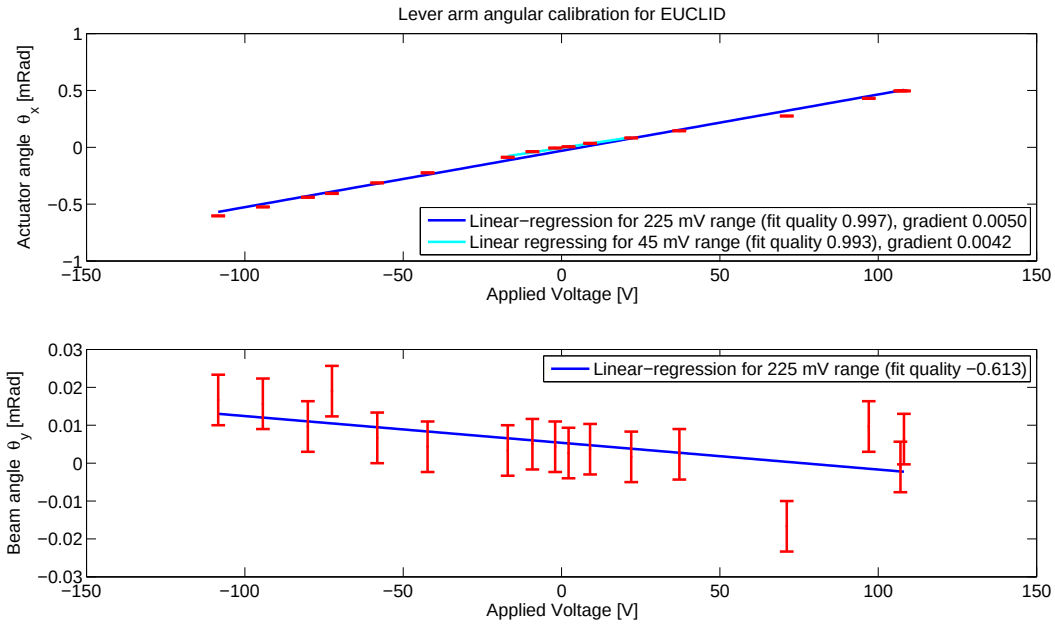

Figure 4.18: Lever arm measurement of angular change in θ_x for the actuator (top plot) and across the y axis (bottom plot), for a 30 cm lever arm and DC input voltages. Plus-minus two micrometer error bars are shown. Linear regression (least squares fitting) has been used to plot the lines, shown for data consistent with both 225 mV and 45 mV peak-to-peak signals (as plotted in Figure 4.16).

Frequency	Voltage P-P	EUCLID measured displacement P-P [ΔL]	Lever arm actuator angle [γ_2]	[$\gamma_2/\Delta L$]
5 Hz	225 mV	2.49 μm	1.15 mrad	460 rad/m
5 Hz	45 mV	380 nm	230 μrad	605 rad/m
5 Hz	24 mV	218 nm	120 μrad	550 rad/m
50 Hz	225 mV	2.38 μm	1.15 mrad	483 rad/m
50 Hz	45 mV	346 nm	230 μrad	665 rad/m
50 Hz	24 mV	216 nm	120 μrad	556 rad/m
500 Hz	225 mV	715 nm	1.15 mrad	1608 rad/m
500 Hz	45 mV	127 nm	230 μrad	1811 rad/m
500 Hz	24 mV	90 nm	120 μrad	1333 rad/m
500 Hz	7 mV	47 nm	36 μrad	766 rad/m

Table 4.4: Tabular summary of results for residual longitudinal motion calibration using EUCLID. The far right column is the calculated tilt angle per unit of residual longitudinal motion.

between residual longitudinal motion and end-mirror tilt motion for each of the two-mirror cavity and the grating cavity. Comparison of the results from 5 Hz, 50 Hz and 500 Hz suggest that the residual longitudinal motion is reducing as the piezo experiences higher frequencies, which may be accompanied by a reduction in the angular tilt generated by the actuator. This tilt may be disproportionately reduced compared to the residual longitudinal motion.

4.8 Calculation of expected signals with significant residual longitudinal motion

In this section we will recalculate the expected ratio of tilt induced noise between the grating cavity and the two-mirror cavity, in light of the significant residual longitudinal motion created by the end-mirror tilt actuator (discussed in Section 4.7). Some additional mathematics is required, as the case of residual longitudinal motion (mathematically equivalent to longitudinal motion induced by a gravitational wave, effect one) was not fully addressed in Chapter 3. It will be found that the expectation is that factor of 2.4 ± 0.5 greater signal should occur in the

grating case compared to the two-mirror case when the end-mirror is tilted. The uncertainty occurs because the starting phase offset Φ between residual longitudinal motion and lateral grating displacement in the grating case is unknown.

The phase-signals calculated in Sections 3.5.1 through 3.7.2 will be compared in this section for our laboratory cavity, where it is found that tilt-displacement in the two-mirror cavity may be neglected, and that our two dominant signals will be tilt-response in the grating cavity and residual-longitudinal-response in the two-mirror cavity (albeit the residual motion is itself caused by the end-mirror tilt). Some important values to note are shown in Table 4.2.

Subscript	Case or cavity
resid	Signal due to residual longitudinal motion of end-mirror (effect one)
eigen	Signal from length change of eigenmode due to its displacement (effect two)
ldg	Signal from lateral displacement of the beam on the grating (effect three)
grat	Refers to grating cavity
tm	Refers to two-mirror cavity

Table 4.5: In the following various subscripts will be used to differentiate between the different noise sources and the two cavities. This table is provided as a quick reference, as the descriptions are also included in the text. See Chapter 3 for a more complete introduction to these effects.

4.8.1 Dominant noise source in the two-mirror case

For the two-mirror cavity there are two sources of phase signal. A change of cavity eigenmode length due to its displacement by tilt; and a residual longitudinal displacement (cavity length change) made by the end-mirror actuator when it tilts. Both can be considered to occur at the end-mirror, and both are some small change ΔL to the cavity length L. Therefore it is sufficient to compare the magnitude of the length changes to determine which source will dominate. It is inappropriate simply sum the amplitude of the length changes, as we do not know the relative phase between them. If they occur in phase the net ΔL will be larger, and if out of phase it will be smaller. The amplitude of the change in cavity eigenmode length is given in terms of the

tilt γ_2 by Equation 3.35, where $R_c = -1$ m, with the constant DC misalignment assumed to be $\gamma_{1,\mathrm{dc}} = -10\,\mu$ rad and $\gamma_{2,\mathrm{dc}} = 10\,\mu$ rad (based on the resolution of the Thorlabs mirror mounts), and where the value for residual longitudinal motion of $\gamma_2 = 460\,\Delta L$ is used (from Section 4.7). Thus we obtain,

$$\frac{\Delta L_{\mathrm{resid}}(\omega_m)}{\Delta L_{\mathrm{eigen}}(\omega_m)} = \frac{\gamma_{2,\mathrm{resid}}(\omega_m)}{\gamma_{2,\mathrm{eigen}}(\omega_m)} \frac{1}{R_c(\gamma_{1,\mathrm{dc}} - \gamma_{2,\mathrm{dc}}) \cdot 460} \approx 1 \cdot 10^3, \tag{4.26}$$

where $\gamma_{2,\mathrm{resid}}$ and $\gamma_{2,\mathrm{eigen}}$ are identified for clarity, see Table 4.5. They are the identical tilt-displacement of the end-mirror γ_2 with frequency response ω_m and therefore cancel. The residual longitudinal motion overwhelmingly dominates, having a far greater effect that the change in eigenmode length. We will therefore neglect the change in eigenmode length in future appreciations. Note that this comparison leading to neglecting the eigenmode length change equally well applies to the diffractive cavity, although there we also have to consider the lateral grating translation effect. This means that our two-mirror cavity measurement is essentially a device to determine the residual longitudinal motion in our system, and to calibrate it to the transfer function of the tilt-actuator.

4.8.2 Calculating residual longitudinal motion for the two-mirror cavity

In Chapter 3 the isolation requirements for the two-mirror cavity were determined without deriving the tilt-induced sideband field at the output of the cavity. It is now necessary to calculate the size of this signal at the output for comparison to the three-port-coupled grating case (having already determined the transfer functions required for an experimental comparison in Section 4.4).

The sideband generation Section 2.1.3 tells us that sidebands are created at particular locations

where phase modulation occurs, and that the amplitude of those sidebands is proportional to the depth of the modulation. At the output of the Fabry-Perot cavity as discussed in Section 4.4 we measure a signal voltage proportional to the phase difference between the carrier experiencing the cavity and a light field unaffected by the cavity (the Pound-Drever-Hall sidebands). This phase change must be proportional to the amplitude of the phase-noise sidebands generated by effective cavity length change (or the lateral grating displacement effect) at the output of the Fabry-Perot cavity.

In order to perform this sideband-field calculation, we parallel the method for a sample gravitational wave in Section 3.7.4, for a two-mirror cavity with a longitudinally displaced end-mirror as shown in Figure 4.19. From this figure, we can write the following equations for the two input fields b_0 and b_2, occurring at some arbitrary angular frequency ω,

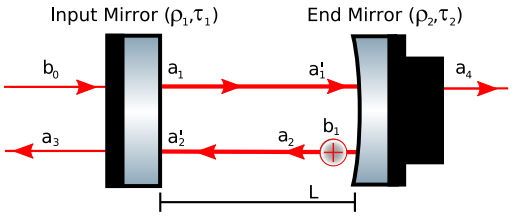

Figure 4.19: Two-mirror Fabry-Perot cavity schematic showing external carrier field input, and sideband field input due to longitudinal displacement of the end-mirror.

$$a_1(\omega) = b_0(\omega) i\tau_1 + a_2'(\omega)\rho_1 \tag{4.27}$$

$$a_1'(\omega) = a_1(\omega) e^{-ikL} \tag{4.28}$$

$$a_2(\omega) = a_1'(\omega)\rho_2 + b_2(\omega) \tag{4.29}$$

$$a_2'(\omega) = a_2(\omega) e^{-ikL} \tag{4.30}$$

$$a_3(\omega) = b_0(\omega)\rho_1 + a_2'(\omega) i\tau_1, \tag{4.31}$$

and solving for the carrier field alone (at frequency ω, with an input only at b_0) obtains,

$$\begin{aligned} a_2(\omega) &= \rho_2 e^{-ikL} \frac{b_0(\omega) i\tau_1}{1-\rho_1\rho_2 e^{-2ikL}} \\ a_2(\omega) &= \rho_2 e^{-ikL} b_0(\omega) i\tau_1 D(\omega) \\ a_3(\omega) &= b_0(\omega)\rho_1 + \rho_2 e^{-2ikL} \frac{b_0(\omega) i^2\tau_1^2}{1-\rho_1\rho_2 e^{-2ikL}} \\ a_3(\omega) &= b_0(\omega)\rho_1 + \rho_2 e^{-2ikL} b_0(\omega) i^2\tau_1^2 D(\omega), \end{aligned} \tag{4.32}$$

where $D(\omega) = 1/(1-\rho_1\rho_2 e^{-2ikL})$. Internal input b_2 (for the upper sideband and at frequency $\omega+\omega_m$) is given by, consistent with Equation 2.7,

$$\begin{aligned} b_2(\omega+\omega_m) &= i\frac{m}{2} a_2(\omega) e^{-i\omega_m t} \\ b_2(\omega+\omega_m) &= i\frac{m}{2} \rho_2 e^{-ikL} b_0(\omega) i\tau_1 D(\omega) e^{-i\omega_m t}, \end{aligned} \tag{4.33}$$

where ω_m is the modulation frequency, m is the phase modulation index (depth, given by the maximum phase change), and following the $m \ll 1$ approximation that only the carrier light field generates sidebands, a_2 is for the carrier field only (given by Equation 4.29). Solving the set of Equations 4.31 for the b_2 (upper sideband) input alone obtains,

$$\begin{aligned} a_2(\omega+\omega_m) &= \frac{b_2(\omega+\omega_m)}{1-\rho_1\rho_2 e^{-2i(k+k_m)L}} \\ a_2(\omega+\omega_m) &= b_2(\omega+\omega_m) D(\omega+\omega_m) \\ a_3(\omega+\omega_m) &= i\tau_1 e^{-i(k+k_m)L} b_2(\omega+\omega_m) D(\omega+\omega_m) \\ a_3(\omega+\omega_m) &= i^3\tau_1^2 b_0(\omega) \frac{m}{2} \rho_2 e^{-i(k+k_m)L} e^{-ikL} D(\omega) D(\omega+\omega_m) e^{-i\omega_m t}, \end{aligned} \tag{4.34}$$

this equation will be used to directly compare the output fields at the frequency of modulation by the end-mirror tilt. To allow such a comparison, we must substitute in the amplitude of the phase change $\Delta\phi$ for the phase modulation index m. The end-mirror tilt is related to the cavity length change by Equation 4.25 ($\gamma_2/\Delta L \approx 460$), itself related to the phase change by

Equation 3.26 ($\Delta\phi = 2\Delta L \cdot (2\pi/\lambda)$), thus obtaining for the modulation index associated the residual longitudinal motion,

$$\frac{2\gamma_2(\omega_m)\cdot 2\pi}{\lambda 460} \approx m_{\text{resid}} \tag{4.35}$$

Equation 4.34 describes the phase modulation sidebands induced by residual longitudinal motion at the output of the cavity. The modulation index to substitute into it is experimentally determined by the EUCLID calibration measurement, and given in Equation 4.35. The amplitude of the phase modulation sidebands is proportional to the amplitude of the phase change, and is equivalent to the signal voltage we detect at the output of the cavity. Hence this prediction for the sideband amplitude at the output of the two-mirror cavity can be used to divide a similar prediction for the grating cavity which will be made in the following section. That division will obtain the expected ratio between the signal voltages experimentally measured from the two cavities.

4.8.3 Calculation of expected signal in grating case

It is now necessary to calculate the size of the phase modulation sidebands at the output of the grating cavity for comparison to the result for the two-mirror cavity derived in the previous section. This is identical to the derivation performed in the previous chapter, in Section 3.7.2 and continued in 3.7.3 for the grating translation phase effect, and Section 3.7.4 for the gravitational wave equivalent longitudinal motion phase effect (the derivation for which applies in this case to the residual longitudinal motion). Therefore we can directly use those results in the form of Equation 3.67 for the output sidebands due to the grating lateral displacement effect and Equation 3.63 for their modulation index. The residual longitudinal motion sidebands for the grating cavity are given by Equation 3.69 with the modulation depth given by Equation 4.35 (the same as for the two-mirror case). The phase offset between these two effects is unknown, and

has been accounted for by introducing the starting phase Φ to the lateral grating displacement effect.

$$\begin{aligned} a_{4,\mathrm{ldg}}(\omega+\omega_m) &= i\frac{m_{\mathrm{ldg}}}{2}b_0(\omega)G_1^2\rho_2 e^{-2ikL}D(\omega)e^{i\omega_m t}e^{i\Phi} \\ +a_{4,\mathrm{resid}}(\omega+\omega_m) &\quad +i\frac{m_{\mathrm{resid}}}{2}b_0(\omega)G_1^2\rho_2 e^{-i(k+k_m)L}e^{-ikL}D(\omega)D(\omega+\omega_m)e^{i\omega_m t} \\ m_{\mathrm{ldg}}(\omega+\omega_m) &= \frac{2\pi R_c\mu}{d\cos\alpha}\gamma_{2,\mathrm{ldg}}(\omega_m), \end{aligned} \tag{4.36}$$

we have diffraction order $\mu = 1$, radius of end-mirror curvature $R_c = -1\,\mathrm{m}$, grating period $d = 1500\,\mathrm{nm}$, physical input angle $\alpha = \pi/4\,\mathrm{rad}$, and $\gamma_{2,\mathrm{ldg}}(\omega_m) = \gamma_{2,\mathrm{resid}}(\omega_m)$ since both effects are generated by the same end-mirror tilt (ldg for lateral displacement of the grating, resid for residual longitudinal motion, see Table 4.5. The cavity is assumed to be held on-resonance for the carrier (as in our experiment) imposing $\exp(-ikL) = 1$, and we assume that the phase sidebands are sufficiently close to the carrier that $D(\omega+\omega_m) \approx D(\omega)$. We select the unknown phase offset Φ between the lateral grating translation effect and residual longitudinal motion effect to consider the maximum and minimum possible outcomes when the sidebands are in-phase and out-of-phase, where $\exp(i\Phi) = \exp(-ik_mL)$ and $\exp(i\Phi) = -\exp(-ik_mL)$ respectively.

$$a_4(\omega+\omega_m) = ib_0(\omega)G_1^2\rho_2 e^{i\omega_m t}e^{-i(2k+k_m)L}D(\omega)\left(\frac{m_{\mathrm{ldg}}}{2} \pm \frac{m_{\mathrm{resid}}}{2}D(\omega+\omega_m)\right) \tag{4.37}$$

It is now possible to divide this equation by Equation 4.34, the equivalent result for the two-mirror cavity, and obtain the expected ratio between the tilt response of the two cavities. This calculation will be performed in the following section.

4.8.4 Comparison of grating and two-mirror cavity tilt response

The upper and lower limits for the phase signal in the grating cavity case have been predicted in Equation 4.37. Similarly, the predicted phase signal in the two-mirror case has been predicted

in Equation 4.34. Since we are taking two different measurements, we have to consider the unknown phase offset Ψ between them, which has been included in the denominator, and $G_1 = \eta_1 \exp(-i\phi_1)$ from Equation 3.55 has also been used, obtaining,

$$\frac{a_{4,\mathrm{grat}}(\omega+\omega_m)}{a_{3,\mathrm{tm}}(\omega+\omega_m)} = \frac{\eta_1^2 e^{-2i\phi_1} e^{-i(2k+k_m)L}\left(\frac{m_{\mathrm{ldg}}}{2} \pm \frac{m_{\mathrm{resid}}}{2} D(\omega+\omega_m)\right)}{i^2 \tau_1^2 \frac{m_{\mathrm{resid}}}{2} e^{-i(2k+k_m)L} e^{i\Psi} D(\omega+\omega_m)} \tag{4.38}$$

$$\frac{a_{4,\mathrm{grat}}(\omega+\omega_m)}{a_{3,\mathrm{tm}}(\omega+\omega_m)} = \frac{\eta_1^2 \left(\frac{m_{\mathrm{ldg}}}{2} \pm \frac{m_{\mathrm{resid}}}{2} D(\omega+\omega_m)\right)}{\tau_1^2 \frac{m_{\mathrm{resid}}}{2} D(\omega+\omega_m)} \tag{4.39}$$

where port $a_{4,\mathrm{grat}}$ is the back-reflected port for the grating cavity and $a_{3,\mathrm{tm}}$ is the reflected port for the two-mirror cavity. In the second of these equations we have recalled that in this experiment we compare the amplitude of the phase signals in both cases, as given by the signal analyser. I.e. the signal analyser effectively discards the starting phase in such a way as to make the comparison equivalent to Equation 4.39. In the above equation, this has set $\exp(-2i\phi_1)/i^2 \exp(i\Psi) = 1$. Substituting in from Equation 4.36 and 4.35 for the modulation indicie, where $R_c = -1\,\mathrm{m}$, $\mu = 1$, $d = 1500\,\mathrm{nm}$, $\alpha = \pi/4\,\mathrm{rad}$, $\lambda = 1064\,\mathrm{nm}$, $G_1 = \eta_1 \exp(-i\phi_1)$ with the first diffraction order amplitude coupling coefficient $\eta_1 = \sqrt{0.01}$, and $\tau_1 = \sqrt{0.02}$, and thus we obtain,

$$\begin{aligned}
\frac{a_{4,\mathrm{grat}}(\omega+\omega_m)}{a_{3,\mathrm{tm}}(\omega+\omega_m)} &= \frac{\eta_1^2}{\tau_1^2}\left(\frac{m_{\mathrm{ldg}}}{m_{\mathrm{resid}} D(\omega+\omega_m)} \pm 1\right), \\
\frac{a_{4,\mathrm{grat}}(\omega+\omega_m)}{a_{3,\mathrm{tm}}(\omega+\omega_m)} &= 0.5\left(\frac{\gamma(\omega_m)}{\gamma(\omega_m)} \frac{(2\pi R_c \mu)/(d\cos\alpha)}{(2\pi \cdot 2D(\omega+\omega_m))/(460\cdot\lambda)} \pm 1\right), \\
\frac{a_{4,\mathrm{grat}}(\omega+\omega_m)}{a_{3,\mathrm{tm}}(\omega+\omega_m)} &= 2.4 \pm 0.5,
\end{aligned} \tag{4.40}$$

which is the expected ratio between the feedback signals for the two-mirror cavity and grating cavity subjected to end-mirror tilt. These are the results plotted in Figure 4.9.

It can be seen from Figure 4.9 that even this much reduced expected ratio between the two-mirror cavity tilt response (shown by the blue lines) and the grating cavity tilt response (shown by the red lines) is larger than that detected. To explain this discrepancy, there are several

features of the plot which should first be explained.

The first is that the two-mirror cavity response (blue lines) exceeds that of the grating cavity (red lines) at low frequencies. This is not possible if the cavities experience the same end-mirror tilt, except due to differing properties of the cavity optics G_2, which have been experimentally compensated for by adjusting the servo gain H. The conclusion to draw is that the cavities do not experience quite the same end-mirror tilt. This is likely due to some (small, since the difference is only a factor of approximately 1.3) alignment error in the DC setup of the cavities, most likely that the two-mirror cavity eigenmode interacts with a portion of the end-mirror which experiences a longitudinal motion 1.3 times greater than the portion of the end-mirror interacted with by the grating cavity eigenmode. Compensating for this effect would translate the blue lines (for the two-mirror cavity) down by the factor of 1.3. This also suggests that the EUCLID measurement error could be bigger than expected, by approximately the same factor of 1.3, since the alignment of the two cavities eigenmodes and the EUCLID device used the same process.

Interestingly, the tilt-response trace for the grating cavity crosses that of the two-mirror cavity at approximately 1 kHz, beyond which the grating cavity tilt response dominates, up until around 10 kHz, where the lines reconverge. This convergence at high frequencies is likely due to resonances within the three-axis piezo causing some residual longitudinal motion dominated resonance mode of mirror motion to be excited, which overwhelms the tilt signal. Beyond approximately 30 kHz the high-voltage amplifier used by the tilt actuator has a roll-off, which essentially eliminates signal to the device before 100 kHz. Hence beyond this value we measure only the noise of the rest of the system in the 'transfer functions'.

The intriguing region is therefore between 1 kHz and 5 kHz in Figure 4.9, with an unfortunate piezo resonance at 3.5 kHz as can be seen in the coherence plot, Figure 4.10. Within this region, we obtain greater than the expected ratio between the grating cavity tilt response and the two-

mirror cavity tilt response. The likely explanation for this is presented in the EUCLID plots shown in Figures 4.16 and 4.17, the most notable feature of which is the reduction in the amplitude of the residual longitudinal motion detected by EUCLID. The factor of reduction is approximately 1.05 between 5 Hz and 50 Hz, and 3.50 between 5 Hz and 500 Hz (the interpretation varies slightly depending on the values chosen for this calculation from Table 4.4). This reduction in residual longitudinal motion is must be accompanied by a reduction in end-mirror tilt, or we would see a separation of the grating cavity and two-mirror cavity responses before 1 kHz. However, it does explain the slope of the tilt feedback signal responses, which begin to reduce noticeably around 150 Hz. It seems likely that the predicted separation of the feedback-response lines in the region 1 kHz to 5 kHz is due to a disproportionate reduction in residual longitudinal motion with increasing frequency. This is supported by the fact that the lines continued to diverge further up to the 10 kHz resonance limit. This result is not inconsistent with the prediction modified by residual longitudinal motion, but does not clearly demonstrate the theory outlined in Chapter 3.

The clearest feature of Figure 4.9 is that this is a difficult measurement to record with a standard three-axis piezo actuator, due to the near equivalence between the residual longitudinal motion signal and the desired tilt motion signal (for the grating cavity). The PI.311 actuator was selected for its high resolution tilt performance, and therefore also has reasonably good orthogonality between the axis of motion driving it, and it is still hard to distinguish the grating effect. Better orthogonalised actuators are not easily available, nor are they so compatible with common Fabry-Perot cavity optics (it is more common to use such devices for flat steering mirrors of smaller substrate radius than our one-inch diameter cavity end-mirror). For these reason, the opportunity to undertake related work using the JIF facility at and in collaboration with the University of Glasgow was pursued. These previously alluded to investigations and their results have been detailed in Section 4.9.

4.9 Suspended optic investigations at the University of Glasgow

Some work for this thesis has been carried out at the Joint Interferometer Facility (JIF) 10m prototype gravitational wave interferometer at the University of Glasgow, one arm of which has been configured as a prototype three-port coupled second-order Littrow configuration diffractive cavity [59]. This work is particularly related to the theoretical discussion led by myself [28], and I have spent several weeks visiting the prototype facility and collaborating in the work being undertaken there. Some brief discussion of the configuration and the methodology will be undertaken here, followed by a presentation of the results which have relevance to both this and the following chapter. The work in this section is presently undergoing internal Ligo Science Collaboration review for publication [60] in a paper of which I am a co-author.

4.9.1 Configuration of the JIF cavity

The prototype diffractive cavity is configured as shown in Figure 4.20 with a separation of approximately 10 m between the grating and the end-mirror, and the three output ports that will be discussed in Chapter 5 are shown. Both the grating and the end-mirror test-masses are triple-suspended from cantilever arms, and both optics and suspensions are located in a vacuum system. This provides far better isolation from seismic (ground vibration) and acoustic (atmospheric vibration) noises than can be achieved on an optical bench. The diffractive optic is an overcoated, low-diffraction efficiency type similar to the one used in the experiment undertaken in my laboratory. Since these are not presently available etched into fused silica or sapphire reference masses a small grating was mounted on the front-face of an aluminium metallic mass, of the same dimensions and mass as a silica test-mass. Prior to the input both elliptical lenses and a waveplate setting the light to p-polarisation were installed (as discussed for

my laboratory experiment in Section 4.6.2). Two sets of sidebands, at 10 MHz and 15.24 MHz, were applied to the input light field so that one set (10 MHz) could be used to investigate the phase effect of grating translation and the other (15.24 MHz) used to lock the cavity. The work of locking the cavity to the Pound-Drever-Hall signal obtained by demodulating the 15.24 MHz sidebands at the transmitted (c_{2t}) port is detailed in the work of Edgar et al [59] with which I was not involved.

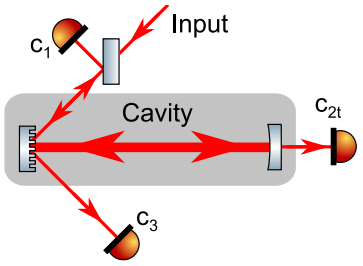

Figure 4.20: Schematic of the relevant portions of the JIF cavity at the University of Glasgow. The initial optics required for laser systems and diffractive cavity implementation (the additional waveplate and elliptical lenses detailed for the tabletop experiment in Section 4.6.2) are not shown. Though the exact layout differs, the effect and effective implementation is the same as discussed in Section 4.2. As I was not involved in the commissioning of the JIF facility, these details will not be further discussed herein.

The forward-reflected (c_3) port was selected for this study, both because it offers the simplest modulation configuration [59] and because of the comparatively large signal strength to be found there. The light directly reflecting from the test mass is in diffraction order zero ($\mu = 0$) and therefore does not experience the grating phase change effect. The light leaving the cavity is coupled out in the negative-first diffraction order ($\mu = -1$), and therefore the grating phase effect will appear imprinted upon this light. This, and the fact that the light entering the cavity is diffracted in the first diffraction order ($\mu = 1$), are the key points in the cancellation effect discussed in Chapter 5.

The 10 MHz sidebands were selected to be anti-resonant when cavity is stable and the grating motionless, and they are sufficiently far outside the FWHM that they will remain anti-resonant for any oscillation frequency applied to the diffractive optic. Thus the 10 MHz sidebands are

effectively only present in the b_0 input field as shown in Figure 5.1. Since the η_2 of the grating used is small, the majority of the power in these sidebands is directly reflected to the forward-reflected a_3 port in diffraction order $\mu = 0$. Therefore there is no phase noise due to lateral grating displacement imprinted upon the 10 MHz sidebands, though they will experience phase noise from longitudinal displacement (as shown in Figure 3.6). The demodulation of these sidebands against the carrier - which does resonate in the cavity and acquires phase noise from in and out coupling in the $\mu = 1$ and $\mu = -1$ diffraction orders respectively - reveals the lateral grating translation effect.

The JIF suspensions allow control to be exercised in almost any degree of freedom, subject to the mounting of an appropriately positioned set of coil-magnet actuators on the test mass. The actuators used to drive the test mass, and the combinations that allows driving in longitudinal, translation and rotational modes are shown in Figure 4.21. Longitudinal driving was possible using the rear-mounted coil actuators (or equivalently for the cavity by displacing the end-mirror using its drivers). As lateral driving had not originally been considered, we were required to install the side-mounted coil actuator in-situ, which was bonded to one of the guide-flanges for the suspension system. Concurrently, we installed a laser velocimeter, configured to directly read out the lateral displacement of diffractive test mass. A test of this lateral driving and measurement system produces Figure 4.22 which shows that the Δx driving of the test-mass using this side-mounted coil has a $1/f^2$ response to a driving signal of fixed amplitude. Any additional twisting motion caused by the difficulty of centering the lateral actuator under this conditions was compensated for using the rear actuators.

4.9.2 Translational driving of the JIF cavity

The mathematics presented in Chapter 5 are required to calculate the effect of lateral grating translation, due to the cancellation effect derived therein. For the forward-reflected output port

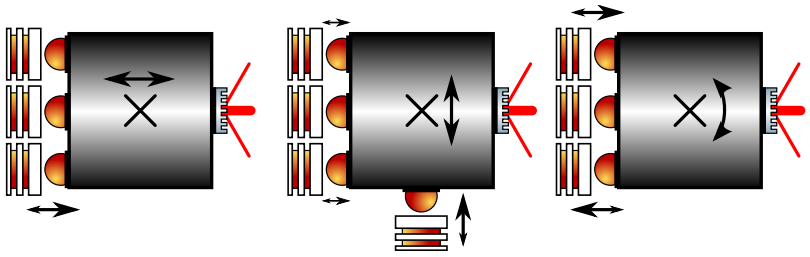

Figure 4.21: Magnets mounted on the JIF diffractive test mass for the coil-drivers to actuate, with the longitudinal (left), translational (center), and rotational (right) driving modes shown. Additionally, note the front-face bolt-down mounting of the grating to a cylindrical, hollow test mass (in fact, a re purposed aluminum reference mass intended for the intermediate stage of the pendulum).

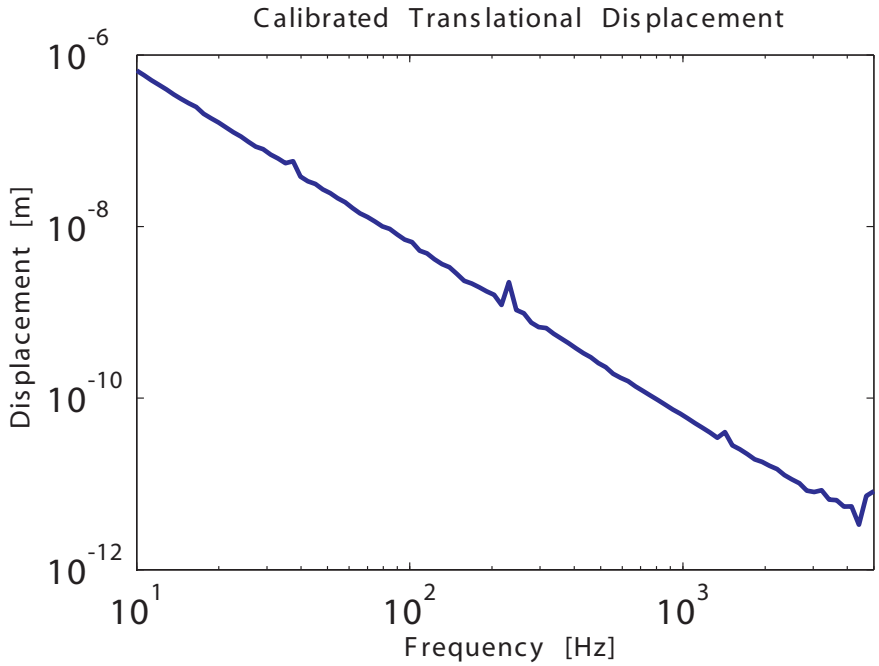

Figure 4.22: Independently measured lateral displacement of the JIF diffractive test mass when subjected to a fixed-amplitude driving signal applied to the side-mounted magnet by a coil-driver actuator.

the sideband induced by lateral grating translation is given by Equation 5.24, which is worth repeating here in its form as given in [60],

$$a_3 = ip_0\eta_1^2 e^{-2i\phi_1}\rho_2\frac{\pi\Delta x}{d}\left(\frac{e^{-2ik_u L}}{1-\rho_0\rho_2 e^{-2ik_u L}} - \frac{e^{-2ik_c L}}{1-\rho_0\rho_2 e^{-2ik_c L}}\right) \tag{4.41}$$

where p_0 is the incident carrier field, η_1 is the first-order diffraction efficiency and ϕ_1 the phase shift on diffraction, ρ_0 is the reflectivity of the grating at normal incidence and ρ_2 the reflectivity of the end mirror, k_u is the wave number of the lateral grating displacement induced sideband and k_c the wave number of the carrier light field, d is the grating period and Δx its lateral displacement, and L is the cavity length.

The frequency response of this lateral grating induced sideband is determined by the first term in the bracket, where the wave vector k_u is set by the modulation frequency with which the grating is oscillated, and related to the frequency of the field by $k = 2\pi f/c$. This term is approximately linear in frequency, so long as that frequency is within the cavity line width (i.e. for frequencies below the cavity full-width-half-maximum). Hence the tilt-motion signal shows an f response (linear with frequency), which appears on the demodulated 10 MHz signal. Therefore when combined with the $1/f^2$ response of the test mass to a signal with a fixed amplitude we expect the lateral grating translation effect to have a $1/f$ response. It should be clear that without this cancellation the pure longitudinal response will have a $1/f^2$ response. For the JIF cavity the FWHM is 13.8 kHz (Table 4.6), so the $1/f$ frequency response applies across the whole frequency range considered. Using the properties of the JIF cavity as given in Table 4.6 we can predict the response of the system to driving in translation, the result of which is shown in Figure 4.23, along with the experimental translational result, and, for comparison purposes, the longitudinal result.

It can be seen that the theoretical and experimental curves for translational driving are in close agreement, which is a vindication of the result discovered in Chapter 5. The critical difference

Quantity	Unit	Value
Calculated finesse	-	1177±27
Length	m	9.822
End-mirror R_c	m	15
FSR	MHz	15.7
FWHM	kHz	13.8±0.64
Measured finesse	-	1107±51
ρ_0	-	0.9986
η_1	-	0.0277
η_2	-	0.0134
τ_1	-	0.0063

Table 4.6: Details of the key features of the JIF cavity, where τ_1 is the transmission of the end-mirror. Measured cavity properties [59].

from the theoretical result is the rising slope measured experimentally above 300 Hz. This rising feature is due to an internal mechanical resonance of the aluminium test mass centered at approximately 1.38 kHz, expected at this frequency from a finite-element simulation and confirmed using an additional test mass of the same type and an acoustic vibrational drive. The particular mounting of the grating on this test-mass can be seen in Figure 4.21. In a full-scale gravitational wave detector the diffractive test-mass would be manufactured from a more appropriate material such as fused silica and therefore peak responses would be both narrower and higher in frequency. However, the low frequency and breadth of the peak observed in these experiments allows observation of the effects of the internal test-mass-modes on the three-port coupled diffractive cavity response. It was possible to avoid driving this internal resonance mode through the use of rotational, rather than lateral, actuation.

4.9.3 Rotational driving of the JIF cavity

It was possible to drive the diffractive test mass rotationally by differential driving of the rear actuators, although this did cause some longitudinal displacement. This rotational driving causes three effects shown in Figure 4.23. First, a residual component of longitudinal motion, which expresses as a $1/f^2$ slope. This was minimised at 42 Hz through careful balancing of the

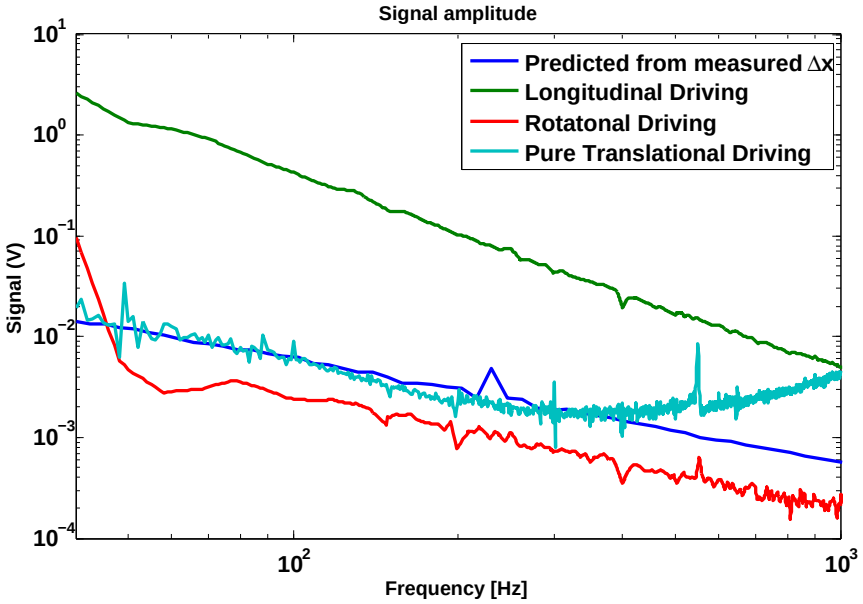

Figure 4.23: Response of the JIF cavity to various grating displacements experimental and theoretical.

amplitude of the driving current sent to each actuator by minimising the 10 MHz demodulated response. Second, a component of translational motion, which expresses as a $1/f$ slope and is therefore expected to dominate above 42 Hz since the $1/f^2$ slope falls of more swiftly. This is as-observed in Figure 4.23, with the rotational trace paralleling the theory translational trace with approximately $1/3$ of its value from 50 Hz onwards. The reduction in signal is due to the rotation of the grating test-mass causing less lateral displacement of the grating than direct lateral displacement of the grating test-mass. The reason 42 Hz was chosen as the minimisation point for longitudinal motion is to avoid a 37 Hz suspension bounce-mode, the roll-on of which can be seen being excited by the rotational motion below 50 Hz.

The third expected effect of rotational motion is a lateral displacement of the eigenmode within the cavity. This will not experience the cancellation effect discussed in Chapter 5, as it does not affect the input beam. The displacement of the eigenmode through rotating one of the optics is the approach I adopted deliberately in Section 4.6.3, although I rotated the end-mirror rather

than the grating. The calculation performed in Section 3.7.2 for the extent of the optical axis lateral displacement remains valid; however, from the starting point of Equation 3.60 we can obtain the grating position in its own reference frame due to our rotation of the grating γ_1, where γ_2 is the rotation of the end-mirror, R_c is the radius of curvature of the end-mirror, and L is the cavity length [52],

$$x'_f \approx -R_c\gamma_2 + (R_c - L)\gamma_1, \tag{4.42}$$

thus the grating displacement is given by,

$$\Delta x_{\gamma_1}(f) = (R_c - L)\gamma_1(f), \tag{4.43}$$

which by converting to a phase change using $\Delta\eta = -2\pi\Delta x/d$ obtains, where d is the grating period,

$$\Delta\eta(f) = \frac{2\pi(R_c - L)\mu}{d}\gamma_1(f), \tag{4.44}$$

it is clear that this will be much smaller than Equation 3.63 (where R_c rather than $R_c - L$ appears) as typically for a flat-curved cavity the resonator g-parameters discussed in Section 4.6.1 cause the choice of end-mirror curvature slightly longer than the cavity length. This fulfils the stability condition even with a relatively large mirror misalignment. Reducing the $R_c - L$ term reduces the expected phase signal proportionally, and given the difficulties in observing this effect even in my tabletop experiment which was optimised for maximum Δx projected by end-mirror tilt, it is not surprising that the JIF measurement is dominated by the translational motion in Figure 4.23.

4.10 Conclusions

In Chapter 3 a prediction comparing end-mirror tilt induced noise between a three-port coupled grating and two-mirror cavity was made. A tabletop experiment was designed for both types of cavity in order to test this prediction. A linear cavity with with a three-port grating as an input coupler was successfully set up. The optical properties of the grating cavity were measured to be as good as those of the two-mirror cavity. A Pound-Drever-Hall scheme was adopted for use with the grating cavity and successfully implemented. It was discovered that the residual longitudinal motion of the end-mirror tilt actuator dominated the end-mirror tilt signal in the two-mirror cavity, and was almost equivalent to the tilt signal in the grating cavity. These dimensionless results were calibrated into an equivalent longitudinal motion which provides an aid for understanding the physical extent of this phase noise source. However, the tabletop experiment does not provide a statement comparing tilt effects between the cavity types, although it does strongly suggest that the lateral grating displacement phase effect exists, and supports our calculation for its functioning made in Chapter 3. Since the tabletop experiment was dominated by residual longitudinal motion, the opportunity to perform experimental work on the JIF grating cavity at and in collaboration with the University of Glasgow was pursued. This used a different experimental methodology, leading to a prediction for the frequency-slope of the tilt-response measurement which was fulfilled. Thus this experiment demonstrated for the first time the additional phase noise predicted in Chapter 3, and furthermore showed the signal compensation which might be employed to reduce the alignment noise (see Chapter 5 for the theoretical explanation). Absolute calibration of the JIF cavity measurements analogous to those for the tabletop experiment has not been undertaken. The JIF has been available for a limited time and an extensive measurement campaign as for the tabletop experiment has not been possible.

Chapter 5

OUTPUT PORT PHASE-NOISE PERFORMANCE

The three port coupled grating cavity is the most promising diffractive cavity configuration. It has the lowest isolation requirement of the three cases considered in Chapter 3. Due to its symmetry, we expect that when the grating is laterally displaced such that it phase-modulates the carrier light field (the externally input field), there may be some cancellation between the noise sidebands generated on input to the cavity and on output from the cavity. We will calculate in this chapter that some suppression of phase noise is to be expected in the forward-reflected output port, and some enhancement of phase noise in the back-reflected output port.

In this chapter we use a steady-state technique (described in Section 2.1.3) to derive coupling of lateral grating displacement to the output ports of a three-port coupled second-order Littrow configuration diffractive Fabry-Perot cavity (as shown in Figure 5.2). Oscillating the grating with lateral displacement causes phase modulation of the carrier light field, which generates sidebands. By introducing a signal to noise ratio (SNR) for each of the three cavity output ports the magnitude of the noise sidebands originating from lateral grating displacement are

compared to the magnitude of a potential gravitational wave signal. For the example of a 3km long Fabry-Perot cavity using Virgo-esque properties as we have in Chapter 3, we find that the forward-reflecting grating port offers the highest SNR at low frequencies. Furthermore, for this example suspension requirements for lateral isolation are computed, and a factor of twenty relaxation at a frequency of 10 Hz can be gained over the transmitted port by observing the forward-reflected port.

5.1 Phase-noise performance of three-port coupled diffractive Fabry-Perot cavity output ports

In the three-port, second-order-Littrow configuration (as shown in Figure 5.2) it is the zeroth-order diffraction (equivalent to the reflection) that retains the light-field in the Fabry-Perot cavity [51]. Since the phase change generated by lateral grating displacement only occurs in diffraction orders $|\mu| \geq 1$ only light fields coupling into or out of the cavity via the grating experience phase change. If the grating is oscillated laterally, this phase change gives rise to noise sidebands which can obscure the gravitational wave signal. In this chapter, we calculate these noise sidebands, and the sidebands appearing in the cavity due to a potential gravitational wave signal, and compare signal to noise at the three cavity output ports. It is found that the forward-reflected port experiences some cancellation of the noise sidebands.

Partial cancellation of the noise sidebands occurs due to the symmetry of the situation. We assume that the cavity is held on resonance for the input light field. On coupling into the cavity in diffraction order $\mu = 1$, the carrier light field generates sidebands proportional to its external input-field amplitude by interacting with the oscillating grating. These input sidebands then resonate in the cavity at a frequency offset from the carrier by the modulation frequency of the grating, and therefore experience less gain than the carrier due to being slightly detuned from

the cavity. The $m \ll 1$ approximation [30] (discussed in more detail in Section 2.1.3) states that only the carrier light field generates sidebands, and hence these input sidebands do not generate sidebands of their own when they are coupled out of the cavity. The carrier itself then couples out of the cavity to the forward-reflected port in diffraction order $\mu = -1$. The carrier amplitude has now been enhanced by the cavity gain, and the output sidebands it generates are proportional to that amplitude. Since these input and output sidebands have opposite sign (from input $\mu = 1$, and from output $\mu = -1$), they will partially cancel with each other. This cancellation is only partial because the input sidebands were slightly detuned from the cavity, and did not experience as much gain as the carrier which generated the output sidebands. Conversely in the back-reflected port the output sidebands are in diffraction order $\mu = 1$ and sum with the input sidebands, so phase-noise is effectively transferred from the forward-reflected to the back-reflected port.

The work included in this chapter has previously been presented in Hallam et al 2009 [28], of which I was the lead author. The additional space herein afforded the opportunity to present the work in a manner suitable for an audience less-well versed in the details of the peculiarities of diffractive optics, and to provide direct links to the other relevant sections of this thesis. An extended discussion of the motivations and applicable situations for this work, particularly relating to the possible configurations shown in Section 5.5 has also been included.

5.2 Frequency domain modeling of phase noise coupling in a grating cavity

In order to quantitatively analyse the coupling of the phase noise introduced by grating displacement to the output ports of a diffractive cavity we perform a frequency domain analysis. By carrying out this analysis for the effect of a potential gravitational-wave signal and the noise

effect of lateral grating displacement we can obtain the signal to noise ratio (SNR) at all three output ports of the grating cavity. The aim is to find the port with the best SNR.

To compare the signal to noise ratio at the different output ports we first determine the grating coupling relations. We then review the mechanism of frequency sideband generation by a laterally displaced grating and identify the complex field amplitudes at the sideband frequency caused by (and in terms of) each carrier light field incident on the grating. Using the coupling relations we calculate each carrier light field incident on the grating in terms of a single external input carrier field. These are then used to determine the amplitude of the input sideband fields. Again utilising the coupling relations we obtain the amplitude of the sideband fields at the output ports. We next derive the amplitude of the potential gravitational wave signal sidebands at the output ports and divide by the grating displacement noise sidebands to obtain the signal to noise ratio.

5.2.1 Coupling relations of a static grating

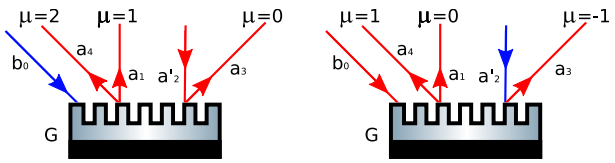

Figure 5.1: Input (b_0, a_2', shown blue) and output (a_1, a_3, a_4, shown red) light field amplitudes at a phase modulating grating in second-order Littrow-configuration in case A, and zeroth-order-Littrow configuration in case B (labels consistent with Figure 5.2). The diffraction orders μ for the blue-coloured input beams are shown.

The coupling relations of a single, static grating are given in [33], which is shown in Equation 3.9. We have adopted the simplified notation given in Equation 5.1 and applied the matrix to

the situation as shown in Figure 5.1.

$$\begin{pmatrix} a_4 \\ a_1 \\ a_3 \end{pmatrix} = \begin{bmatrix} G_2 & G_1 & G_0 \\ G_1 & \rho_0 & G_1 \\ G_0 & G_1 & G_2 \end{bmatrix} \begin{pmatrix} b_0 \\ a_2' \\ 0 \end{pmatrix}. \tag{5.1}$$

5.2.2 Coupling relations of an oscillating grating

Consider the case of an oscillating grating with two incident light fields shown in Figure 5.1: In case A the external input field has amplitude b_0 and in case B the field has amplitude a_2'. Frequency sideband generation for a grating oscillating with angular frequency ω_m and modulation index m will be demonstrated for output a_1 in case A. The oscillating grating causes phase modulation of the diffracted fields [52]:

$$a_1 = b_0 G_1 e^{-im\cos(\omega_m t)}. \tag{5.2}$$

The a_2' field does not appear, because it is in the $\mu = 0$ diffraction order and therefore not modulated. The complex field amplitude resulting can be expanded using the Bessel function $J_k(m)$ [35] [3], (see Section 2.1.3). In the case $m \ll 1$ it is sufficient to consider terms linear in m. It follows that only $k = -1, 0, 1$ need to be considered resulting in coefficients:

$$J_1(m) = m/2, \qquad J_0(m) = 1, \qquad J_{-1}(m) = -m/2. \tag{5.3}$$

Thus obtaining:

$$a_1(\omega) + a_1(\omega+\omega_m) + a_1(\omega-\omega_m) = b_0(\omega) G_1 \left(J_0(m) + iJ_1(m)e^{i\omega_m t} - iJ_{-1}(m)e^{-i\omega_m t} \right), \tag{5.4}$$

$$a_1(\omega)+a_1(\omega+\omega_m)+a_1(\omega-\omega_m)=b_0(\omega)G_1\left(1+i\frac{m}{2}e^{i\omega_m t}-i\frac{m}{2}e^{-i\omega_m t}\right). \quad (5.5)$$

When a grating is laterally oscillated to a maximum displacement of Δx the modulation index is given by $m=2\pi\Delta x\mu/d$, where d is the corrugation period of the grating and μ is the diffraction order, resulting in [52]:

$$a_1(\omega)+a_1(\omega+\omega_m)+a_1(\omega-\omega_m)=b_0(\omega)G_1\left(1+i\frac{\pi\Delta x\mu}{d}e^{i\omega_m t}-i\frac{\pi\Delta x\mu}{d}e^{-i\omega_m t}\right). \quad (5.6)$$

The terms including $e^{\pm i\omega_m t}$ are the sidebands. In the following we will compute the upper sideband amplitude in a cavity with the grating as the input coupler. The amplitude in front of the $e^{i\omega_m t}$ as computed in Equation 5.6, when coupled through the grating, are the sideband amplitudes for output a_1 in case A (a_{1A} [61], [62]). First order diffraction ($\mu=1$) from the grating is the coupling between b_0 and a_{1A}, obtaining:

$$a_{1A}(\omega+\omega_m)=ib_0(\omega)\frac{\pi\Delta x}{d}G_1e^{i\omega_m t}. \quad (5.7)$$

Having demonstrated the calculation of the sideband amplitude for output a_1 in case A we will now write the result for outputs a_3 and a_4 in case A obtaining a_{3A} and a_{4A} using the same method. Zeroth order diffraction ($\mu=0$) occurs between b_0 and a_{3A} and therefore no sidebands are generated by lateral grating displacement. Second order diffraction ($\mu=2$) occurs between b_0 and a_{4A} so the upper sideband amplitude obtained is:

$$a_{4A}(\omega+\omega_m)=ib_0(\omega)\frac{2\pi\Delta x}{d}G_2e^{i\omega_m t}. \quad (5.8)$$

Having dealt with case A we proceed to case B in Figure 5.1. Zeroth order diffraction ($\mu=0$) occurs between a_2' and a_{1B} and therefore no sidebands are generated. Negative-first order

diffraction ($\mu = -1$) occurs between a_2' and a_{3B} so the upper sideband amplitude obtained is:

$$a_{3B}(\omega + \omega_m) = -ia_2'(\omega)\frac{\pi\Delta x}{d}G_1 e^{i\omega_m t}. \tag{5.9}$$

First order diffraction ($\mu = 1$) occurs between a_2' and a_{4B} so the upper sideband amplitude obtained is:

$$a_{4B}(\omega + \omega_m) = ia_2'(\omega)\frac{\pi\Delta x}{d}G_1 e^{i\omega_m t}. \tag{5.10}$$

where a similar result can be obtained for the lower sideband if so required.

5.2.3 Coupling relations of an oscillating grating as Fabry-Perot cavity input optic

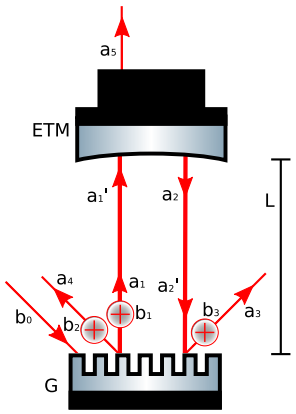

Figure 5.2: External input port b_0, internal input ports b_1, b_2, b_3 (marked by encircled addition symbols) and transfer ports a_q in a grating cavity.

To determine the transfer function for the generated noise sidebands to the output ports a_3, a_4 and a_5, and the input carrier field to ports b_1, b_2 and b_3 (in Figure 5.2) it is necessary to know the port to port coupling relations for our three-port coupled diffractive cavity of interest. Hence the coupling relations for the end mirror (ETM) with amplitude transmission coefficient

τ and amplitude reflection coefficient ρ must be known:

$$\begin{pmatrix} a_2 \\ a_5 \end{pmatrix} = \begin{bmatrix} \rho_2 & i\tau_2 \\ i\tau_2 & \rho_2 \end{bmatrix} \begin{pmatrix} a_1' \\ 0 \end{pmatrix}, \tag{5.11}$$

and for the space of length L between the grating and mirror:

$$\begin{pmatrix} a_1' \\ a_2' \end{pmatrix} = \begin{bmatrix} e^{-ikL} & 0 \\ 0 & e^{-ikL} \end{bmatrix} \begin{pmatrix} a_1 \\ a_2 \end{pmatrix}, \tag{5.12}$$

where $k = \omega/\mathrm{c}$, with ω the angular frequency of the light and c the speed of light. Hence it is possible to write the local coupling relations for the diffractive cavity shown in Figure 5.2 including the internal inputs discussed in Section 5.2.2 at ports b_1, b_2 and b_3, with all inputs at some arbitrary frequency:

$$\begin{aligned} a_1 &= b_0 G_1 + a_2' \rho_0 + b_1 \\ a_1' &= a_1 e^{-ikL} \\ a_2 &= a_1' \rho_2 \\ a_2' &= a_2 e^{-ikL} \\ a_3 &= b_0 G_0 + a_2' G_1 + b_3 \\ a_4 &= b_0 G_2 + a_2' G_1 + b_2 \\ a_5 &= a_1' i\tau_2. \end{aligned} \tag{5.13}$$

For the purposes of simplification, we define the resonance term of the cavity:

$$D(\omega) = \frac{1}{1 - \rho_2 \rho_0 e^{-2ikL}}, \tag{5.14}$$

where the frequency dependence on the RHS is provided by the wavevector $k = \omega/c$. By

performing some substitution we obtain the port to port relations only in terms of the input ports b and the fixed cavity parameters:

$$\begin{aligned}
a_1 &= (b_0 G_1 + b_1) D(\omega) \\
a_1' &= (b_0 G_1 + b_1) D(\omega) e^{-ikL} \\
a_2 &= (b_0 G_1 + b_1) D(\omega) \rho_2 e^{-ikL} \\
a_2' &= (b_0 G_1 + b_1) D(\omega) \rho_2 e^{-2ikL} && (5.15) \\
a_3 &= b_0 G_0 + (b_0 G_1 + b_1) D(\omega) \rho_2 e^{-2ikL} G_1 + b_3 && (5.16) \\
a_4 &= b_0 G_2 + (b_0 G_1 + b_1) D(\omega) \rho_2 e^{-2ikL} G_1 + b_2 && (5.17) \\
a_5 &= (b_0 G_1 + b_1) D(\omega) e^{-ikL} i\tau_2, && (5.18)
\end{aligned}$$

again, with all inputs at some arbitrary frequency.

5.2.4 Carrier field solution

From the carrier amplitude present at a_2' we can determine the sideband amplitudes at b_1 (Equation 5.7), b_2 (Equations 5.8 and 5.10) and b_3 (Equation 5.9). To obtain the carrier amplitude at a_2' it is necessary to solve Equation 5.15 with an example input field at port b_0 of arbitrary angular frequency and amplitude $p_0 e^{-i\omega_c t}$ and no field at the internal input ports b_1, b_2, b_3, hence obtaining:

$$a_2' = p_0 G_1 D(\omega_c) \rho_2 e^{-2ik_c L}, \quad (5.19)$$

where a_2' is the complex field amplitude of the carrier field. Since this solution is specific to the carrier, we distinguish it by using the subscript c, and perform some simplification by introducing

$B_c = D(\omega_c)\rho_2 e^{-2ik_c L}$, obtaining,

$$a_2' = p_0 G_1 B_c, \tag{5.20}$$

an alternative restatement of Equation 5.19.

5.2.5 Input sideband fields

There is now sufficient information to determine the sideband field amplitudes b_1, b_2 and b_3. These are the linear sums of the sidebands created by the oscillating grating with the impinging fields in b_0 and a_2'. Using Equations 5.7 through 5.10 and 5.20 we can now write:

$$b_1 = ip_0 G_1 \frac{\pi\Delta x}{d}, \tag{5.21}$$

$$b_2 = ip_0 G_2 \frac{2\pi\Delta x}{d} + ip_0 G_1^2 B_c \frac{\pi\Delta x}{d}, \tag{5.22}$$

$$b_3 = -ip_0 G_1^2 B_c \frac{\pi\Delta x}{d}, \tag{5.23}$$

where an input field of the amplitude p_0 at port b_0 has been used, and all fields were at the sideband frequency, allowing the $\exp(i\omega t)$ components to be canceled leaving b_1, b_2, b_3 as complex amplitudes.

5.2.6 Sideband fields at outputs

To determine the sideband field amplitude at the outputs a_3, a_4 and a_5 we consider the total field at the outputs (given by Equations 5.16 through 5.18). Setting the external input at port b_0 to zero leaves the internal inputs which are expressions of the sidebands. Equations 5.21 through 5.23 for the internal inputs are substituted into these output field equations allowing them to be compared in terms of the fixed cavity properties and p_0. The sideband fields

have different frequencies ($\omega_u = \omega_c + \omega_m$ for the upper sideband, $\omega_l = \omega_c - \omega_m$ for the lower sideband) and hence we address them separately, upper sideband first:

$$a_3 = ip_0 G_1^2 \frac{\pi\Delta x}{d}(B_u - B_c), \tag{5.24}$$

$$a_4 = ip_0 G_1^2 \frac{\pi\Delta x}{d}(B_u + B_c) + ip_0 G_2 \frac{2\pi\Delta x}{d}, \tag{5.25}$$

$$a_5 = -p_0 G_1 \frac{\pi\Delta x}{d} \frac{B_u}{\rho_2 e^{-ik_u L}} \tau_2. \tag{5.26}$$

a_3, a_4 and a_5 are complex amplitudes associated with the upper sideband at each output, whilst p_0 is the complex amplitude for the carrier field input in the port b_0. ω_u is the absolute frequency of the upper sideband and $B_u = D(\omega_u)\rho_2 e^{-ik_u L}$, analogous to our previously defined B_c. The calculation can be repeated to show that the lower sideband has the same magnitude as the upper at all output ports. We have thus computed the optical signal in all output ports generated by lateral motion of the grating.

5.3 Signal coupling in a grating cavity

In this section we consider the interaction between the cavity and a potential gravitational wave propagating perpendicular to the cavity axis. The gravitational wave imposes phase modulation sidebands onto the light-field inside the cavity.

The modulation index of the gravitational wave can be expressed in terms of an equivalent displacement of the mirror Δz resulting in modulation index $m = 4\pi\Delta z/\lambda$. The effect of this displacement appears at cavity internal input b_1 in Figure 5.2 with no input in ports b_2 and b_3. The port-to-port coupling relations given in Section 5.2.3, and specifically Equations 5.16 through 5.18 for the output ports, can be used since the cavity coupling relations are unaffected by the case chosen (displaced grating or incident gravitational wave).

The carrier field amplitude a_2' can still be used from Equation 5.20 as the carrier field is by definition unaffected when changing from the displaced grating to incident gravitational wave case. Hence from the modulation index and the carrier field present, again using the example input field of amplitude p_0, we obtain the internal input amplitude:

$$b_1 = ip_0 G_1 B_c \frac{2\pi\Delta z}{\lambda}. \tag{5.27}$$

Therefore the output amplitudes at the upper sideband frequency are:

$$a_3 = ip_0 G_1^2 \frac{2\pi\Delta z}{\lambda} B_c B_u, \tag{5.28}$$

$$a_4 = ip_0 G_1^2 \frac{2\pi\Delta z}{\lambda} B_c B_u, \tag{5.29}$$

$$a_5 = -p_0 G_1 \frac{2\pi\Delta z}{\lambda} \frac{B_c}{\rho_2 e^{-ik_c L}} \frac{B_u}{\rho_2 e^{-ik_u L}} \tau_2. \tag{5.30}$$

We have thus computed the optical signal in all output ports due to a potential gravitational wave signal.

5.4 Ratio of signal to noise at the outputs of a grating cavity

The ratio of gravitational wave signal to lateral grating displacement noise (the signal to noise ratio) will be used as a figure of merit to evaluate the interferometric length sensing performance of the different diffractive cavity output ports. In order to derive the SNR the absolute field amplitude in the gravitational wave case (Equations 5.28 through 5.30) will be divided by the absolute field amplitude in the grating lateral displacement case (Equations 5.24 through 5.26) for each output[1]. We obtain the following signal to noise ratios at the output port of the

[1]Note that for a standard cavity with equivalent finesse, the SNR will be infinity as in principle two-mirror cavity input mirrors are insensitive to lateral displacement. In reality however in any suspension system there

equivalent subscript:

$$\mathrm{SNR}_3 = \Lambda_{\mathrm{cav}} \frac{B_u}{B_u - B_c}, \tag{5.31}$$

$$\mathrm{SNR}_4 = \Lambda_{\mathrm{cav}} \frac{B_u}{B_u + B_c + 2G_2/G_1^2}, \tag{5.32}$$

$$\mathrm{SNR}_5 = \Lambda_{\mathrm{cav}} / \rho_2 e^{-ik_c L}, \tag{5.33}$$

with

$$\Lambda_{\mathrm{cav}} = \frac{2d\Delta z B_c}{\lambda \Delta x}. \tag{5.34}$$

These equations reveal the differences between the ratio of gravitational wave signal to lateral grating displacement noise for the three cavity output ports. This SNR is frequency independent for the case of the output port in transmission of the cavity end mirror (a_5), while the SNR at the other two output ports contain the modulation frequency dependent term B_u.

It was found that the SNR for the two output ports a_3 and a_4 includes the SNR from inside the cavity Λ_{cav}, multiplied by a fraction containing the different resonance factors for the carrier light field and the sidebands. Apart from the small G_2/G_1^2 term the only difference between Equations 5.31 and 5.32 is whether the resonance terms of the carrier and sideband in the denominator are added or subtracted. The important feature of these equations is that $B_u \approx B_c$ for small modulation frequencies (i.e. modulation frequencies within the cavity bandwidth). This brings the denominator in Equation 5.31 close to zero, thus strongly increasing the SNR at port a_3, i.e. resulting in a partial cancellation of the phase noise introduced from lateral grating displacement.

is always a coupling from lateral excitation to longitudinal displacement.

5.4.1 Numerical result

In this section we present a quantitative analysis for one example configuration. We choose a cavity length of $L = 3\,\mathrm{km}$, $\rho_2 = \sqrt{0.99995}$ (50 ppm power transmittance) and $\rho_0 = \sqrt{0.95}$. Demanding that the $\mu = 1$ diffraction order propagates normally to the grating for the input beam imposes the grating design requirement $d \leq 2\lambda$ [56]. The grating phase relations further impose the minimum possible value of $\eta_2 \geq 0.0127$. From [33] for minimum η_2 we find that $G_2 = -0.0127$. G_1 is fixed by the required cavity input parameters. Together G_1 and G_2 set the value of the last term in the denominator in Equation 5.32, and it is small compared to the other terms of the denominator. The cavity is set to resonance for the carrier light, imposing $e^{-2ik_cL} = 1$ and the modulation frequency ω_m of the lateral grating displacement is chosen to be 10 Hz.

Our interest focuses on the relative magnitude of the frequency sidebands. As in Chapter 3 we set $\Delta z/\Delta x = 1$ in order to compare potential gravitational-wave signal to the effect of grating displacement. Since we are dealing with complex field amplitudes for this analysis we take the absolute value of the ratios[2] given in Equations 5.31 to 5.33, yielding the following result:

$$|\mathrm{SNR}_3| = 3181, \tag{5.35}$$

$$|\mathrm{SNR}_4| = 79, \tag{5.36}$$

$$|\mathrm{SNR}_5| = 158. \tag{5.37}$$

In all output ports the SNR is found to be greater than one, as the cavity suppresses the displaced grating phase noise sidebands with a factor of 158 as seen in the transmitted output port; however, a factor of twenty improvement in the SNR can be obtained through the cancellation of input and output grating displacement sidebands in the forward-reflected (a_3) port compared

[2] The ratio contains a real part as well as an imaginary part. We assumed that the readout quadrature of each of the three output ports can be chosen individually by adding a proper local oscillator, i.e. performing a homodyne measurement.

to the transmitted (a_5) port.

For proposed interferometric gravitational wave detector layouts the end-mirror will be highly reflective (ρ_2 will be close to one) and therefore the complex field amplitudes for the potential gravitational wave signal (Equations 5.28 through 5.30) will obey the relations $a_3 \gg a_5$, $a_4 \gg a_5$. There will be approximately half the signal in the forward-reflected port with good SNR, half will be in the back-reflected port with poor SNR and very little will be in the transmitted port.

In a next step, instead of a single frequency of interest, we consider modulation frequencies covering the full detection band of gravitational wave detectors. As SNR_3 and SNR_4 are frequency dependent, we normalise them to SNR_5 and plot them over frequency to obtain Figure 5.3.

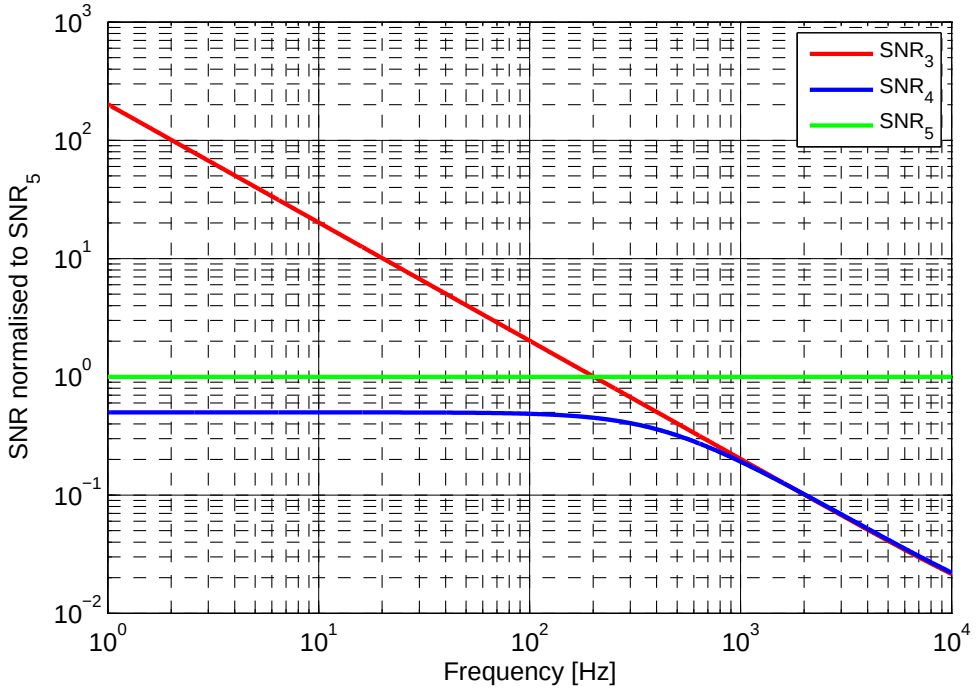

Figure 5.3: Signal to noise ratio of gravitational wave equivalent mirror displacement and lateral grating displacement at the three different output ports of a grating gravity. All traces are normalized to SNR_5.

At low modulation frequencies where the sidebands are to a good approximation resonant in

the cavity, imposing $B_u \approx B_c$ the forward-reflected port (a_3) has good cancellation between the input and output sidebands generated by the grating lateral displacement. This results in high SNR compared to the transmitted port (a_5). In the back-reflected port (a_4) summation occurs instead of cancellation and hence the SNR is lower than in the transmitted port. As the modulation frequency diverges from the cavity resonance, the sidebands do resonate in neither gravitational-wave nor the grating lateral displacement case as B_u trends to zero. Thus the sideband contribution generated when the carrier field exits the cavity (the B_c terms in the denominator of Equations 5.31 and 5.32) dominates causing the SNR of the reflected ports to converge below the level of the transmitted port.

5.4.2 Suspension requirements

To ease comparison of the results derived above we determine the potential suspension requirements for a grating cavity used as an arm cavity within the planned Advanced Virgo detector. Using the current Advanced Virgo design sensitivity [63] we plot in Figure 5.4 the corresponding tolerable lateral grating motion for each of the three potential readout ports of the grating arm cavity.

We have found that we can relax by a factor of twenty at 10 Hz (Figure 5.4) the suspension requirement for the the un-suppressed transmitted (a_5) port by utilizing the forward-reflected (a_3) port for the signal readout. This suppression depends on cancellation between noise sidebands which we have calculated for the case of the lateral suspension of the grating. It is likely that this suppression will also apply to the input pointing (as misaligned input pointing also changes the alignment of the field circulating in the cavity [64]) and hence the alignment stability requirement for the injection optics. However sidebands due to end-mirror angular misalignment are not suppressed, as they are only generated when light is coupled out of the cavity. In Chapter 3 and published in Freise et al [52] it was found that without suppression of the grating lateral

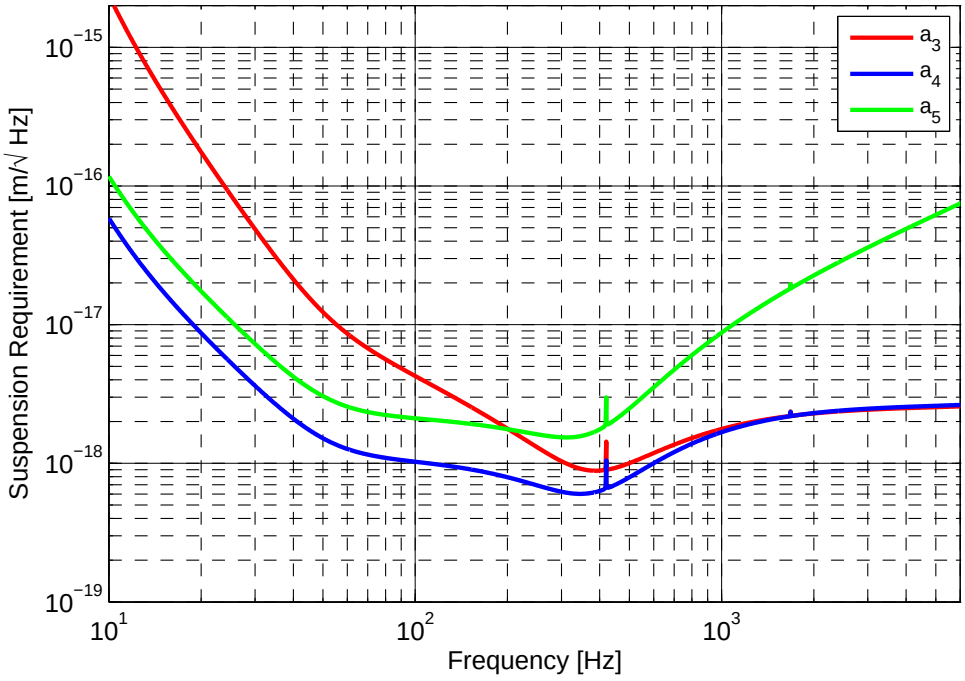

Figure 5.4: Suspension requirement for the maximum tolerable lateral grating displacement that is necessary to achieve the Advanced Virgo design sensitivity. The suspension required strongly depends on the actual readout port as well as the frequency of interest. At low frequencies the phase noise suppression in port a_3 allows significant relaxation of the required suspension isolation. The narrow peak around 410 Hz is due to a resonance in the Advanced Virgo design, not a grating effect.

displacement using a three-port-coupled grating cavity rather than a standard two-mirror cavity, in the Advanced Virgo case, requires improving the end-mirror angular alignment suspension requirement by five orders of magnitude. The equivalent improvement required for the injection optics alignment stability and grating lateral suspension can be relaxed by a factor of twenty by choosing the forward-reflected port for the signal readout, at least in the lower frequency band. Above 200 Hz this geometrical effect no longer suppresses coupling of lateral grating displacement in the forward-reflected port. In this case it is preferred to use the transmitted port for readout; however, the fixed SNR set by the cavity properties is not beaten, and the system is no longer entirely reflective.

The encouraging results presented above increase the application prospects of grating coupled Fabry-Perot cavities in large-scale gravitational wave detectors, but the problem raised by Freise et al of end-mirror angular alignment remains.

5.5 Future work on interferometer configurations

As has been discussed the motivation for the work undertaken in this chapter was twofold. First, to determine if there was a possible cancellation of the grating displacement phase - which we found that there was - and second, to allow future work on grating interferometer configurations, into which the calculations of this chapter can simply be included as required - i.e. to allow the three-port-coupled configured grating Fabry-Perot cavity to be used as a single optical element. In Figure 5.5 we sketch diagrams of some possible configurations, and a standard transmissive Michelson (a) for comparison. In (b) we see a configuration where the forward-reflected ports are dumped or detected immediately, possibly for use as supplementary control readouts. They could only become gravitational wave detection ports as suggested earlier in this chapter (since they experience the phase noise cancellation discussed therein) if some virtual interferometry (electronic combination of signals) is used. In (c) the outputs are combined with a beam splitter

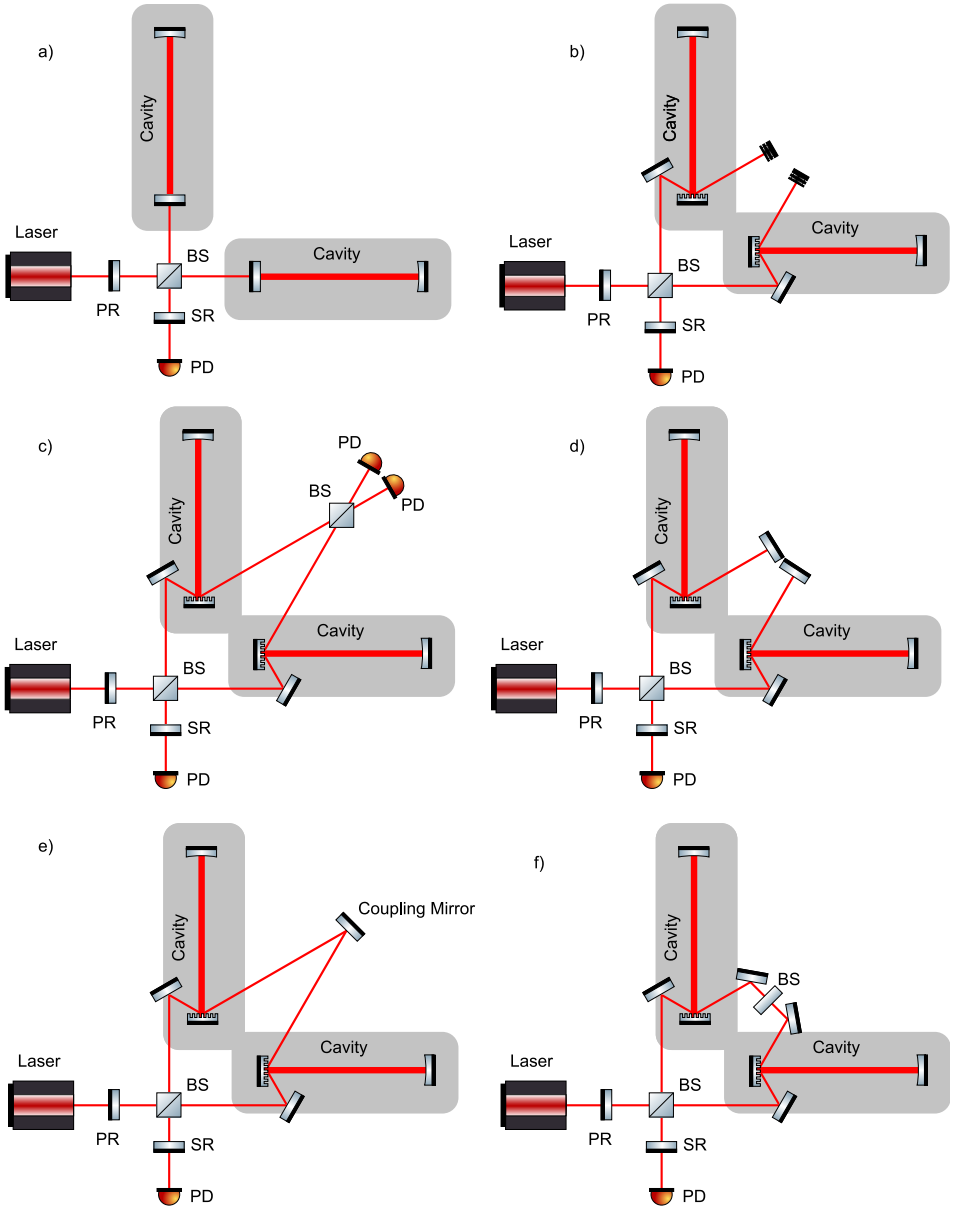

Figure 5.5: Sketch diagram of various possible all-reflective interferometer configurations; (a) for comparison standard transmissive Michelson with both power and signal recycling is shown labeled; (b) a dual three-port-coupled second-order-Littrow configuration design, with the forward-reflected output ports dumped or detected; (c) introducing a beam splitter between these forward-reflected output ports allows their signals to be combined; (d) introducing mirrors recoupling the forward-reflected light back into its cavity of origin; (e) introducing a mirror that recouples the forward-reflected light from one cavity back into the other cavity, with the phase relation set by the position of this mirror; (f) introducing a beam splitter that allows some of the forward-reflected light to be coupled into the other cavity, and some back into its cavity of origin, with the proportion being set by its reflectivity and transmittance.

before detection. It might then be possible to perform demodulation and detection at this port, with a reduced need for virtual interferometry. These options all involve detection, and therefore destruction, of the light from the forward-reflected output ports.

It is possible to recirculate this forward-reflected light, by reflecting its own cavity as shown in option (d). Alternatively, the light could be reflected and injected into the other cavity via its forward-reflected output port as in option (e). Diagrammatically, it can be seen that in this configuration the interferometer shares some of the characteristics of both the Michelson (where light is returned from the individual arms) and a Sagnac (where light circulates around the interferometer). The parallel is far from exact; however, and this configuration should have some interesting properties. The alert reader will notice that option (f) is essentially option (d), when the beam splitter reflectivity is unity; and option (e) when the beam splitter is wholly transmissive. It may be though that a partial recirculation and partial circulation to the other cavity is the most useful condition. This extensive configuration work can now be undertaken, using the results of this thesis. With all these recirculating configurations, the forward-reflected ports can still be used as detection ports in transmission of whatever optics are used there, even without the need to introduce additional pick-off beams.

5.6 Summary and Outlook

An additional noise source for diffractive interferometers is lateral grating displacement relative to the beam causing path-length differences that couple phase-noise into the gravitational wave detection channel, as discussed in Chapter 3 and demonstrated in Chapter 4. The grating-cavity end-mirror angular alignment suspension requirement derived therein (five orders of magnitude higher than that required by a two-mirror cavity), and associated likely increases in injection optic pointing and lateral grating stability were a significant impetus against using diffractive cavities.

The diffraction order (μ) dependence of the frequency sideband amplitude and the symmetry inherent in the three-port-coupled grating cavity suggested that the phase noise generated on input to the cavity might cancel with the phase noise generated at output from the cavity.

To determine the effect we carried out a frequency domain analysis to calculate the coupling of lateral grating displacement to the different output ports of a three-port-coupled grating cavity. For the output port in forward-reflection of the grating we found a suppression of phase noise originating from lateral grating displacement over the transmitted port, resulting in a factor of twenty relaxation in the lateral displacement isolation requirement at 10 Hz. This will likely also apply to the injection optics pointing stability. This factor will increase with a wide cavity bandwidth and hence the noise suppression will be greater in cavities of lower finesse.

The work carried out in this chapter will be useful for future working diffractive Fabry-Perot cavities. Particularly, whichever authors explore exciting configuration ideas for interferometers utilising diffractive Fabry-Perot cavities, such as those detailed in Section 5.5, will find the contents of this chapter necessary to make full noise appreciations for their designs.

Chapter 6

CONCLUSIONS

The theme of this thesis is alignment issues in diffractive interferometers. Diffraction gratings were proposed to allow all-reflective interferometer configurations, particularly potentially replacing the input optics of Fabry-Perot arm cavities. This is expected to reduce thermal noises, particularly thermoelastic, thermorefractive, Brownian and thermal lensing in the substrates of transmissive interferometers. Due to the additional input-output ports of some diffractive optical elements, and particularly the three-port coupled grating Fabry-Perot cavity, new and exciting interferometer configurations become possible with the use of diffraction gratings.

These new optical configurations also give rise to a new noise source. Lateral displacement of a diffraction grating, or of a laser beam on a diffraction grating, causes a phase change to occur in the diffracted orders of the beam. For gravitational wave interferometers with Fabry-Perot arm cavities this causes physical lateral grating displacement, input optic pointing (laterally displacing the input beam) and cavity alignment (laterally displacing the cavity eigenmode) to couple phase noise into the gravitational wave signal channel. The isolation requirements against end-mirror tilt for a Virgo-esque gravitational wave interferometer have been computed in Chapter 3 and found to be five orders of magnitude more severe for the three-port grating

cavity compared to a standard two-mirror cavity, and eight orders of magnitude more severe for the two-port grating cavity compared to a two-mirror cavity. The three-port cavity performs better than the two-port cavity because the three-port cavity suppresses this lateral displacement phase noise by the cavity finesse, whilst the two-port cavity does not. Hence configuration is vital for determining the noise performance of interferometers featuring diffractive components. The long lever of the arm cavities in an interferometric gravitational wave detector means that small end-mirror tilts create large lateral displacements of the cavity eigenmode on the input optic. Alignment control for such cavities is already difficult, and it is presently unrealistic to impose the additional alignment precision diffractive optics would require. Presented in Chapter 4 is experimental work carried out by myself on an optical bench at the University of Birmingham, where I implemented both a two-mirror and a three-port coupled grating cavity and induced end-mirror tilt in order to measure this phase-noise effect. This measurement did not clearly show the expected ratio between the two-mirror and three-port grating cavities due to residual longitudinal motion of the end-mirror tilt actuator. Alternatively, this may be thought of as insufficient enhancement of the tilt to lateral displacement due to the short lever arm of a tabletop cavity. The overall configured shape of a diffractive interferometer and its details such as length are critical to determining the extent of this phase-noise source.

Gratings are now being considered for other applications, such as the use of grating waveguide coatings, where diffraction is used within a single optical element to directly replace a single optic such as a cavity input mirror without changing the cavity configuration. This does not eliminate the substrate but rather substantially reduces the thickness of the high-reflective dielectric coatings that standard mirrors require. It has recently been found that the thermorefractive and thermoelastic noise in such coatings dominates that in the substrate. Since gratings are considered for a variety of applications, it is important to understand all the features of grating systems. This thesis deals with alignment-to-phase coupling in extensive new detail, comprising both theoretical and experimental work. Theoretical work in Chapter 5 has

shown that for a three-port coupled grating cavity that the phase noise from physical lateral displacement of the grating, and from input optic pointing, experiences a partial cancellation in the forward-reflected output port, and a summation in the back-reflected port. Using the Joint Interferometer Facility 10 m prototype at (and in collaboration with) the University of Glasgow we performed a set of measurements detailed in Section 4.9 that both confirmed the expected noise level, and its reduction in the forward-reflected output port. This was possible because the suspended optics provide a much quieter interferometer and also allow very precise steering and actuation of individual degrees of freedom, following the extensive work of the Glasgow group on mirror suspension systems and orthogonalisation of their actuation system. Future work will investigate other interferometer configurations made possible by diffractive optics, probably using the powerful, relatively low-noise tool of the three-port grating cavity as a complete optical element. Some sketches that take advantage of the noise cancellation in the forward-reflected port have been included herein. In another direction, the work of this thesis will be applied to grating waveguide coatings, and other diffractive elements under consideration, to determine if and how much phase noise is created by their internal diffraction orders.

. . .

Appendix A

ELECTRONIC CIRCUIT DIAGRAMS

Much of the electronics utilised in the experimental Chapter 4 of this thesis were built by the author using the facilities of the University of Birmingham, usually to slightly modified designs of H. Vahlbruch and B. Hage from the AEI Max Planck Institute for Gravitation Physics in Hannover. The only notable exception is the matrice box for control of the 3-axis piezo actuator responsible for tilting the end-mirror, which was of my own design.

A.1 Local Oscillator

The local oscillator consisted of an oscillator source box driving the EOM directly with the modulation (schematic shown in Figure A.1 and A.2), and another channel suitable for directing to the mixer for demodulation purposes. So that many photodetectors could be used to perform Pound-Drever-Hall locking schemes from the same laser source a dedicated splitter was then used to create multiple buffered outputs (schematic shown in Figures A.3 and A.4). Since only one of these is required per optical table this author was not required to manufacture them. The work of building the oscillator box was carried out by electronics technician M. Beasley

and the splitter box was by fellow doctoral student A. Perreca [26], although some adjustment of the output power to match output of the local oscillator channel used to the required mixer input power was necessitated through adjustment of potentiometer P1 in Figure A.4.

A.2 Photodetectors

Two photodetectors were used, JPD1 for the offset locking (schematics shown in Figure A.5) where R1 $= 2\,k\Omega$, C19 $= 10\,$pF, R5 $= 0.3\ k\Omega$, R13 $= 1\,k\Omega$, R9 $= 0.14\,k\Omega$, R9 $= 0.3\,k\Omega$ (only the lower channel was used). A separate photodetector JPD3 was used for the Pound-Drever-Hall locking (schematics shown in Figures A.6 and A.7) where R7 $= 1\,k\Omega$ and R5 $= 82\,k\Omega$ giving a gain of 3.5; R11 $=2\,k\Omega$ and R10 $= 82\,k\Omega$ giving gain 1.5.

A.3 12 MHz Mixer

Only a single 12 MHz mixer was built conforming to the specification shown in Figure A.8, A.10 and A.10. In the last of these the Local Oscillator input was applied at a power of 0 dBm and therefore was input at X5 rather than LO-In. Therefore resistors R9, R10 and R11 were also not installed. Since only a single mixer channel was required the channel B, although it was entirely installed, was not used and sheet four of the circuit diagram entirely relating to it has been omitted.

A.4 Offset Box

Fortuitously an offset box that had been constructed previously by Dr. S. Chelkowski was available for my use in offset locking the cavity. The schematic for the offset box is shown in

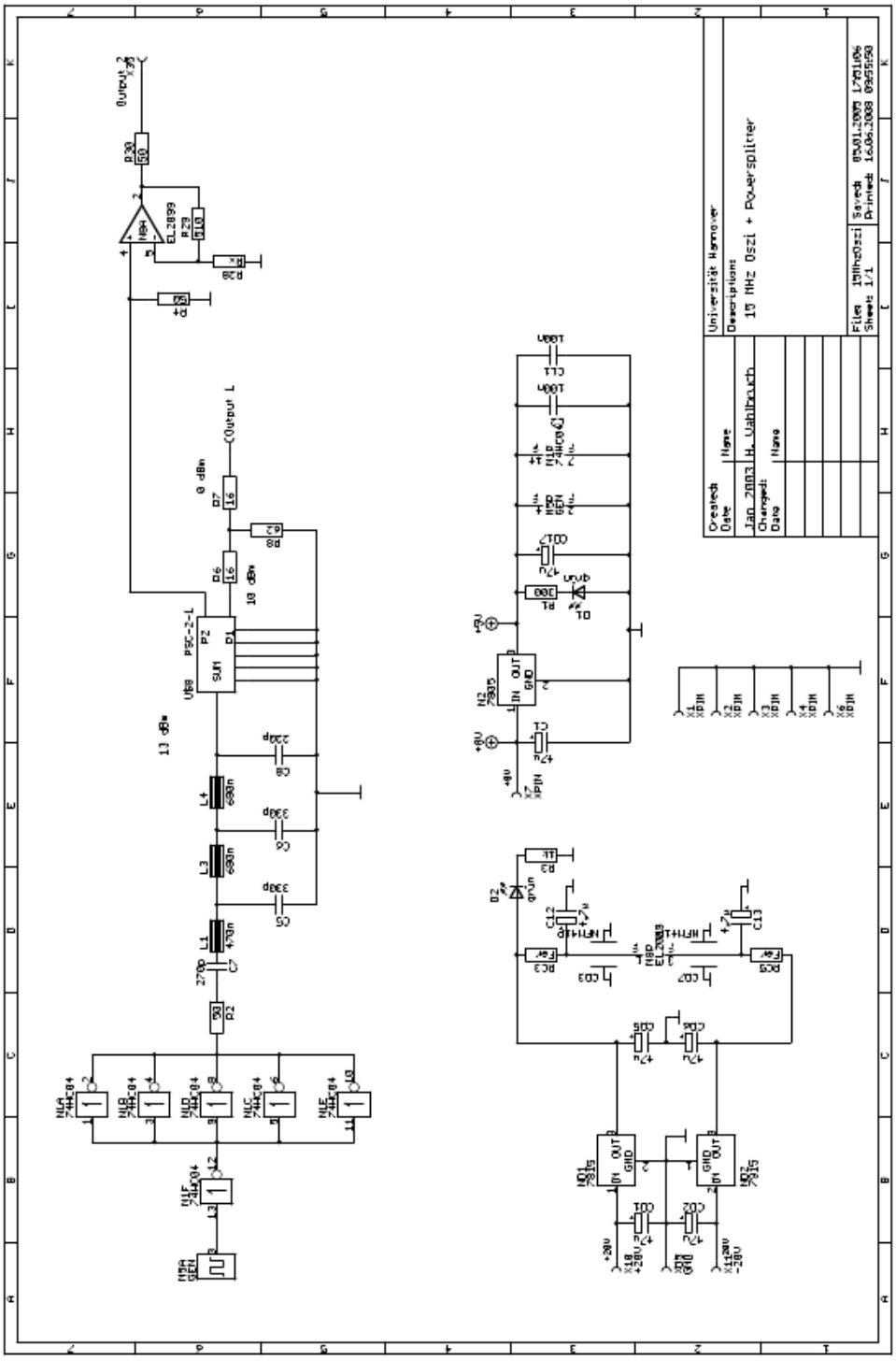

Figure A.1: Local Oscillator Source Box 1/1.

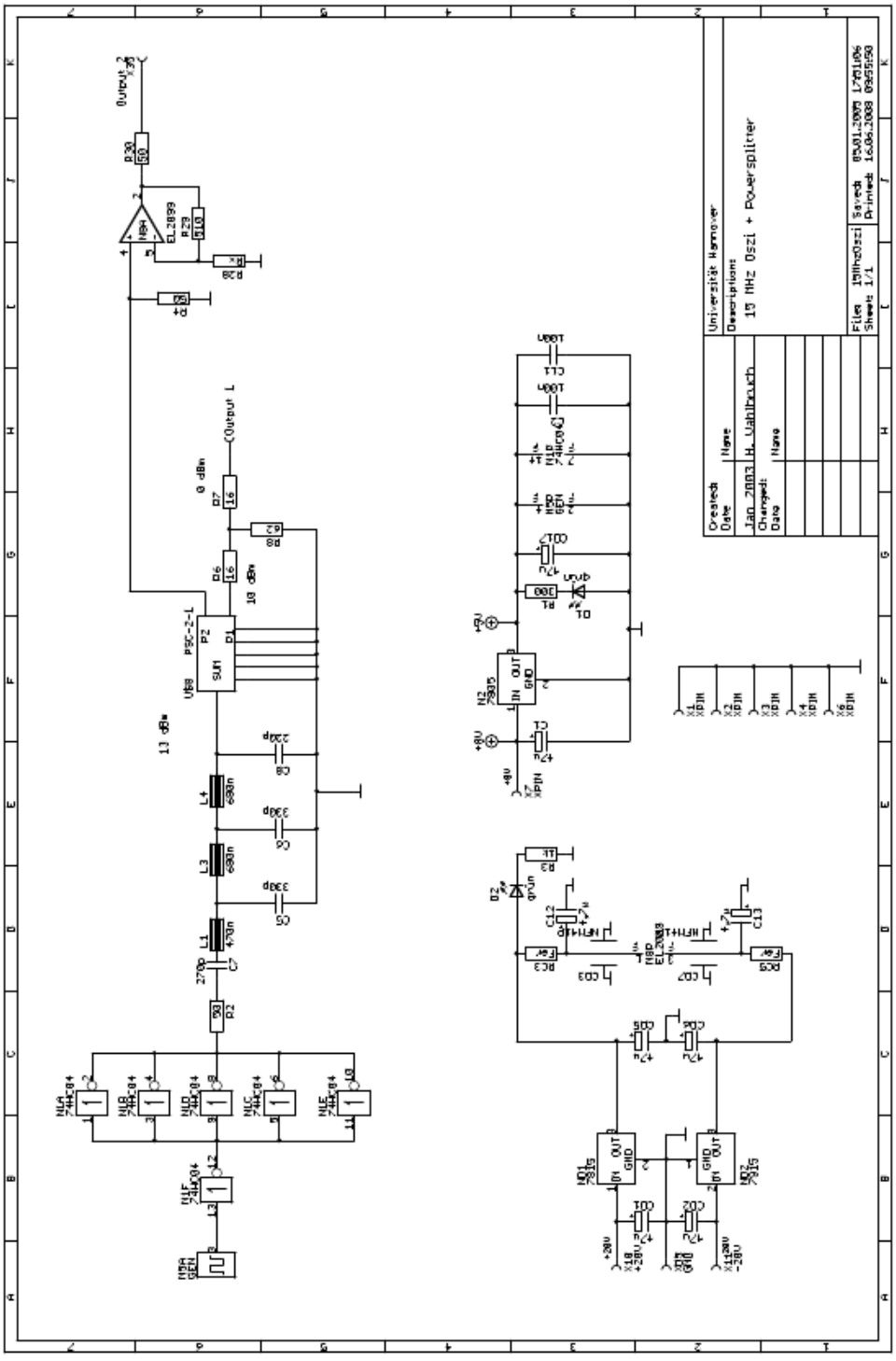

Figure A.2: Local Oscillator Source Box 1/1.

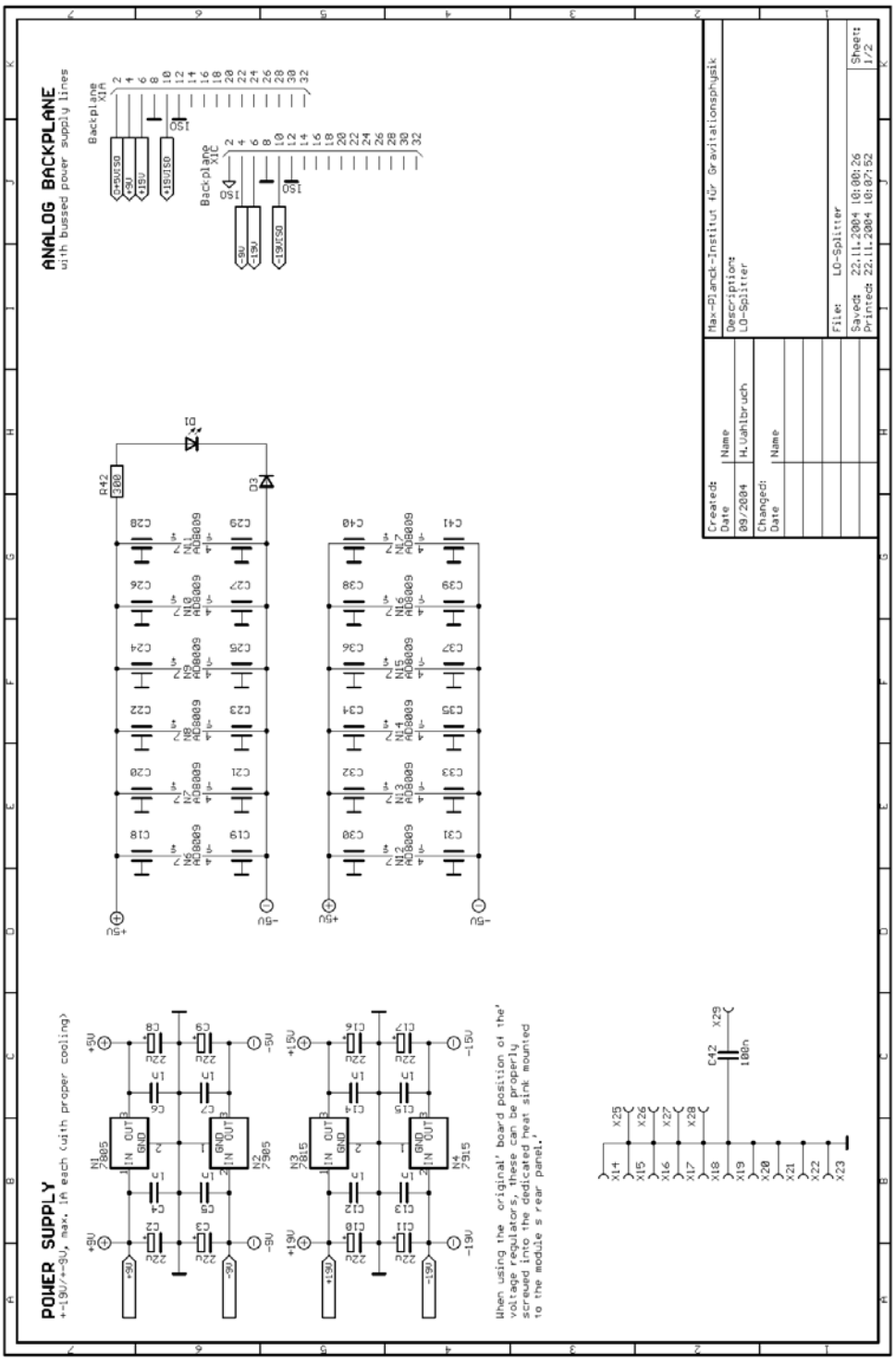

Figure A.3: Local Oscillator Splitter Box 1/2.

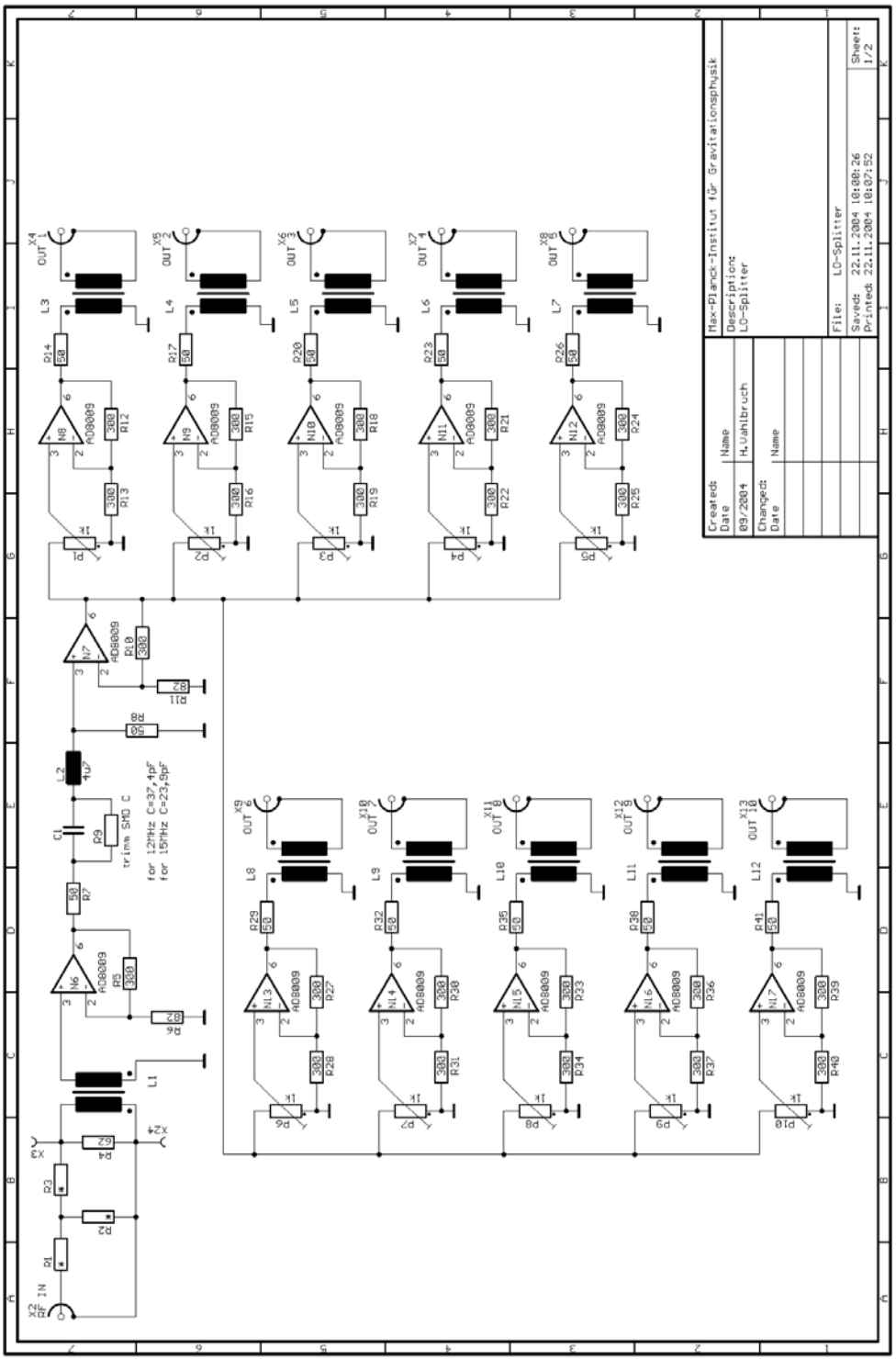

Figure A.4: Local Oscillator Splitter Box 2/2.

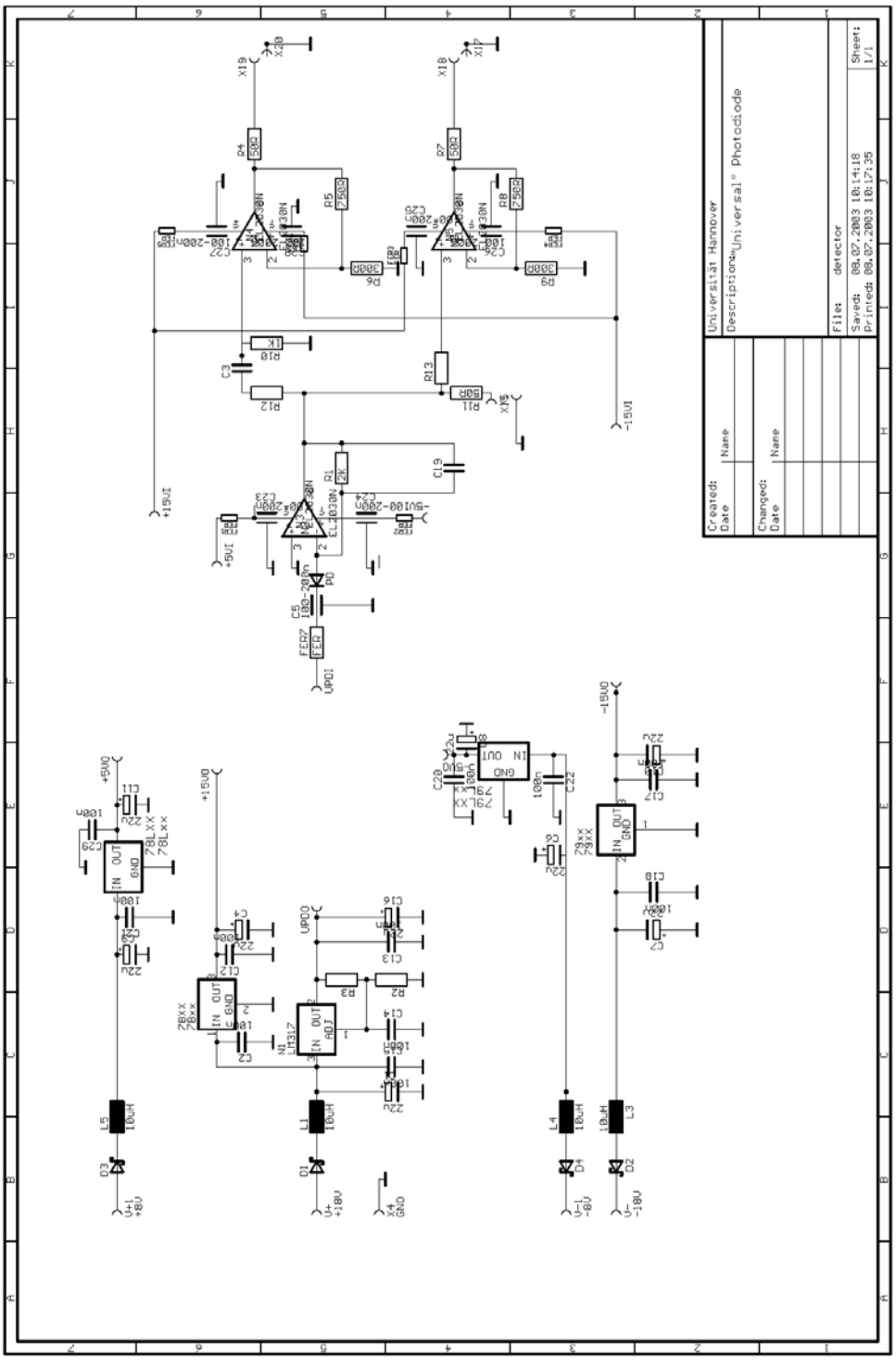

Figure A.5: Universal (broadband) Photodetector used in transmission (for offset locking) 1/1.

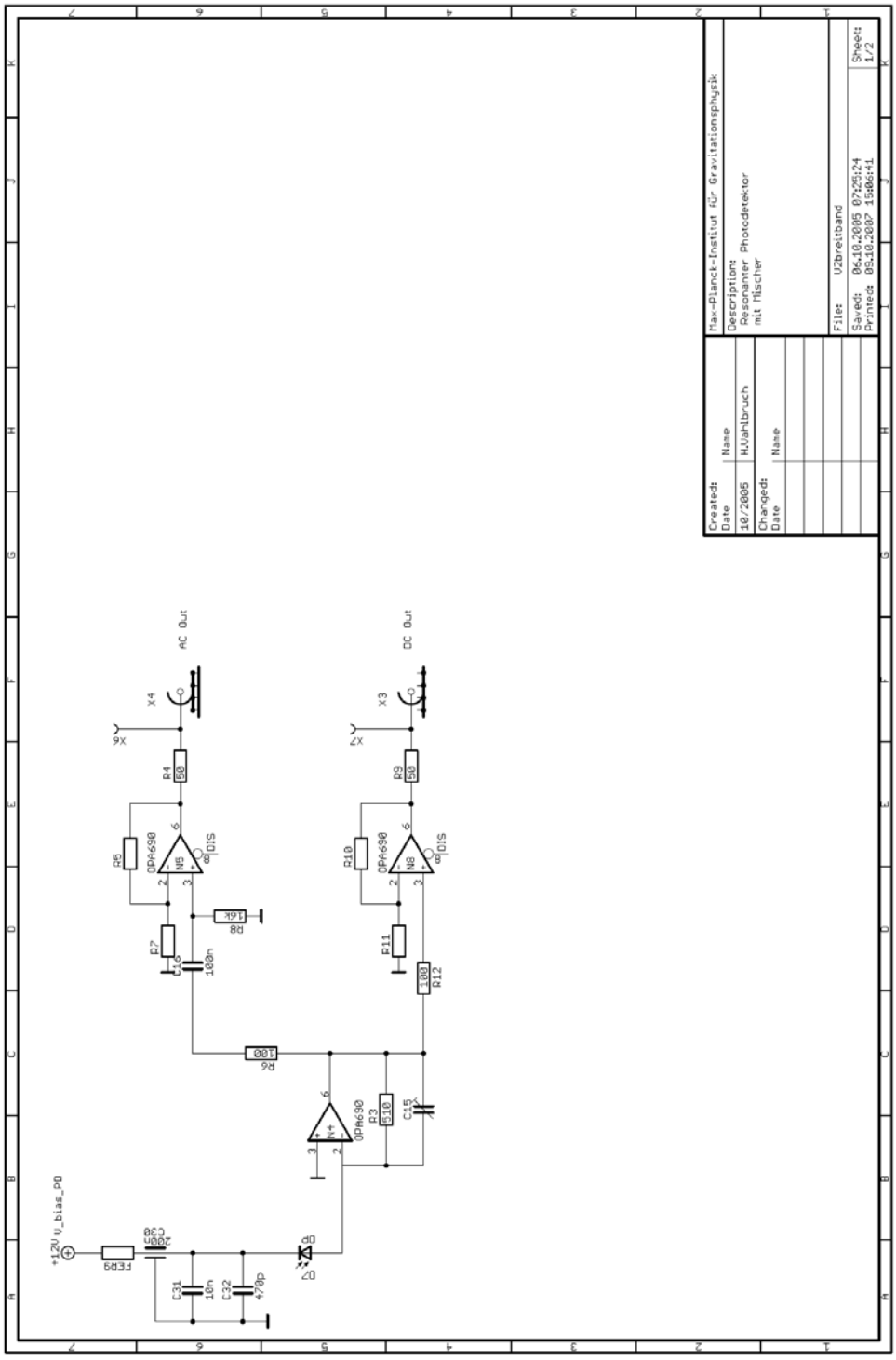

Figure A.6: Broadband Photodetector used in back-reflection (for PDH locking) 1/2.

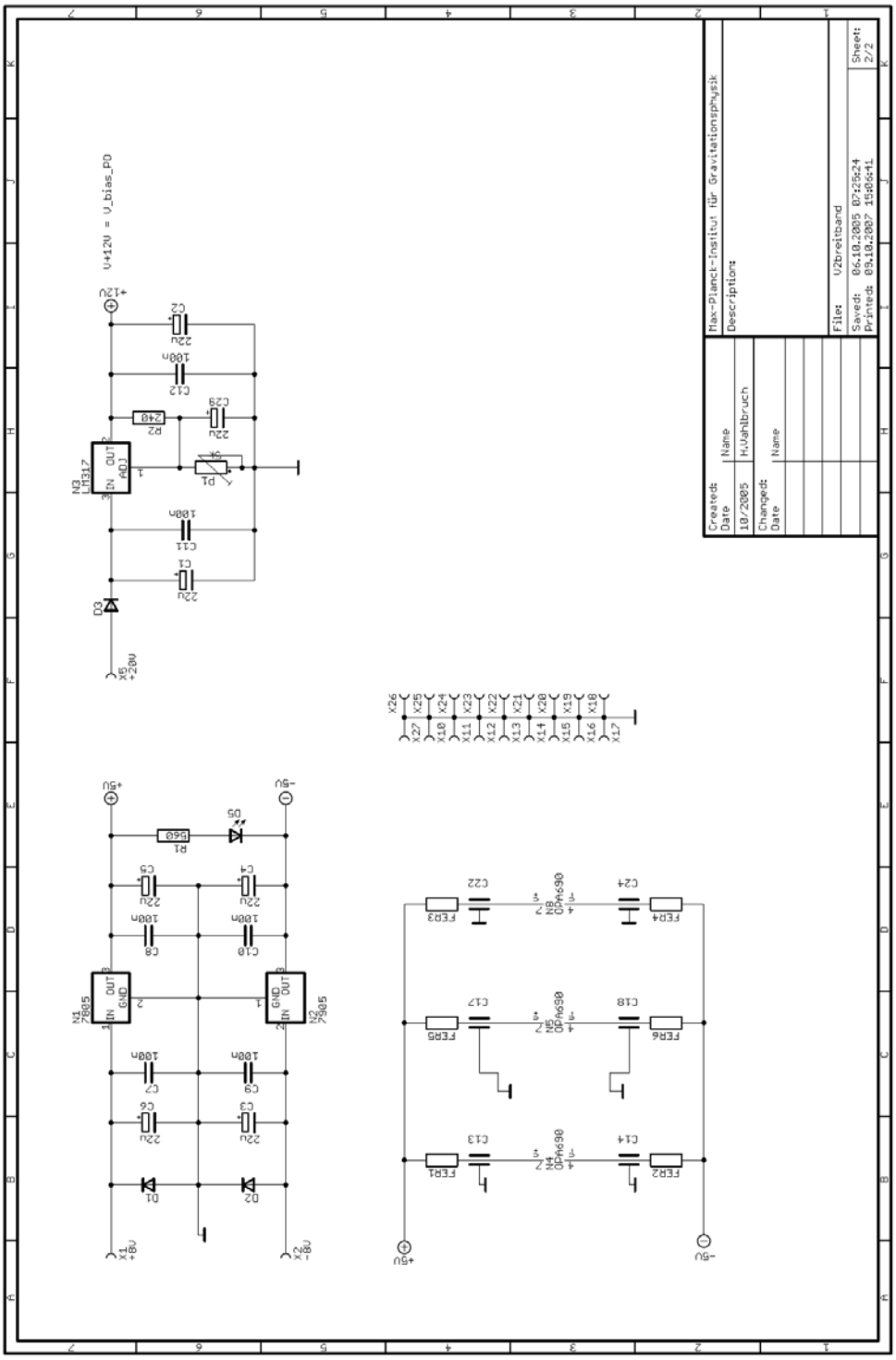

Figure A.7: Broadband Photodetector used in back-reflection (for PDH locking) 2/2.

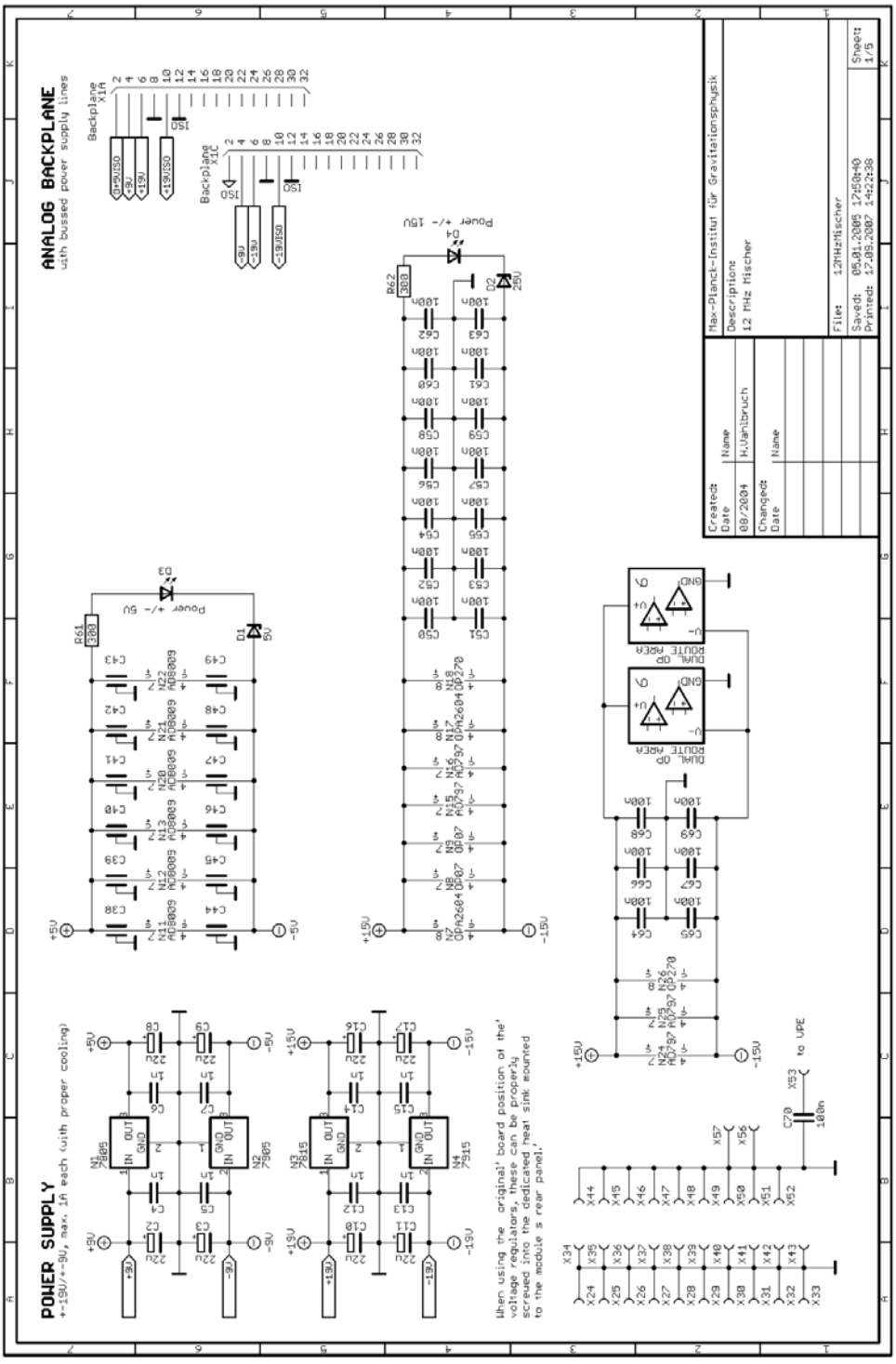

Figure A.8: 12 MHz Mixer 1/3.

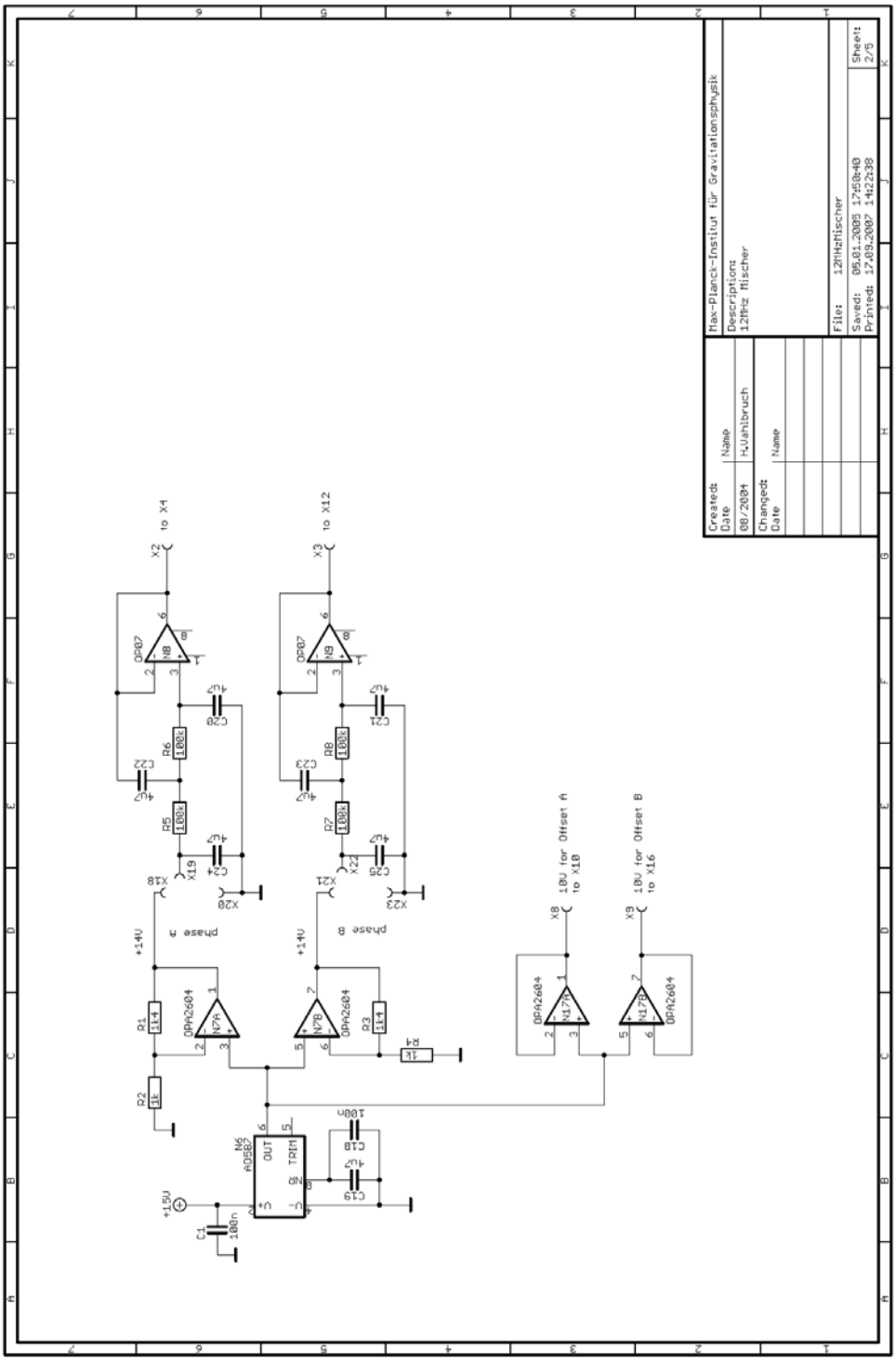

Figure A.9: 12 MHz Mixer 2/3.

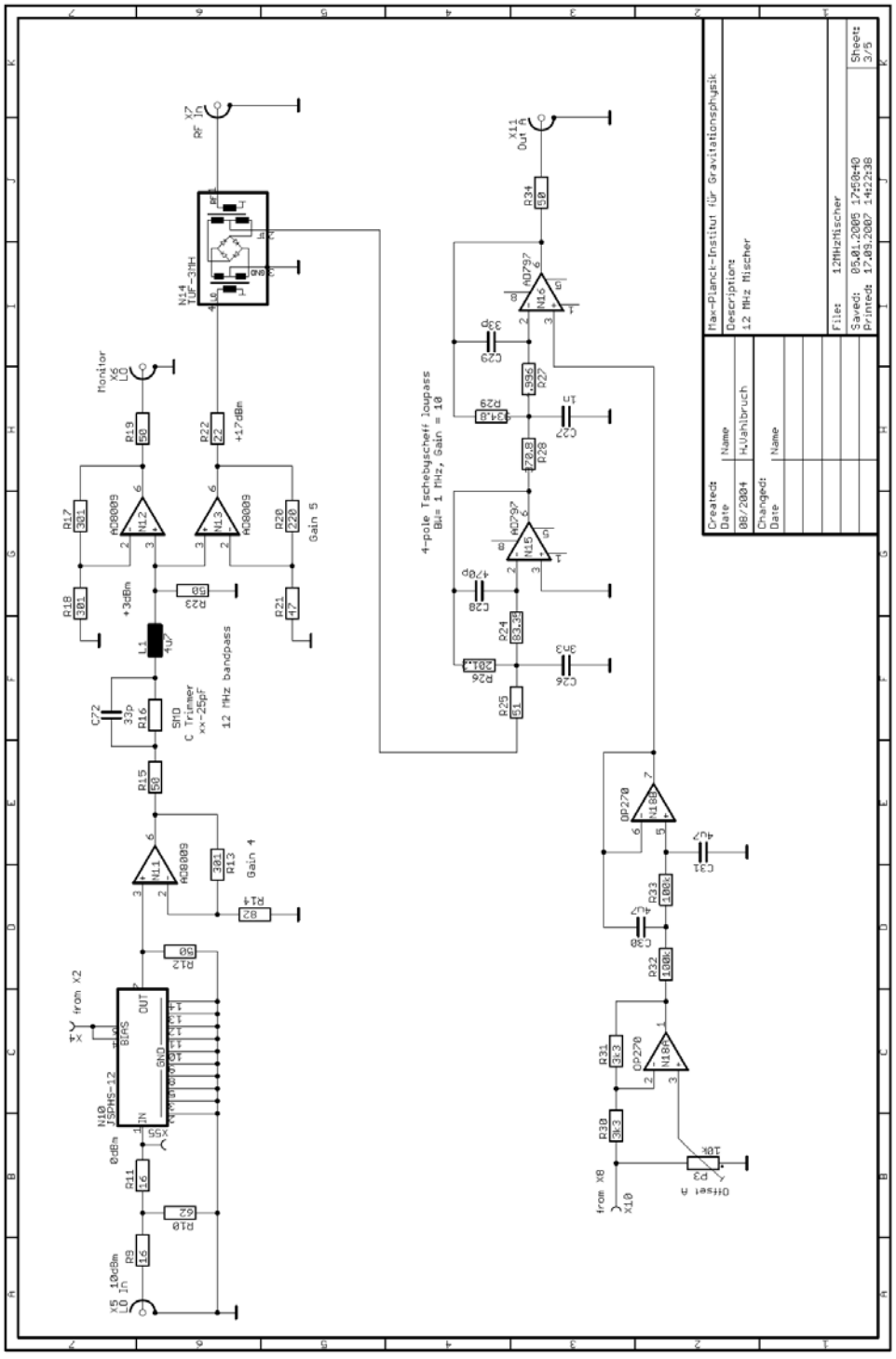

Figure A.10: 12 MHz Mixer 3/3.

Figures A.11 and A.12.

A.5 Buffer Box

The schematic of the buffer-box is shown in Figure A.13

A.6 Servo

The servo JMH3 was built according to the specification shown in Figures A.14 through A.17. The integrators (universal I and D) detailed in Figure A.16 were modified several times, but the final settings were that all integrators used a 1.1 $k\Omega$ resistor and integrator one a 1 μF capacitor giving corner frequency 144 Hz, integrator two a 47 nF capacitor giving corner frequency 3.06 kHz and integrator three a 22 nF capacitor giving corner frequency 6.5 kHz.

A.7 High Voltage Amplifier

The high-voltage amplifier conformed to the specifications shown in Figures A.18 through A.21. This applies for the high voltage amplifier used to lock the cavity by providing laser frequency feedback. A commercial, three-channel model was used to provide amplification to the matrice box signals used to drive the three-axis piezo end-mirror actuator.

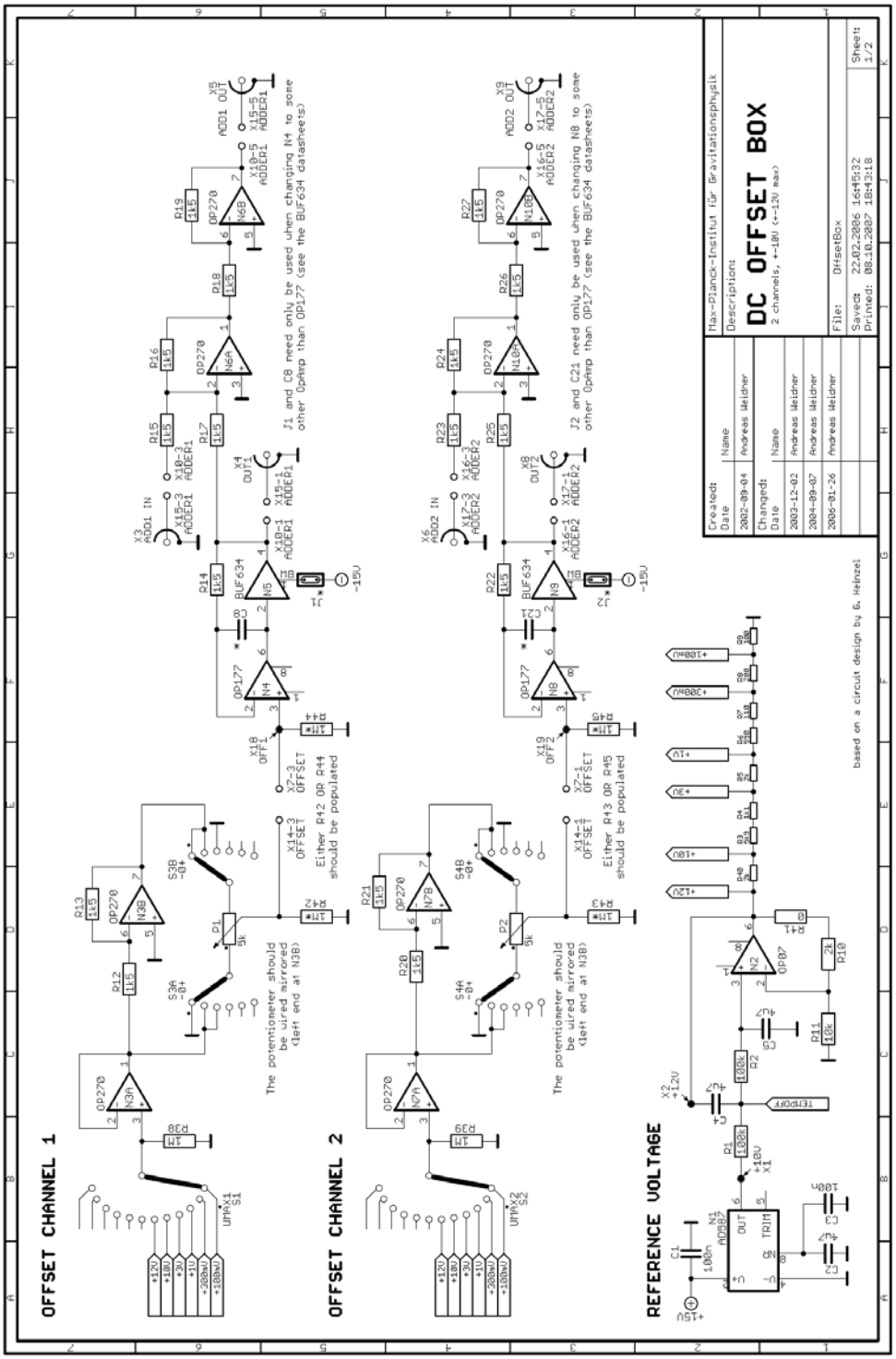

Figure A.11: Offset Box 1/2.

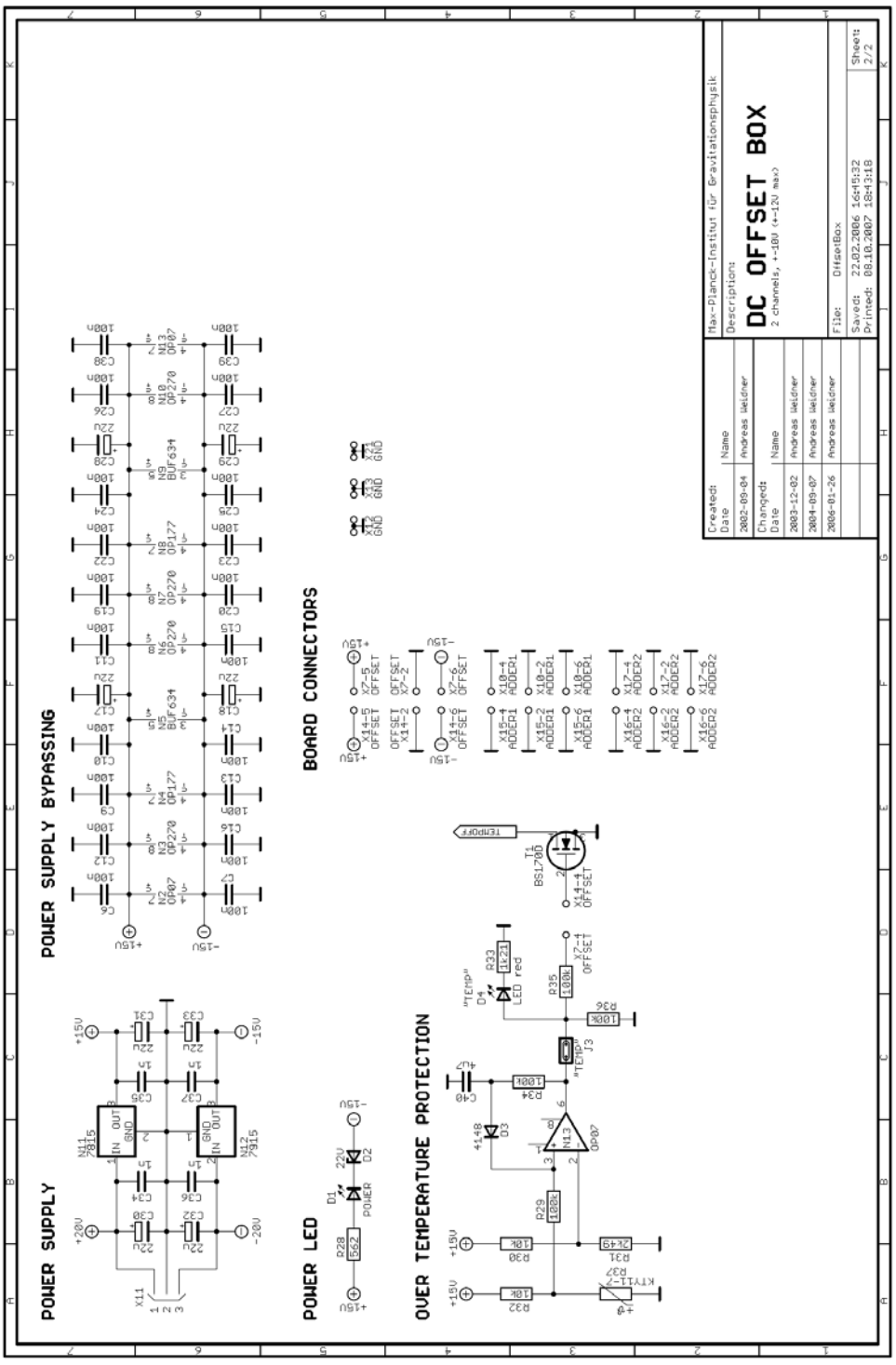

Figure A.12: Offset Box 2/2.

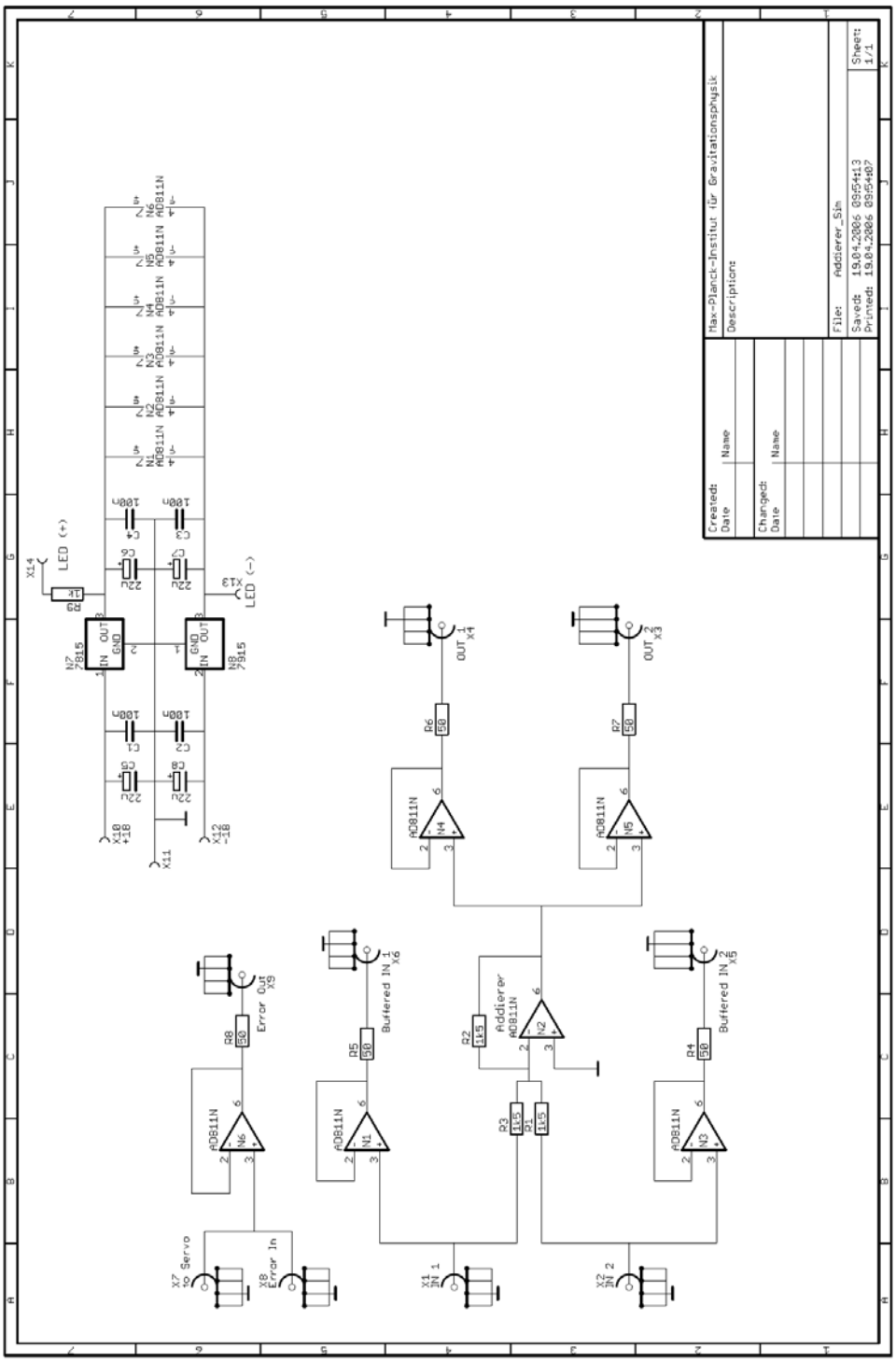

Figure A.13: Buffer Box 1/1.

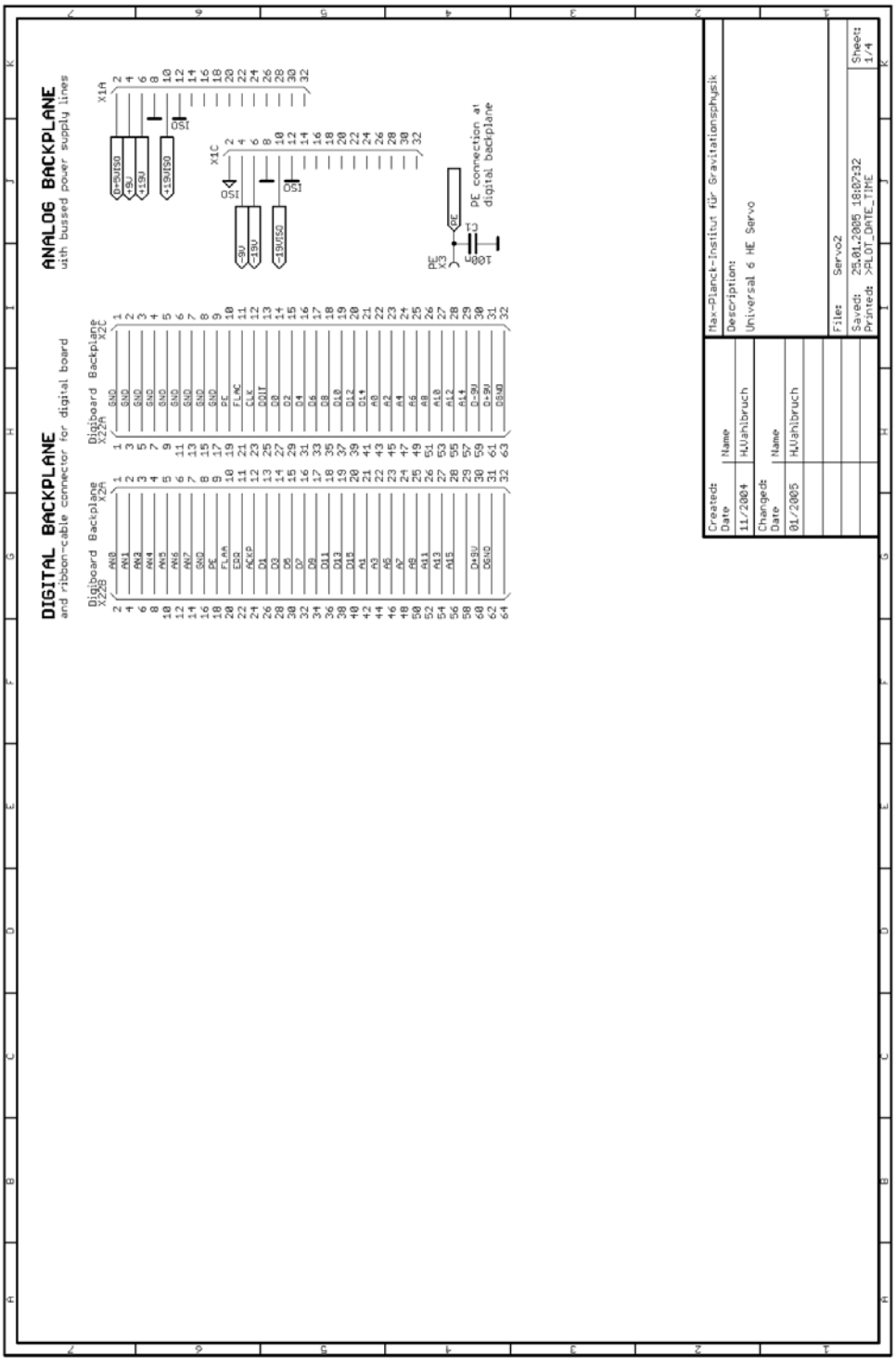

Figure A.14: Servo 1/4.

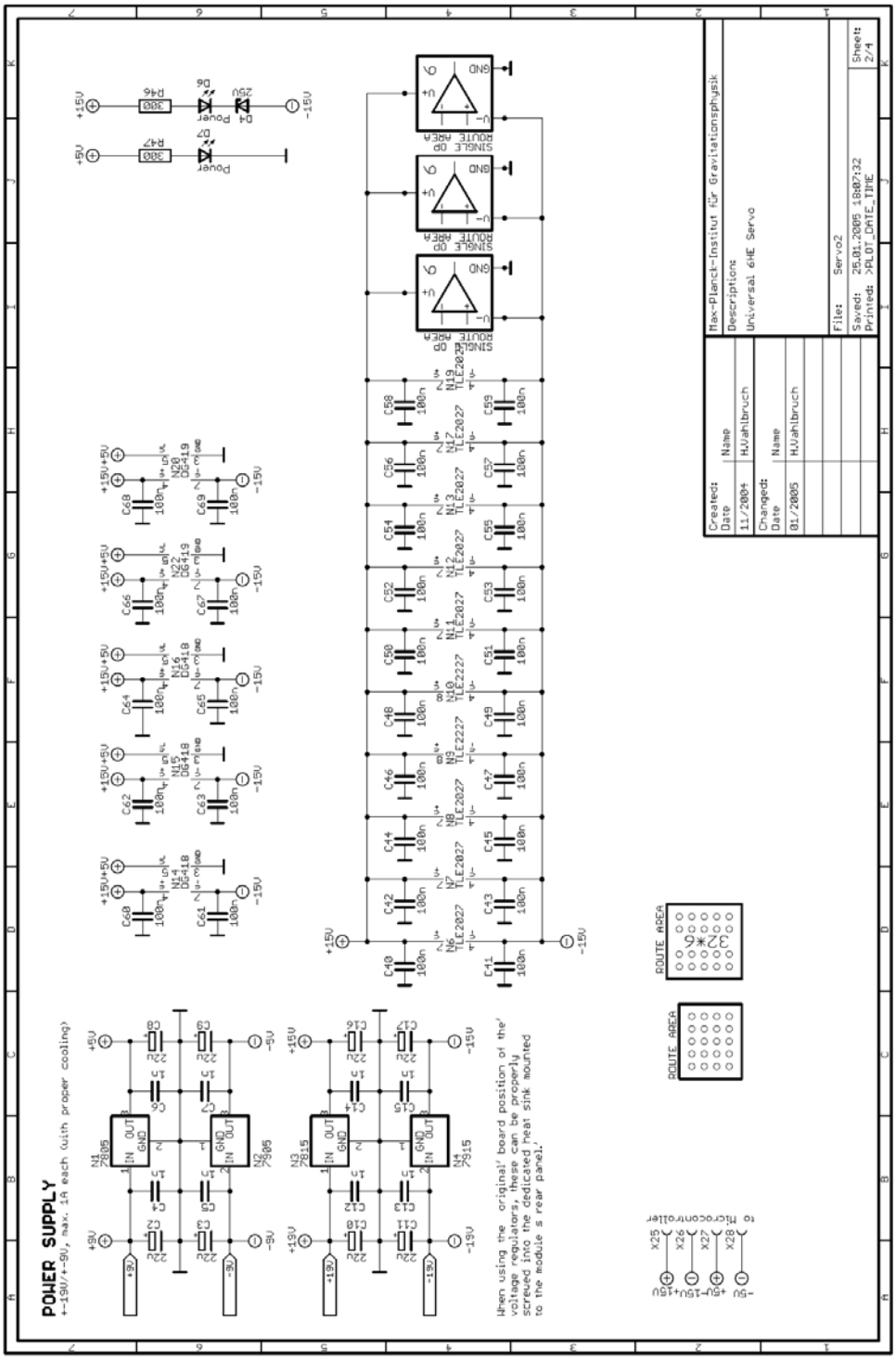

Figure A.15: Servo 2/4.

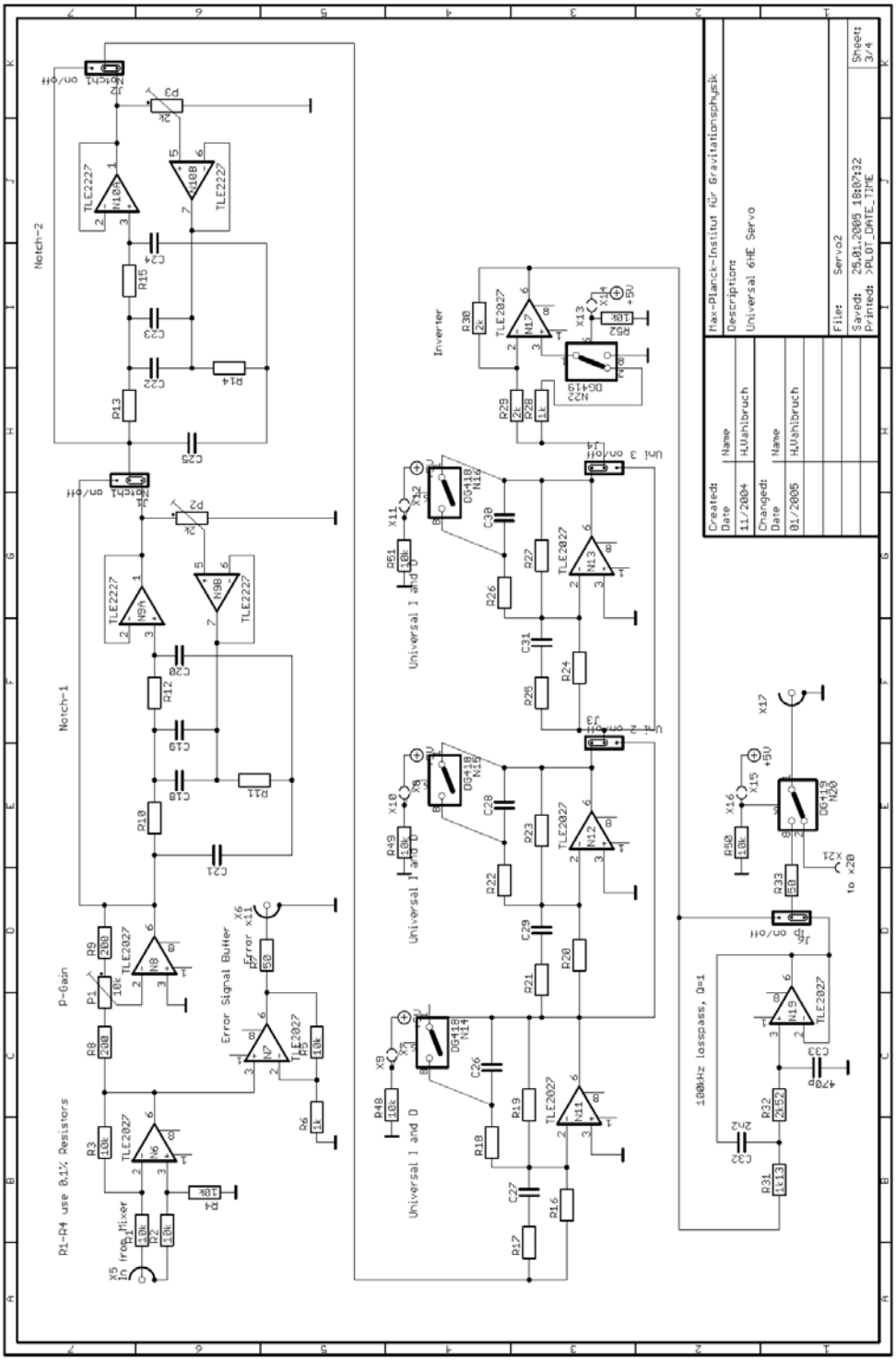

Figure A.16: Servo 3/4.

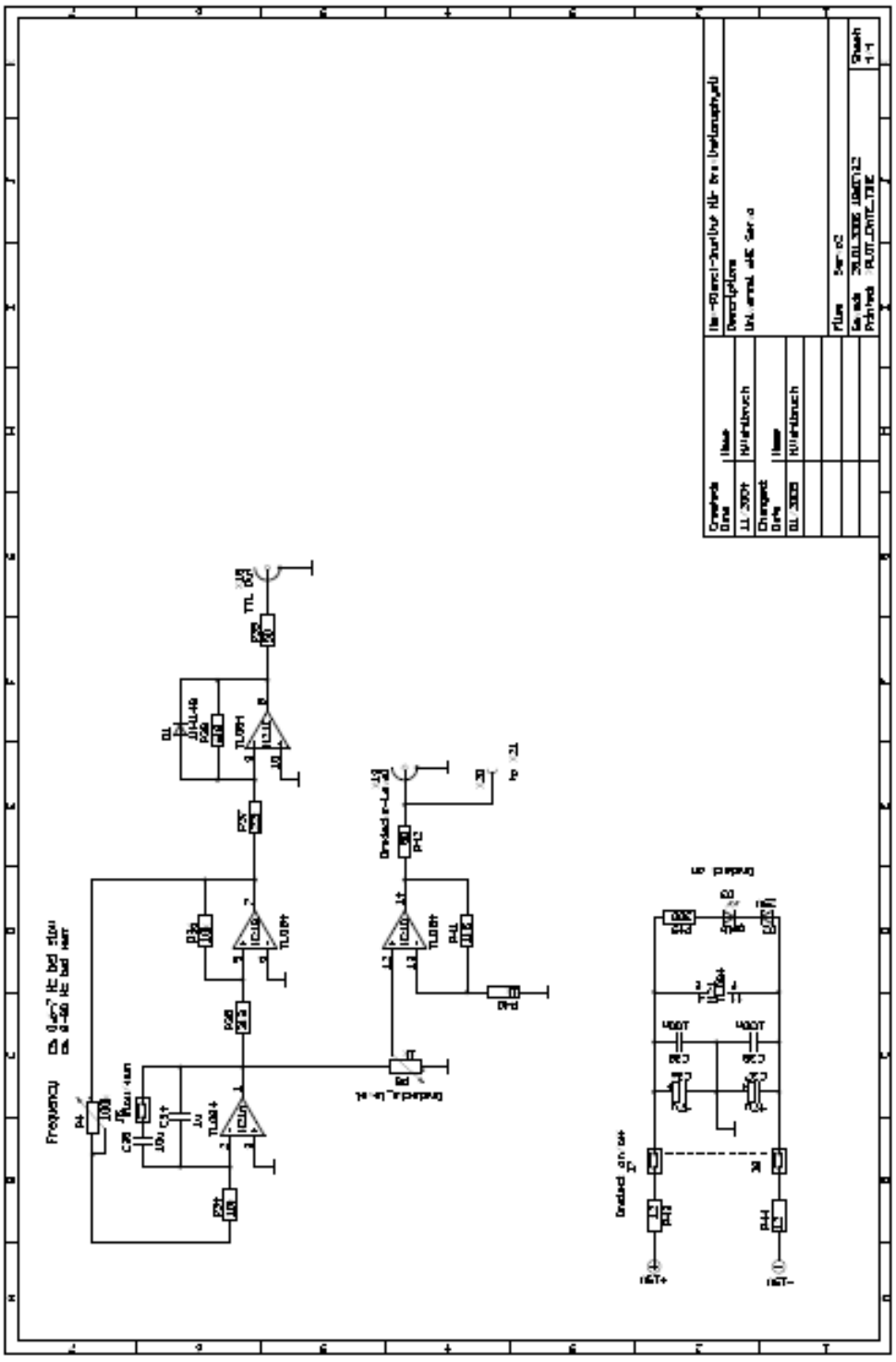

Figure A.17: Servo 4/4.

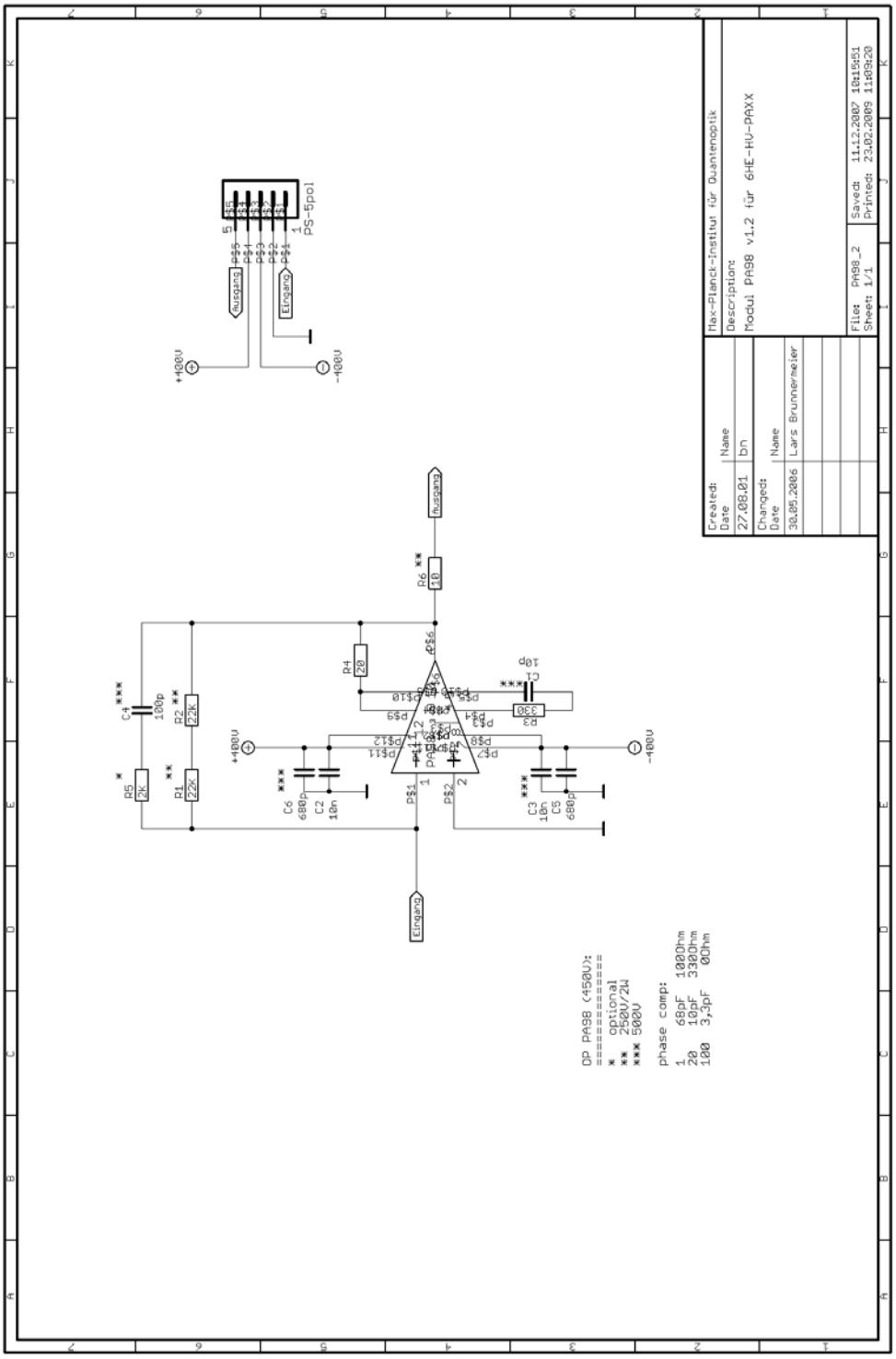

Figure A.18: High Voltage Amplifier 1/4.

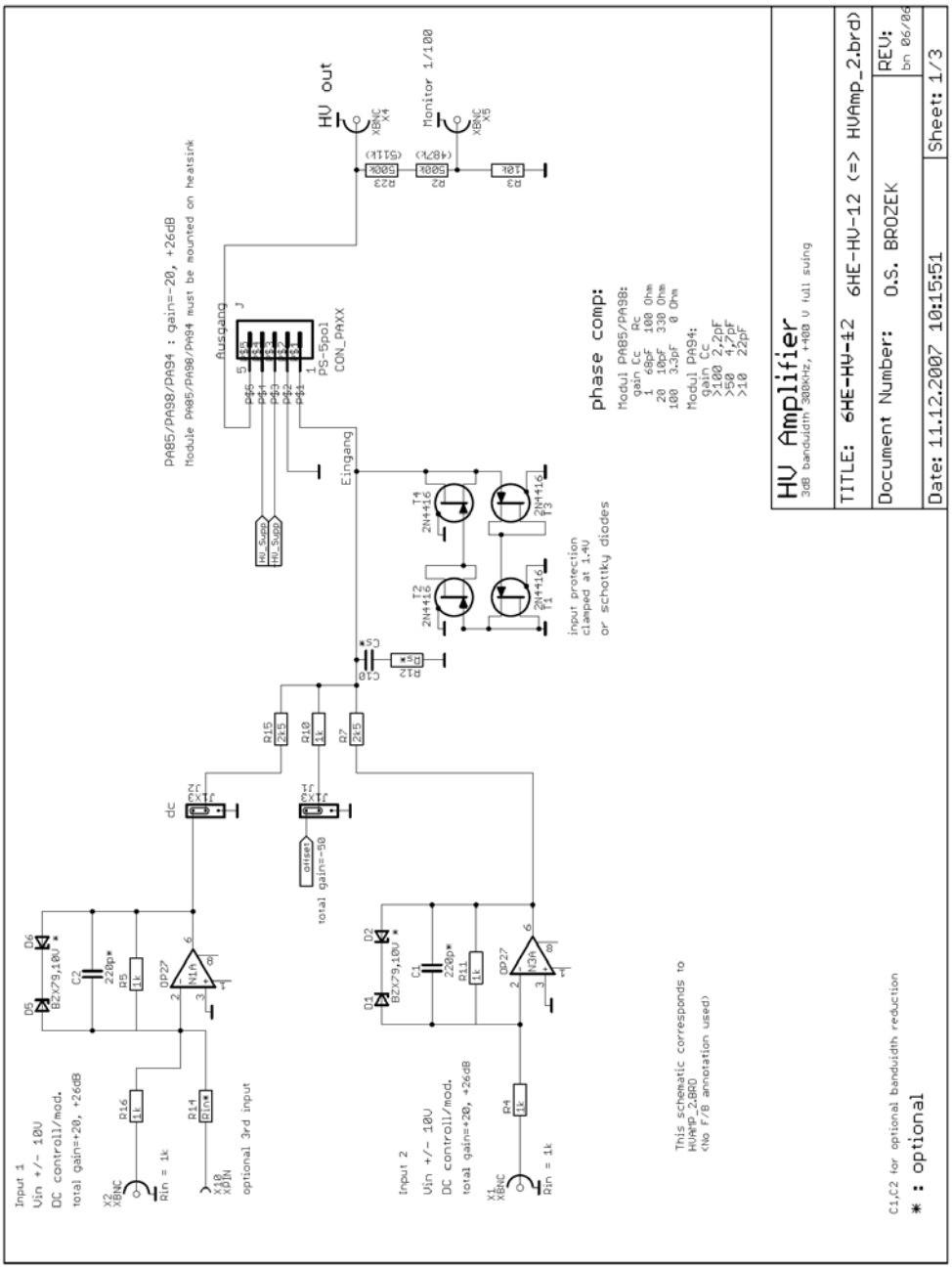

Figure A.19: High Voltage Amplifier 2/4.

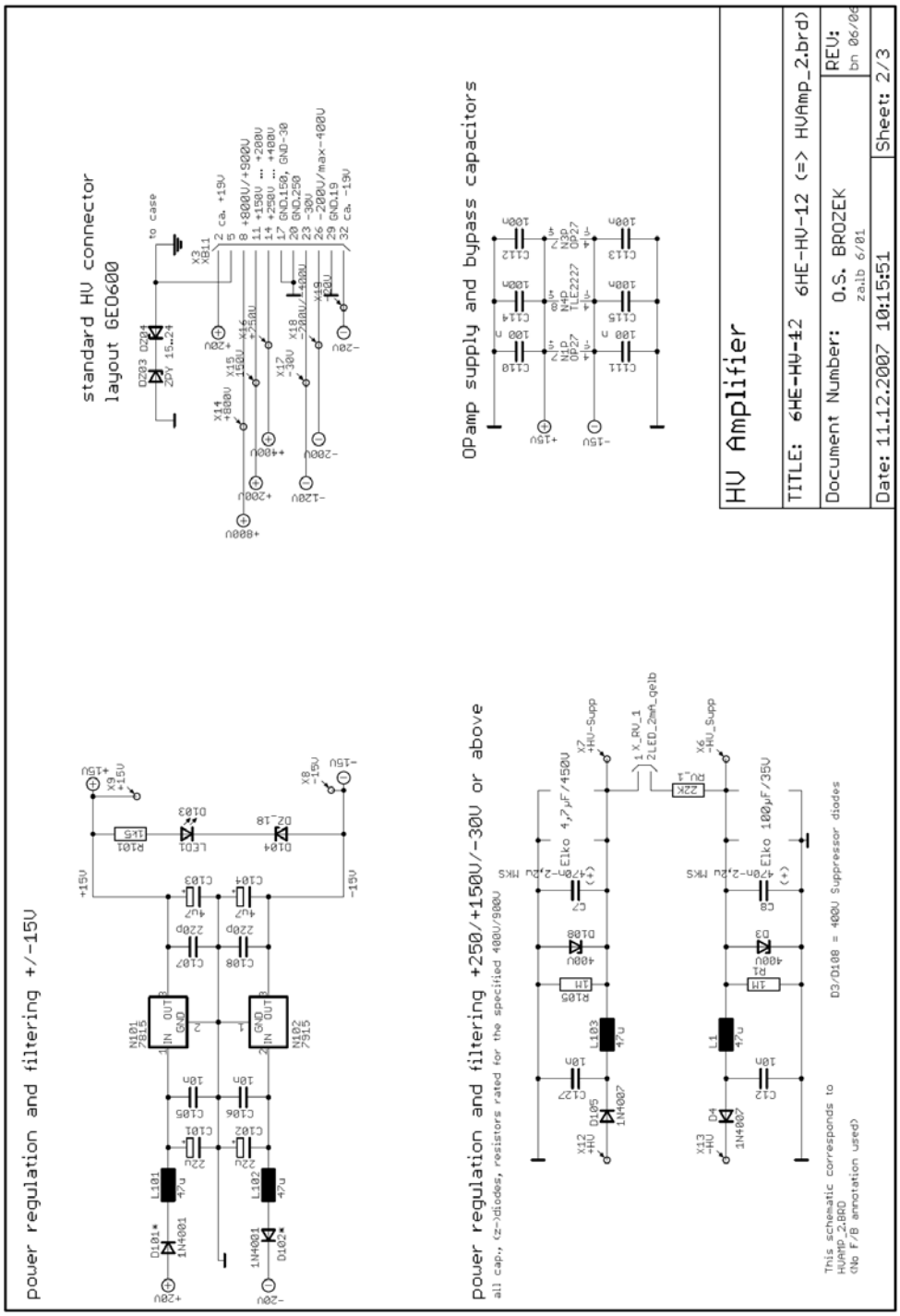

Figure A.20: High Voltage Amplifier 3/4.

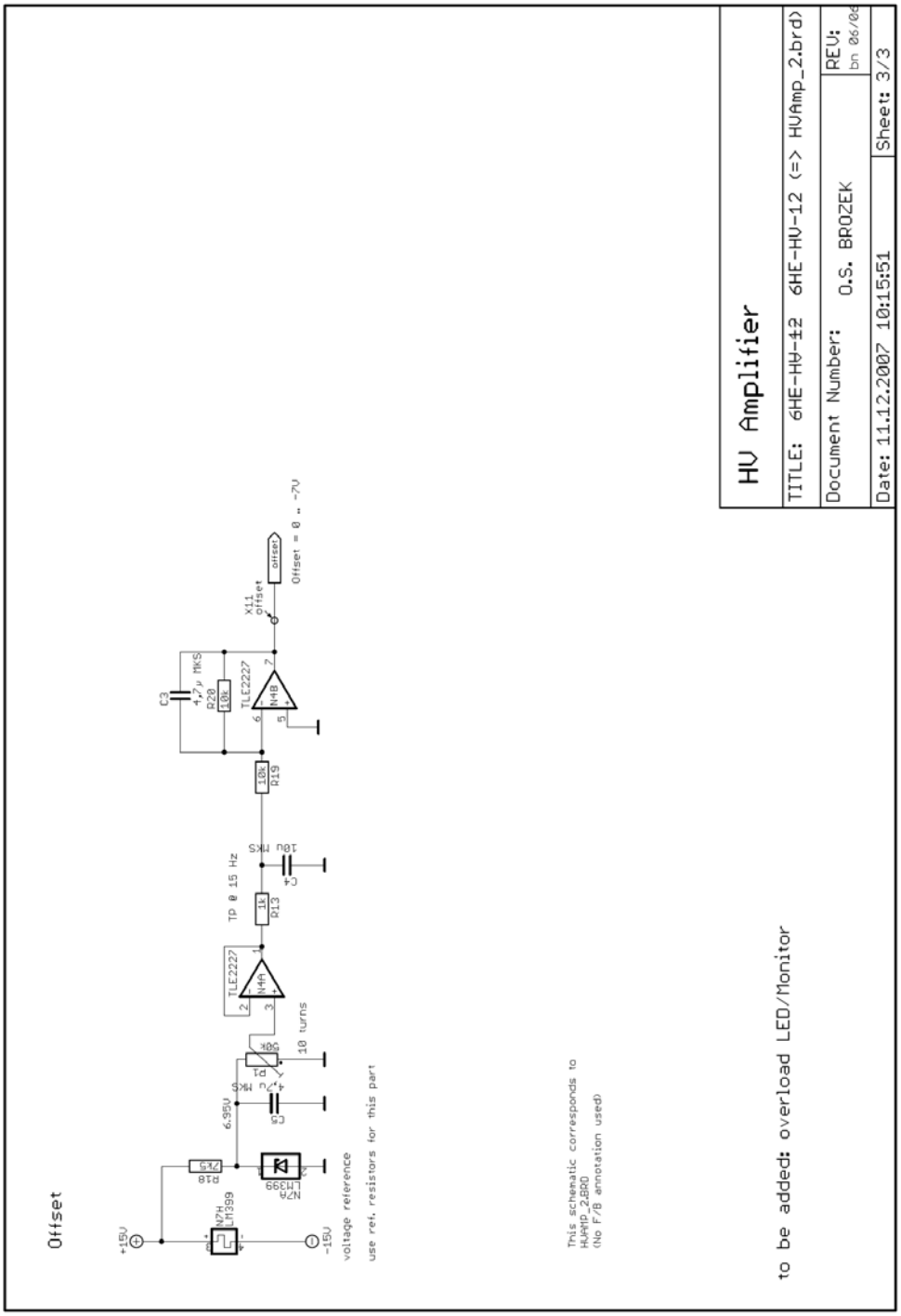

Figure A.21: High Voltage Amplifier 4/4.

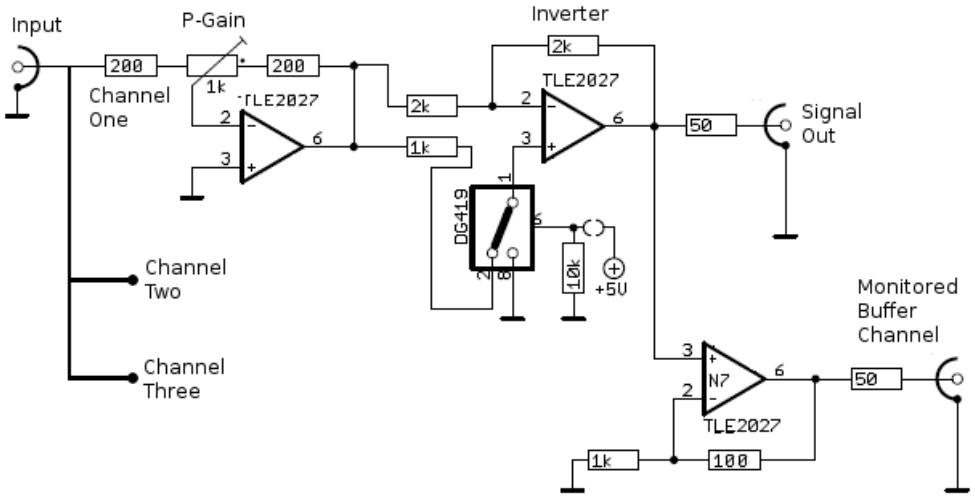

Figure A.22: Matrix Box 1/1.

A.8 Matrice Box

The matrice box was designed by this author to the schematic, with the power system omitted, is shown in Figure A.22. A single input is taken from a constant signal source or a network analyser if a transfer function is to be taken. It is connected to three identical channels of which only channel one is shown in the schematic. This splitting is not buffered, as the input power is arbitary and can be varied as desired. The first stage is a potentiometer controlled gain adjustment allowing the relative amplitude of the three channels. The second stage is an inverter since to generate pure tilt motion it will be necessary for there to be a $\pi/2$ phase difference between the piezos - i.e. one side of the end-mirror must be 'pushed' whilst the other is 'pulled'. This is then sent to the signal output. The signal output is also buffered to a monitor port, which allows the gain setting to be adjusted a known amount whilst the end-mirror tilt is in operation (removing the need to iterate improvement between checking the setting and running the test).

A.9 Quadrant Photodetector

The quadrant photodetector was built to the design as shown in Figures A.23, A.24 and A.25. It was necessary to slightly modified the board layout to accomodate a new pin arrangement for the quadrant photodiode itself, but this did not affect the schematic layout of the detector.

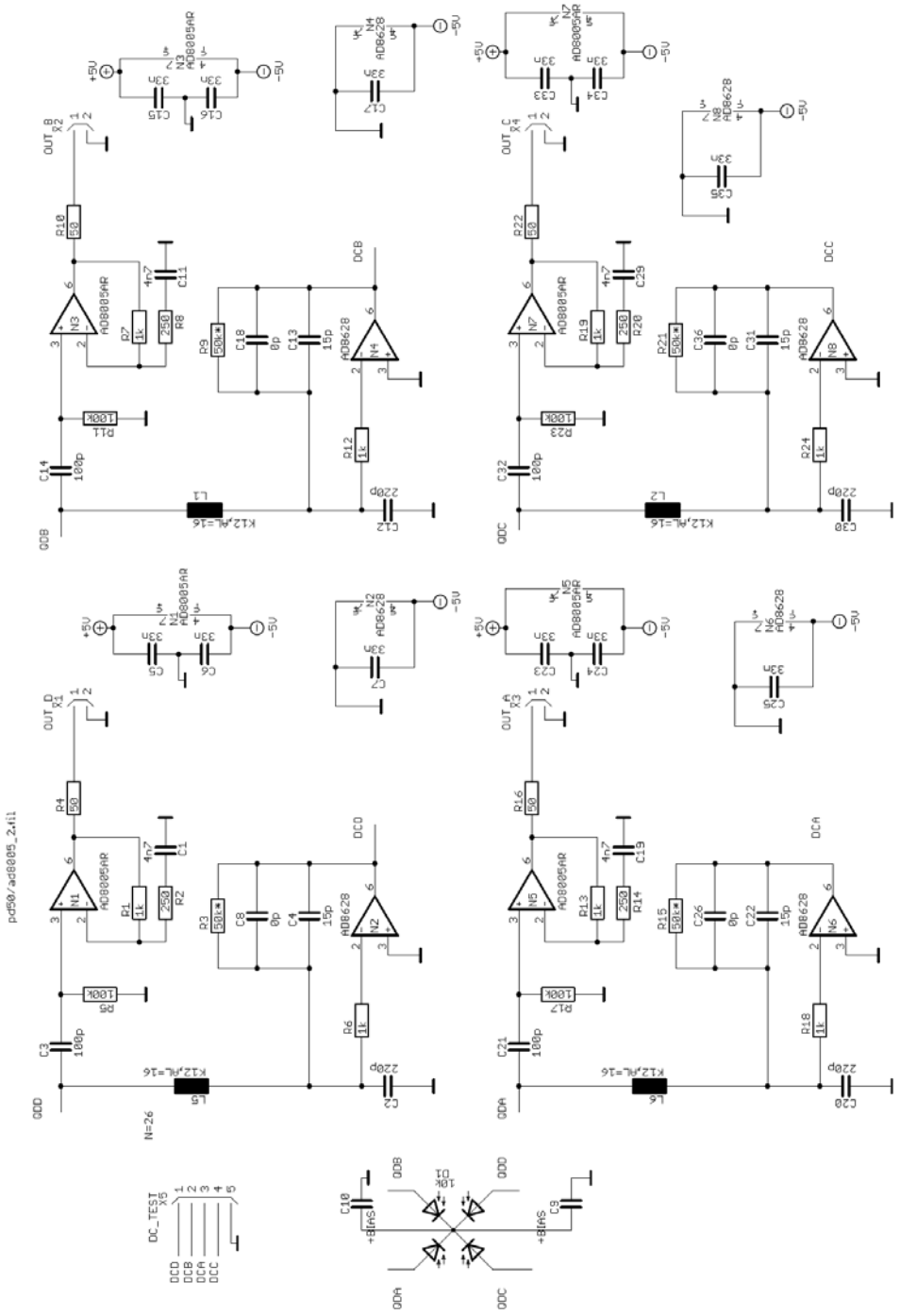

Figure A.23: Quadrant Photodetector 1/3.

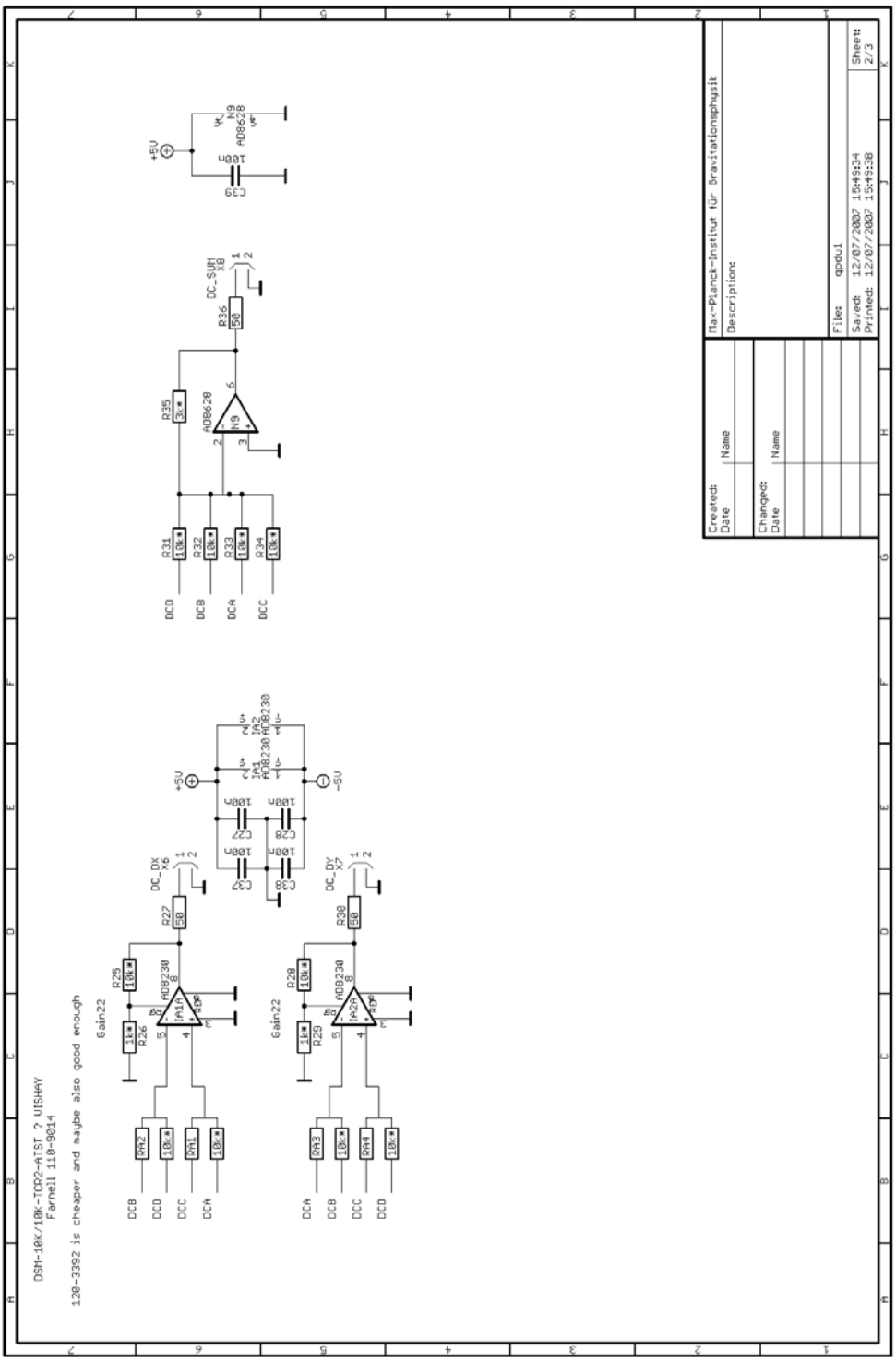

Figure A.24: Quadrant Photodetector 2/3.

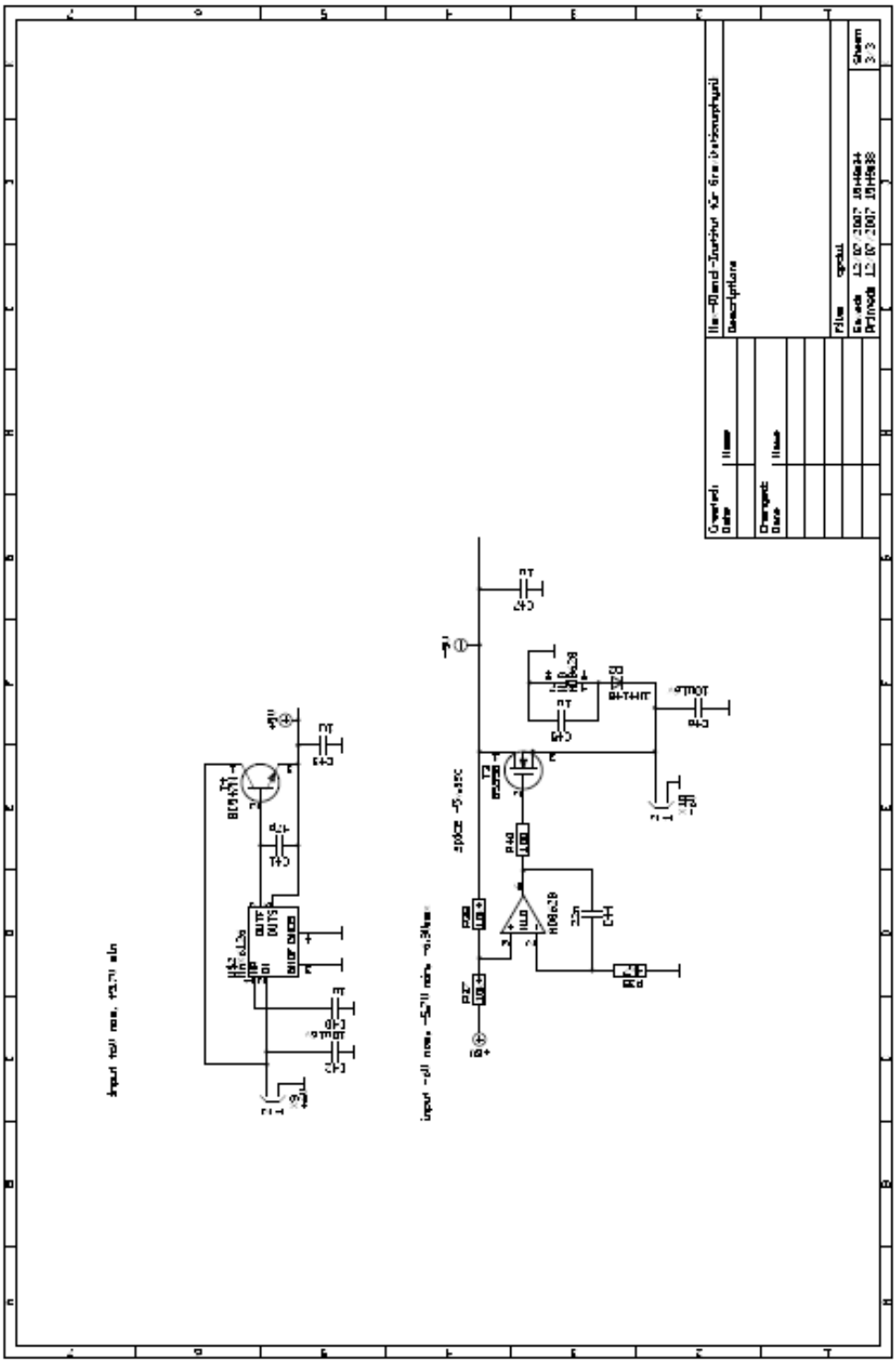

Figure A.25: Quadrant Photodetector 3/3.

Appendix B

IMPLEMENTATION OF THE INITIAL BEAM

B.1 Laser beam characterisation

A variety of steps were required to prepare the experimental setup before the work of obtaining the transfer functions discussed in the previous section could begin. These steps will now be discussed in the order which they were performed. Broadly, this starts with the laser and works forward through the experiment to the Fabry-Perot cavity.

The goal was to implement a two-mirror Fabry-Perot cavity, and to be able to switch between it and a three-port coupled grating cavity relatively easily. The full optical layout used is shown in Figure B.1, for the grating cavity configuration. The starting point was an empty optical table, so the first step was to install the optics shown in Figure B.2: A laser and the initial optics it required. Next, the beam was collimated to be effectively uniform over the range in which we would be operating ($\sim 3\,\mathrm{m}$). Some additional optics were added to allow easy varying

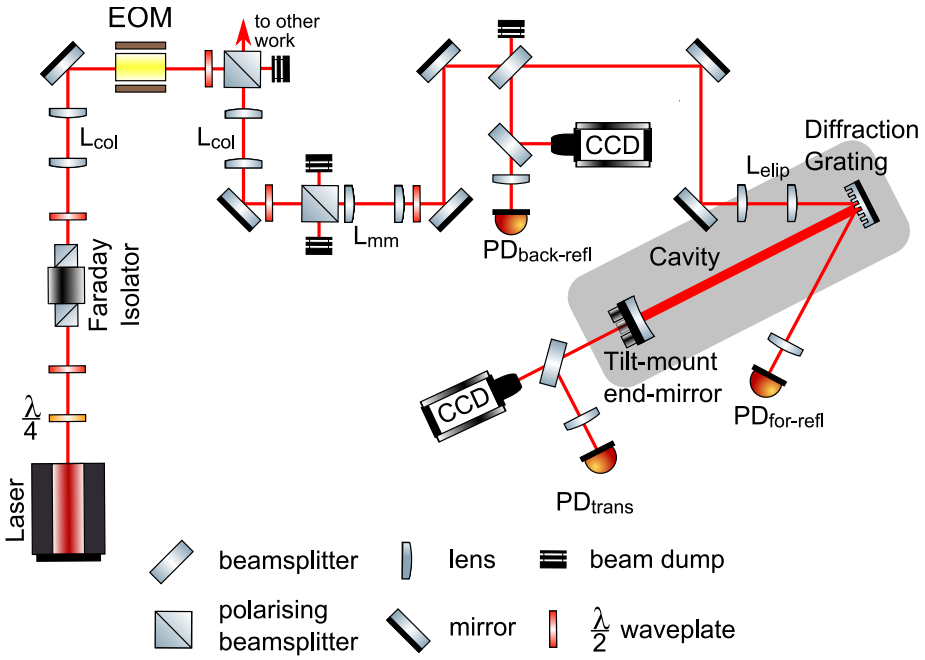

Figure B.1: The full optical layout used in the experiment, shown for the grating cavity configuration.

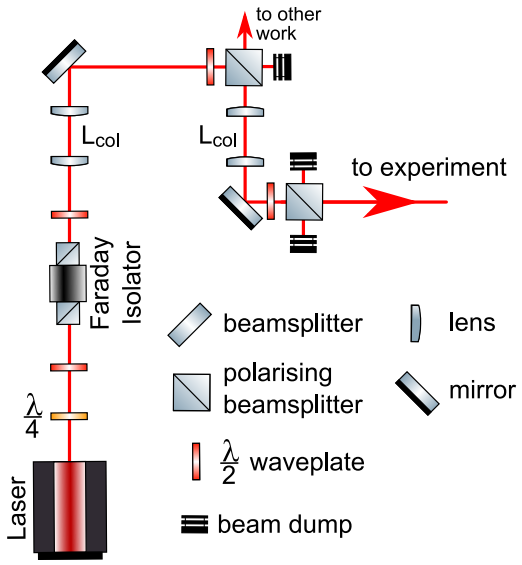

Figure B.2: The initial optics of the laser, the collimation lenses and the power splitting and adjusting apparatus.

of the laser power entering the experiment - this was important because the laser was the light source for several experiments sharing this optical table, and therefore power output from the laser itself had to remain constant.

B.1.1 Faraday isolator and other initial optics

In this section we will deal with the $\lambda/2$ and $\lambda/4$ wave plate immediately following the laser, the Faraday Isolator, and the $\lambda/2$ wave plate following that. The purpose of these optics is to prevent the back-reflected beam from the experiment from re-entering the laser. The correct operation of the laser depends on a ring cavity contained within a crystal inside the laser. The purpose of this cavity is to take the output of a pair of relatively low-quality lasing diodes and amplify a unique output frequency given by the resonance of the crystal. In the case of our $\lambda = 1064\,\text{nm}$ laser, the crystal is an neodymium-doped yttrium aluminium garnet, more commonly known as Nd:YAG and actually having formula $\text{Nd} : \text{Y}_3\text{A}_{\text{l}5}\text{O}_{12}$. In our case this is a 1 W Mephisto model supplied by Innolight. We have mentioned previously adjusting the laser frequency, and this is accomplished either by using a piezoelectric within the laser or, if a large low-frequency adjustment is required by adjusting the temperature of the crystal. Light returning from the experiment and interacting with the laser can be harmful to the quality of the laser beam produced and even to the laser itself. The Faraday isolator is included to prevent light returning from the experiment to enter the laser.

The Faraday isolator is composed of three components: An input polariser, a Faraday rotator and an output polariser. A slightly more complete discussion of polarisation can be found in Section 4.6.2. The input polariser allows the passage of vertically polarised light only, requiring the use of a $\lambda/4$ wave plate before the Faraday isolator to linearise the laser's elliptically polarised output, and a $\lambda/2$ wave plate to convert it fully to vertical polarisation. Once the light has passed the input polariser, its polarisation is then further rotated by $\pi/4\,\text{rad}$ by the Faraday

rotator. The output polariser is set to allow passage of this $\pi/4$ rotated polarisation. Returning light from the experiment at this $\pi/4$ rotated polarisation can freely enter the Faraday rotator where it is again rotated by $\pi/4$ rad and therefore obtains horizontal polarisation, which cannot then pass through the input polariser. Fundamentally, these input and output polarisers are the same as appropriately rotated polarising beam splitters, and the Faraday rotator may be any one of a number of ferromagnetic materials - most use crystals - subject to a transverse magnetic field that causes this Faraday effect. A final $\lambda/2$ wave plate is installed after the Faraday isolator so the light field polarisation can be controlled.

B.1.2 Beam-analysis and collimation

In order for the cavity to achieve its designed gain from the input power to the circulating power, the input Gaussian beam wavefronts should be mode-matched to the cavity mirror curvatures as has been discussed in Section 2.3.6; however, it is more convenient to do this if the initial beam is collimated over the length that we may desire to use (~ 3 m). Once the beam is collimated, we can introduce additional path length in front of the mode-matching lenses without changing the mode matching into the cavity.

Therefore the laser beam was profiled with a WinCamD-UCM from Laser2000 and the first-stage analysis to obtain the beam width (defined across the beam from points at 0.135 times the peak power) at the measurement location was performed using their Dataray software, version 6.0. This was repeated at a range of distances measured from the Faraday isolator. The plot of beam waist position and radius shown in Figure B.3 was obtained using the relations demonstrated in Section 2.3.5 and a fitting subroutine. The waist determined is before the Faraday isolator and inside the laser. Rather than tediously calculating the position of the required collimating lenses by hand, the program JAMMT (Just Another Mode Matching Tool) was used JAMMT was ported into Java by Nico Lastzka from Andre Thuering's original program

GROB. This provided positions for the collimating lenses, which were installed, and the process repeated. I decided I was less than fully satisfied with the general quality of the collimation (since my experiment was arranged at the far end of the optical table from the laser), and added an additional pair of collimating lenses in my unique beam path after the $\lambda/2$ wave plate and polarising beam-splitter pickoff for the other experiment. The JAMMT calculation for this second pair of collimating lenses (f=80 mm, f=100 mm) is shown in Figure B.4, which also shows the lenses mode-matching into the cavity (f=-50 mm, f=100 mm) and has its zero at the power-separating beam-splitter. Since the beam was well-collimated after this, it was not possible to obtain a plot of the type shown in Figure B.3, since measurement errors were larger than the 'signal' of the beam's dispersion over the distance studied - which was the point of performing the collimation. Therefore the collimation was successful, and I moved on to installing other optical elements.

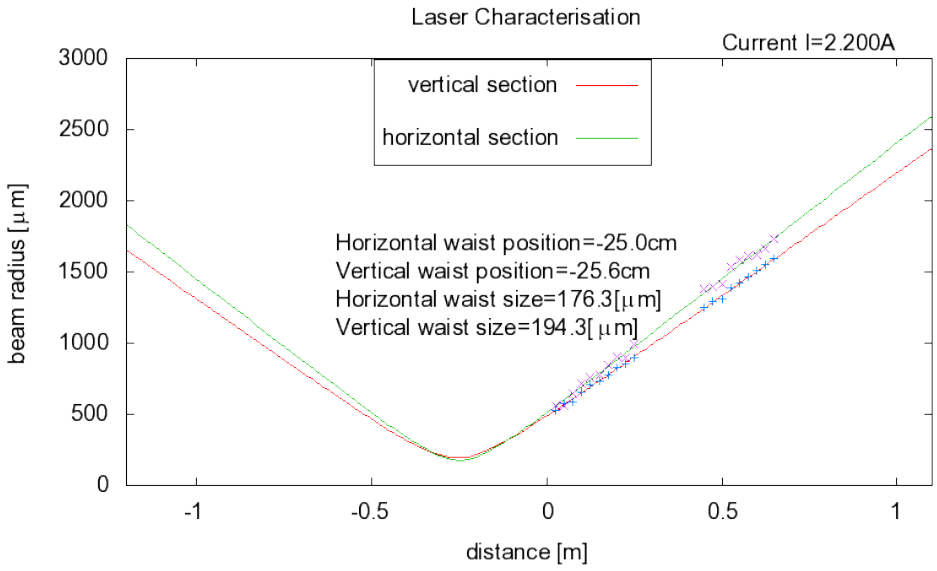

Figure B.3: Uncollimated analysis of the laser beam, $z = 0$ set at the Faraday isolator.

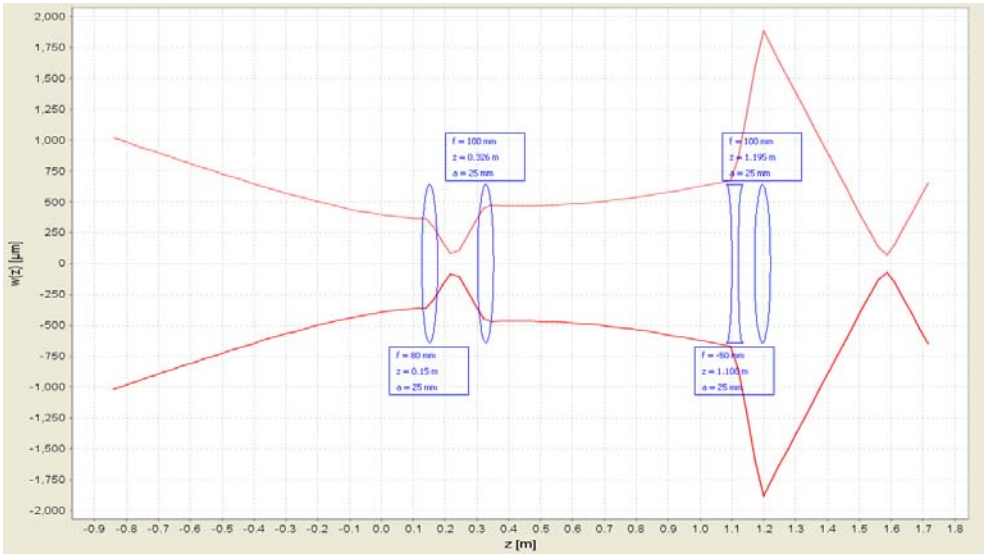

Figure B.4: JAMMT Collimating calculation, $z = 0$ set at the power-separating beam splitter between the experiments of this optical table.

B.1.3 Power splitting

It has previously been mentioned that the pickoff for the other experiment featured a $\lambda/2$ wave plate and polarising beam-splitter. A light field is composed of S- and P-polarised light, and the $\lambda/2$ wave plate re-adjusts the proportion of a light field in each polarisation. A polarising beam-splitter transmits one polarisation and reflects the other. Therefore such a combination allows the beam to be split into two controlled powers between two experiments. An additional $\lambda/2$ wave plate and polarising beam-splitter pair was introduced after the split between the experiments. This second power-adjusting system dumped its reflected light, to allow the power in my experiment to be independently adjusted.

B.2 Cavity implementation

It was decided to implement the two-mirror cavity first. This way, any strange response of the system would be due to some error and could be resolved, rather than being an unexpected

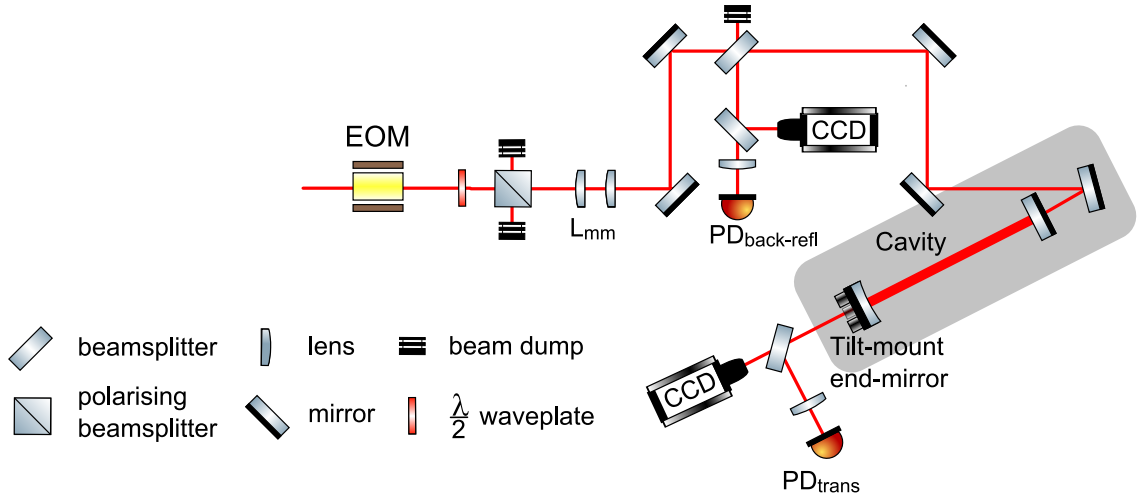

Figure B.5: The optics added to those shown in Figure B.2 in order to implement the two-mirror Fabry-Perot cavity.

grating effect. Therefore the optics shown in Figure B.5 were added to those shown in Figure B.2, with the diagram of the fully installed system being shown in Figure B.1 for reference.

Appendix C

IMPLEMENTATION OF THE TWO-MIRROR CAVITY

C.1 Mode Matching

The requirement to be able to use a grating as an input optic imposes that that input optic be flat. This imposes that its radius of curvature is infinite. The unique location along the beam path where the radius of curvature of the propagating wavefronts is infinite is at the beam waist. Therefore, the beam waist must lie close to the surface of the input mirror, and within the radius of curvature of the end-mirror for the cavity to be stable. A -1 m radius of curvature was chosen for the end mirror when determining the resonator g-parameters in Section 4.6.1. The gross mode matching was therefore performed by an iterative process of laser beam analysis with the WinCamD, JAMMT simulation, and addition and adjustment of the position of appropriate mode matching lenses. The final pair of lenses selected (f=-50 mm, f=100 mm) and their positions as determined by JAMMT have been shown in Figure B.4 which has its zero at the power-separating beam-splitter. The first and last iterations of the WinCamD beam

analysis with the lenses installed are shown in Figure C.1 and C.2 respectively, which take their zero from the last turning mirror.

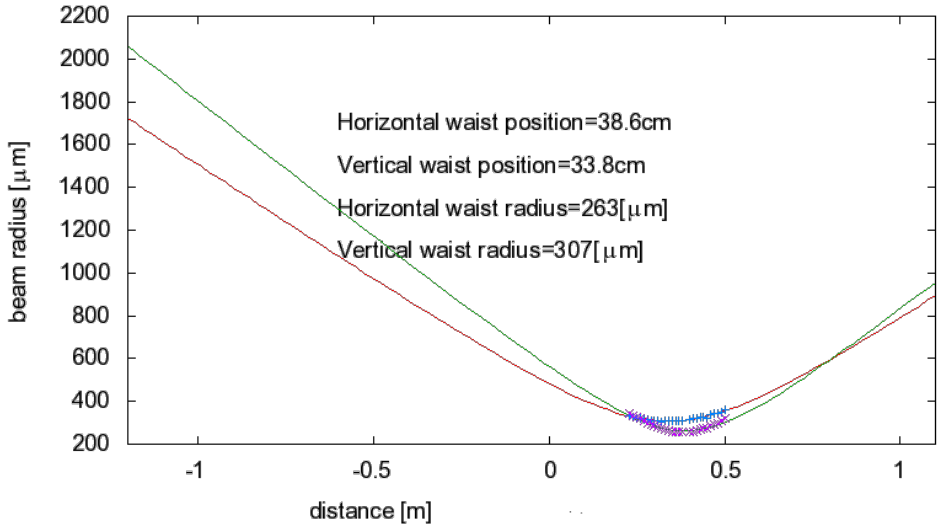

Figure C.1: Beam profile before mode matching improvement iterations

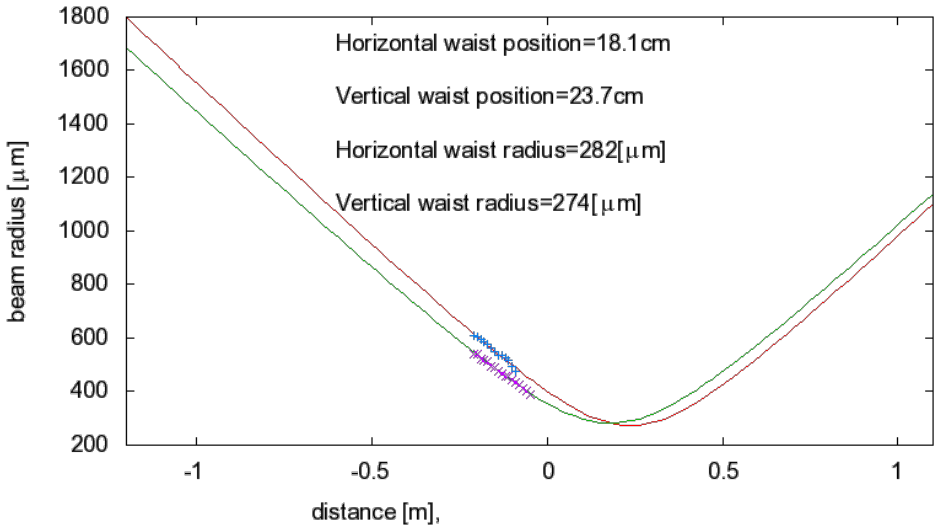

Figure C.2: Beam profile after mode matching improvement iterations

The work of mode-matching using lenses, installed and positioned with the combined tools of JAMMT and the WinCamD beam analyser sufficed to roughly position the beam waist. The two-mirror cavity was then installed, using the optics shown in Figure B.5 and the following procedure: Five additional turning mirrors were added, to increase the path length sufficiently that the beam waist fell on the optical table, and so that the geometry of the cavity position

would allow direct replacement of the fifth turning mirror and the cavity input mirror with a grating as shown in Figure C.4.

The two-mirror cavity was installed, as were the transmitted photodetector $\mathrm{PD}_{\mathrm{trans}}$ optics. Ramping the cavity showed the resonant transverse electromagnetic zero-zero (TEM_{00}) mode as shown in Figure C.3 (the smaller side peak is the TEM_{01} mode which falls close to the zero-zero mode). It was then possible to lock the cavity, as detailed in the following section.

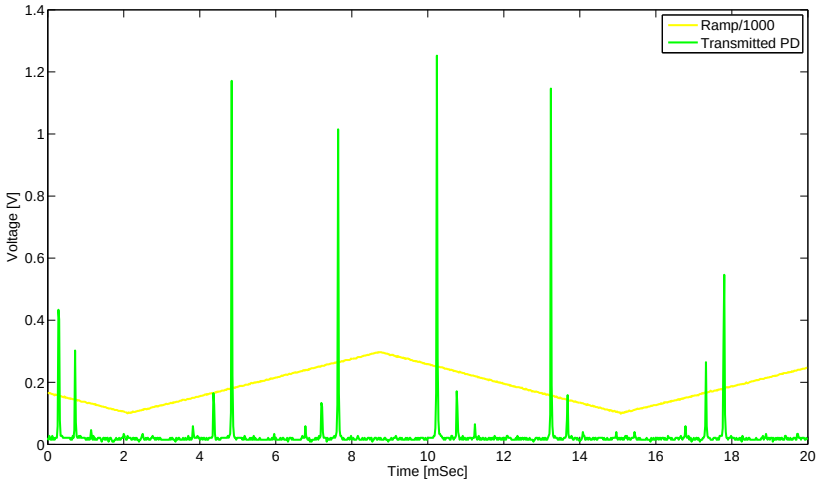

Figure C.3: Ramping of laser frequency in a Fabry-Perot cavity.

C.2 Offset Locking

Initially, the reflected detection port as shown in Figure B.5 was not implemented, and the transmitted port was used to offset-lock the cavity. This used a locking scheme as shown in Figure C.4. The transmission photodiode $\mathrm{PD}_{\mathrm{trans}}$ generates a signal of a similar form to that seen in 2.4 when the cavity is ramped, and the error signal from that ramping is shown in Figure C.3. This was offset by the offset box so that the side-slope of the peak fell at zero volts, defining an operating point to which the cavity was then locked using the servo and high-voltage amplifier feeding back to the laser frequency. The transmission photodiode was the DC

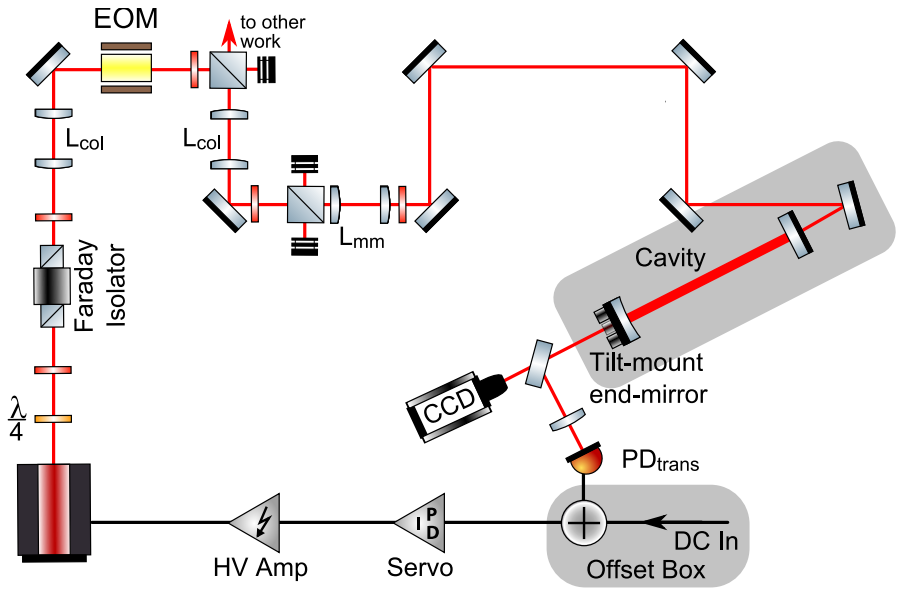

Figure C.4: System used for offset locking of two-mirror Fabry-Perot cavity.

output port of photodetector JPD2, with the transfer function shown in Figure C.5. The servo that performed the locking was servo JMH3, and its transfer function is show in Figure C.6, for the particular gain-setting of 0.8. This servo had integrators of cut-off frequency 144 Hz and 6.5 kHz which were used in locking the cavity. The integrators increase the feedback at frequencies below their cut-off by integrating the error signal over time. This is necessary to deal with larger low-frequency seismic effects. The high-voltage amplifier (HV Amp) has a flat transfer function. Schematics for the electronics used can be found in Appendices A. Once the cavity was locked, it was possible to investigate the noise features of the cavity by taking a spectrum, which is discussed in the following section.

C.2.1 End-mirror mount replacement

The error signal of the offset-locked cavity was connected to a spectrum analyser. A substantial spike was found close to 100 Hz, which was determined to be due to the end-mirror mount. The Thorlabs-modular mount was replaced with a monolithic aluminium mount, and both frequency and end-mirror position locks were performed. This demonstrates that the end-mirror mount

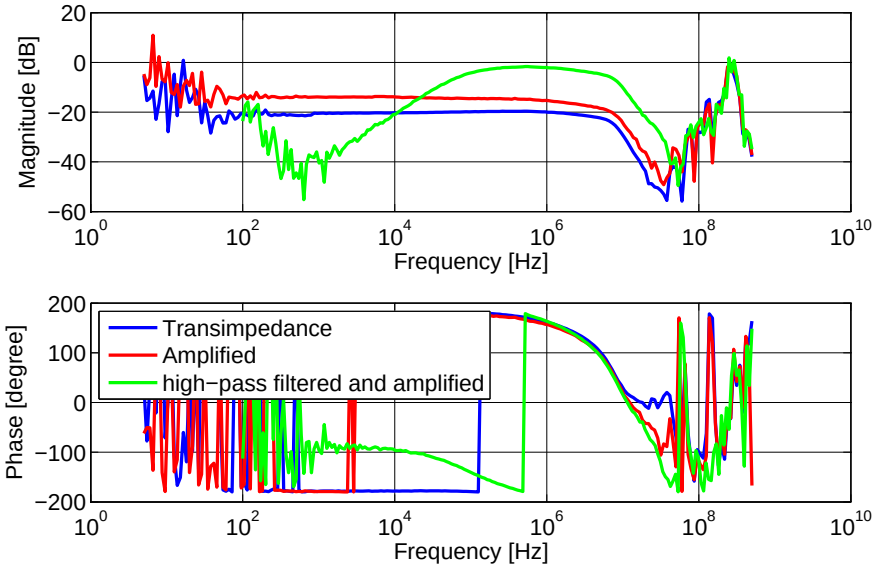

Figure C.5: Transfer function of JPD2

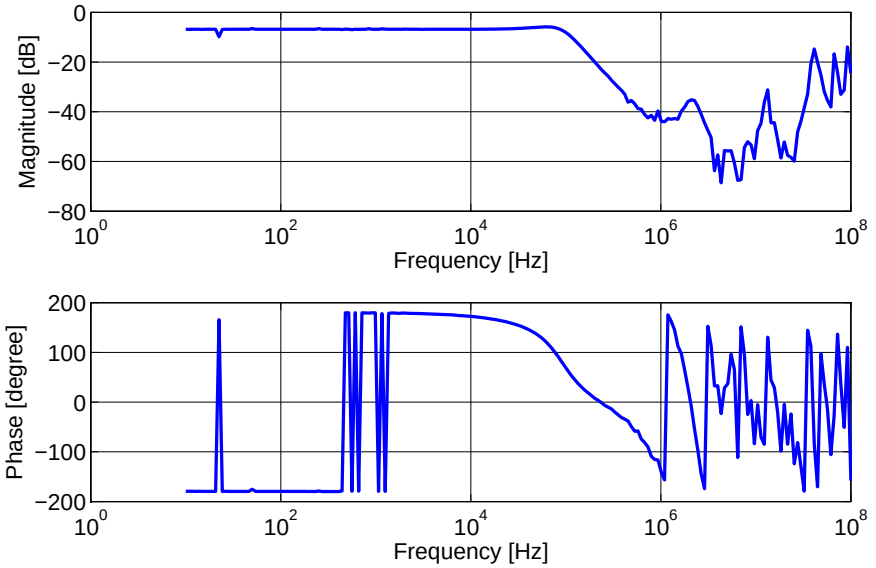

Figure C.6: Transfer function of servo JMH3.

performance was good even when the piezo attached to it was feeding back signal to the mirror. The resulting improvement from using this new mirror mount is shown in Figure C.7. There is a relatively high base noise level in this measurement, because only a few averages, rather than a few hundred averages, were taken. The substantial peak can be seen near to 100 Hz, and shown to be reduced and shifted slightly upwards in frequency with the new mirror mount.

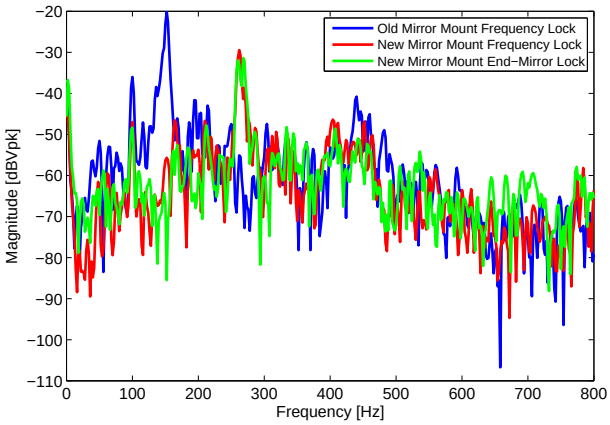

Figure C.7: FFT scan of cavity. The error signal is plotted versus frequency, showing the old mirror mount, new mirror mount with the cavity frequency locked, and the new mirror mount with the cavity end-mirror locked. Note that the first has a higher peak from the mirror mount, and the the last two are much the same, indicating that longitudinal displacement of the end mirror under normal locking conditions does not excite resonances.

C.3 PDH Locking

Once offset locking had demonstrated that the cavity was functional, the reflection detection port was implemented. The feedback loop was then reconfigured to lock the cavity with the Pound-Drever-Hall modulation-demodulation technique rather than the offset-lock. The scheme used is shown in Figure C.8. In the case of the Pound-Drever-Hall scheme, because the DC signal is not of interest (only the beat between the 12 MHz sideband and the carrier) a high-pass filter is used after the transimpedance stage of the photodiode. This allows a larger gain to be applied to the relevant high-frequency component of the signal without saturating the

electronics. The transfer function of the reflected photodetector (identified as JPD3) is shown in Figure C.9. The schematic for this photodiode, and for the mixer used for the demodulation are also shown in Appendices A. The servo and high-voltage amplifier were the same as used for the offset lock. A plot of the error signal obtained by ramping the laser frequency is shown in Figure C.11, and a single error peak is shown in Figure C.10. A spectrum of the locked cavity was taken (using 100 averages), feeding back to the laser frequency, and is shown in Figure C.12. Even on an isolation table noise which is presumed to be seismic is significant between 100 Hz and 1 kHz.

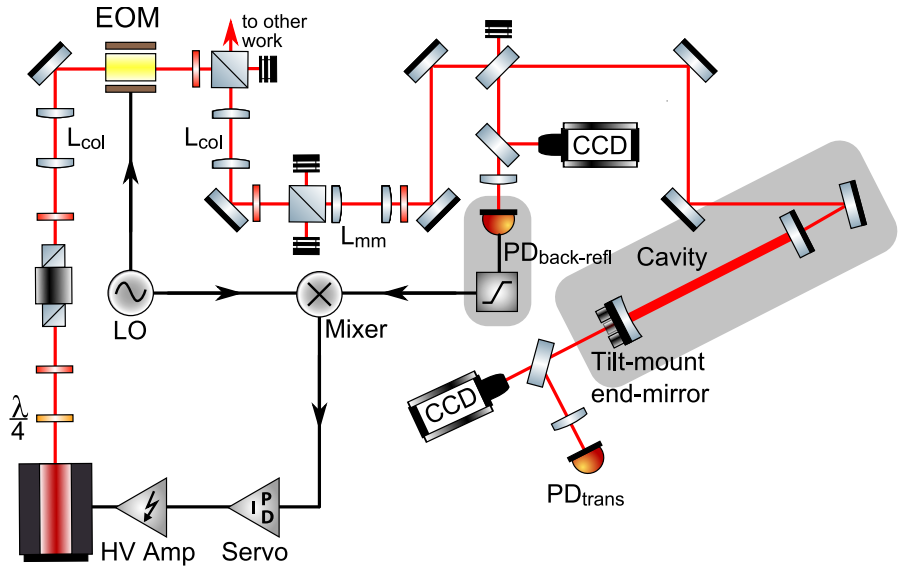

Figure C.8: System used for Pound-Drever-Hall locking of two-mirror Fabry-Perot cavity. LO is the Local Oscillator, providing a 12 MHz signal to be imprinted on the beam (modulating it) by the electro-optic modulator (EOM). The LO signal is also sent to the mixer to be demodulated with the signal detected by the reflected photodiode $\mathrm{PD}_{\mathrm{back-refl}}$. The high-pass filter is part of the photodetector assembly, after the transimpedance (photodiode current to voltage conversion) stage. Its presence here is not contradictory with other figures shown in this thesis - the photodetector design comprises several appropriately buffered output ports, one of which has a high-pass filter.

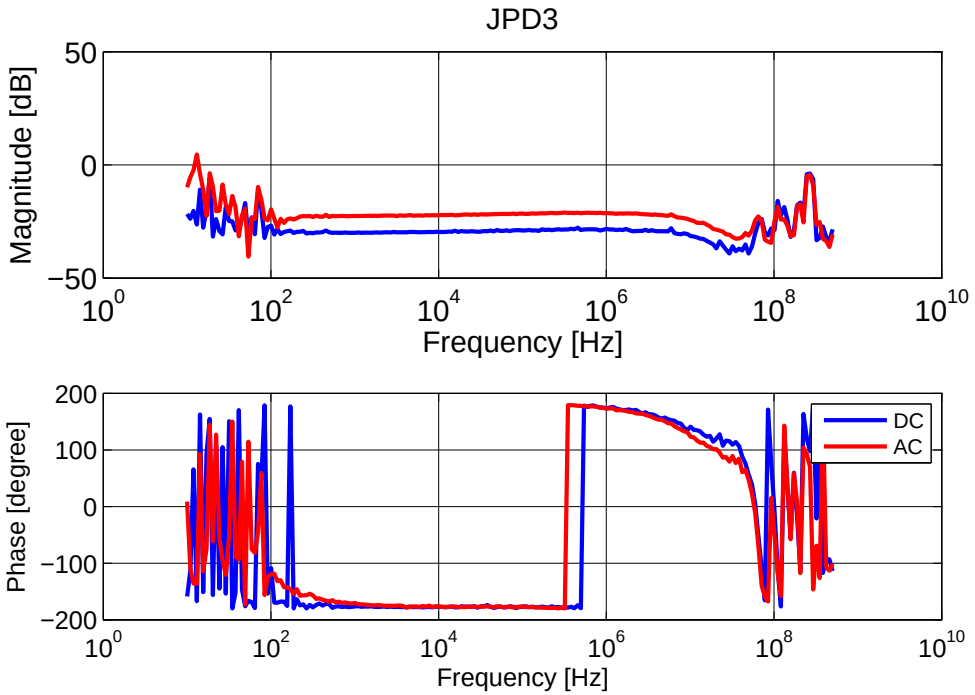

Figure C.9: Transfer function of the JPD3 photodetector used as the reflected photodetector in Figure C.8. This transfer function was taken with a dedicated photodiode tester. JPD3 has three output ports, hence the three traces, all buffered: Trace DC directly from the transimpedance stage; trace DCA from an inverting amplifier after the transimpedance stage; and trace AC high-pass filtered, then processed by an inverting amplifier, also directly after the transimpedance stage. I.e. DCA and AC are in parallel, not in series.

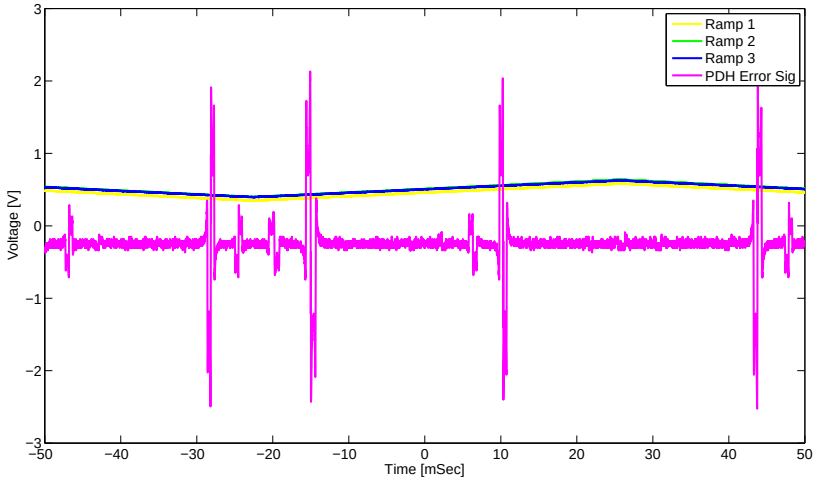

Figure C.10: Ramping of laser frequency in a Fabry-Perot cavity to be locked with the Pound-Drever-Hall modulation-demodulation technique. Three equal ramps are required, as this plot was recorded by ramping the end-mirror, which is mounted on a three-axis piezo (in this case driven linearly).

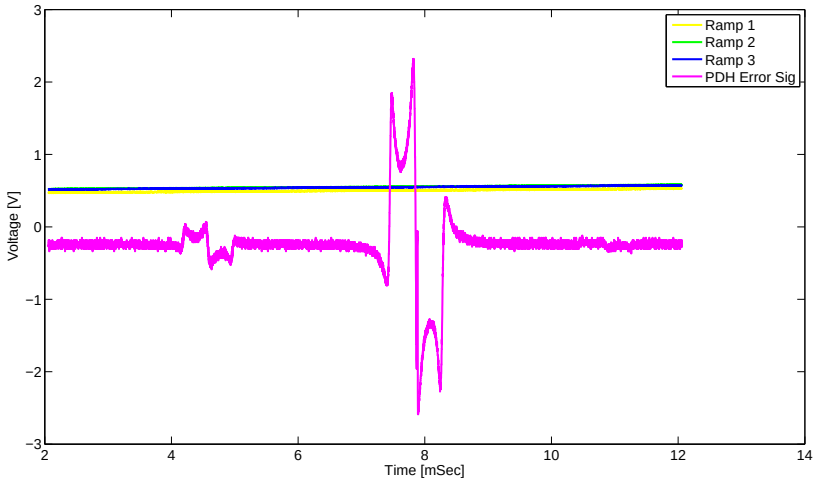

Figure C.11: Ramping of laser frequency in a Fabry-Perot cavity, showing a single Pound-Drever-Hall error peak. The ramp appears flat because of the short time-axis used.

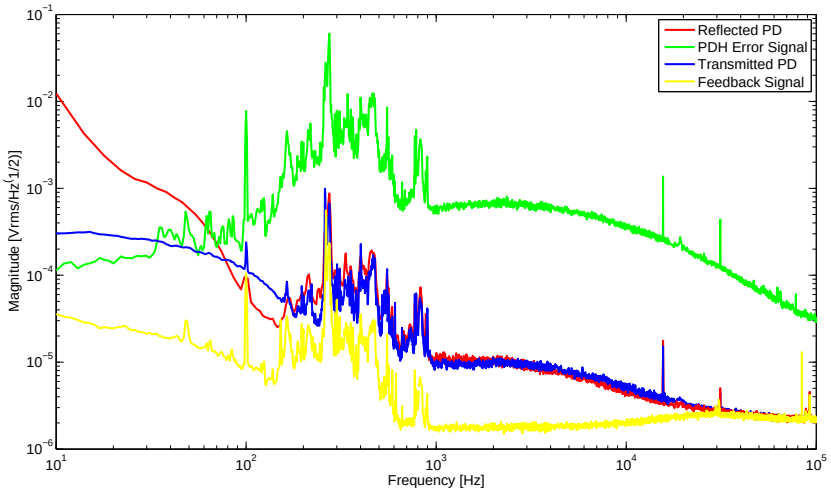

Figure C.12: Spectrum of PDH locked cavity, taken using one hundred averages. Reflected and transmitted photodetector signals, both DC, are shown, as is the Pound-Drever-Hall error signal and the feedback signal to the laser frequency used to lock the cavity.

Appendix D

END MIRROR TILT ACTUATOR

Our experimental result will be a pair of transfer-functions, comparing the phase signal generated by coherent injection of end-mirror tilt into the two-mirror cavity to that from injection into the grating cavity. In order to take these transfer functions, it is necessary to have a method of generating a consistent end-mirror tilt. To generate this end-mirror tilt, the end-mirror was mounted on a three-axis piezo actuator, (which was itself mounted in a Thorlabs micro positioning mirror-holder for cavity alignment purposes). The actuator chosen was a Physik Instrumente PI.311, shown schematically in Figure D.1, featuring three piezoelectric stacks arranged in a triangular formation. By differentially driving these three piezos it is possible to make any combination of motion on three axis: z (longitudinal), θ_y (vertical tilt or pitch) and θ_x (lateral tilt or yaw). It is the last of these which provides tilt that displaces the cavity eigenmode across the grating striations.

D.1 Coupling matrix for tilt only motion

In order to differentially drive this three-axis piezo, a matrix box was constructed, the schematic of which is shown in Appendix A. It takes a single input, which is split into three, with each channel having an independent gain control and inverter. The inverter is required as it is necessary to drive at least one piezo π out of phase with the others to create tilt - one piezo must 'pull' one side of the mirror whilst the other two 'push' the opposite side. The transfer function of this matrix box is shown in Figure D.2.

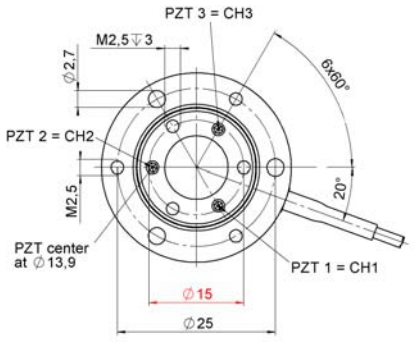

Figure D.1: Schematic diagram of the PI.311 three-axis piezo tilting device utilised, all linear dimensions in mm, with the 15 mm tilting baseline shown in red. Source: Physik Instrumente GmbH.

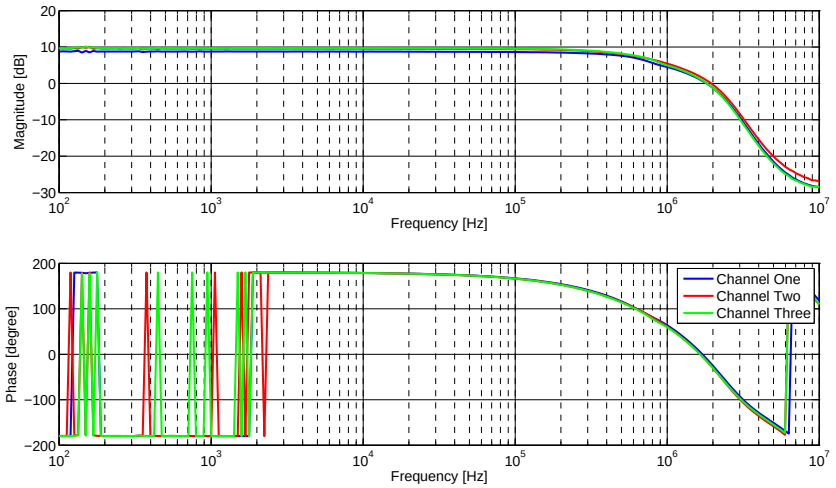

Figure D.2: Matrix box transfer function.

The matrix required to drive the three-axis piezo for pure θ_x motion depends on the orientation of the three axis piezo, in rotation about its own central axis. Two ideal situations and the more likely slight deviation from the ideal case, as shown in Figure D.3, will now be discussed. The rotation axis for pure θ_x is shown as a dotted line in Case One, bisecting the A piezoelectric stack. To rotate around this axis in this case, the piezos must displace as shown in the lower portion of the figure. The A piezo remains stationary while the B and C piezos displace with equal amplitude but π out of phase with each other. Since the three piezoelectric stacks within the PI.311 are rated for voltages from 0 to 100 V a 50 V DC offset was applied equally to all three piezos, with this voltage alone setting the length of piezo A, and the starting positions of piezos B and C in Case One. Therefore it was possible to apply a signal voltage of up to ± 50 V to each of the piezoelectric stacks. Hereafter, we will now deal only with the signal voltage applied to the piezos, distinct from this fixed offset.

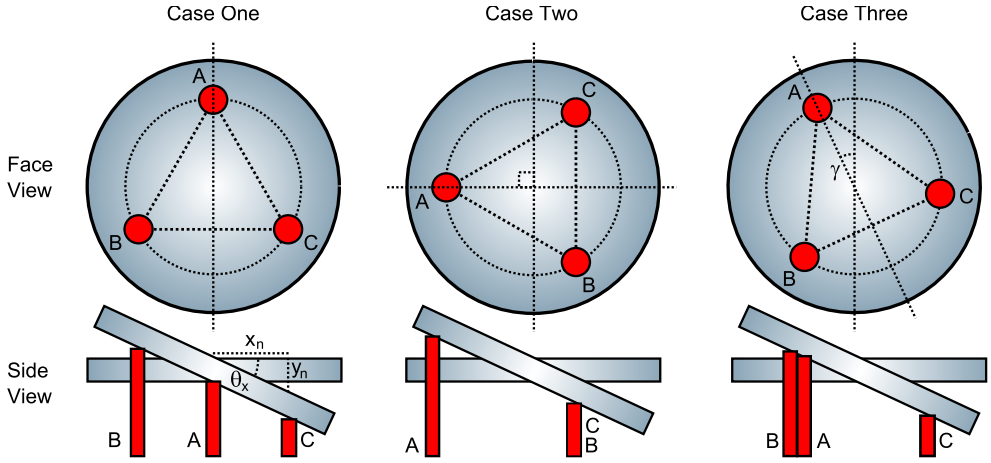

Figure D.3: Three axis piezo rotational position.

For the required displacement y_n of a given piezo, we can relate the angle of tilt of the mirror θ_x and the distance that piezo is from the desired rotational axis x_n by writing,

$$\tan \theta_x = \frac{y_n}{x_n}, \tag{D.1}$$

which must be true for all piezos attached to the mirror, if we wish to make pure θ_x tilt motion.

Therefore we can equivalently write,

$$\frac{y_{\mathrm{A}}}{x_{\mathrm{A}}} = \frac{y_{\mathrm{B}}}{x_{\mathrm{B}}} = \frac{y_{\mathrm{C}}}{x_{\mathrm{C}}}, \tag{D.2}$$

where A, B and C are the piezos shown in Figure D.3. Since the signal voltage applied to the piezos is proportional to the extension or contraction of the piezo this equation defines the coupling matrix that will be generated by the matrix box, with the voltage applied being proportional to the distance from the desired θ_x rotational axis. Thus we can write the matrix that must be applied in Case One,

$$\begin{pmatrix} \Delta z_A \\ \Delta z_B \\ \Delta z_C \end{pmatrix} = \begin{pmatrix} 0\kappa_A \\ 1\kappa_B \\ -1\kappa_C \end{pmatrix} \cdot V_{in}, \tag{D.3}$$

where $\Delta z_{A,B,C}$ is the length change experienced by each particular piezo stack from the input

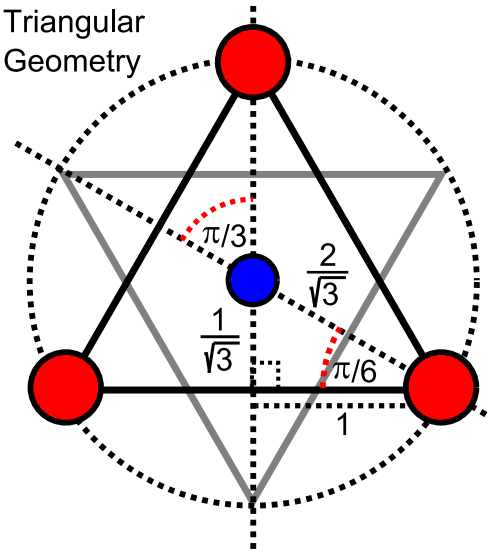

Figure D.4: Triangular geometry for the x-direction position of the piezoelectrics when the three-axis actuator is rotated. The positions of the piezos are shown red, and the center of rotation of the piezoelectric is shown blue. A unit length, half of one side of the triangle, is defined.

voltage, $\kappa_{A,B,C}$ is the coefficient linking voltage to expansion of the associated piezoelectric

stack, and V_{in} is the input voltage to the matrix box. If the piezo is rotated through ninety degrees as shown in Figure D.3 Case Two, then it is necessary to drive the B and C piezos with equal amplitude and phase, and the A piezo π out of phase and with an increased amplitude. Geometrical calculation shown in Figure D.4 allows us to calculate the appropriate driving matrix for pure θ_x tilt motion in Figure D.3 Case Two, given by,

$$\begin{pmatrix} \Delta z_A \\ \Delta z_B \\ \Delta z_C \end{pmatrix} = \begin{pmatrix} -2/\sqrt{3}\kappa_A \\ 1/\sqrt{3}\kappa_B \\ 1/\sqrt{3}\kappa_C \end{pmatrix} \cdot V_{in}, \tag{D.4}$$

and similarly for the general Case Three, the matrix can be written as,

$$\begin{pmatrix} \Delta z_A \\ \Delta z_B \\ \Delta z_C \end{pmatrix} = \begin{pmatrix} \frac{2}{\sqrt{(3)}} \sin(\pi+\gamma)\,\kappa_A \\ \frac{2}{\sqrt{(3)}} \sin\left(\frac{\pi}{3}+\gamma\right)\kappa_B \\ \frac{2}{\sqrt{(3)}} \sin\left(-\frac{\pi}{3}+\gamma\right)\kappa_C \end{pmatrix} \cdot V_{in}, \tag{D.5}$$

of which both Equations D.3 and D.4 are solutions with $\gamma = 0$ and $\gamma = 3\pi/6$ respectively. From this, we can see that for any rotation angle γ of the three-axis piezo actuator, there will be some correct combination of voltages applied to piezos A, B and C that will make pure θ_x tilt motion. The corollary to this is that for any combination of voltages that make tilt-only motion combining θ_x and θ_y, we can define a new θ_x' axis rotated by γ with respect to the θ_x axis. The rotation will then occur purely around this θ_x' axis.

In the case of the two-mirror Fabry-Perot cavity, the response to end-mirror tilt in the θ_x and θ_y directions is the same. Therefore any fixed amplitude, pure tilt angular displacement of the mirror will generate the same cavity locking error signal. This can be used to identify the driving matrix for pure tilt motion.

As we have seen from Equation D.2 for pure tilt motion the amplitude of the signal voltage must

be proportional to the magnitude of the distance from the θ_x' axis. Summing the magnitude of the displacements in Equation D.5, we find that Equation D.3 (Case One in Figure D.3) represents the minimum sum, and Equation D.4 (Case Two) represents the maximum. Both cases have $\pi/3$ rotational symmetry as shown in Figure D.4, if the input voltage signals are switched to the appropriate piezo with rotation. The tilt-effect of a fixed amplitude signal (piezo length change) is inversely proportional to its distance from the θ_x' tilt-axis. Therefore the tilt generated will be maximised in Case One and minimised in Case Two for a given sum of the root-mean-square voltage applied to all piezos, so long as the piezos are correctly configured for tilt-only motion.

It should be noted that the above depends on making pure tilt motion, which is a very specific region within the parameter space of all possible control matrices. The most likely possibility is that a combination of tilt and z-direction longitudinal displacement will be made. The geometry and minimisation of this longitudinal displacement will be discussed in the next section. It should be noted that any minimising of longitudinal motion by reducing a signal proportional to the amplitude of the tilt will also tend to home in upon Case Two, which will likely not generate tilt in θ_x. This can be resolved by rotation the piezo (about its own central axis) through γ, till the rotation axis θ_x' generated is coincident with θ_x, which can be checked using a lever arm and CCD camera. This also eliminates any component of θ_y tilt.

D.2 Longitudinal displacement effects

As a starting point we consider Case One from Figure D.3. This is shown in side view in Figure D.5, on the left hand side. On the right hand side is shown the same three-axis actuator orientation, when piezos A and B are driven to too high an amplitude compared to piezo C. This can be conceptualised as a pure tilt about an axis offset from the center of the mirror. Alternatively, it can be considered as a combined tilt and Δz longitudinal motion at the center

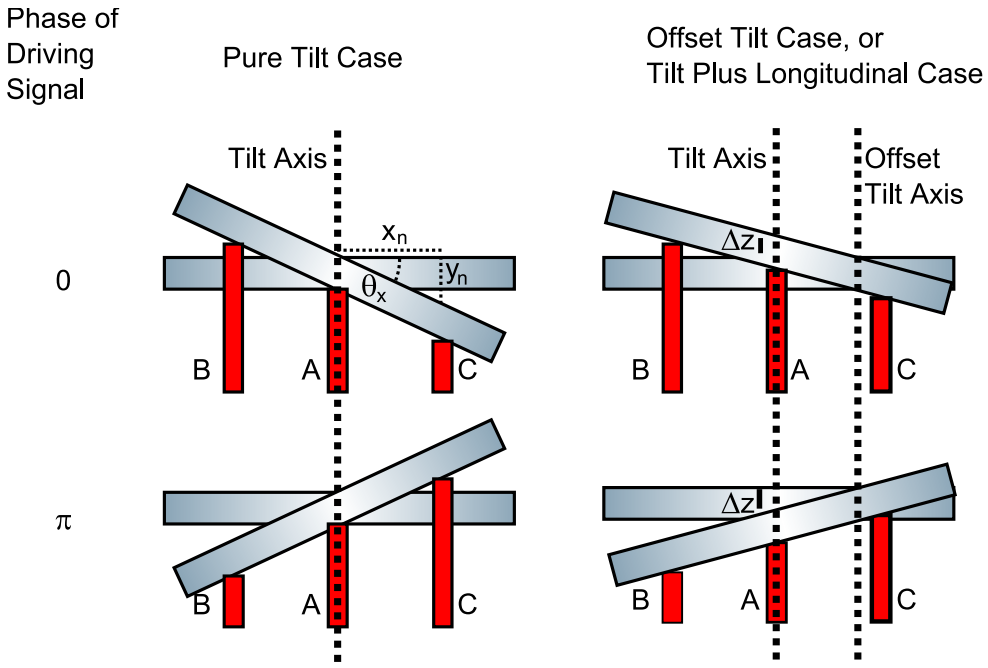

Figure D.5: Schematic of three axis piezo for combined longitudinal and tilt.

of the mirror.

Experimentally we only care about the tilt and longitudinal displacement of the end-mirror where the cavity eigenmode interacts with it. This will be close to the center of the mirror, so the second of the conceptualisations detailed above is more useful. Since it is unlikely that the cavity eigenmode can be positioned perfectly on the center of the mirror by the cavity alignment, some adjustment to the control matrix will be made to offset the tilt-axis such that the cavity eigenmode sits on it.

D.3 Minimisation of residual longitudinal motion

The experiment is designed for θ_x tilt-only motion of the end-mirror, projecting the beam across the surface of either a diffraction grating for the three-port coupled grating cavity or a mirror for the two-mirror cavity. The phase-signal due to the lateral grating translation effect can then

be revealed by comparing the two cavities. This imposes that residual longitudinal motion (and θ_y tilt) be minimised such that the lateral grating translation effect dominates in the grating case.

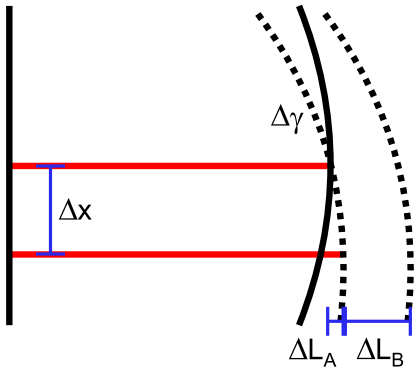

Figure D.6: Schematic diagram for misalignment of a cavity (two-mirror shown, optical-axis displacement equivalent for diffractive). The residual longitudinal motion $\Delta L = \Delta L_A + \Delta L_B$, the sum of its unavoidable and experimentally-introduced components.

The total residual longitudinal motion is given by $\Delta L = \Delta L_A + \Delta L_B$, as shown in Figure D.6. This has components ΔL_B due to non-linearity of the actuator and ΔL_A due to any error in centering the laser beam on the mirror. This is not the same as the unavoidable longitudinal motion calculated in Section 3.5.2 which assumed laser beam centering (prior to displacement of the eigenmode by end-mirror tilt). These are experimental errors which must be minimised.

The rotational axis θ_x' about which an arbitrary tilt occurs is separated from the θ_x rotational axis by the angle γ, which can be measured with a lever-arm and CCD camera. As noted above, this allows us to optimise the driving matrix for tilt over longitudinal motion on any rotational axis θ_x', then rotate the piezo such that θ_x' is coincident with θ_x. This is when the beam spot detected at the end of the lever arm sweeps parallel to the surface of the optical table.

Minimising the longitudinal motion will be achieved by adjusting the driving matrix to minimise a particular readout signal. This was achieved for the final result by using the EUCLID device which was used as an additional readout sensitive to longitudinal mirror motion and insensitive to angle. A CCD camera was used to image both scattered light from the laser beam on the

mirror surface, and to directly detect that light in transmission of the end-mirror to ensure that the EUCLID sensing beam interacted with the same spot on the end-mirror as the cavity eigenmode.

There is a minimum of both angular and longitudinal motion for the $(0,0,0)$ coupling matrix, when the matrix box attenuates the input voltage signal to zero. Similarly, under certain circumstances it is possible to shift from a nearly tilt-only driving matrix to a tilt-plus-longitudinal driving matrix and still see a reduction in signal (longitudinal via EUCLID or cavity locking error signal). This can occur if adjusting the matrix reduces the mirror motion such that it closely approaches the $(0,0,0)$ minimum, rather than the local minimum of tilt-only motion. Practically this can occur when the proportion of residual longitudinal motion increases, but the absolute value measured by EUCLID is lower because the overall attenuation of the matrix box has increased).

In order to avoid this $(0,0,0)$ minimum, a constant V_{RMS} sum of the inputs to the piezoelectric stacks was maintained. Such an approach will be successful at identifying a matrix for pure tilt motion, so long as $\kappa_{\mathrm{A}} \approx \kappa_{\mathrm{B}} \approx \kappa_{\mathrm{C}}$ (the coefficient linking applied voltage to extension of the piezo) is similar for all three piezos.

This approach will also, taken to the extreme case of having eliminated all residual longitudinal motion and with equal κ values, select Case Two in Figure D.3, since Equation D.4 represents the maximum voltage solution of Equation D.5 for a fixed tilt-motion (inversely and equivalently, the minimum tilt-motion solution for a fixed voltage). However, it is likely that longitudinal effects will dominate over this slight selection effect. Since we will transform θ_x' to θ_x by rotating the piezo through γ, the exact rotation axis θ_x' initially selected it is inconsequential.

In the process of selecting the best possible pure tilt case the following procedure was used: Initially a 117 V amplitude 10 Hz sawtooth-wave signal was applied to each of the three-axis-piezo's three piezoelectric actuators. The sum of the root-mean-square (RMS) of the three

actuator signals was 203.2 V. This generated pure longitudinal motion, which was checked using a 2 m long lever-arm and a CCD camera. The control-matrix of the three actuators was tweaked to minimize longitudinal motion in the following manner: Inverting two of three channels, simultaneously adjusting their attenuation with respect to the third, then adjusting their attenuation with respect to each other. The input power was then in- or decreased such that the 203.2 V RMS-sum was maintained, to allow equivalent comparison between cases with different attenuations on the different channels. The transfer functions of the final, optimised coupling matrix from the single input to the monitor-output port for each of the three piezos in the actuator is shown in Figure D.7. Note the roll-off at approximately 30 kHz. Each of the three possible 'pairs' of actuators (one-two; one-three; two-three) were combined and adjusted in this way to discover the best-performing pair (although the piezo is well-built and uniform, idiosyncrasies in the mounting of the mirror can have an affect). As this pair had to scan the beam across the grating striations in the x direction, the lever-arm was again used to determine the angle of scanning and the end-mirror was rotated so tilt occurred in θ_x. The residual longitudinal motion remaining is measured in Section 4.7.

D.4 Functioning of EUCLID

EUCLID is a black-box interferometric device. It contains one arm of a Michelson interferometer, with the second arm being provided by the surface of the object whose displacement is to be measured. Two beams of different polarization exist in the EUCLID interferometer. The phase change due to a path length difference between the arms of an interferometer is usually given by $\phi = 2\pi\Delta\zeta/\lambda$, and the displacement of one interferometer arm (in this case, the residual longitudinal motion of our cavity end mirror) is usually given by,

$$z_{\text{resid}} = \frac{\phi}{2\pi} \cdot \frac{\lambda}{2} \tag{D.6}$$

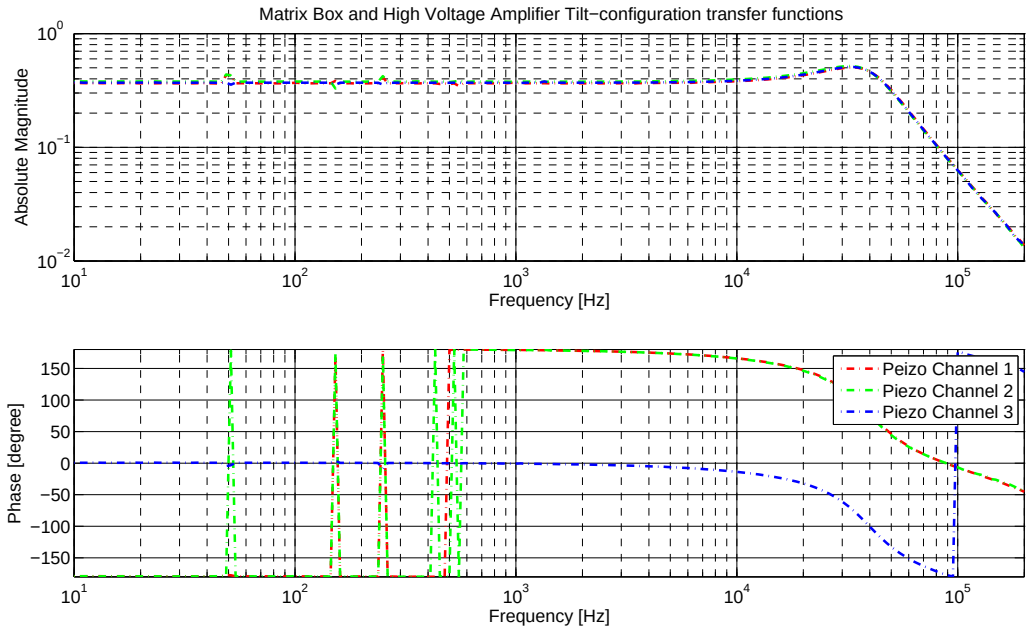

Figure D.7: The transfer functions of the final, optimised coupling matrix from the single input to the monitor-output port for each of the three piezos in the actuator.

For EUCLID this is in fact not the case [65] [66]. In order to create the angular insensitivity of the device, a polarising beam splitter was used to create the Michelson interferometer. Initial optics ensure that light composed equally of P and S polarisation drives the Michelson so there is equal power in each arm. Emplacing $\lambda/4$ wave plates in the interferometer arms rotates the polarisation by $\pi/2$ ($\pi/4$ on the outward trip and $\pi/4$ on the return trip). Thus the reflected light is wholly transmitted through the polarising beam splitter, and the transmitted light is wholly reflected from the polarising beam splitter. No light returns to the laser-diode source (port A in Figure 2.1). All light is directed to port B in Figure 2.1. A combination lens and mirror at port B forms a catseye which retroreflects the light back to the polarising beam splitter. The polarisation does not change with this reflection, so the light is entirely directed back into its arm-of-origin. There it experiences the $\pi/2$ polarisation shift again, whereupon it exits the Michelson interferometer through port A, where it is split off and detected in horizontal and vertical polarizations using additional waveplates and polarising beam splitters. It is the catseye which corrects for any angular misalignment (intentional tilt, in this case) of the surface to be

detected [67]. Since the light twice experiences the arms of the Michelson interferometer before detection, Equation D.6 acquires an additional factor of two, becoming,

$$\Delta z_{\text{resid}} = \frac{\phi}{2\pi} \cdot \frac{\lambda}{4} \tag{D.7}$$

The output signal required to determine this motion is ϕ. This can generally be obtained by [65] [66],

$$I_n = I_{\text{out}} \left(1 + V \cos\left(\phi + (n-1)\frac{\pi}{2}\right)\right) \tag{D.8}$$

where $V = (I_{\max} - I_{\min})/(I_{\max} + I_{\min})$. Therefore,

$$\phi = \arctan\left(\frac{I_1 - I_2}{I_2 - I_3}\right) - \frac{\pi}{4} \tag{D.9}$$

the difference outputs of which generate a circular Lissajous pattern when plotted against each other. In this case, EUCLID lacks a I_3 output, and therefore the Lissajous pattern is offset. Ignoring the reflection losses and the offsets, the EUCLID difference outputs are given by:

$$I_1 = \frac{I_{in}}{8}(\sin\Delta\phi + 1) \tag{D.10}$$

$$I_2 = \frac{I_{in}}{8}(\cos\Delta\phi + 1) \tag{D.11}$$

Practically, imperfections in the set-up - particularly that EUCLID uses a 850 nm beam and our optics are optimised for a 1064 nm laser - causes the Lissajous pattern to be elliptical, and a fitting routine was used to restore its circularity.

Displacement $z = \lambda/4$ produces a complete revolution of the Lissajous pattern, and therefore sets the maximum detectable displacement speed at [65] [66],

$$\frac{\delta z}{\delta t} = \frac{\lambda}{4} f_s \tag{D.12}$$

with sampling frequency f_s. For this purpose we wish to measure an oscillation, and this requires at least eight samples per repetition (four in each direction of the stroke). In order to be able to determine the extent of the position reliably (since circularity of the Lissajous pattern was restored with a fitting routine) an order of magnitude more samples is useful. Since the maximum sampling rate of our post-processing apparatus was approximately 50 kHz we were limited to a maximum testing rate of 500 Hz. EUCLID residual longitudinal motion results at 5, 50 and 500 Hz are presented for a range of input voltages to the tilt actuator in Section 4.7.

Appendix E

CALIBRATION OF FIGURE 4.9

E.1 Calibration of Figure 4.9 y-axis from measured voltages to longitudinal displacement per unit tilt

The results shown in Figure 4.9 were plotted on [m/rad] y-axis recalibrated from the [Volt/Volt] dimensionless y-axis of the raw tilt actuator driving voltage to feedback signal voltage transfer function shown in Figure E.3. To do this we calibrated the input voltage to the end-mirror tilt actuation system to a tilt [rad]; and calibrated the input voltage of the cavity locking actuator to an equivalent longitudinal displacement [m]. Considering Figure 4.5 then the input to end-mirror tilt is x_S (7 mV), which has been calibrated to the angle of tilt generated at DC using the level arm and WinCamD in Section 4.7, Figure 4.18, Table 4.4, obtaining end-mirror tilt of,

$$\frac{\Delta\theta_x}{x_S} = 5\left[\frac{\mu\text{rad}}{\text{V}}\right]. \tag{E.1}$$

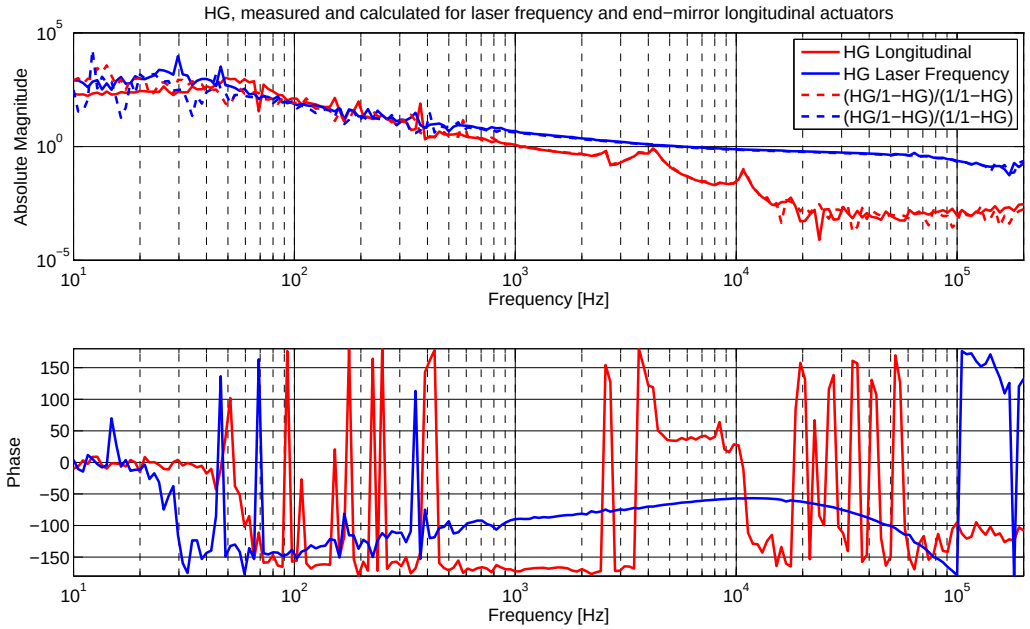

Figure E.1: Open-loop transfer functions with longitudinal end-mirror ($H_P G_P$) and laser frequency ($H_L G_L$) actuation. A factor 100 attenuation had to be applied to the H_P in order to lock the cavity at all.

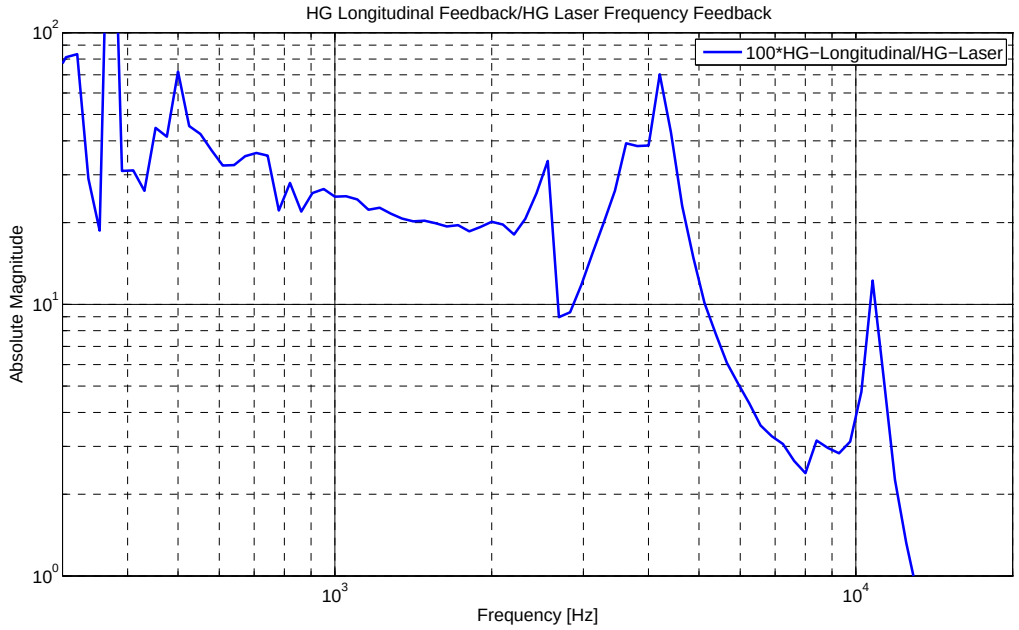

Figure E.2: Longitudinal end-mirror open loop transfer function divided by laser frequency actuation open loop transfer function.

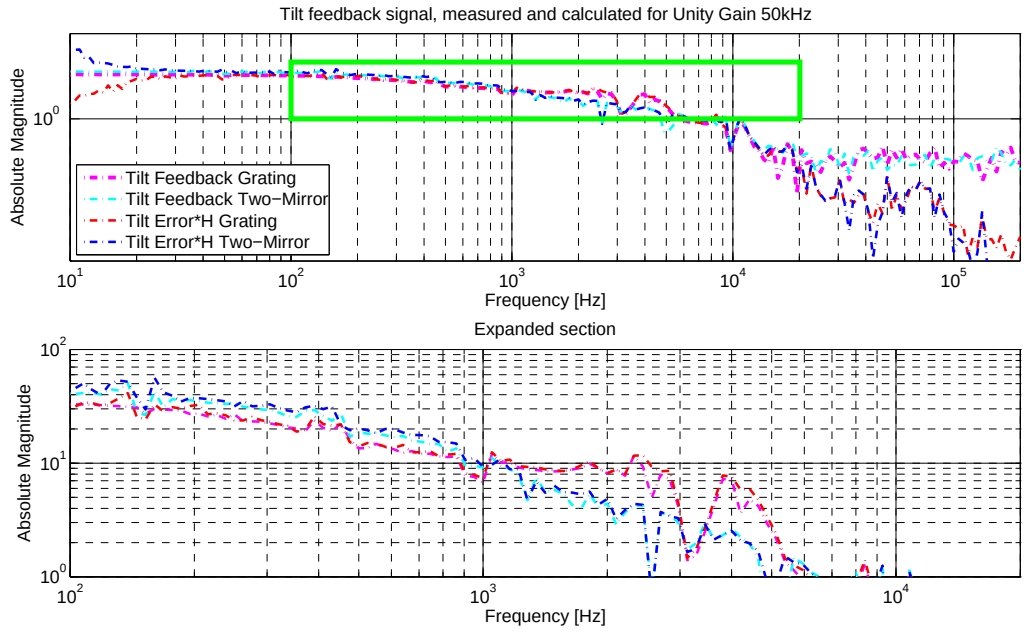

Figure E.3: Tilt to feedback signal transfer functions, calculated from measurements and measured directly, for both the two-mirror and grating cavities. This is the raw data for Figure 4.9 with an uncalibrated y-axis.

The complexity arises with knowing the conversion from cavity locking actuator input voltage x_C to equivalent longitudinal displacement created by the actuator. This should be a simple matter because the transfer functions of Figure E.3 measure x_C/x_S, and the particular input voltage x_S used was recorded (7 mV) and therefore the feedback signal x_C is known. Hence we should merely have to multiply this transfer function by the input voltage x_S and the specified longitudinal motion of the actuator in [meters per Volt]; however, the end-mirror actuator was required for creating the end-mirror tilt. Hence the feedback locking the cavity was applied to the laser frequency, and the conversion to equivalent longitudinal displacement is difficult for laser frequency feedback.

Considering Figure 4.5 we can see that the transfer function x_C/x_S was performed with the actuator and driving electronics of the laser (G_{1L}) locking the cavity where we would now prefer end-mirror longitudinal displacement had been used (G_{1P}). The desired result can be obtained

by,

$$G_{1L}\frac{G_{1P}}{G_{1L}} = G_{1L}\frac{G_{1P}G_2G_3H_P}{G_{1L}G_2G_3H_P}, \tag{E.2}$$

where the fraction can be determined by a simple division of open-loop transfer functions for each actuator, provided G_2, G_3 and H are constant. These measurements were then taken. The open-loop transfer function with the cavity locked using laser frequency is shown blue in Figure E.1, the end-mirror longitudinal motion transfer function (which required some reconfiguration of the end-mirror driving matrix) is shown red. G_2 and G_3 are naturally the same between the two different locks as the optics and detection system remain the same (this calibration measurement was carried out using the two-mirror cavity, though it could equally have been done with the grating cavity). It was necessary to apply a 20 dB attenuator to the (otherwise unchanged) servo to lock the cavity when feedback was applied to the end-mirror longitudinal position, resulting in $H_L = 100H_P$, which thus obtains,

$$G_{1L}\frac{G_{1P}}{G_{1L}} = G_{1L}\frac{G_PH_P}{G_LH_L}\frac{H_L}{H_P} = G_{1L}\frac{G_PH_P}{G_LH_L} \times 100, \tag{E.3}$$

this result is shown in Figure E.2. The low-frequency features below about 300 Hz are likely the result of acoustic noise, and the high-frequency features above 2.5 kHz are entirely from the transfer function of the end-mirror three-axis actuator. Even in an optimised pure-longitudinal mode this device has various resonances of its three individual piezos and their interactions. Hence the region of smooth phase between 300 Hz and 2.5 kHz was selected to determine a single ratio between these transfer functions of ~ 20 for all frequencies (recall that we are interested in the equivalent longitudinal displacement, not the actual voltage signal one would have to apply to this particular end-mirror longitudinal position actuator to generate that displacement). Thus we obtain the equivalent longitudinal motion via the equation,

$$\Delta L/x_S = \frac{x_C}{x_S} \times 20 \times \frac{\Delta L}{\Delta V} \tag{E.4}$$

where $x_S = 7\,\text{mV}$ and $\Delta L/\Delta V = 6\,\mu\text{m}/100\,\text{V}$ from the three-axis piezo specification (for longitudinal-only configuration). Dividing this Equation by Equation E.1 obtains,

$$\Delta L/\Delta\theta_x = \frac{x_C}{x_S} \times \frac{20 \cdot 6 \times 10^{-6}/100}{5 \times 10^{-6}} = \frac{1.2}{5}\left[\frac{\text{m}}{\text{rad}}\right]. \tag{E.5}$$

This calibration result for longitudinal motion per unit tilt is intuitively correct, as we know that translating the beam across a full period of the grating (1500 nm, requiring a 5×10^{-6} rad tilt with a 30 cm lever arm), creates a full 2π phase rotation; the same as for displacing the end-mirror through a full wavelength (1.064×10^{-6} m), so we expected approximately $(1/5)$[m/rad]. The result is shown plotted in Figure 4.9, which reproduces the raw data of Figure E.3 with an appropriately calibrated y-axis.

Bibliography

[1] K. S. Thorne. Gravitational Waves. In E. W. Kolb and R. D. Peccei, editors, *Particle and Nuclear Astrophysics and Cosmology in the Next Millenium*, pages 160–+, 1995. 1

[2] P. Aufmuth and K. Danzmann. Gravitational wave detectors. *New Journal of Physics*, 7:202–+, September 2005. 1, 2, 5, 8

[3] Andreas Freise. *The Next Generation of Interferometry: Multi-Frequency Optical Modelling, Control Concepts and Implementation*. PhD thesis, Universitat Hannover, 2003. 1, 159

[4] C Cutler and K.S. Thorne. An overview of gravitational-wave sources. *arXiv:gr-qc/0204090v1*, 2002. 2, 3, 4, 5

[5] Daniel Anthony Shaddock. *Advanced Interferometry for Gravitational Wave Detection*. PhD thesis, Australian National University, 2000. 2, 5

[6] A. N. Lommen and D. C. Backer. Using Pulsars to Detect Massive Black Hole Binaries via Gravitational Radiation: Sagittarius A* and Nearby Galaxies. *Astrophysical Journal*, 562:297–302, November 2001. 3

[7] Samuel J Waldman (for the LIGO Science Collaboration). Status of ligo at the start of

the fifth science run. *Classical and Quantum Gravity*, 23(19):S653–S660, 2006. 4, 5, 6, 14

[8] F Acernese et al. Virgo status. *Classical and Quantum Gravity*, 25(18):184001 (9pp), 2008. 4

[9] M. Punturo. The virgo sensitivity curve. *Virgo note VIR-NOT-PER-1390-51*, 2004. 7, 9, 10

[10] S. Braccini and VIRGO Collaboration. The VIRGO suspensions. *Classical and Quantum Gravity*, 19:1623–1629, April 2002. 8

[11] M. et al Ando. Stable Operation of a 300-m Laser Interferometer with Sufficient Sensitivity to Detect Gravitational-Wave Events within Our Galaxy. *Physical Review Letters*, 86:3950–3954, April 2001. 8

[12] S. Sato, S. Miyoki, S. Telada, D. Tatsumi, A. Araya, M. Ohashi, Y. Totsuka, M. Fukushima, and M.-K. Fujimoto. Ultrastable performance of an underground-based laser interferometer observatory for gravitational waves. *Physical Review D*, 69(10):102005–+, May 2004. 8

[13] M Punturo et al. The third generation of gravitational wave observatories and their science reach. *Classical and Quantum Gravity*, 27(8):084007, 2010. 8

[14] R. Passaquieti. Virgo an Interferometer for Gravitational Wave Detection. *Nuclear Physics B Proceedings Supplements*, 85:241–247, May 2000. 8, 9, 11, 12

[15] K. S. Thorne and C. J. Winstein. Human gravity-gradient noise in interferometric gravitational-wave detectors. *Physical Review D (Particles, Fields, Gravitation, and Cosmology)*, 60(8):082001–+, October 1999. 8

[16] P.R. Saulson. *Fundamentals of Interferometric Gravitational Wave Detectors*. World Sci-

entific, 1994. 9

[17] A. Buonanno and Y. Chen. Signal recycled laser-interferometer gravitational-wave detectors as optical springs. *Physical Review D*, 65(4):042001–+, February 2002. 9

[18] J. E. Mason. Signal extraction and optica design for an advanced gravitational wave interferometer. *Ph.D. Thesis*, November 2001. 11

[19] V. B. Braginsky, V. P. Mitrofanov, and K. V. Tokmakov. On the thermal noise from the violin modes of the mass suspension in gravitational wave antennae. *Phys. Letters A*, 186:18–20, 1993. 12

[20] Y. Levin. Internal thermal noise in the LIGO test masses: A direct approach. *Phys. Rev. D*, 57:659–663, January 1998. 12

[21] S. Rowan, J. Hough, and D.R.M. Crooks. Thermal noise and material issues for gravitational wave detectors. *Physics Letters A*, 347(1-3):25 – 32, 2005. Einstein Special Issue - Special Issue in celebration of this year's World of Physics and the centenary of Einstein's annus mirabilis. 13, 15

[22] J. Degallaix, C. Zhao, L. Ju, and D. Blair. Thermal lensing compensation for AIGO high optical power test facility. *Classical and Quantum Gravity*, 21:903–+, March 2004. 14

[23] R. W. P. Drever. Concepts for Extending the Ultimate Sensitivity of Interferometric Gravitational Wave Detectors Using Non-transmissive Optics with Diffractive or Holographic Coupling. In *Proceedings of the Seventh Marcel Grossman Meeting on recent developments in theoretical and experimental general relativity, gravitation, and relativistic field theories*, pages 1401–+, 1996. 15

[24] A. Bunkowski, O. Burmeister, D. Friedrich, K. Danzmann, and R. Schnabel. High reflectiv-

ity grating waveguide coatings for 1064 nm. *Classical and Quantum Gravity*, 23:7297–7303, December 2006. 15

[25] R. Nawrodt, A. Zimmer, T. Koettig, T. Clausnitzer, A. Bunkowski, E. B. Kley, R. Schnabel, K. Danzmann, S. Nietzsche, W. Vodel, A. Tünnermann, and P. Seidel. Mechanical Q-factor measurements on a test mass with a structured surface. *New Journal of Physics*, 9:225–+, July 2007. 15, 76, 89

[26] Antonio Perreca. *Experimental demonstration of Displacement Noise Free Interferometry*. PhD thesis, University of Birmingham, 2010. 16, 182

[27] K.-X. Sun, M. M. Fejer, E. Gustafson, and R. L. Byer. Sagnac Interferometer for Gravitational-Wave Detection. *Physical Review Letters*, 76:3053–3056, April 1996. 16

[28] J. Hallam, S. Chelkowski, A. Freise, S. Hild, B. Barr, K. A. Strain, O. Burmeister, and R. Schnabel. Coupling of lateral grating displacement to the output ports of a diffractive Fabry-Perot cavity. *Journal of Optics A: Pure and Applied Optics*, 11(8):085502–+, August 2009. 18, 64, 145, 157

[29] J. Mizuno and I. Yamaguchi. Method for analyzing multiple-mirror coupled optical systems. *Journal of the Optical Society of America A*, 16:1730–1739, July 1999. 20, 29

[30] Jun Mizuno. *Comparison of optical configurations for laser-interferoemtric gravitational-wave detectors*. PhD thesis, Universitat Hannover, 1995. 20, 157

[31] G. B. Arfken and H. J. Weber. *Mathematical methods for physicists 6th ed.* 2005. 21, 42

[32] E. Hecht and A. Zajac. *Optics 4th (International) Edition*. Addison-Wesley Series in Physics, Reading, Mass.: Addison-Wesley, 2003. 23, 50

[33] A. Bunkowski, O. Burmeister, K. Danzmann, and R. Schnabel. Input-output relations for

a three-port grating coupled fabry-perot cavity. *Opt. Lett.*, 30:1183–1185, 2005. 25, 28, 56, 86, 158, 168

[34] E. D. Black. An introduction to Pound-Drever-Hall laser frequency stabilization. *American Journal of Physics*, 69:79–87, January 2001. 27

[35] A Freise. *FINESSE 0.99.8 User manual*. University of Birmingham, 2008. 31, 159

[36] James E. Mason. *Signal Extraction and Optical Design for an Advanced Gravitational Wave Interferometer*. PhD thesis, California Institute of Technology, 2001. 32

[37] A.E. Siegman. *Lasers*. University Science Books, 1986. 33, 34, 35, 37, 125

[38] B. Friedland. *Control system design: An Introduction to State Space Methods*. McGraw-Hill, New York, 1986. 39

[39] R. W. P. Drever, J. L. Hall, F. V. Kowalski, J. Hough, G. M. Ford, A. J. Munley, and H. Ward. Laser phase and frequency stabilization using an optical resonator. *Applied Physics B: Lasers and Optics*, 31:97–105, June 1983. 41

[40] Eric Black. Notes on the pound-drever-hall techniques. LIGO Technical Note, 1998. LIGO-T980045-00-D. 41, 44

[41] T. Day. *Frequency-Stabilized Solid State Lasers for Coherent Optical Communications*. PhD thesis, STANFORD UNIVERSITY., 1991. 41

[42] Eric D. Black, Akira Villar, Kyle Barbary, Adam Bushmaker, Jay Heefner, Seiji Kawamura, Fumiko Kawazoe, Luca Matone, Sharon Meidt, Shanti R. Rao, Kevin Schulz, Michael Zhang, and Kenneth G. Libbrecht. Direct observation of broadband coating thermal noise in a suspended interferometer. *Physics Letters A*, 328(1):1 – 5, 2004. 48, 76

[43] The Virgo Collaboration. Advanced virgo preliminary design. Technical report, Virgo, 2008. 49, 65, 71, 74, 83, 84, 95

[44] H von Helmholtz. *J. f. Math.*, 57:7, 1859. 50

[45] G Kirchhoff. *Berl. Ber.*, page 641, 1882. 50

[46] G Kirchhoff. *Ann. d. Physik.*, 18:663, 1883. 50, 53

[47] M. Born and E. Wolf. *Principles of Optics, chapter 8*. October 1999. 50, 51, 52, 53

[48] H. C. Scientific Books: Treatise on Light, April 1913. 50

[49] K. X. Sun and R. L. Byer. All-reflective Michelson, Sagnac, and Fabry-Perot interferometers based on grating beam splitters. *Optics letters*, 23(8):567–569, April 1998. 53, 77

[50] A. Bunkowski. *Laser Interferometry with Gratings*. PhD thesis, 2006. 54, 77, 122

[51] A. Bunkowski, O. Burmeister, P. Beyersdorf, K. Danzmann, R. Schnabel, T. Clausnitzer, E.-B. Kley, and A. Tünnermann. Low-loss grating for coupling to a high-finesse cavity. *Optics Letters*, 29:2342–2344, October 2004. 55, 86, 124, 156

[52] A. Freise, A. Bunkowski, and R. Schnabel. Phase and alignment noise in grating interferometers. *New Journal of Physics*, 9:433–+, December 2007. 57, 62, 64, 68, 69, 70, 72, 78, 79, 83, 90, 91, 97, 152, 159, 160, 170

[53] L. Li and J. Hirsh. All-dielectric high-efficiency reflection gratings made with multilayer thin-film coatings. *Optics Letters*, 20:1349–1351, June 1995. 77

[54] M. D. Perry, R. D. Boyd, J. A. Britten, D. Decker, B. W. Shore, C. Shannon, and E. Shults. High-efficiency multilayer dielectric diffraction gratings. *Optics Letters*, 20:940–942, April 1995. 77

[55] T. Clausnitzer, J. Limpert, K. Zöllner, H. Zellmer, H.-J. Fuchs, E.-B. Kley, A. Tünnermann, M. Jupé, and D. Ristau. Highly efficient transmission gratings in fused silica for chirped-pulse amplification systems. *Appl. Opt.*, 42:6934–6938, December 2003. 77

[56] T. Clausnitzer, E.-B. Kley, A. Tünnermann, A. Bunkowski, O. Burmeister, K. Danzmann, R. Schnabel, S. Gliech, and A. Duparré. Ultra low-loss low-efficiency diffraction gratings. *Optics Express, vol. 13, Issue 12, p.4370*, 13:4370–+, June 2005. 88, 89, 122, 168

[57] A. Bunkowski, O. Burmeister, K. Danzmann, R. Schnabel, T. Clausnitzer, E.-B. Kley, and A. Tünnermann. Demonstration of three-port grating phase relations. *Optics Letters*, 31:2384–2386, August 2006. 122

[58] MM. CH. Fabry and A. Perot. Théorie et applications d'une nouvelle méthode de spectroscopie interférentielle. *Annales de Chimie et de Physique*, 16(115), 1899. 122

[59] M. P. Edgar, B. W. Barr, J. Nelson, M. V. Plissi, K. A. Strain, O. Burmeister, M. Britzger, K. Danzmann, R. Schnabel, T. Clausnitzer, F. Brückner, E.-B. Kley, and A. Tünnermann. Experimental demonstration of a suspended diffractively coupled optical cavity. *Opt. Lett.*, 34(20):3184–3186, 2009. 125, 145, 146, 150

[60] B. Barr, M. Edgar, J. Nelson, M. Plissi, S. Huttner, B. Sorazu, K. Strain, O. Burmeister, M. Britzger, D. Friedrich, R. Schnabel, K. Danzmann, J. Hallam, A. Freise, T. Clausnitzer, S. Bruckner, E-B. Kley, A. Tunnermann, B. Barr, K. A. Strain, O. Burmeister, and R. Schnabel. Translational, rotational and vibrational coupling into phase in diffractively-coupled optical cavities (awaiting publication). 2011. 145, 149

[61] Gerhard Heinzel. *Advanced optical techniques for laser-interferometric gravitational-wave detectors*. PhD thesis, MPI fuer Quantenoptik, 1999. 160

[62] J. Mizuno and I. Yamaguchi. Method for analyzing multiple-mirror coupled optical systems.

Journal of the Optical Society of America A, 16:1730–1739, July 1999. 160

[63] S Hild, G Losurdo, and A Freise. Sensitivity options for the advanced virgo preliminary design. Technical report, Virgo, 2009. 170

[64] E. Morrison, D. I. Robertson, H. Ward, and B. J. Meers. Experimental demonstration of an automatic alignment system for optical interferometers. *Appl. Opt.*, 33:5037–5040, August 1994. 170

[65] C. C. Speake and S. M. Aston. Interferometric sensing for drag-free satellites. In J. Hough & G. H. Sanders, editor, *Society of Photo-Optical Instrumentation Engineers (SPIE) Conference Series*, volume 5500 of *Presented at the Society of Photo-Optical Instrumentation Engineers (SPIE) Conference*, pages 120–128, September 2004. 239, 240

[66] C. C. Speake and S. M. Aston. An interferometric sensor for satellite drag-free control. *Classical and Quantum Gravity*, 22:269–+, May 2005. 239, 240

[67] C.C Fabian, E.P-A; Speake. Mirror tilt immunity with the cat's eye reflectors. *Journal of Applied Optics (in press)*, 2011. 240